Author Manuscript
Author Manuscript
Author Manuscript
Author Manuscript

HHS Public Access
Author manuscript
Chem Rev. Author manuscript; available in PMC 2023 December 21.

Published in final edited form as:
Chem Rev. 2022 July 27; 122(14): 12046–12109. doi:10.1021/acs.chemrev.1c01025.

Catalysis and Electron Transfer in *de Novo* Designed Metalloproteins

Karl J. Koebke[a], **Tyler B. J. Pinter**[a], **Winston C. Pitts**[a], **Vincent L. Pecoraro**[a,*]
[a]: Department of Chemistry, University of Michigan Ann Arbor, MI 48109 USA

Abstract

One of the hallmark advances in our understanding of metalloprotein function is showcased in our ability to design new, non-native, catalytically active, protein scaffolds. This review highlights progress and milestone achievements in the field of *de novo* metalloprotein design focused on reports from the past decade with special emphasis on *de novo* designs couched within common subfields of bioinorganic study: heme binding proteins, mono-metal and di-metal containing catalytic sites, and metal-containing electron transfer sites. Within each subfield, we highlight several of what we have identified as significant and important contributions to either our understanding of that subfield or *de novo* metalloprotein design as a discipline. These reports are placed in context both historically and scientifically. General suggestions for future directions that we feel will be important to advance our understanding or accelerate discovery are discussed.

Graphical Abstract

---

[*] Corresponding Author: vlpec@umich.edu.

The authors declare no competing financial interest

Author Manuscript

Author Manuscript

Author Manuscript

Author Manuscript

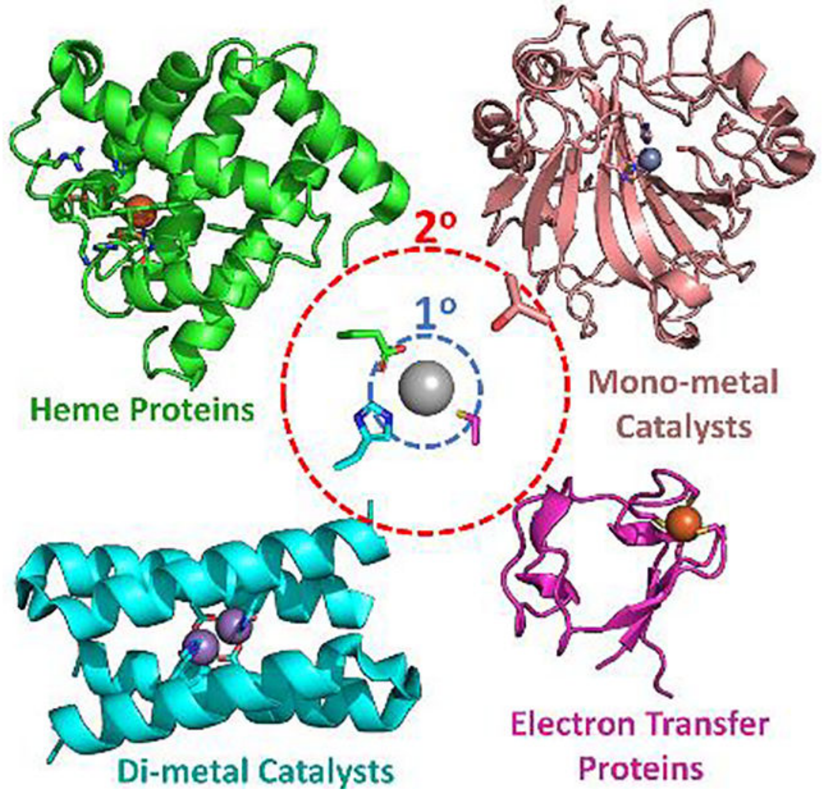

1. Introduction

De novo protein designers strive to create proteins from first principles, testing our understanding of the protein sequence-structure-function relationship by designing well folded and functional protein sequences without deferring to nature.[1–2] Focusing on metalloproteins (those in which a bound metal is necessary for function) the goal becomes similar to that of enzyme design, to correctly position a number of amino acid side chains relative to one another in order to confer function.[3] However, unlike Directed Evolution or protein re-engineering, which utilize pre-existing scaffolds found naturally in the biosphere, the *de novo* approach must also establish defined sequences that will confer a desired protein architecture such as α-helical coiled coils or helical bundles as their starting points. Replicating the metal coordination environments of metalloproteins in non-native scaffolds erases many interactions outside of the primary coordination sphere such as secondary sphere or long-range interactions. This allows researchers to determine characteristics of the primary sphere within a generic protein environment. Using Copper nitrite reductase as an example, techniques using native protein scaffolds can investigate the effects of secondary coordination sphere residues by mutating these residues to Ala to break their function or transplant the primary sphere into a native protein scaffold to try to build in that function but the complicated nature of these systems makes it difficult to investigate fundamental questions (Figure 1).[4–5] *De novo* protein design allows the primary sphere to be separated from native protein folds in a way reminiscent of small molecule models while maintaining aqueous solubility.[6–7] As the metalloprotein design field has matured, researchers have

Author Manuscript

Author Manuscript

Author Manuscript

Author Manuscript

developed more complex design strategies which aim to incorporate interactions beyond the primary coordination sphere to determine the effects of these longer-range interactions by building these systems from the ground up. This review will highlight work from the last ten years focused on four *de novo* designed metalloprotein subfields: porphyrin binding proteins, monometallic enzymes, bimetallic enzymes, and metal-containing electron transfer proteins. Within each subfield we discuss how these studies have advanced our understanding of the simplest functional unit of the parent metalloenzyme. Throughout, we highlight specific strategic design approaches to incorporate interactions beyond the primary coordination sphere. Finally, we consider potential future directions within each subfield and for the *de novo* metalloprotein design community as a whole.

2. Heme Protein Design

Heme proteins have long fascinated the bioinorganic community perhaps because myoglobin was the first protein crystal structure solved by X-ray Diffraction.[8] While oxygen transport and storage is the most well-known function, heme-containing enzymes catalyze a broad range of reactions such as hydroxylation, halogenation, oxygenation, disproportionation of H_2O_2, as well as oxidation and haloperoxidation of organic molecules.[9–16] Heme protein design, therefore, has significant potential industrial, pharmaceutical, and biotechnological applications.

Evolution has tuned heme-containing enzymes to be stable and functional within the well-defined environment of biological systems. These native conditions may not be amenable to biotechnology applications so enzymes that function at elevated temperatures or within nonaqueous solvents are in constant high demand. Designed proteins that are functional in harsher environments would, therefore, be a boon to industry. Peroxidases are a particularly tantalizing enzyme target as they catalyze oxidative reactions on a variety of substrates using only water and H_2O_2.[17–18] High production costs and protein stability issues of native enzymes make peroxidases and other heme proteins valuable targets to protein designers. *De novo* enzymes are also often more promiscuous than native enzymes, acting more like their primordial counterparts, which can be a boon or bane depending on the scope of the intended application.[19]

In this section, we review work on *de novo* designed heme enzymes within the last ten years. Specifically, we highlight work by the DeGrado and Lombardi labs on whole scaffold redesign, c-type maquettes of the Anderson lab, and pH dependent ligation within a helical structure. Several reviews dedicated to a historically complete and comprehensive discussion on heme protein design are recommended for interested readers.[20–21]

2.2. Covalent Heme Attachment

One of the complications of *de novo* heme enzyme design is leaving an open coordination site for substrates after binding the cofactor. A common approach is to attach the porphyrin to the peptide scaffold covalently. For example, the Pavone lab has previously used deuterohemin covalently attached to two peptides to create bis-His coordinated artificial heme-protein mimics within a minimal protein environment. Although simple, these constructs have been shown to adopt well-defined secondary and tertiary geometries with the

Author Manuscript Author Manuscript Author Manuscript Author Manuscript

deuterohemin correctly positioned between the two helical peptides.[22–23] More recently, the scaffold has been modified to remove one of the heme-coordinating His ligands to mimic the 5 coordinate active site of a heme enzyme.[24] Mimochrome VI used two different peptides (one 14 AA long with a ligating His and the other 10 AA long) covalently attached to the porphyrin to create a design where the heme-iron would be bound with a single His, leaving the distal Fe site open for catalysis (Figure 2). This strategy was adapted from previous work with cobalt porphyrins.[25–26]

The design of Mimochrome VI includes covalent bonds between the ring of the deuteroheme and Lys9 side chains of the two peptides. Interchain ion pairs were included to stabilize the secondary structure of each peptide. At extremely low pH (2.0) the UV-visible absorption spectral data were consistent with a high spin ferric porphyrin (S=5/2); as the pH was increased from 2.0 to 5.5 the absorption data indicated histidine binding to the axial face of the porphyrin with a pKa of 3.4.[27–28] Further increasing the pH from 6.5 to 8.5, spectral changes consistent with the replacement of a distal water by a hydroxide were observed with a pKa of 7.4, indicating that a 5-coordinate deuteroheme binding mimochrome was successfully developed.[29–30] Ligand binding to Mimochrome VI was observed using NO and CO for the ferric and ferrous forms, respectively.[31–33] Peroxidase activity of Mimochrome VI was assessed with H_2O_2 and 2,2’-azino-di(2-ethyl-benzothiazoline-6-sulfonic acid) (ABTS) or guaiacol.[34–35] Compared to horse radish peroxidase (HRP), Mimochrome VI has a k_{cat} 11-fold slower if both enzymes are assessed at their optimal pH conditions (pH 4.6 for HRP, pH 6.5 for Mimochrome VI) but turns over faster than HRP by 7-fold at neutral pH. Substrate recognition, however, was notably unremarkable as indicated by K_M values in the micromolar range similar to that of H42A variants of hHRP.[36] It is useful to acknowledge that K_M in many of the studies presented in this review may have a different meaning than its standard interpretation due to the lack of a defined substrate binding site in many *de novo* metalloproteins. Similar results were observed for the nitration of phenol with NO_2^-; Mimochrome VI has the highest product yield for a peroxidase mimic, comes within 4-fold k_{cat} of soybean peroxidase, and remains active under conditions that inactivate the native enzyme.[37–38]

Mimochrome VI’s success as a peroxidase mimic demonstrates that a simple design with a mono-His coordinated porphyrin can achieve catalytic efficiencies approaching those of native enzymes without any intentionally designed secondary coordination sphere interactions. Next, the Pavone lab sought to increase the complexity of their design strategy and incorporate some of the secondary coordination sphere interactions present in native peroxidases.[39] They designed hydrogen bonding interactions between the proximal His and a nearby Asp as well as a distal Arg residue, based on HRP.[40–41] The Mimochrome scaffold was too small to include additional design elements, so a four helical bundle (4HB) scaffold, that is based on the bis Met heme found sandwiched between two Fe_2 containing 4HB’s in bacterioferritin, was selected (Figure 3).[42] While 4HB based heme binding protein scaffolds are well established, only a few examples contain the unsaturated coordination site necessary for catalytic activity.[43–44]

The final MP3 design is a 4HB scaffold based on the heme binding site in bacterioferritin, using a pair of minimized helical bundles from this protein. The two heme-coordinating Met

Author Manuscript

Author Manuscript

Author Manuscript

Author Manuscript

residues were replaced, one with an axial His ligand, the other with a distal Ser to open the active site. The secondary sphere Asp and Arg residues found in HRP were positioned along the helices at appropriate geometries (Figure 4). The porphyrin was covalently bound to the peptides via Lys residues, similar to the strategy used in Mimochrome constructs. It is debatable whether a minimized protein structure like this is truly *de novo* metalloprotein design. We have included these kinds of investigations in our review because the structures are similar to those created by more standard *de novo* design and through them we can learn many of the same lessons about secondary coordination sphere interactions.

MP3 displays good peroxidase activity with K_M(ABTS) of 0.34 mM, K_M(H_2O_2) of 172 mM and k_{cat} of 535 s^{-1} and was most active at pH 6.5 in the presence of 40% 2,2,2,-trifluoroethanol (TFE) to stabilize its alpha helical structure. MP3 had a pH titration monitored by UV-Vis found three transitions with midpoints at 3.37, 5.91, and 7.62 assigned to His coordination, deprotonation of the proximal Asp, and water exchange to hydroxide, respectively. Based on magnetic circular dichroism (MCD) analysis, the ligation of His at low pH initially pushes the spin equilibrium towards low spin, but upon hydroxide binding the system becomes predominantly high spin. This differs from what is observed for native HRP and more closely resembles Mb at high pH.[45–47] Further investigation with electron paramagnetic resonance (EPR) spectroscopy found that this discrepancy was likely due to the distal Arg in MP3 weakly interacting with the bound hydroxide. Compared to the original Mimochrome VI design without secondary sphere interactions, MP3 successfully increased the k_{cat} from 371 s^{-1} to 535 s^{-1}, but the K_M for both H_2O_2 and ABTS also increased by 3–5 fold leading to an overall catalytic efficiency decrease of 2–3 fold. These values are comparable to R38A-hHRP in which the secondary sphere Arg residue has been removed, consistent with spectroscopic analysis that the Arg in MP3 does not interact with the bound substrate as the design intended.[48] The authors suggested that the MP3 distal Arg may have more structural freedom and is, therefore, not oriented correctly for catalysis. Future peroxidase designs would focus on improving this interaction and add a distal His residue not included in MP3.

2.2. Bringing Stability to Heme Design

Despite successes in *de novo* designing proteins that bind porphyrin cofactors, structural information that could be used to improve function rationally was lacking because many of these maquette-based designs exhibit multiple structures in solution.[49–52] Only one *de novo* heme binding protein crystal structure was available at the time; it was crystallized in the absence of heme, showed no obvious space for cofactor binding, and so provided little information on the holo structure.[53] To address this gap in knowledge, Polizzi and DeGrado set out to create a hyperstable porphyrin binding protein that would permit systematic structural analysis by considering contributions to binding from the entire scaffold. This strategy was inspired by studies of native proteins where long-distance amino acid residues can have significant impact on ligand interactions.[54–57]

The DeGrado lab had previously attempted to incorporate this design philosophy using a step-wise approach where the tertiary structure was parameterized to form an antiparallel coiled-coil before hydrophobic packing; this resulted in porphyrin binding proteins lacking

Author Manuscript

Author Manuscript

Author Manuscript

Author Manuscript

unique conformations for high-resolution structure solutions.[58–60] Revisiting this idea, they interconnected the design of the ligand binding site and the hydrophobic core while including flexibility in the protein backbone, a first in *de novo* metalloprotein design.[61] This design was based on a previous *de novo* protein (SCRPZ2) which bound a much larger cofactor than the target Zn porphyrin, allowing the program space to repack the hydrophobic core around the bound ligand.[60] The ligand was manually docked into this scaffold, and small backbone changes were made using Backrub within the Rosetta program suite.[62] Several rounds of fixed-backbone sequence optimization, followed by minimization of the backbone and sidechains, changed 70% of the internal amino acids and used different rotamers for many of the remaining 30%. This scaffold, named PS1, was therefore designed to accommodate the porphyrin and ligand site (Figure 5).

Holo-PS1 is monomeric and displays impressive thermodynamic stability with an extrapolated melting temperature (T_m) above 120 °C. NMR structures of both the apo- and holo-PS1 were obtained and were remarkably similar. By redesigning the entire protein around the intended ligand, apo-PS1 retains the core packing structure of the holo state, predisposing it for binding the Zn porphyrin. Unlike the previously solved apo-heme maquette structure, apo-PS1 does not hydrophobically collapse its heme binding pocket, likely due to having predominantly Ala and Gly side chains surrounding this pocket. The authors also suggested that residues as far as 20 Å from the binding site were predisposed towards ligand binding.

This holistic protein design strategy was next applied to the problem of a two-domain protein.[63] Natural proteins often use a combination of well folded domains to enable more complex function.[64] Combinations like this allow for redox-active proteins which combine multiple cofactors for long range electron transfer as well as proteins with allosteric regulation where ligand binding at one domain controls a secondary catalytic domain.[65] Previous multiple domain designs were appended end-to-end or inserted, but none had redesigned the complex from scratch.[66–68] Pirro and DeGrado combined the porphyrin binding domain of PS1 with an Fe_2 binding domain from the Due Ferri (DF) family detailed in section 4.1.[69] While previous protein design studies have incorporated multiple cofactors, the lack of high-resolution structures limited their instructive value.[50, 58, 70–75]

Structural comparison between apo- and holo-PS1 indicated that the apo state exists in a more open conformation. This could enable ZnP binding to PS1 to affect the properties of a nearby DF catalytic site. Both PS1 and DF are 4HB scaffolds, but they have different helical offsets and registers, making their direct combination a challenge. The first step was to determine the optimal positioning of the two bundles relative to one another (Figure 6). This process was simplified by reducing the number of variable search parameters to two, the distance separating the domains and the rotation angle between the two bundles, before using the search program MASTER to determine designable confirmations on a contour plot.[76] The optimum orientation found by this analysis was 21.5 Å apart and −33.8° to accommodate the left handed twist of the two bundles. To limit the impact on function in fusing the functional sites together, sequence redesign was limited to helical segments that connected the bundles and were well beyond the first or second shell of cofactor binding sites.

Author Manuscript Author Manuscript Author Manuscript Author Manuscript

The structure of the first construct in this series, DFP1, with both ZnP and Zn_2 bound, was solved to 3.5 Å. The two cofactors were 12 Å apart and the crystal structure matched the predicted computational design impressively well with RSMD of 0.8 Å. The design strategy of DFP1 focused on stability, but this tight packing left the DF active site inaccessible to substrates. Similar issues with making DF proteins catalytically active have been investigated within the DF series themselves. Using a strategy established from studies of the DF family, the active site was opened up by mutating four nearby Leu and Ala residues to Gly to create DFP3. Even with four highly disruptive mutations like this, DFP3 was exceptionally thermostable with T_m in 4 M guanidinium of 71° C for $Zn(II)_2$-DFP3, 83.2° C for ZnP-DFP3 and 87.3° C for $Zn(II)_2$-ZnP-DFP3. UV-visible absorption spectra of $Co(II)_2$-DFP3 (Co(II) is often used as a spectroscopic probe of Zn(II) coordination) showed pentacoordinate Co-coordination indicating greater ligand access compared to DFP1.[69, 77–79] Finally, the activity of $Fe(II)_2$-DFP3 and $Fe(II)_2$-ZnP-DFP3 were compared to determine the effects of ZnP binding on DF catalysis using the two electron oxidation of 4-aminophenol (4AP) to quinone imine. Both forms showed similar overall catalytic efficiency but upon ZnP binding, K_M increased 4-fold while k_{cat} decreased 7-fold. Molecular Dynamics (MD) simulations to investigate this apparent allosteric effect on catalysis implicated a shift in the Tyr18 residue in the second coordination sphere upon ZnP binding. In the absence of ZnP, Tyr18 occupies an undesigned conformation, interacting with a backbone carbonyl instead of the intended Glu72 primary coordination sphere ligand. Upon ZnP binding, the Tyr18 repositions to its designed confirmation within the intended H-bond network due to steric blocking by the large cofactor. Thus, allosteric regulatory communication was demonstrated within a designed scaffold, opening up another dimension of complexity to protein designers.

Thus far, the ZnP binding scaffolds from the DeGrado lab were redox inactive and not designed for ligand binding. A common feature of heme enzymes is binding dioxygen or H_2O_2 to make high-valent species.[15, 80] This requires that substrates have access to the active site and that the powerful oxidants created are controlled from reacting with the protein itself. The DeGrado lab extended their previous design of the ZnP-PS1 to bind Mn diphenylporphyrin (MnDPP) and explored how these questions could be tackled by protein design.[81] Mn-aryl porphyrins can perform a variety of oxidative reactions like those of native hemes using high-valent Mn(IV) or Mn(V) species.[82]

The challenge of incorporating a MnDPP cofactor is that the design must balance substrate access with control of the high-valent species. Natural oxidases and peroxidases often allow access for H_2O to the cofactor, which is displaced during the reaction.[15, 83] By including a dioxygen bound to the Mn during design, the authors hypothesized that substrates would be able to access the cofactor in the final design (Figure 7). MPP1 was designed by positioning the MnDPP cofactor along the central axis of the bundle using the backbone from PS1 and extending the protein scaffold to fully encompass the larger cofactor. Dioxygen from an oxy-p450 structure was positioned at the open coordination site of the MnDPP to maintain an open active site.[84]

Interior residues around the cofactor were cycled through an iterative flexible backbone design process similar to the design of PS1, with some restrictions. Trp and Tyr residues

Author Manuscript

Author Manuscript

Author Manuscript

Author Manuscript

were not allowed within 12 Å of the cofactor to avoid oxidation. Met and Cys were disallowed entirely to avoid undesirable heme ligation. Gly and Ala residues were used to surround the cofactor binding site to avoid hydrophobic collapse. Four variants with different loops were created; two showed signs of multiple conformations in solution similar to previous maquette designs. Of the remaining two, the final design, MPP1, was readily crystallized, had only 35% of its interior residues in common with the original PS1 scaffold, and showed no evidence for binding the original cofactor ZnP.

UV-visible absorption spectral data of MnDPP bound to MPP1 was consistent with 6-coordinate Mn(III), suggesting that the intended His/H_2O coordination design was correctly incorporated. Upon oxidation with $NaIO_4$, a Mn(V)-oxo intermediate species accumulated then slowly returned to Mn(III) with a half-life of 12 minutes.[85–87] Adding thioanisole to the reaction mixture greatly decreased the Mn(V)-oxo intermediate's half-life and mass spectrometric analysis confirmed a methyl phenyl sulfoxide product was formed, showing that this intermediate is reactive and accessible to substrates as designed.[88–89] It is important to note that the cofactor alone is unable to produce this species. Instead, it is slowly decomposed in the presence of $NaIO_4$, suggesting that MPP1 stabilizes the Mn(V)-oxo species.

Holo-MPP1 was also the first *de novo* designed porphyrin binding protein crystal structure to be resolved to 1.75 Å. Comparison of the crystal structure to the computational design showed remarkable similarity with the backbone having only 0.6 Å RMSD. The cofactor was also positioned precisely where it was designed to fit, differing by only 0.5 Å RMSD though it was rotated axially by 55 degrees. Two water molecules were positioned where the two oxygen atoms had been included in the design. Overall, this design strategy allowed for structural resolution of *de novo* porphyrin binding proteins for the first time and showed an impressive success rate as all four of the designed scaffolds correctly bound the cofactor, despite the fact that two showed signs of conformation averaging by NMR.

2.3. *C*-Type Maquettes

The maquette approach to *de novo* metalloprotein design has been adapted to a variety of different cofactors. Prior to the work of Anderson and Dutton, cofactors were usually incorporated *in vitro* while *in vivo* incorporation showed limited success.[90–91] Designed proteins have severely limited synthetic biology applications if the protein is not expressed in a functional form *in vivo*. *B*-type heme maquette designs had also been restricted to bis-His heme coordination sites, which are not suitable for enzymatic activity. Covalent attachment of a *c*-type heme would allow for protein engineering modifications without cofactor loss.[92–94] Towards this goal, Anderson and Dutton designed a maquette that could interface with cellular machinery to insert a *c*-type heme covalently (Figure 8).[95]

A previously reported *b*-type heme maquette, that reversibly bound oxygen similar to natural oxygen transports proteins and preferentially bound O_2 over CO, was used as the starting scaffold.[96] Loops were added between the dimeric sections of the maquette to permit more complex designs and a site for covalent attachment of a *c*-type heme was added to test if the cofactor would be incorporated *in vivo*. A survey of the Protein Data Bank (PDB) for *c*-type heme recognition sequences culminated in the sequence CIACH and this was built

Author Manuscript
Author Manuscript
Author Manuscript
Author Manuscript

into helix 2 of the scaffold and a His on helix 4 was included as a distal ligand. Lastly, His residues were designed into helices 1 and 3 to generate a potential secondary binding site for a *b*-type heme. This construct, named C2, was cloned into the pMal-p4x periplasmic expression vector which uses an *N*-terminal signal peptide and the sec translocon for periplasmic transport before *in vivo* cleavage.[97–98] *E. coli* co-transformed with a pEC86 vector containing the ccmA-H cassette was used for C2 expression so cells could produce the required cytochrome *c* maturation machinery.[99] Later attempts to incorporate the *c*-type heme *in vitro* after expression of apo-C2 proved unsuccessful, showing the necessity of the cytochrome *c* maturation machinery for this strategy. The authors proposed that the success of this strategy implies that the maturation machinery interacts with proteins in a dynamic or molten state, with broad specificity, for it to interact with a *de novo* designed scaffold.

In vivo incorporation of the *c*-type heme into C2 was confirmed by MALDI-TOF mass spectrometry. C2 was also resistant to acidified 2-butanone, which partitions non-covalently attached hemes, and showed an identical spectrum to that of horse heart cytochrome *c* using the pyridine hemochrome assay.[100–101] Fe(II/III) EPR and UV-visible absorption spectral data of C2 were consistent with a 6-coordinate bis-His *c*-type heme.[102] Surprisingly, despite significant modifications from the original design, C2 maintained the ability to reversibly bind O_2, which is uncommon in native *c*-type cytochromes.[103–106] This result suggests that while *c*-type heme proteins capable of oxygen transport are rare in nature, it is not due to intrinsic differences between the *b*- and *c*-type heme cofactors.

The porphyrin of Holo-C2 could also be demetallated, and the iron replaced with a zinc for light-activated electron transfer, without displacing the porphyrin. This is consistent with the cofactor being covalently linked to the protein.[107] Adding a *b*-type heme to this Holo-Zn-C2 construct quenched the observed fluorescence by 40%, suggesting that electron transfer can occur between the two porphyrin metal centers.[108] Given that native systems often closely pack *c*-type hemes for multi-heme electron transfer chains, the success of this electron transfer between porphyrins in a *de novo* system is particularly exciting for protein engineers. Covalent attachment of the cofactor also opens up additional interesting heme coordination sphere options such as His/Met to adjust cofactor redox potential or a 5-coordinate His for catalysis; these coordination modes are challenging to include in a *b*-type heme system.

Continuing from this work, Watkins and Anderson explored the robustness of this design strategy by creating a suite of *c*-type heme maquettes.[109] Their goal was to create a more stable *c*-type heme maquette which could be engineered for O_2 activation rather than O_2 binding. The original C2 maquette was a 138 AA antiparallel 4-helix bundle and bound O_2 analogous to neuroglobin, a 6-coordinate O_2 binding protein.[110] A suite of proteins was created from this original design. Each design had different *c*-type heme binding sites or covalent attachment points (Figure 9). Several constructs with multiple *c*-type heme binding motifs were also designed to attempt a multi-heme electron transfer chain. Seven new constructs were designed. *C*-type heme incorporation showed surprising robustness, with only a single construct of the new set (C3C4) displaying no *in vivo* heme incorporation. Importantly, all four single site *c*-type heme designs correctly incorporated the cofactor

Author Manuscript Author Manuscript Author Manuscript Author Manuscript

regardless of the position of the binding sequence, and all the constructs could bind a second *b*-type heme to form mixed B/C maquettes.

The hemes in all four mixed B/C type heme constructs differed in redox potential by about 40 mV while the one dual *c*-type heme construct had a 53 mV difference, a promising first step towards synthetic electron transfer chains of *c*-type hemes.[111] All of the new constructs were more thermodynamically stable than the original C2 (T_m = 35 °C) with C3 being the most stable (T_m = 59 °C). MD simulations with GROMACS MD and CHARMM found that the heme propionate groups of the C1 and C2 designs are positioned within the protein hydrophobic core, while those of C3 and C4 are oriented towards the solvent, forming salt bridges with nearby Lys residues (Figure 10).[112–113] The authors hypothesize that cofactor orientation was the driving force behind the improved thermodynamic stability of C3 and C4.

In vivo incorporation of a catalytic heme cofactor within a man-made protein is a major goal of synthetic biology as this could create enzymes applicable in a plethora of industrial applications as cheap, green catalysts.[50, 114–115] Towards this end, Watkins and Anderson redesigned one of the above mentioned stable *c*-type maquettes (C4) and opened up the active site to substrate access for catalytic activity.[116] Natural heme peroxidases contain a 5-coordinate *b*- or *c*-type heme iron with a single His residue bound to the metal.[15] The authors hypothesized that removing one of the His ligands from the C4 maquette would allow for peroxidase activity within the scaffold. C46 was created by removing the *b*-type heme binding site from C4 which improved the T_m from 51 °C to 84 °C. Next, C45 was created by removing the distal His on helix 2 (Figure 11). This created a mono-His ligated *c*-type heme maquette whose thermodynamic stability was unperturbed (T_m = 86 °C).

UV-visible absorption spectral data of C45 was consistent with those of cytochrome *c*, with a water occupying the “empty” axial coordination site. pH titrations exhibited a transition at 8.11, similar to that observed for hydroxide replacing water in Mb.[30, 104] O_2 binding to the more open construct is also an order of magnitude faster than in the original C4 construct. Imidazole titration of Fe(II) or Fe(III) C45 reproduces the spectral features of 6-coordinate *c*-type heme maquettes C4 or C46. Demonstrating that a 5-coordinate *c*-type heme had been incorporated successfully, the authors investigated its catalytic properties. They found that when H_2O_2 is mixed with C45 it can turn over ABTS with K_M (H_2O_2) 94mM, K_M (ABTS) 379 μM, k_{cat} 1200 s^{-1} and k_{cat}/K_M of 3.2×10^6 M^{-1} s^{-1} at an optimal pH of 8.6. This catalytic efficiency approaches that of native HRP (k_{cat}/K_M 5.13×10^6 M^{-1} s^{-1}), though the initial activation of H_2O_2 is about 400 times slower which the authors hypothesized was due to the lack of key secondary sphere amino acids.[41, 48] Compound I with a Trp radical was isolated by mixing H_2O_2 with Fe(III)-C45 in the absence of substrate and confirmed using UV-visible absorption and EPR spectral matching to cytochrome *c* peroxidase compound I.[117–118]

C45 recapitulates the activity of the native HRP, and thus showcases the power of man-made biocatalysts. C45 is resilient to high temperatures and organic solvents and is promiscuously catalytic with reactivity to guaiacol, *p*-anisidine, luminol, and the prodrug isoniazid. This promiscuity and *in vivo* cofactor incorporation make it a strong candidate for directed

Author Manuscript Author Manuscript Author Manuscript Author Manuscript

evolution approaches. Further work has explored the substrate and reactivity promiscuity of this construct and the application of directed evolution to *c*-type Maquettes to tune carbene transfer reactivity.[119–121]

Several natural heme proteins can perform carbene transfer to a nucleophile through a metallocarbenoid intermediate (Figure 12).[122–126] Stenner and Anderson hypothesized that if the same intermediate could be formed in C45, it might be capable of promiscuous carbene transfer. When Fe(III) C45 was mixed with ethyl diazoacetate (EDA) a carbene precursor spectral signature, consistent with that of carbene:iron porphyrin complexes, built up over 60 seconds and remained for up to 20 minutes without degradation.[127] Similar intermediate species were observed with more bulky benzyl-diazoacetate and tert-butyl-diazoacetate carbene precursors. The authors hypothesized that the inherent flexibility of the C45 *de novo* scaffold enables it to incorporate these bulky substrates. Compared to an engineered cytochrome *c* from *Rhodothermus marinus* (*Rma*-TDE) with established carbene transferase activity, C45 bound EDA more rapidly and possibly with a higher affinity while producing identical spectra.[128]

The metallocarbenoid intermediate of both C45 or *Rma*-TDE can perform carbene transfer with styrene, a common carbene acceptor.[122] Analysis of the C45 carbene transfer products by HPLC identified them as (*R*,*R*) or (*S*,*S*) enantiomers of the expected product with 77% enantiomeric excess of (*R*,*R*). Previous results by NMR indicated that C45 was in a transient structural state, a common property of *de novo* designed proteins, and it is interesting to note that this does not preclude high enantiomeric selectivity. Arguably, this flexibility is a factor in allowing substrate access to the active site. Directed evolution through successive rounds of error-prone PCR was used to invert C45's enantioselectivity from 77% *ee* of the (*R*,*R*) product to 99% *ee* of the (*S*,*S*) product. This new construct was named AP3.2 and differed from C45 by 8 mutations. Spectroscopic and electrochemical characterization of AP3.2 provided no obvious explanation as to why these mutations would lead to such a drastic change, a common result for random directed evolution methods.[129] A further push towards incorporating *c*-type maquettes within synthetic biology was made by showing that C45 could produce the NAD(P)H precursor niacin as part of a reaction cascade.[119] This suggests that it is possible to input C45 as part of a life-sustaining artificial reaction pathway from pyrrole to nicotinamide. Initial tests with C45 and a *Bacillus subtilis* esterase as a cascade *in vivo* look promising. Once incorporated into a strain with the native aspartate pathway for nicotinic acid mononucleotide production knocked out, this could become a life sustaining pathway and the first time a bacterium is reliant on a *de novo* metalloenzyme.[130–131]

2.4. Ligand Switching

The versatility of heme protein reactivity relies on variations in the iron coordinating ligands (His, Tyr, Cys, or Met) and modification of the heme binding environment through secondary sphere effects. While there are many examples of designed heme proteins that use His ligation, examples that use axial Cys ligation are relegated solely to small molecule mimics of heme proteins.[132–133] The Ivancich and Pecoraro labs investigated His and Cys as competing ligands to the same cofactor by presenting both within a single *de novo* protein.[134] This study used the GRAND family of peptides which have been extensively

Author Manuscript Author Manuscript Author Manuscript Author Manuscript

studied for the incorporation of transition metal or heavy binding sites using His and Cys residues.[135–138]

Free hemin was titrated into GRAND L16C L30H (GRL16CL30H) where the 16th helical position was mutated to Cys and the 30th position mutated to His. Heme was added at pH 7, but the pH could be reversibly changed from 6 to 11 without heme disassociation. UV visible absorption and EPR spectroscopies were used to characterize heme binding at each pH condition. At pH 7.14, a 5-coordinate heme iron UV visible absorption signal with an LMCT at 640 nm, similar to that of peroxidases, was observed.[15] This species' EPR spectrum was consistent with a high-spin Fe(III), indistinguishable from that of heme penta-coordinated to imidazole. These results indicate that the heme is bound to the His30 residue as an axial ligand, forming a 5-coordiante heme iron at neutral pH (Figure 13b). As the pH was increased to 9.5, the UV visible absorption and EPR spectra shifted, consistent with a 5-coordinate Cys ligated heme iron, with a Soret band at 397 nm and a broad LMCT band at about 625 nm (Figure 13a).[139–141] As pH continued to increase up to 10.5, the UV visible absorption spectra shifted to a split Soret, with peaks at 360 and 420 nm, and LMCT bands at 540 and 570 nm. This and the EPR spectral changes were consistent with a 6-coordinate Cys ligated species.[142–143] Similar equilibria and conversions between spin states have been reported for cytochrome P450 enzymes.[139, 144] In summary, when His and Cys ligands are present within this *de novo* construct, the heme iron is 5-coordinate His bound at neutral pH, converts to 5-coordinate Cys bound as pH increases to 9.5, and, finally, becomes 6-coordinate Cys with a hydroxide completing the coordination sphere when pH is increased to 10.5 and above (Figure 14). These assignments were confirmed using single binding site variants of each ligating residue (GRWL16C or GRWL30H). Redox studies confirmed that His or Cys ligation is maintained upon redox cycling.

Analytical ultra-centrifugation (AUC) analysis showed that heme incorporation converted GRWL16CL30H from a three-stranded coiled-coil (3SCC) to a four-stranded coiled-coil (4SCC). While this is unexpected, GRAND peptides can be converted to two stranded coiled coils at acidic pH conditions, and a conversion from parallel 3SCC to antiparallel 4SCC caused by minimal perturbations to the structure has literature precedent.[145–146] The heme to peptide binding ratio was confirmed as 1:2, indicating each 4SCC is capable of binding two heme cofactors. The authors hypothesized that the 4SCC construct is best described as an antiparallel dimer of dimers and that the pH switch between His and Cys coordination is due to weak imidazole coordination favoring heme dissociation at basic pH. Similar weak His ligation has been observed for other model systems.[147] Deprotonation of the competing Cys ligand at these pH conditions allows it to ligate in replacement of the His residue.

Future studies with this system will elucidate more clearly the binding of the heme prosthetic group in all three coordinated states. In addition, one might anticipate studies assessing the differential placement of His and Cys residues in other sequence positions in order to shift coordination preferences in this system. Finally, the reported reaction of ABTS when the heme has been activated by peroxide suggests that this system will have interesting reactivity that may be controllable through the simple expedient of changing pH.

Author Manuscript Author Manuscript Author Manuscript Author Manuscript

2.5. Summary

Heme and other porphyrin-containing scaffolds were some of the first *de novo* designed metalloproteins. Previously, these were almost exclusively 6-coordinate heme-iron systems that bound using nitrogenous ligands and were too thermodynamically flexible for high resolution structural information. The DeGrado and Lombardi groups have developed highly stable porphyrin binding scaffolds by treating the protein design holistically, redesigning the entire protein matrix around the cofactor. They used this strategy to design Zn-porphyrin binding constructs which were structurally characterized to high resolution as well as a Mn-porphyrin binding construct capable of catalysis (Figure 15).[61, 63, 81] The Pavone lab designed a heme protein with an open iron coordination site, permitting catalytic capabilities, by covalently attaching deutoerohemin to miniature peptide constructs. Their attempts to incorporate secondary sphere interactions in a second-generation construct did not improve peroxidase activity (Figure 15).[24, 39]

The Anderson lab created *c*-type maquettes that covalently incorporate *c*-type heme cofactors *in vivo* using native maturation machinery.[90, 109] They next made 5-coordinate designs of these constructs and showed they were catalytically active for a variety of reactivities (Figure 15).[116] Using directed evolution, they shifted the enantioselectivity for one reaction from 75% *ee* of one enantiomer to 99% *ee* of the other.[119–121] Lastly, the Pecoraro and Ivancich labs designed a construct that presented both His and Cys ligands to a heme and created a reversible pH-based ligation switch which may be used in later work to control reactivities by changing pH conditions (Figure 15).[134]

These examples demonstrate success in protein design beyond the primary coordination sphere of the metal and expand on the possibilities of *de novo* heme protein design. Interestingly, attempts to rationally design secondary sphere interactions were not shown to improve reactivity. One future milestone will be incorporation of substrate-activating secondary sphere residue interactions, similar to the approach of the Pavone lab working on MP3. Using *c*-type maquettes for covalent attachment, which permits more options for heme-iron ligation, and the DeGrado lab’s method of protein redesign are particularly intriguing approaches that could be used for this purpose. The His-Cys pH-based switch system of the Pecoraro and Ivancich labs requires further characterization before more complicated design elements, such as secondary sphere interactions, can be attempted. Taken together, the recent progress in designing *de novo* porphyrin binding proteins shows that there are intriguing design lessons to be learned and many more problems to solve before scientists can accomplish what Nature has been doing for millennia.

3. Non-Heme Designed Metalloenzymes

Following initial successes in designing heme proteins, the *de novo* metalloprotein design community branched out into a number of other metalloprotein families. We will first discuss work to incorporate mono-metal catalytic sites within *de novo* scaffolds. This includes work targeting the hydrolytic $ZnHis_3$ site of carbonic anhydrase (CA), the redox active catalytic $CuHis_3$ site of Cu nitrite reductase (CuNiR), and various work on superoxide dismutase (SOD) or Cu monooxygenases.[148–153] Designing a *de novo* mono-metal catalyst presents several challenges such as completing metal ion coordination sphere and enforcing

Author Manuscript Author Manuscript Author Manuscript Author Manuscript

preferred coordination geometry changes upon redox activity while maintaining sufficient active site flexibility for efficient catalysis.

3.1. Carbonic Anhydrase Mimics

We begin with work that purposefully or serendipitously created mimics of the CA $ZnHis_3$ site. CA is found throughout nature and is essential for a number of essential biological functions such as respiration and the regulation of pH through the reversible hydration of CO_2.[149] Human carbonic anhydrase II is one of the most efficient enzymes known with rates approaching the limit of diffusion.[154] The importance and well-studied nature of this enzyme, as well as its relatively simple primary coordination sphere, made it an appealing target for design (Figure 16). The Pecoraro lab specifically targeted CA activity due to the protein's threefold symmetric binding site. This was ideal as the lab had prior experience designing threefold symmetric Cys_3 heavy metal binding sites. The Kuhlman lab created metal-mediated *de novo* protein-protein interfaces that generated a CA mimic as a side effect. First, we will focus on work within three stranded coiled-coils (3SCCs).

Previous work within the Due Ferri system remarked on the difficulty of balancing structural stability and catalytic activity (see section 4.1).[78] The Pecoraro lab sought to attack this problem using two distinct metal binding sites within a 3SCC construct (TRIL9CL23H), a $ZnHis_3H_2O$ site for CA catalytic activity and a $HgCys_3$ site for structural stability.[155] This was the first example of a *de novo* designed mononuclear metalloenzyme and scaffold with two metal binding sites of different function. Hg(II)TRIL9CL23H was more thermodynamically stable than either the binding site in the absence of Hg(II) (apo-form) or the protein in the absence of the heavy metal binding site. Similar results had been observed in previous work using heavy metal binding peptides.[145, 156–159] This extra stability permitted structural analysis by protein crystallography, a feature that is uncommon with *de novo* designed metalloproteins. The crystal structure of Hg(II)Zn(II)TRIL9CL23H showed that the Zn(II) site was a structural mimic for the primary coordination sphere of CA (Figure 17).

Given these structural similarities, Hg(II)Zn(II)TRIL9CL23H was investigated for carbonic anhydrase activity by following *para*-nitrophenyl acetate (*p*NPA) hydrolysis and CO_2 hydration. At optimal pH conditions (9.5), Hg(II)Zn(II)TRIL9CL23H hydrolyzed *p*NPA for at least 10,000 turnovers with a k_{cat} of 3.8×10^{-2} s^{-1} and k_{cat}/K_M of 17.6 $M^{-1}s^{-1}$, an order of magnitude more efficient than the best reported small molecules at the time and only 100-fold less active than native h-CAII.[160–164] Previous work had shown that removing a critical secondary sphere Thr199 residue decreased the activity of h-CAII approximately 100-fold and shifted the pK_a of the bound water from 6.8 to 8.3.[154] These two observations were consistent with the lower activity and shifted pK_a of the designed peptide, supporting the hypothesis that Hg(II)Zn(II)TRIL9CL23H faithfully recapitulated the primary coordination sphere of CAII.[154, 165] CO_2 hydration by Hg(II)Zn(II)TRIL9CL23H showed similar results, with an efficiency roughly 70-fold faster than previously reported models and within 50-fold of CAII.[166–168] This study showcases the power of *de novo* metalloenzyme design to isolate a single component of catalysis (in this case the role of the primary coordination sphere) that would be difficult using native metalloenzymes where it can be difficult to separate the

Author Manuscript

Author Manuscript

Author Manuscript

Author Manuscript

impact of losing secondary sphere interactions from any other influences from the native scaffold.

Since Hg(II)Zn(II)TRIL9CL23H successfully mimicked the structural parameters of the primary coordination sphere of CA, the next step was to increase the complexity of the design and try to match the activity of the native enzyme. Towards this goal, the Pecoraro lab investigated the effect of the ZnHis$_3$ site's position within the scaffold.[169] Previous work with Cys$_3$ sites within 3SCC scaffolds showed that the helical position of the binding residue (a vs d) and the position of the site along the peptide scaffold can impact heavy metal binding properties, but this had not been explored with a catalytic center.[170–172] They removed the heavy metal binding site from the original design, creating TRIWL23H, and found minimal effects on both Zn(II) binding affinity and hydrolytic activity. While the heavy metal binding Cys$_3$ site is not beneficial to these parameters, it does stabilize the scaffold at higher pH conditions where catalytic activity is greatest and was maintained in later designs.

The first repositioned metal binding site construct was TRIL9HL23C in which the positions of the heavy metal and transition metal binding sites are swapped. Based on the previous crystal structure, one would expect the water bound to the more *N*-terminally located Zn(II)His$_3$ active site to be more solvent exposed, but catalytic efficiency remained similar to the original while Zn(II) affinity decreased by an order of magnitude. TRIL9CL19H was created next to determine the effect of moving the Zn(II)His$_3$ site from an a site in the heptad repeat to a d site and again Zn(II) affinity was significantly decreased (5-fold) more so than catalytic efficiency (< 2-fold decrease). Reaction kinetic evaluations of these constructs showed that repositioning the Zn(II)His$_3$ metal binding site towards the *N*-terminus of the scaffold increased substrate and solvent access (improving k_{cat}); similarly increasing K_M values meant the overall effect on catalytic efficiency was minimal. To summarize, this study showed that the three primary sphere ligands alone (3 His) are the only requirement for CA activity and that the active site can be repositioned within the 3SCC scaffold to modify features of catalysis such as substrate access.

Thus far the Pecoraro lab had explored CA activity of His$_3$ sites within C$_3$ symmetric 3SCC systems, but more recent work has sought to break this restraint through the formation of heterotrimeric 3SCCs. The formation of heterotrimeric 3SCCs had been accomplished by other labs without a metalloenzyme focus, but these solutions either required the use of all hydrophobic layers in the scaffold for heterotrimer formation or non-native amino acids.[173–175] Tolbert and Pecoraro instead created a design which used heavy metal templated assembly to create A$_2$B or AB$_2$ heterotrimers. Because there are 8 remaining core layers, this allowed for the incorporation of a metal binding site at the opposite end of the helical scaffold, which could provide either first or second coordination sphere asymmetric transition metal catalytic sites.[176] This strategy uses a Pb(II) ion bound in a trigonal pyramidal geometry to Cys residues in an a or d heptad position.[138, 177–178] By modifying the adjacent layer (toward the N terminal site for an a site cysteine or toward the C terminal layer for a d cysteine site) with an Ala (A monomer) instead of Leu (B monomer) in the secondary sphere a single A$_2$B heterotrimer was preferentially formed with a Cys or A$_2$B and AB$_2$ species with d Cys layers. Interestingly, similar discrimination

Author Manuscript

Author Manuscript

Author Manuscript

Author Manuscript

was not observed when Hg(II), which forms trigonal planar complexes, was utilized as the templating cation. Pb(II) heterotrimer specificity was evaluated by^{207}Pb NMR, a technique highly sensitive to the Pb(II) ion's environment. The d Cys A_2B or AB_2 heterotrimers were fully selective while the a Cys A_2B heterotrimer was about 80% of a mixed oligomer state.[177]

Crystal structures of Pb(II) bound Ala homotrimers determined that the Pb(II) ion pointed to the opposite pole of the helix then where the alanine substitution was incorporated. At the same time, the Cys residues rotated to place the thiolate sulfur atoms towards the cavity generated by replacing leucine with alanine. This same phenomenon was observed regardless of whether the Cys residues were in an a or d position (Figure 18). The cavity that forms when Ala is present fills with water molecules (these solvents are ejected by the more sterically demanding Leu) and were shown to form strong H-bonds to the thiolate sulfurs. The orientation of the waters with respect to the Sulfur atoms depended on whether the Cys was in an a or d layer. The authors hypothesized that the stabilizing force of these water molecules hydrogen bonding with the Pb(II) bound Cys residues counters the hydrophobic stabilization of introducing Leu into this position, leading to a low energy mixed layer of two Ala and one Leu.

Quantum Mechanics/Molecular Mechanics (QM/MM) simulations determined that the a and d Cys_3 positions were not identical in energy profile, instead the d layer exhibited larger energy differences between the desired and undesired oligomer forms leading to specific heterotrimer formation while the a Cys construct only preferentially formed A_2B heterotrimers. Substituting Pb(II) with Hg(II) in the Cys site or changing the position of the Ala/Leu layer both abolished heterotrimer formation, consistent with the authors' proposed mechanism. Once heterotrimer formation was confirmed, the authors next moved to coupling this to catalysis by combining the d Cys A_2B heterotrimer with a His_3 CA catalytic site with Leu, Thr, or Asp in the secondary coordination sphere. After determining that Zn(II) binding did not affect heterotrimer formation the authors investigated *p*NPA hydrolysis kinetics with varying secondary sphere layer compositions. Though modest (10–20%), the authors did observe enhancement of catalytic efficiency when a single Thr or Asp was incorporated within the secondary sphere layer compared to Leu_3, Thr_3, or Asp_3 layers. This strategy will be limited to systems that are insensitive to the presence of Pb(II) and which are not sufficiently oxidizing to modify the cysteines residues. Never-the-less, these results were a major breakthrough in conceptual *de novo* protein design as they open the door for preparing true dissymmetry in the outer or inner coordination spheres of catalytic centers embedded within simple peptidic constructs. It will be interesting to see whether this heterotrimeric 3SCC scaffold strategy can more greatly enhance other enzymatic activities in future work.

An alternative approach to avoid the 3-fold symmetry of the 3SCC scaffold is to prepare antiparallel 3-helix bundles (3HB) made from a single polypeptide chain. Towards this end, the Zn(II)His_3 site from Hg(II)Zn(II)TRIL9CL23H was incorporated into an asymmetric 3HB scaffold originally developed by the DeGrado lab called α_3D.[179–182] Previously, α_3D had been used to examine heavy metal binding to Cys_3 sites; α_3D H3 was made by mutating those same positions to His instead of Cys (L18H, L28H, L67H) (Figure 19).[183–184]

Author Manuscript

Author Manuscript

Author Manuscript

Author Manuscript

Compared to Hg(II)Zn(II)TRIL9CL23H, α_3D H3 bound Zn(II) 6-fold tighter but was 2.6-fold less efficient at CO_2 hydration. It is important to note that even with this activity decrease, α_3D H3 reacted faster than any small molecule mimics of carbonic anhydrase and fell within 1–3 orders of magnitude of native enzyme activity.[168, 185] These results suggest that the CA activity of a Zn(II)His_3 site (with a water completing an approximate tetrahedral zinc coordination sphere) is intrinsic, remaining active after installation in different scaffolds such as the 3SCC or 3HB.

In parallel with the Pecoraro lab work, the Kuhlman lab was developing *de novo* CA models, but with a focus on metal directed protein-protein interfaces. Enzymatic active sites often occur at protein interfaces, whether between hetero or homo oligomeric complexes.[186–187] On average, such interfaces feature cavities and clefts twice the volume of those on protein surfaces and are hypothesized to be a likely evolutionary pathway to the formation of new active sites.[188–189] Most previous work on *de novo* metalloprotein design had focused on creating a metal binding site within an existing scaffold, but little had been done on metal binding sites at protein-protein interfaces.[190] While an interesting target, the *de novo* design of a protein-protein interface remains a challenging problem due to the complex web of interactions that must be accounted for. Der and Kuhlman designed a *de novo* protein-protein interface between two helix-turn-helix motifs derived from the Rab4-binding domain of rabenosyn to test whether designed Zn binding interactions could overcome suboptimal protein-protein interface packing.[191–192] The design strategy used Rosettamatch, searching for monomeric proteins that could accommodate His_2 patches. The initial 600 hits from this search were filtered down to eight candidate scaffolds of which only one, MID1, was found to be expressed and form dimers in solution. MID1 had two His_4 Zn binding sites at the ends of the dimer bundle and hydrophobic residues (Met38, Tyr41, and Phe42) at the dimer interface. It bound Co(II), Zn(II), and Ni(II) with K_D's of 4300 nM, 410 nM, and less than 30 nM, respectively, with no measurable affinity for other divalent cations. When scaffolds that lacked either the $ZnHis_4$ binding site or hydrophobic interface residues were examined the authors found that while each design feature allows for weak dimer association alone, the combination of the two enable robust dimer formation.

MID1 was uncharacteristically amenable to protein crystallization for a *de novo* designed metalloprotein with apo, Co(II)-, and Zn(II)-bound crystal structures available. While the metal bound structures matched the computational designs, the orientation of the monomers in the apo structure were more antiparallel than the perpendicular orientation in the metal bound structures (Figure 20). Close inspection of the Zn(II)MID1 crystal structure showed that one of the His residues (His35) did not coordinate Zn(II) as intended, and that another His bound the Zn ion with δN rather than the ϵN. A series of Glu-containing mutants were created to make His_3Glu 4-coord Zn(II) binding sites, but no improvement in the binding affinity was observed.

Given the ability of metals to enforce protein-protein interactions, their inherent reactivity, and the increased likelihood of potential substrate clefts at these interfaces, Der and Kuhlman hypothesized that metal mediated protein interfaces would be catalytically active. The authors investigated the structural Zn(II) sites of MID1 for CA activity.[193] The previously published crystal structure of Zn(II)MID1 showed a $ZnHis_3$ metal

Author Manuscript Author Manuscript Author Manuscript Author Manuscript

binding site with a tartrate (from crystallization buffer) occupying the fourth coordination position (Figure 21). The size of the nearby binding pockets (6 Å and 4 Å deep) are sufficient for common CA substrates, so Zn(II)MID1's ability to hydrolyze *p*NPA or *para*-nitrophenylphosphate (*p*NPP) was investigated. Zn(II)MID1 hydrolyzes *p*NPA with a K_M of 0.42 mM, k_{cat} of 0.3 s-1, and k_{cat}/K_M of 630 M^{-1} s^{-1} compared to Hg(II)Zn(II)TRIL9CL23H at 23 M^{-1} s^{-1} or native CAII at 2550 M^{-1} s^{-1}.[155, 163] Extensive controls demonstrated that this activity arose from the ZnHis$_3$ site; inactive H35E and H12E variant crystal structures, which completed the 4-coordinate zinc, showed that open coordination site of Zn(II)MID1 were essential for activity.

The unplanned catalytic activity of a metal-mediated protein-protein interface is a strong argument for a similar evolutionary pathway for natural metalloenzymes. Comparing their construct to Hg(II)Zn(II)TRIL9CL23H, the authors suggested that Zn(II)MID1 has a more shallow but accessible substrate binding cleft compared to a Zn(II)His$_3$ which is fully buried within a 3SCC. This leads to faster k_{cat} and tighter K_M as well as an overall more efficient enzyme. In comparison to the native enzyme, Zn(II)MID1 has a 200-fold slower k_{cat} while K_M is 50-fold tighter, indicating that activation of the substrate is lacking rather than substrate recognition. The authors suggest that the difference in k_{cat} may be due to secondary sphere interactions.

It is often easy to conclude that missing long distance interactions and subtle scaffold changes could differentiate *de novo* metalloenzymes from their native counterparts and that incorporating these design elements would greatly improve catalysis. Putting this into practice, however, too much about the structure-function relationship remains unknown to rationally incorporate these properties. One way to 'blindly' incorporate these long-range effects is to use processes such as directed evolution where activity screening directs the design process. Studer and Hilvert applied this process to a single chain version of MID1 called MID1sc linking the dimer structure with a Gly-Ser chain and removing one of the Zn sites to simplify analysis while maintaining similar levels of *p*NPA hydrolysis (Figure 22).[194] Libraries of MID1sc variants were created by cassette mutagenesis, DNA shuffling, or random mutagenesis and screened using a racemic fluorogenic ester assay developed by the authors. The initial MID1sc hydrolyzed this ester with a modest k_{cat} of .011 s^{-1} and k_{cat}/K_M of 18 M^{-1} s^{-1} with two-fold preference for the *R* conformer.

After 9 rounds of library generation and screening, MID1sc9 had 20 mutations (about 20% of all residues) from the original MID1sc. The putative Zn binding residues (His39, His61, and His65) were probed by mutagenesis to determine if the Zn-binding site had been modified during evolution. While H61A and H65A variations decreased catalytic efficiency as expected, H39A did not show an impact on activity, suggesting that the binding site had repositioned. A new His residue was introduced during evolution and mutating this (H35A) reduced activity by >1000-fold, suggesting that the new zinc binding site consisted of His35, His61, and His65. A final construct, MID1sc10, was rationally designed from MID1sc9 by eliminating nearby potential metal coordinating residues with E32Q, H39A, and E58Q mutations. MID1sc10 hydrolyzed the ester substrate with k_{cat} of 1.64 s^{-1} and k_{cat}/K_M of 980000 M^{-1} s^{-1} (10,000-fold higher than the original MID1sc). The catalytic proficiency of MID1sc10 was similar to that of native enzymes and outperformed artificial

Author Manuscript Author Manuscript Author Manuscript Author Manuscript

esterases, including catalytic antibodies, computationally designed enzymes, and engineered metalloproteins, by several orders of magnitude.[155, 193, 195–201] MID1sc10 even managed to out compete some native enzymes by 100-fold, such as the h-CAII reaction with *para*-nitrophenol (*p*NP) and the hydration of CO_2.[163, 202] Although the selection pressure process used a racemic mixture of the fluorogenic ester, MID1sc10 has a 990-fold kinetic preference for the *S* configuration of the ester compared to the original construct's 2-fold preference for the *R* configuration. The authors hypothesized that the evolution process led to the Zn center deprioritizing structural stability, since Zn binding had no effect on thermal stability of MID1sc10, while it increased MID1's melting temperature by 24 °C (Figure 23).[191]

A crystal structure of MID1sc10 was solved with Zn(II) and a substrate transition state mimic bound to a resolution of 1.34 Å. MID1sc10 adopts a similar helical bundle fold as the original MID1, but the crossover angle between the two bundles drastically changed to 47°, 37° more offset than MID1. The substrate pocket is deeper in MID1sc10 while a Q36P mutation kinks the second helix, facilitating His35 zinc binding. Second coordination sphere interactions, such as a H-bond from Gln58 to the backside nitrogen of His61 (part of the Zn(II)His_3 binding site) were suggested to tune reactivity.[149, 203] Interactions between Arg68 and the substrate transition state analog suggest this residue may assist in leaving group departure. Overall, this work showcases the power of directed evolution to find unintuitive solutions to problems within protein design. The success of MID1sc10 compared to previous designed esterases (even after similar directed evolution campaigns), reveals the power of metals for catalysis and the importance of metalloenzyme design and natural evolution pathways.

The MID1sc scaffold has more recently been evolved to target Diels-Alder reactivity, a useful reaction for which few native enzymes are capable.[204–208] This reaction has been targeted by several labs using different scaffolds, but the authors suspected that a transition metal's incorporation may allow for higher efficiency than previous attempts.[209–213] They targeted the Lewis-acid-catalyzed reaction of azachalcone and 3-vinylindole to determine whether a *de novo* enzyme could be evolved to selectively produce a single product, given several possible competing reaction pathways.

Directed evolution requires some starting activity. Using Rosetta, the authors incorporated E32L and K68W mutations into MID1sc to create a construct, called DA0, with Diels-Alder activity 2-fold over that of background as a starting point. Over several rounds of variation and selection, 12 mutations were incorporated to produce DA7 with five orders of magnitude improvement over the original construct (Figure 24). Similar to the Hilvert lab's previous work with MID1sc, a drastic change to the Zn binding site was essential to this improvement. The original His39, His61, His65 binding site was converted to Cys35, His61, His65 with a reduction in crossover angle between helix-turn-helix fragments as determined by X-ray diffraction. The authors hypothesized that the stronger ligation of Cys35 compared to the original His39 allowed for this large conformational shift which created an enclosed pocket that could accommodate both intended substrates. Though their previous work to produce an esterase had a similar conformational change, it did not have any detectable Diels-Alderase activity.

Author Manuscript

Author Manuscript

Author Manuscript

Author Manuscript

The catalytic proficiency of DA7 was calculated as 2.9×10^{10} M^{-1}, a record Diels-Alderase activity at the time.[214–217] The authors hypothesized that the improved activity was in part due to hydrogen-bonding interactions with substrates from Arg28 and Gln80. This, and previous work of the Hilvert lab, indicate that the flexibility and substrate promiscuity of *de novo* metalloenzymes make them ideal candidates for directed evolution. It will be exciting to see how much further MID1sc and other *de novo* metalloenzymes can be pushed using this technique.

Analysis of proteins deposited into the PDB indicates that modern enzymes on average are at least 100 amino acids in length, near the minimum required to fold into a globular protein with a well-defined hydrophobic core.[218] Given the sequence space involved, how Nature managed to screen for activity in initial stages of evolution remains unknown. This conundrum led to the hypothesis that the first enzymes were evolved from short self-assembling peptides, diminishing the sequence search space necessary to screen.[219–220] While most of this review focuses on alpha helical scaffolds for metalloenzyme design, simple heptapeptides which alternate between polar and apolar residues can self-assemble into extended beta sheets with a variety of conformations making it possible that these amyloid structures were some of the first enzymes.[221–224] Rufo and Korendovych explored this possibility in the context of metalloenzymes by investigating the catalytic properties of Zn(II) binding amyloid forming peptides similar to the secondary structure of CA’s active site (Figure 25).[201] The authors modified a minimal beta sheet forming heptapeptide sequence LKLKLKL by replacing the Lys residues at 2 and 4 with His residues and varying the 6th position between acidic, neutral, or basic residues with varying pKa values to determine their effects as general acids/bases in the secondary sphere. An initial peptide series varying the 6th position found Gln substitution to be the most active with k_{cat}/K_M for *p*NPA of 30 M^{-1} s^{-1}. Arg, Lys and Tyr were also found to improve activity compared to Glu, His, or Asp in this position.

The authors hypothesized that the activity enhancement of Gln was due to its ability to promote amyloid formation. This hypothesis was tested by creating variants in which the hydrophobic residues were substituted with those that should increase (Iso or Val) or decrease (Ala) amyloid formation.[225–226] The most active of this series (Iso) was combined with a Gln in the 6th position to make the peptide IHIHIQI which enhanced the k_{cat}/K_M to 360 M^{-1} s^{-1}, only an order of magnitude lower than CA itself and comparable to the fastest designed systems.[163] (Table 1) Structural studies were done on all designed peptides to determine if fibril formation was correlated with activity as expected. CD and IR spectroscopies were used to confirm beta-sheet formation while thioflavin binding and negative stain transmission electron microscopy confirmed fibril formation. Based on these analyses the initial Leu containing peptides (i.e. LHLHLQL) require Zn(II) for beta sheet formation while the more active Iso containing peptides do not require Zn(II), consistent with the authors’ hypothesis. Co(II) driven fibril formation was investigated to gain insight into the coordination sphere around the metal using Co(II) as a spectroscopic probe for Zn(II). UV-Visible absorption spectroscopy of the Co(II)(IHIHIQI) was consistent with tetrahedral coordination, in good agreement with structural models made using Rosetta software.[227] The authors hypothesized that mixtures of these peptides could be used to produce new catalytic enhancements compared to the individual peptides, allowing for

Author Manuscript Author Manuscript Author Manuscript Author Manuscript

a combinatorial approach to enzyme evolution. This hypothesis was bolstered by the observation of synergistic effects between two peptides when they are used to make mixed fibrils compared to mixtures of preformed fibrils. Since this initial study the Korendovych lab followed up with Cu(II) binding amyloids capable of activating oxygen, providing further evidence that these structures can catalyze a diverse set of reactions.[228–229]

3.2. Copper Nitrite Reductase

As we've seen*, de novo* metalloprotein design focuses on fundamental questions pertaining to the interaction between protein scaffold and metal structural or catalytic site. An additional layer of complexity when it comes to designing mono-metal metalloenzymes occurs when the metal is redox active. In this case, the designed metal binding site must accommodate both oxidation states, which can have different preferred geometries. The Pecoraro lab has been attempting to design one of the simplest redox active mono-metal centers, the type 2 $CuHis_3$ site from Cu nitrite reductase (CuNiR) (Figure 26).[7] Copper metalloenzymes are involved in numerous biological functions. One of the most interesting from an agricultural standpoint is the ability to reverse the nitrification process which produces toxic runoff from fertilizer.[148, 231–232] CuNiR has two Cu metal binding sites, one for electron transfer and one for catalysis, that it uses to convert nitrite to nitric oxide.[233–235] CuNiR's electron transfer site is a Type 1 Cu and the catalytic center is a Type 2 Cu with His_3 ligation and a water bound in a distorted tetrahedral geometry. Once substrate binds, the electron necessary for catalysis is transferred from the Type 1 center to the Type 2 center in a gated mechanism.

One of the benefits of *de novo* metalloprotein design is that researchers can easily separate a complex system like CuNiR into its constituent parts and study them individually. The His_3 Zn(II) binding site in the crystal structure of Hg(II)Zn(II)TRIL9CL23H overlays remarkably well with the Type 2 Cu center from native CuNiR (Figure 27).[235] This structural overlay, and that both Zn(II) and Cu(I) are d_{10} metals, lead Tegoni and Pecoraro to hypothesize that this His_3 binding site could act as a model of the type II active site of CuNiR. A simplified scaffold, lacking the heavy metal binding Cys_3 site, was created (TRIL23H) to characterize Cu(I) and Cu(II) binding.

Nuclear Magnetic Resonance (NMR) analysis at various pH conditions determined that Cu(I) bound with a pK_a of 4.45 (His side chain deprotonation). X-ray absorption near edge spectral (XANES) analysis of the 1s to 4p transition of Cu(I)TRIL23H was consistent with a 3-coordinate Cu(I) complex while extended X-ray absorption fine structure (EXAFS) analysis confirmed His binding through outer-shell scattering consistent with imidazole ligation.[236–237] Cu(II)TRIL23H was characterized by both absorption and EPR spectroscopies which were consistent with a $Cu(II)His_3$ site and one or two waters bound.[238] Titration of Cu(II)TRIL23H with nitrite compressed the hyperfine coupling constant observed in EPR spectral data as observed with nitrite binding to native CuNiR.[233] Cu(I) and Cu(II) affinities were determined to be 3.1 pM and 40 nM respectively.[239] Using these stability constants, the redox potential of CuTRIL23H was calculated to be 400–500 mV vs NHE, around 200 mV more positive than native CuNiR but nitrite reducing range (~1300 mV vs NHE at pH 6.0).[148, 235, 240]

Author Manuscript Author Manuscript Author Manuscript Author Manuscript

When Cu(I)TRIL23H was mixed with nitrite, a UV-visible absorption spectral signature indicative of Cu(II)TRIL23H accumulated over 70 minutes. NO gas production was confirmed by trapping as $[Fe(NO)(EDTA)]^{2-}$. With excess ascorbate to re-reduce the Cu, the system became catalytic and ascorbate oxidation could be followed at 265 nm.[241] FTIR spectral analysis did not detect N_2O, a common side product observed with small molecule models of CuNiR. After pH optimization to pH 5.8, the first order rate constant was determined to be $4.4 \times 10^{-4}\ s^{-1}$. Thus, by switching out the Zn for a Cu, the authors demonstrated that the scaffold was a competent CuNiR, both structurally and catalytically. This scaffold was the first stable, functional, and water soluble *de novo* Type 2 Cu site, but this model reacted much slower than its native counterpart which has a first order rate constant of ~1500 s^{-1}. Within native $CuHis_3$ sites, there is a wide range of functionality from electron transfer centers like the CuH center of peptidylglycine alpha-hydroxylating monooxygenase (PHM), to that of CuNiR acting as a catalytic active site.[153, 242–244] Further work on CuNiR models investigated how the protein environment could tune the reactivity of $CuHis_3$ sites.

The Pecoraro lab next modified long-range charged amino acids within this CuNiR model.[245] Similar residues in native metalloproteins fine-tune redox potentials, impacting the enzymatic activity.[246–249] The redox potential of CuTRIL23H is relatively positive compared to native CuNiR, which the authors hypothesized was due to the stabilization of the Cu(I) oxidation state in a trigonal planar geometry within the 3SCC environment. Methods to tune the redox potential to that of a native CuNiR could improve the reactivity. Lys22, Lys24, and Glu27 were mutated to neutral or opposing charge amino acids to increase the negative charge around the Cu-site by as much as −12 (Figure 28). This shift in charge decreased the Cu(I) affinity of the construct by as much as 2 orders of magnitude, while Cu(II) affinity was invariant, leading to a 100 mV reduction in the redox potential and a 3.5-fold increase in CuNiR activity. UV-visible absorption and EPR spectral data of constructs with a K22E mutation collected at different pH were consistent with Glu22 interacting with the primary coordination sphere through a hydrogen bond to His23. While this caused a measurable increase in activity, the effect was modest and the second sphere interaction of this Glu22 are difficult to confirm without additional structural information.

The effects of secondary sphere mutations on the activity of CuTRIL23H were next investigated.[250] Previous studies of Cys_3 sites within 3SCCs had shown that the coordination mode of Cd(II) could be modified by adjusting the hydrophobic packing above or below the metal binding site, which tuned water access to the metal.[170, 251–252] Similar behavior was seen with Pb(II) and Hg(II). Basically, converting leucine to alanine provided internal space for water to enter the hydrophobic region near the metal site that allowed for solvation or new H-bonding to protein ligands, while more sterically demanding ligands like D-Leu (DL) could block water from entering the coiled coil.[176, 253] It was, therefore, potentially instructive to apply the same changes to catalytic sites. CuTRIL23H contains Leu residues above and below the metal binding site so water access should be minimized. Effects of decreasing or increasing steric bulk around the $CuHis_3$ site was investigated by mutating these Leu packing layers to either Ala above or below (reducing steric bulk) or Ile/D-Leu above (enhancing steric bulk toward the Cu binding site) (Figure 29). The other strategy investigated in this study was the rational design of secondary coordination sphere

Author Manuscript Author Manuscript Author Manuscript Author Manuscript

interactions with Asp residues. Mutations of Asp98 in native CuNiR decrease its activity by up to 2 orders of magnitude.[4] Therefore, designing similar interactions in *de novo* scaffolds could lead to reactivity enhancements; Leu layers adjacent to the $CuHis_3$ site of CuTRIL23H were mutated to Asp to establish such an interaction.

Pseudo-first order rate constants of CuNiR activity were unaffected by increased steric bulk in CuTRIL23H L19I or L19DL, but incorporation of Asp in those positions increased the rate constant by up to 75 times compared to the parent design ($4.6 \times 10^{-4}\ s^{-1}$ up to $3.5 \times 10^{-2}\ s^{-1}$). While this suggests that the secondary sphere interaction was correctly incorporated, a similar enhanced rate was observed when Ala was positioned above or below the $CuHis_3$. The authors hypothesized that the enforced C_3 symmetry of the TRIL23H scaffold led the Asp_3 layers to interact with one another, rather than the bound substrate, decreasing steric bulk similar to the Ala_3 layers. X-ray absorption spectroscopy showed some coordination differences in the Cu(I) oxidation states of each of these constructs with Ala_3 or Asp_3 layers above the active site leading to more 2-coordinate character (Cu-N distance of 1.86–1.88 Å) while Ala_3 or Asp_3 layers below did not affect coordination (Cu-N distance of 1.91–1.93 Å). This suggested that the steric bulk above, but not below, the $CuHis_3$ enforces the Cu(I) into an unpreferred trigonal geometry. While investigating factors that correlated with increased CuNiR rate, the authors determined that the 1s to 4p transition energy observed in XANES analysis increased by as much as 1 eV for higher activity constructs. While intriguing, this correlation is currently unexplained structurally or mechanistically and its predictive value remains limited.

While this article is mainly focused on the effects of the primary and secondary coordination spheres, a study using non-native amino acids in a TRIL23H scaffold is worth mentioning briefly.[254] Native Type 2 Cu sites like those of CuNiR (catalytic center) and PHM (electron transfer center) differ in His coordination modes; all His ligands within CuNiR bind the Cu through the imidazole epsilon nitrogen (N_ε) while those of PHM bind through the delta nitrogen (N_δ).[255–256] These differences in functionality are consistent with a long-standing hypothesis based on comparison of Cu metalloprotein function and structures deposited within the PDB.[257] Essentially, N_δ bound copper leads to a more rigid environment that facilitates fast electron transfer while N_e is associated with a more flexible coordination mode that assists in catalysis. Using His residues methylated at either the N_δ or N_ε nitrogen positions, the Pecoraro lab determined that N_ε ligation was two orders of magnitude more active than N_δ ligation towards CuNiR activity. Electronic differences between His and methylated His also had the side benefit of increasing the CuNiR rate up to as much as $0.12\ s^{-1}$ compared to $4.6 \times 10^{-4}\ s^{-1}$ for CuTRIL23H. Steady state kinetics revealed that by combining the δ_m-Imidazole side chain and the relieved steric bulk that accompanies the leucine to alanine mutation in the secondary coordination sphere, K_m was reduced by a factor of 1.4 compared to CuTRIL23- δ_mH and did not influence the k_{cat}, which suggest that the modest 2-fold increase in the rate to a maximum of $0.30\ s^{-1}$ was due to increase in substrate affinity. This study is an excellent example of design strategies enabled by *de novo* scaffolds that are more challenging within native systems.

These studies had improved the CuNiR activity of TRIL23H by around three orders of magnitude, but still fell short of native CuNiR by three to four orders of magnitude. It could

Author Manuscript

Author Manuscript

Author Manuscript

Author Manuscript

be impossible to reach native rates without incorporating secondary sphere interactions, since Asp98 or His255 mutations decrease CuNiR activity by 2–3 orders of magnitude.[4] The authors' previous attempts at incorporating these interactions within the TRI system was hampered by the enforced C_3 symmetry of the scaffold; however adapting heavy metal templated heterotrimers for asymmetric 3SCC catalytic sites, as discussed above with *de novo* Zn enzymes, promises an opportunity to begin exploiting asymmetric coordination spheres (both first and second) around the metals.[176]

As was employed for carbonic anhydrase mimics (see section 3.1), the Pecoraro lab attempted to generate asymmetric environments around copper by incorporating a $CuHis_3$ site within the α_3D and GRα_3D scaffolds to investigate the effect of single Asp or His residues near the active site and the overall effect of large scaffold changes on CuNiR catalysis.[258] The same $CuHis_3$ site was 6 times more active when incorporated into α_3D and up to 18 times more in the more stable scaffold GRα_3D. That the surrounding protein matrix could impact a metal center's function is not novel, but it had only recently been recognized in *de novo* metalloprotein design (see section 2.2).[61] The CuNiR activities of scaffolds containing Asp residues positioned above or below the $CuHis_3$ binding site or a fourth His residue were determined using a series of constructs previously investigated for CuSOD activity (see section 3.3).[259] Every construct with active sites divergent from the parent construct GRα_3D H3 had decreased activity, some to such a degree that their activity matched that of the original TRIWL23H (18-fold less than GRα_3D).

Finally, there is also an interest in increased complexity within *de novo* metalloprotein design to include both electron transfer and catalytic sites within the same construct, similar to the strategy employed by native CuNiR, so repositioning of the $CuHis_3$ site within the GRα_3D was investigated. Repositioning the $CuHis_3$ site 22 Å towards the *N*-terminus of the scaffold decreased the CuNiR activity by 18-fold (Figure 30). Given the wide variety of different CuNiR constructs with different strategies for their design, it is tempting to try to find factors that correlate with activity across the entire spectrum of designs within this study. Similar to work within the TRI system, the energy and intensity of the Cu(I) XANES 1s to 4p transition correlated with changes in coordination number and activity (3-coordinate being less active and 2-coordinate more active).

3.3. Superoxide Dismutase

Superoxide dismutase (SOD) is a primary defense against oxidative damage in organisms. SODs are enticing targets for metalloenzyme design due to multiple examples of different metal environments capable of the same reaction at diffusion limited rates. $FeHis_3Asp$, $MnHis_3Asp$, $NiHis_2Cys$, CuZn dual metal systems, and recently $CuHis_4$ systems have been characterized.[150, 261–269] The reduction potentials of these metal sites are tightly controlled around the optimal 0.36 V, the midpoint between oxidation and reduction of superoxide.

One of the earliest *de novo* design investigations of SOD mimics targeted the $MnHis_3AspH_2O$ coordination sphere of MnSOD (Figure 31a).[270] The Mn binding peptide MHB was created by modifying a helix-loop-helix peptide previously used to study heme binding (dA1).[271–272] EPR spectroscopy confirmed Mn(II) binding to the peptide based on decreasing intensity of the six EPR lines, a property that has a long history of use to study

Author Manuscript Author Manuscript Author Manuscript Author Manuscript

Mn(II) interaction with designed peptides.[273] Mn(II) titration determined a stoichiometry of 1.16 Mn(II) per peptide and binding affinity of 36 μM. The original parent peptide dA1 showed no significant affinity for Mn(II) suggesting that the designed binding site of MHB was effective. MHB was also specific to Mn(II) and showed no binding to either Fe or Cu. Finally, the SOD activity of Mn(II)MHB was tested, using xanthine-xanthine oxidase nitro blue tetrazolium methods and determined a k_{cat} of $3.7 \times 10^5\ M^{-1}\ s^{-1}$, indicating four order of magnitude lower activity than native MnSOD ($k_{cat} = 3.78 \times 10^9\ M^{-1}\ s^{-1}$).

Cu-only SODS are a more recently discovered class of SODs, with four His residues coordinating Cu(II) in a pseudo-trigonal pyramid (Figure 31b).[267] The Pecoraro and Policar labs used the three helical bundle (3HB) scaffold GRα_3D to design Cu-only SODs and test the effect of the fourth ligand's identity on reactivity and redox potential by designing binding sites consisting of three His (H3), four His (H4), His$_2$Asp binding plane with a third His outside this plane (H2DH), or His$_3$ binding plane with an Asp outside the plane (H3D) (Figure 32).[259] Cu(II) EXAFS of these constructs were all consistent with 4-coordinate N- or O-bound Cu(II) with average bond lengths of 1.94 Å to 1.95 Å while Cu(I) XANES data were consistent with 2- or 3-coordinate Cu(I). Cu(II) EPR spectra of the constructs were consistent with 4-coordinate Cu(II) in a distorted square planar geometry, but GRα_3D H3 and GRα_3D H4 had complicated spectra fit as multiple species with similar intensity.[274]

As mentioned above, the redox potential of SOD is critical for function. The redox potentials of the four constructs were calculated and found to range from 420 mV vs NHE (GRα_3D H2DH) to 550 mV vs NHE (GRα_3D H3). The potentials did not correlate with the activities determined by McCord-Fridovich assay; GRα_3D H4 had the lowest activity at $1.1 \times 10^6\ M^{-1}\ s^{-1}$ but a redox potential of 463 mV vs. NHE while the other three constructs fell within 2.6 to $3.0 \times 10^6\ M^{-1}\ s^{-1}$ though their redox potentials ranged from 420 to 550 mV vs. NHE.[275–277] These results suggest that the identity or presence of a fourth ligand from the scaffold is not a necessity for Cu-only SOD activity, though it can be used to modulate the redox potential of the bound Cu. Previous low molecular weight mimics of Mn and Cu SODs found a correlation between activity and the redox potential with those closer to 360 mV vs NHE having the highest activity, so it is surprising that no such correlation was observed in this *de novo* Cu-only SOD series.[278–279] The authors hypothesize that the rate limiting step for SOD activity within these designed proteins may be product release or conversion between metal oxidation states which would obfuscate the usually observed trend in SOD activity.

3.4. O-O and O-H bond activation

De novo metalloprotein design has successfully created a number of systems for hydrolytic, reductive, dismutative, and oxidative reactions (see sections 3.1, 3.2, and 3.3) but the activation of O-O or O-H bonds for alternative energy applications is less explored. As reserves of fossil fuels dwindle it is imperative that the scientific community is ready with a plethora of methods to meet energy demands using abundant resources like O_2 and H_2O.[283–285] Cu metalloenzymes are involved in numerous biochemical processes that use O_2, likely linked to the trigonal geometry of Cu which promotes inner sphere binding of O_2, making a *de novo* Cu metalloenzyme for O-O or O-H activation an enticing

Author Manuscript

Author Manuscript

Author Manuscript

Author Manuscript

target.[274, 286–289] Mitra and Chakraborty have recently explored this possibility using a $CuHis_3$ site within a 3SCC similar to the design of the CuNiR reported by the Pecoraro lab, but using a different 3SCC sequence and the $CuHis_3$ positioned more towards the *N*-terminus of the peptide at the 9th position.[7, 290]

The crystal structure of ArCuP was solved to 1.45 Å and showed Cu bound to the three His residues through epsilon nitrogen, a common feature of native Cu enzymatic active sites in comparison to Cu electron transfer centers which are usually bound by the delta nitrogen.[257] No waters were observed bound to the Cu which the authors suggested may result from cryoreduction of the Cu(II) species to Cu(I) during irradiation, a common issue when collecting X-ray crystal structures of Cu(II) proteins. EPR and UV-visible absorption spectroscopic studies of ArCuP in solution indicated waters bound to the Cu(II) site.[291–293] Adding H_2O_2 to Cu(II)ArCuP or Cu(I)ArCuP produced a stable Cu-OOH species similar to that observed in streptavidin systems.[294] Given that ArCuP does not possess the H-bonding thought to stabilize the Cu-OOH species in the streptavidin system, the authors suggested that forming the Cu-OOH species within the hydrophobic core prohibits dimeric Cu-O-O-Cu species from forming. This species also formed 4-fold faster with Cu(I) than Cu(II) ArCuP. This is similar to lytic polysaccharide monooxygenase (LPMO) reaction with H_2O_2 in which Cu(II) reduction to Cu(I) is thought to prime the system.[295–296]

LC-MS/MS analysis of the CuArCuP reaction with H_2O_2 determined that the reaction produced hydroxyl radicals and several residues were oxidized at distances of 5–28 Å from the active site Cu (Figure 33). Similar oxidative damage of the protein is observed when H_2O_2 is used as the terminal oxidant in Cu monooxygenases such as LPMO.[295, 297] Lastly, ArCuP was immobilized to a pyrolytic graphite electrode for electrocatalytic reduction of H_2O_2. Kinetic analysis determined that ArCuP had a K_M of 3 mM for H_2O_2 (comparable to some native systems attached to electrodes but an order of magnitude greater than the benchmark horseradish peroxidase) and a k_{cat} of 0.72 s^{-1} at pH 7.5 which was ~7-fold slower than a comparable native system.[298–299] This application of *de novo* Cu metalloenzyme design to O-O and O-H bond activation is an exciting avenue of research and it will be interesting to see how this system continues to develop.

The Korendovych lab has also applied their catalytic amyloid strategy to the investigation of oxygen-activation by *de novo* Cu enzymes.[228–229] After successfully creating a Zn binding amyloid CA mimic scaffold, Makhylnets and Korendovich investigated redox catalysis by replacing Zn with Cu and looking at the oxidation of 2,6-dimethoxyphenol (DMP). (scheme 1)[201, 300–301] The authors started with 16 peptides that were previously shown to produce Zn binding amyloids capable of catalysis. Upon adding Cu to these peptides, one (11, Ac-IHIHIQI-$CONH_2$) catalyzed DMP oxidation an order of magnitude above baseline activity. Similar to the previous work, peptides containing hydrophobic residues promoting amyloid formation showed improved activity; but, it is important to note that Cu-amyloid formation is not the sole requirement as the amyloid beta peptide (Ab 1–40) can form amyloids upon binding Cu but does not catalyze DMP oxidation.[302] EPR spectral comparisons of active and inactive Cu-bound peptides showed classic type 2 features indicative of CuN_3O_1 or CuN_2O_2 coordination for both groups but that the two groups were distinct from one another.[303]

Author Manuscript Author Manuscript Author Manuscript Author Manuscript

Amyloid formation appears to lock the His residues into a geometry which activates Cu for DMP oxidation.

Lengyel and Korendovych showcased the utility of catalytic amyloids by applying this strategy to the hydrolysis of paraoxon, a common organophosphate pesticide with low background hydrolysis (7.97×10^{-7} min^{-1} at pH 7.8) that causes it to remain in the environment for extended periods.[229, 304] During an initial screening, peptide 7IY (Ac-IHIHIYI-NH_2) showed high activity and was further characterized. Kinetic analysis of Cu(II)7IY found the k_{cat}/K_M to be 1.7 M^{-1} min^{-1} and catalytic enhancement (k_{cat}/k_{uncat}) of 3.5×10^3 at pH 8.0, values on par with small molecule catalysts and catalytic antibodies, but less than previously described engineered enzymes.[304–312]

One of the benefits of catalytic amyloids is that they can function as heterogeneous catalysts. The authors demonstrated this capability using a catalytic flow system by trapping peptides on a 0.22 μm syringe filter. While the amyloids had reduced catalytic efficiency when deposited, substrate passed through the filter was still measurably converted to product. Cu(II)7IY was also sufficiently promiscuous to allow tandem catalysis of two reactions, a marked benefit of a *de novo* designed metalloenzyme compared to their native counterparts.

3.5. Summary

Designing mono-metal metalloenzymes arguably requires more control over the coordination sphere than designing heme proteins as the designed scaffold must satisfy more than two open coordination sites of the metal while maintaining flexibility for catalysis. The Pecoraro, and Kuhlman, and Korendovych labs have put efforts into recreating the $ZnHis_3$ site of carbonic anhydrase. The Pecoraro lab began their work with carbonic anhydrase in mind, creating a His_3 site within a three-stranded-coiled-coil that was only two orders of magnitude slower than native CAIII.[155] Further work with this system determined that the $ZnHis_3$ site's catalytic efficiency was largely unaffected by both repositioning of the site within the 3SCC or changing the scaffold to a three-helical bundle suggesting that $ZnHis_3$ primary sphere mimics of CA are generally active and this observed reactivity was not due to unforeseen or unplanned long range interactions specific to the scaffolds examined.[169, 179] The Kuhlman lab created a *de novo* Zn-directed protein-protein interaction between two Helix-Turn-Helix peptides which was shown to be capable of CA catalysis at higher efficiencies than those within the 3SCC system (Figure 34).[191, 193] Later, the Hilvert and Kuhlman labs revisited this construct, converted it to a single chain, and turned it into an enantioselective esterase using directed evolution which incorporated long distance effects such as a 37° offset between helices (Figure 34).[194] Rufo and Korendovych recreated the $ZnHis_3$ site of CA within amyloid forming peptides with interesting implications for metalloenzyme evolution (Figure 34).

Redox active metalloenzymes have proven more difficult to recapitulate using *de novo* design because two oxidation states of the metal can affect designs. The Pecoraro lab has reported several studies on the Type 2 Cu center of CuNiR, first by switching their CA mimic to a CuNiR by exchanging Zn with Cu.[7] Focus on long distance, secondary sphere, and even primary sphere (epsilon vs. delta nitrogen of His) effects have improved on the original rate up to 730-fold, but there is still a 3–4 order of magnitude rate gap compared

Author Manuscript

Author Manuscript

Author Manuscript

Author Manuscript

to native CuNiR.[245, 250, 254] Most recently, a $\mathrm{CuHis_3}$ site with several possible secondary sphere designs was incorporated into the asymmetric scaffold $\mathrm{GR\alpha_3D}$ which showed that CuNiR activity is sensitive to metal site design and position within the scaffold (Figure 34).[258] Superoxide dismutase (SOD) and monooxygenase mimics have been worked on by several labs and the Cu-only SOD constructs show surprising insensitivity to the usually observed correlation of redox potential and catalytic efficiency.[259, 290]

The *de novo* design of mono-metal metalloenzymes is a strong showcase for the lessons we can learn about the simplest functional unit necessary for metalloenzyme activity. This cuts to the heart of the question of secondary sphere interaction by first determining the activity of a metalloenzyme where all such interactions have been wiped clean. That one can use the same $\mathrm{His_3}$ scaffold and create a hydrolytic catalyst only two orders of magnitude short of native examples as well as a redox catalyst seven orders of magnitude from native examples hints at where challenges remain. Designing secondary sphere interactions has proven more challenging and has thus far only been accomplished through non-rational design either through happenstance (with a H-bond to a $\mathrm{His_3}$ site within the CuNiR systems) or through directed evolution in the CA systems. While directed evolution is a powerful technique, further studies which investigate the effects of these long-range mutations are required if we are to gain information about the effects of secondary sphere amino acids within *de novo* systems.

Computational protein design is a powerful technique that has been under-utilized within mono-metal metalloenzyme design. Given the sensitivity of CuNiR activity to the local environment, a study of how hydrophobic repacking impacts activity is warranted. This may lead to strategies that permit the incorporation of secondary sphere amino acids with the necessary orientation for improved catalysis. Finally, it is exciting to see progress towards alternative energy applications of *de novo* metalloenzymes. Though these are currently in early development and the possibility of incorporating secondary sphere interactions into these designs are unknown. Incorporation of secondary sphere interactions similar to work on CuNiR models could investigate their effects on peroxide reduction. While mono-metalloenzyme active sites appear simple, there is immense complexity beyond the primary coordination sphere yet to be fully investigated or understood.

4. Di-Metal Cluster Metalloenzymes

We now move from the design of metalloenzyme active sites that contain a single metal ion to those that contain two. The symmetric nature of di-iron cluster metalloenzymes made them an early target for *de novo* design through the use of retrostructural analysis to determine the minimal components necessary for function.[69] Since this initial study, a wide variety of design strategies have been applied to the Due Ferri family of *de novo* 4 helix bundle (4HB) proteins; from changes to the primary and secondary coordination sphere, to modification of the overall protein scaffold enabling more complex designs. Throughout this work, the DeGrado lab focused on developing a stable, but also functional active site. These are often-competing goals and the Due Ferri story is an interesting case study of attempts to have one’s cake and eat it too.

Author Manuscript Author Manuscript Author Manuscript Author Manuscript

4.1. DueFerri System

Diiron enzymes are responsible for a number of different biologically necessary functions such as reversible oxygen binding, phosphatases, hydrolysis, and oxidative processes.[313–316] The DeGrado lab has long investigated how these proteins tune their reactivity using a dimetal binding *de novo* scaffold system called Due Ferri (DF). The first DF design was created by a retrostructural analysis of EXXH containing diiron proteins, including three ferroxidases, ribonucleotide reductase, Δ^9 ACP desaturase, and methane monooxygenase.[42, 69, 317–323] While this group show less than 5% sequence identity, all of their active sites are based on a relatively simple pseudo-222-symmetric four-helix bundle motif. Thus, the geometry of the active sites can be described by a D_2-symmetric model with six adjustable parameters. The coordination environment of the metal cluster consists of Glu and His ligands coordinated to each metal with two Glu residues bridging the metals (Figure 35). Lombardi and DeGrado designed a stripped down version of this binding site using a D_2-symmetric four-helix bundle consisting of 21 amino acid helices. After including all the structural constraints determined by retrostructural analysis, functional secondary sphere amino acids were added; an Asp residue to H-bond with the ligating His and a Tyr to H-bond with the non-bridging Glu. Once these constraints were included, the 4HB was hydrophobically repacked computationally and by visual inspection with almost identical results.[324] The final design was a 48 residue long protein named DF1.

DF1 forms an alpha helical structure in solution and binds Zn(II), Co(II), and Fe(II). Co(II)$_2$-DF1's UV-visible absorption spectrum was in reasonable agreement with the literature values of Co(II) substituted bacterioferritin.[325] The crystal structure of Zn(II)$_2$-DF1 was solved to a resolution of 2.5 Å and matched the computational design with an RMSD of 0.55 Å for backbone atoms and 0.41 Å for atoms within 10 Å of the metal binding site. This match to the designed structure extended to the secondary sphere Asp and Tyr residues which correctly formed their designed H-bond pairs.

Later work by Di Costanzo and DeGrado focused on methods to increase substrate access, with the intention that Fe(II)$_2$-DF1 would be catalytically active.[326] Reconstitution of metal-bound DF1 required denaturing and refolding, indicating that substates could not access the active site in the folded protein. The crystal structure showed vacant metal coordination sites but Leu13 occluded solvent access. DF1 L13A was created, and Mn(II)$_2$-DF1 L13A was structurally characterized to a resolution of 1.7 Å and compared to the three dimensional structures of Mn(II) substituted diiron-oxo proteins such as ribonucleotide reductase and bacteroferritin.[42, 327] The Mn(II)$_2$-DF1 L13A crystal structure showed that DMSO (from the crystallization buffer) was bound to the Mn(II)$_2$ site in a bridging orientation and several water molecules filled the pocket, indicated a more opened active site due to the L13A mutation (Figure 36). Previous examples of exogenous bridging organic ligands were thought to occupy the position normally taken by substrates in the catalytic cycle.[323, 328] The Mn-Mn distances within the three crystallographically unique structures of Mn(II)$_2$-DF1 L13A ranged from 3.6 to 3.9 Å, matching the range of di-Mn(II) substituted forms of bacterioferritin (4.0 Å) or ribonucleotide reductase R2 (3.6–3.7 Å). Shorter distances are often observed for di-Mn(III) forms of catalase, suggesting that the Mn was bound in the

Author Manuscript Author Manuscript Author Manuscript Author Manuscript

Mn(II) oxidation state. Secondary coordination sphere interactions originally designed in DF1 were largely unaffected by the DF1-L13A variation.

Solution characterization was impeded by the limited solubility of DF1 L13A, so further studies used the more water soluble DF2 which also has an Ala residue at the 13th position.[329] The $Fe(III)_2$-DF2 optical spectrum was similar to those of Fe(III)-O-Fe(III) containing proteins and inorganic complexes.[330–333] Azide titration of $Fe(III)_2$-DF2 showed that two azide molecules could bind to the active site. Given that the coordination number of the $Fe(III)_2$-DF2 is expected to be saturated (based on the structure of $Mn(II)_2$-DF1 L13A), the authors suggested that the protein ligands might change coordination mode for azide to bind. Such changes are well precedented in natural diiron proteins and are thought to be allowed by the flexibility of the carboxylate ligands which can switch between monodentate and bidentate binding modes.[321, 328, 334–335] Overall, this study concluded that the DF1 structure was stable enough to allow destabilizing mutations for solvent access, and that these mutations enabled small molecules to bind to $Fe(III)_2$-DF2, a massive step towards the creation of a *de novo* oxygen dependent diFe enzyme.

Active sites of native metalloproteins are often preorganized for metal binding in the apo state, requiring that polar residues be buried within the hydrophobic core at the expense of protein stability.[329] This preorganization is thought to be how the protein imparts non-ideal coordination geometries on the metals rather than vice versa. Maglio and DeGrado investigated the thermodynamic stability of DF1, DF1 L13A, and L13G to determine the cost of carving out substrate access channels as well as the level of preorganization within the DF1 active site.[336] Based on guanidinium titrations followed by circular dichroism (CD) DF1 L19A mutation decreases the stability of the scaffold by 5.6 kcal/mol while the L19G variant destabilized the scaffold by an even greater 10.8 kcal/mol. These values were consistent with native proteins, indicating that further destabilizing modifications to incorporate additional design elements might have to be compensated by alternative approaches to increase structural stability.[337–340]

The apo structure of DF1 was solved by NMR and compared to the di-Zn(II) derivative to determine the level of preorganization in the active site. The superposition of these structures showed that they were similar overall down to the second shell interactions such as Glu10 accepting H-bonds from Tyr17 and Asp35 from His39. A larger rotation of the helices to expose some active site amino acids to solvent was also observed (Figure 37). While the structure of the *N*-terminal helices was invariant, the *C*-terminal helices were rotated 30°, exposing Glu-36 and His-39 to solvent compared to the more buried orientation of these residues in the holo structure. The authors suggested that DF1's inability to maintain a fully preorganized active site could be related to its small size. A similar study with heavy metal binding Cys_3 active sites showed that preorganization was maintained in the apo state; but, this was with the more easily accommodated Cys residues, so it is possible that the preorganization penalty was less in this case.[341]

To this point, the DeGrado lab laid the ground work for *de novo* Fe_2 catalysts, but the work of Kaplan and DeGrado is when this first came to fruition.[342] The scaffold for this work was DF_{tet}, a heterotetrameric four stranded coiled coil which allowed for a combinatorial study

Author Manuscript

Author Manuscript

Author Manuscript

Author Manuscript

using different substrate access increasing mutations (L15$_a$A/G or A19$_b$G) to investigate the optimum substrate access for catalysis.[343] Oxidation of 4-aminophenol (4AP) was followed by quenching and spectroscopically detecting the quinone monoimine product using established methods.[344–346] L15 and A19 were chosen for mutation based on models of DF$_{tet}$ with 4AP within the active site which indicated that these two amino acids would make unfavorable contacts with the substrate. Kinetic analyses of combinations of these mutations found that the greatest effect (~25-fold increase) was observed when all four positions were Gly (Figure 38). It is particularly interesting that such a measurable effect can be observed upon slight changes such as when two carbon atoms are added to the active site (4Gly to 2Gly2Ala constructs). This showcases the fine tuning of designed metalloenzymes that can be accomplished outside of the primary coordination sphere.

Unfortunately, the DF$_{tet}$ system, while convenient for a combinatorial study, was overly complex to structurally characterize. Faiella and Lombardi applied the lessons of increasing substrate access through Gly residues to the better characterized DF system creating DF3.[347] Introduction of four Gly residues into the DF1 structure directly would likely result in an unfolded protein, based on the previous study by Maglio and DeGrado which determined that two Leu to Gly substitutions destabilized the complex by 10.8 kcal/mol and left the free energy of unfolding at only −12.7 kcal/mol.[336] To improve the stability of the scaffold, the interhelical turn of DF1 was redesigned by searching through the PDB database for the most common amino acid sequences that adopt a similar turn geometry.[69, 348] This analysis resulted in the V24-K25-L26 loop of DF1 being substituted with T24-H25-N26 and this, combined with two Leu to Gly mutations (to bring together 4 Gly in the complex), created DF3.

DF3 was well-folded in solution, suggesting that the loop redesign successfully compensated for active site destabilization. DF3 oxidized 4AP with similar efficiency as DF$_{tet}$-G4. DF3 had a similar reaction profile to established Fe$_2$ enzymes, reacting with 3–5-ditert-butyl-catechol 5-fold faster than 4AP but *para*-phenylendiamine reacted 75-fold slower and *ortho*-phenylendiamine did not react at all.[349–350] Zn(II)$_2$-DF3 was structurally solved by NMR (Figure 39). Zn(II)$_2$-DF3 contained the expected H-bonds within its redesigned loop, matching the computational model with an RMSD of 1.2 Å. Comparison of Zn(II)$_2$-DF1 and Zn(II)$_2$-DF3 showcases the opened substrate channel which allows for enzymatic activity. Overall, this study is an excellent example of a consistent theme of research within the Due Ferrie system, the warring factors of stability and catalysis within enzymes. The authors successfully walked the tightrope between these two properties by redesigning the interhelical loop in tandem with opening the active site.

Despite the limited set of metals readily available in nature, metalloenzymes can have a number of different functions. For example, iron enzymes are quite prolific. Even within the much smaller subset of non-heme Fe$_2$ enzymes, one observes peroxidation, oxidation, and NO reduction catalysis.[351–362] Reig and DeGrado explored how primary and secondary sphere modifications change the metal reactivity within the DF family of scaffolds.[78] This required transferring the established activity into a single-chain version of DF called DFsc which would permit asymmetry in the active site.[363] G4DFsc was designed by incorporating

Author Manuscript

Author Manuscript

Author Manuscript

Author Manuscript

four Gly mutations (A10G, A14G, A43G, A47G) into DFsc to mimic the successful strategy used in both the DFtet and DF3 scaffolds (Figure 40).

At the time, the only structurally characterized N-oxygenase containing an Fe_2 active site was *para*-aminobenzoate *N*-oxygenase (AurF). This protein was used as the design target for two-electron oxidation of activated quinols to *N*-oxygenation of anilines.[364–365] The active site of AurF matches that of G4DFsc closely excepting a third ligating His residue bound to one of the two Fe. G4DFsc I100H was designed including Y18F or Y18L modifications to incorporate this His interaction and provide sufficient space within the active site for coordination, but neither construct was successful (Figure 40). After several redesigns, a H-bond network from His100 to His81 terminating with Asn37 proved necessary to correctly incorporate the third His residue at position 100. The final construct (3His-G4DFsc) was only folded in the presence of divalent metal ions, showcasing the consistent battle between stability and function, but correctly incorporated those metals in the designed 2:1 ratio when present.

The incorporation of this third His residue nearly abolished 4AP oxidation activity but enabled the construct to *N*-hydroxylate *para*-anisidine. Following the reaction of 3His-G4DFsc with *para*-anisidine by UV-visible absorption spectroscopy, an intermediate product absorbing at 360 nm was observed which disappeared over several hours to a final product absorbing at 445 nm. HPLC and MS analysis identified the final product as 4-nitroso-4’-methoxydiphenylamine resulting from a reaction of the intermediate product *para*-nitrosoanisole with unreacted *para*-anisidine (Figure 41). Thus, the authors had not only shown that the *de novo* Due Ferri scaffold could be converted from one reactivity to another, but that the differences in reactivity seen in native AurF compared to other natural Fe_2 enzymes could be accounted for largely through the third His within the active site.

Given the unprecedented nature of the reactivity switch from G4DFsc to His3-G4DFsc, Snyder and Solomon put out two spectroscopic studies to determine the cause. The first investigation focused on how the primary sphere alterations affected O_2 activation.[366] Among native Fe_2 enzymes, a number of ligand geometries are possible, largely due to the ability of carboxylate residues to switch between mono- or bidentate coordination (Figure 42).[323, 334, 367–368] The AurF modelled in His3-G4DFsc has an even larger difference in its active site, with 3-His/4-carboxylate instead of the 2-His/4-carboxylate of more standard Fe_2 enzymes leading to a spectroscopically distinct peroxy intermediate.[369] Snyder and Solomon used near-IR (NIR), circular dichroism (CD), magnetic circular dichroism (MCD), and variable-temperature variable-field (VTVH) MCD spectroscopies to evaluate the $Fe(II)_2$ active sites of G4DFsc, His3-G4DFsc, and G4DFsc(Mut3) to determine the effects of increased solvent access, primary coordination sphere changes, and helix-stabilizing residues. G4DFsc(Mut3) was a new construct made for this study which included the secondary sphere mutations present in His3-G4DFsc but lacks the third His in the active site.

NIR MCD spectroscopy determined that $Fe(II)_2$His3-G4DFsc differed drastically from $Fe(II)_2$G4DFsc and $Fe(II)_2$G4DFsc(Mut3), with three bands observed rather than two, suggesting higher coordination at the $Fe(II)_2$ site in $Fe(II)_2$His3-G4DFsc. VTVH MCD

Author Manuscript Author Manuscript Author Manuscript Author Manuscript

curves of all three constructs indicated that their MCD bands (whether two or three) derive from two non-equivalent Fe ions. Based on these analyses, and the energy of the observed MCD peaks, the authors concluded that $Fe(II)_2$G4DFsc and $Fe(II)_2$G4DFsc(Mut3) were best described as two inequivalent 5-coordinate trigonal bipyramidal Fe(II) with weak coupling from the two bridging carboxylates (Figure 43B).[354, 370] Previous analysis of $Fe(II)_2$DFsc showed it was best described as a split 4/5-coordinate Fe_2 site similar to ribonucleotide reductase. This difference in coordination is likely due to H_2O binding to one of the Fe due to greater solvent access.[371] Finally, the same analysis of $Fe(II)_2$His3-G4DFsc found it was best described as a 6/5-coordinate Fe_2 site with the third His residue binding to make a 6-coordinate Fe (Figure 43C). Stopped-flow kinetic analysis of O_2 reactivity found that DFsc's reaction rate was similar to that of natural Fe_2 enzymes at 2 s^{-1}, but increased solvent access in G4DFsc decreased this to 0.02 s^{-1} while G4DFsc(Mut3) was further decreased to 2×10^{-3} s^{-1}.[372] Based on VTVH MCD analysis, this lower reaction rate correlated with the strength of the superexchange pathway from bridging carboxylate ligands allowing for two-electron reduction at a single Fe.

The authors suggested that one of the deficiencies in the DF system for oxygen reactivity was a lack of positions at which O_2 could or strong carboxylates could bridge the two Fe ions to allow for efficient superexchange between them. Snyder and Solomon continued their spectroscopic study in the DF system by focusing on how the incorporation of a third His residue in the active site switches reactivity from oxygenase to arylamine oxidase.[373] Reactivity of 4AP was investigated under tightly controlled anaerobic conditions with $Fe(II)_2$-G4DFsc or $Fe(II)_2$-3HisG4DFsc with substrate bound before O_2-saturated buffer was added to complete the reaction. Under these conditions, the two constructs oxidize 4AP at the same rate. Previously when O_2 and 4AP were added at the same time, the two His variant was much faster than the three His variant. Following 4AP binding by MCD, they found that 4AP binding perturbed the $Fe(II)_2$ site to a single Fe(II) center, but both 4AP-$Fe(II)_2$-G4DFsc and 4AP-$Fe(II)_2$-3HisG4DFsc were 6/5-coordinate trigonal bipyramidal Fe(II) centers (Figure 44). This indicated that 4AP binding increases the coordination number of the two His construct while the iron coordination environment of the three His construct is maintained.

The authors suggested that 4AP coordination replaced His100 in the active site, consistent with kinetic studies where 4AP binds to the two His construct with a rate (0.027–0.042 s^{-1}), an order of magnitude higher than it does in the three His construct (0.0046 s^{-1}). Given that both constructs react with O_2 at a similar rate (0.02–0.04 s^{-1}), the apparent difference in reactivity under aerobic conditions for 4APoxidation is due to oxidation to the inactive $Fe(III)_2$ state outcompeting substrate binding in the three His construct whereas the two processes are comparable in rate for the two His construct. Next, the differential oxygenation of *para*-anisidine by G4DFsc or 3His-G4DFsc was investigated. Slight shifts to both constructs' NIR CD and MCD spectra upon addition of *para*-anisidine indicated that the substrate bound near the active site but not directly to either Fe(II) (Figure 45). While both constructs could incorporate the substrate, the three His construct increased antiferromagnetic coupling between the two Fe(II) while it decreased upon binding to the two His construct which the authors concluded was the cause of their differential reactivity.

Author Manuscript Author Manuscript Author Manuscript Author Manuscript

One of the most fascinating features of native metalloenzymes is their ability to produce highly reactive intermediates without releasing these into solution or degrading the protein. For example, several DF proteins were capable of one- or two-electron oxidative chemistry but a net four electron reduction without radical release had not yet been achieved. Chino and Lombardi set out to create a DF scaffold which could sequester the reactive intermediate of 4AP oxidation 4-benzoquinone monoimine (4BQM) inside the protein active site and therefore change the reaction pathway to a 4 electron reduction.[77] Their target for redesign was the native metalloenzyme toluene mono-oxygenase (TMO).[374–375] TMO's active site is asymmetric, so the researchers used a DF scaffold in which two different alpha-helical hairpins (referred to as the K chain and the Z chain) are covalently linked together by Cu(I) catalyzed click chemistry (Figure 46).[376–378] Mutations were introduced within this asymmetric scaffold to modulate active site access (G13$_K$T with L33$_K$Q and G9$_Z$F with Y17$_Z$L and Y17$_K$F), form new H-bond networks (L43$_K$N with L29$_Z$Q), and improve the overall packing (Q16$_K$L and I14$_K$A) to create DF-C1 (Figure 46). CD, UV-visible absorption and NMR spectroscopic analysis of DF-C1 showed it was well-folded in solution and capable of binding two metal ions. Co(II)$_2$-DF-C1 absorption spectra were consistent with either both Co being 5-coordinate or mixed 5/6-coordinate, as is common for Co(II) reconstituted Fe$_2$ proteins.[379–380] Unlike the original DF3 design, when Fe(III)$_2$-DF-C1 oxidized 4AP, no 4BQM was observed. HPLC analysis determined the product was the oxidation/condensation derivative of 4AP, an analogue of a Barndrowski's base (Figure 47).[350] The authors suggested that this product was generated by 4AP binding to the active site of Fe$_2$-DF-C1, reacting with a second 4AP to produce a dimer which, when released to solution, reacts with a third 4AP molecule to create the final product. Docking studies of the 4AP dimer indicated that part of the active site redesign had resulted in π-stacking interactions from Phe9 which may have guided dimer formation. Thus, a *de novo* scaffold that was capable of a single two-electron oxidation was tuned by active site redesign at multiple secondary sphere locations to perform sequential two-electron oxidations. This is the most recent report on DF engineering alone, independent of the more recent porphyrin binding investigations (see section 2.2).[61, 63]

4.2. Mn$_2$ cluster binding for electron transfer and catalysis

While the Lombardi and DeGrado labs have explored different metal-substituted Due Ferri constructs, these were always with the overarching goal of learning about the Fe$_2$ system. The Allen lab has taken a different tactic to *de novo* bimetal protein design by targeting photosystem II using Mn$_2$ binding proteins and later applying these design strategies to models of catalase.[381–382] The Mn$_4$Ca cluster of photosystem II is necessary for water oxidation and has been investigated using a plethora of structural and spectroscopic techniques, but questions remain.[383–389] For example, the redox midpoint potential of the Mn$_4$Ca cluster is a critical parameter but has been difficult to measure directly.[390–392] Also, the Mn$_4$Ca cluster is in a distorted cuboidal arrangement enforced by the surrounding protein, but the role of surrounding residues remains under debate.[393–396] Due to the complicated nature of photosystem II, the authors used the evolutionarily related bacterial reaction center of *Rhodobacter sphaeroides* and tested *de novo* four-helix bundle Mn$_2$ proteins for their ability to bind and reduce the bacteriochlorophyll dimer (Figure 48).[397]

Author Manuscript Author Manuscript Author Manuscript Author Manuscript

The homodimeric Due Ferrie protein DF2t was used as the scaffold for this study.[78, 348] Three different Mn_2 binding proteins were created using this template: P0 with a single Mn_2 binding site, P1 with three separate Mn_2 binding sites spanning the 4HB, and P2 with two Mn_2 binding sites. The structure of P0 was solved to a resolution of 1.75 Å and overlaid well with previous Mn_2 DF proteins.[326, 398–399] Time resolved spectral analysis in the presence of the P_{865} dimer showed that all three *de novo* Mn_2 proteins could transfer electrons and compete with the charge-recombination reaction of $P_{865}{}^{+}Q_A{}^{-}$. P1 (with three Mn_2 binding sites) was the most effective at decreasing dimer bleaching and this effect decreased as the number of Mn_2 binding sites decreased. Whether this pattern arose due to the number of Mn_2 binding sites increasing the possibility of electron transfer or because of other parameters that differ between the constructs (such as midpoint potential) is unknown. Docking studies using Rosetta compared the inter-protein distance expected for P0 interacting with the reaction center (17 Å) and the native electron transfer protein cytochrome c_2 (11 Å). This 6 Å increase in inter-protein distance should decrease the rate of electron transfer from 10^6 s^{-1} down to 10^3 s^{-1} but this was not confirmed experimentally.[400–402] This is one of only a few examples of *de novo* designed metalloproteins interfacing with native biological machinery, showcasing the potential of designed proteins to replace components of complex multiprotein systems.

The electron transfer capabilities of these Mn_2 cluster proteins were impressive, but upon inspection the structure of P0 more closely resembled the enzymatic Mn_2 cluster of Mn-catalase (Figure 49). Mn-catalase serves a similar function as its heme-based corollary (conversion of H_2O_2 into O_2 and H_2O) but functions in anaerobic bacteria rather than aerobic organisms.[403–404] Olson and Allen created a suite of Mn_2 *de novo* proteins with metal binding sites in different positions.[382] Four different constructs were characterized and investigated for catalase activity by the production of O_2 and the loss of H_2O_2. P0, P1, and P2 from the previous *de novo* Mn_2 work were included in this study as well as P3, which repositioned the non-central Mn cluster further from the central Mn cluster, and P4, which removes the central Mn cluster from P3. (Figure 50)

EPR spectroscopy of the Mn-bound constructs (except for P4 that aggregated when Mn bound) found no spectral features to indicate magnetically interacting Mn(II) ions, which is likely related to the increased Mn separation in the cluster (4 Å) compared to native Mn-Catalase (3.0 to 3.4 Å).[405] CD analysis determined that most of the construct series was well folded in solution with the exception of P3 which did not appear to be fully alpha helical in the apo state. Kinetic analysis of H_2O_2 degradation determined that P1 and P3 which contain three Mn_2 clusters react at approximately double the rate of P0 and P2, which contain one or two Mn_2 cluster sites, respectively. Kinetic analysis of P1, following O_2 production, determined that this construct had a k_{cat} and K_M of 10^{-4} s^{-1} and 200 mM, respectively, compared to 2–3 × 10^5 s^{-1} and 80–350 mM for native Mn-catalase.[403–404] Overall, the authors showed that the number of Mn_2 clusters had a significant impact on catalase function while the position of those clusters did not. It is interesting to note that the K_M of P1 was comparable to that of native Mn-Catalase, but the k_{cat} falls 9 orders of magnitude short. This suggests that future design should focus on improving substrate activation, such as inclusion of secondary sphere interactions found in native Mn-Catalase.

Author Manuscript

Author Manuscript

Author Manuscript

Author Manuscript

4.3. Summary

The Due Ferri system is one of the longest continuous stories of metalloprotein design. After the initial design of a di-metal binding 4HB by retrostructural analysis, Di Constanzo and DeGrado made the first step towards enzymatic activity by opening up substrate access through a L13A mutation.[69, 326] Studies of apo-DF1 determined that these mutations were highly destabilizing.[336] DF_{tet}, a heterotetrameric 4SCC variant, was the first to be catalytically characterized; and the best combination for oxidation of 4-aminophenol (4AP) was two Leu/Ala to Gly mutations (Figure 51).[342] DF_{tet} could not be structurally characterized, so Faiella and Lombardi applied the Gly mutations to DF1, but these were too destabilizing for the less thermodynamically stable scaffold.[347] They incorporated these mutations by concurrently changing the initial scaffold beyond the active site; they redesigned the loop between helices to increase stability. The final design, DF3 oxidized 4AP at similar rates as the DF_{tet}-G4 system.

Reig and DeGrado investigated Due Ferri active site changes that modified reactivity from hydroquinone oxidation to N-hydroxylation.[78] A single chain variant of DF3 called G4DFsc was made and a third His residue was incorporated into the active site to mimic the binding geometry of *para*-aminobenzoate *N*-oxygenase (AurF). Remarkably, this completely switched the reactivity and His3-G4DFsc showed no reaction with 4AP but did *N*-hydroxylate *para*-anisidine. Follow-up studies by Snyder and Solomon found that His3-G4DFsc could still perform 4AP oxidation, but substrate binding was slower than metal center oxidation and inactivation under aerobic conditions.[366, 373] Chino and Lombardi developed a scaffold that sequesters reactive intermediates by redesigning DF3 to incorporate the asymmetric active site of toluene mono-oxygenase (Figure 51).[77] They changed a *de novo* scaffold capable of a single two-electron oxidation to one that is capable of two two-electron oxidations. Finally, while most work on Due Ferri has focused on creating Fe_2 enzymes, the Allen lab used these scaffolds to mimic Mn_2 clusters. They showed that these clusters could interact with other biological machinery through electron transfer to the bacterial reaction center of *Rhodobacter Sphaeroides* and possess Mn-catalase activity (Figure 51).[381–382]

These reports on the Due Ferri system showcase the different strategies employed to study metalloenzymes. Between the DeGrado and Lombardi labs, they have changed from homodimeric to heterotetrameric, single chain, or even heterodimeric scaffolds. This was in pursuit of balancing the stability and catalytic activity of these systems. There have also been notable successes at designing DF secondary sphere interactions. Multiple constructs have shown the benefit of opening space for substrate access and the DF_{tet} system demonstrated that even a single carbon increase in steric bulk had a measurable effect on 4AP oxidation. Several reports have incorporated hydrogen bonds between His or Asp residues with primary sphere ligands.

The impact of these secondary sphere interactions on structure and catalysis is a yet under-investigated property. Often, these are included in the initial DF redesign strategy, but this obfuscates its effects from those caused by other redesigned mutations. For example, DF-C1 had 12 mutations from the DF3 sequence to mimic the active site of Toluene Monooxygenase.[77] Applying many redesign strategies (substrate access opening, H-bond

Author Manuscript Author Manuscript Author Manuscript Author Manuscript

network, active site reshaping) to the same construct at once is impressive but information about the impact of each modification is lost. It would be interesting to see additional combinatorial studies (like DF_{tet}) or more details on the effect of single amino acid changes (Snyder and Solomon) applied to more recent DF family constructs.[342, 366, 373]

5. Non-heme electron transfer sites

As *de novo* metalloenzyme designs increase in complexity, aspects beyond the primary or even secondary coordination sphere of the metal will need to be included. For many metalloenzymes, this includes other metal centers which assist in catalysis indirectly. The combination of a structural metal binding site with a catalytic active site has been accomplished, but the more intricate combination of an electron transfer site coupled to an enzymatic site has not been reported.[155] Much work has been done on heme electron transfer proteins, but the goal of combining different metal-binding sites within a single scaffold would be assisted by the design of smaller electron transfer sites. Here, we limit our focus to design of FeS cluster proteins and cupredoxin mimics. With multiple research groups contributing, we are coming closer and closer to the goal of designs that can mirror the complexity found in nature.

5.1. FeS Cluster proteins

FeS clusters are one of the most common electron transfer elements within biological systems and are thought to be evolutionary remnants from an era when the Earth's atmosphere was more reducing.[406] Interest in their design has grown lately as they are an important part of a number of systems with possible alternative fuel applications such as photosystem I, complex I, and hydrogenases.[407–410] Chains of FeS clusters are particularly desirable design targets as they are likely to be required for the application of hydrogenases to electrodes or photoelectron sources.[411–412] Common FeS clusters include the $FeCys_4$ metal center of rubredoxin as well as [2Fe-2S], [3Fe-4S], and [4Fe-4S] clusters. *De novo* design efforts have been centered on rubredoxin and [4Fe-4S] clusters so these will be the focus of this section.[413]

The simplest form of an FeS cluster is the $FeCys_4$ binding site of rubredoxin, and this made it an early target of *de novo* metalloprotein design (Figure 52). Lombardi and Pavone created a miniaturized rubredoxin to determine the smallest functional unit of the native structure.[414] Rubredoxins are small proteins with a high-spin Fe in a tetrahedral Cys_4 binding site.[415] Structural analysis determined that within 17 Å of the Fe, the native protein had a pseudo-C_2 symmetry axis with Cys residues at i and i+3 positions of two type 3 β-hairpins.[416–419] C_2 axes were included in previous designs by Lombardi and Pavone (DF1 and mimochromes) to simplify design and decrease the peptide length necessary for synthesis.[23, 25–26, 147, 420–422] While the authors determined that a peptide of only 5 AA in length could recapitulate the primary coordination sphere of rubredoxin, this was extended to 11 AA to destabilize undesirable diastereomeric forms. The final design, METP, used the sequence from Cys39 to Phe49 of rubredoxin with a number of modifications to avoid steric clashes (Phe40Thr, Phe49Ile) and reinforce dimer formation (Val41Lys, Pro45Asn, Lys46Aib) (Figure 53).

Author Manuscript

Author Manuscript

Author Manuscript

Author Manuscript

METP successfully bound Co, Zn, and Fe ions in an apparent tetrahedral Cys_4 geometry. Co(II)METP absorption spectroscopy was in agreement with Co(II)-substituted rubredoxin with d-d transitions characteristic of tetrahedral geometry and an LMCT band at 350 nm indicative of Cys ligation.[423–426] Zn(II) binding was determined by competition with Co(II)METP and while no spectroscopic information could be obtained, the construct's lower affinity for Co(II) (53.5 μM) than Zn(II) (2.7 μM) is consistent with tetrahedral coordination.[427–428] METP bound Fe(II) and formed a red color upon air oxidation indicative of Fe(III)METP. This color irreversibly faded within less than a minute in water, but was much more stable in MeOH, where the Fe(III)METP absorption spectrum was recorded. Fe(II) and Fe(III)METP had absorption spectra consistent with native rubredoxins.[429–430] Overall, this minimal model correctly recapitulated the primary coordination sphere of native rubredoxin in the Fe(II) and Fe(III) oxidation states, but its stability and functionality as an electron transfer center in water was not modelled.

Arguing that the previous system had failed to go through reversible redox cycles because of lacking tertiary structural constraints, Nanda and DeGrado created a more complex design to address the immediate secondary structure surrounding the rubredoxin Fe binding site.[431] This was notable in that few studies had include beta sheet structure design elements at the time. Following retrostructural analysis the environment around the Fe in rubredoxin was described as two beta hairpins related by C_2 symmetry. Each hairpin was redesigned with an additional *C*-terminal appendage that would interact with the opposite hairpin with the goal of increased tertiary structural complex stability (Figure 53). Initial studies with this dimeric design were promising, but these scaffolds were only stable for four redox cycles so further redesigns attempted to create a single chain version.

The dimers were fused together with a tryptophan zipper motif and the active-site cysteines were rationally redesigned for the new topology while other amino acids were chosen with the SCADS methodology developed by Kono and Saven (Figure 54).[432–433] The final design (RM1) was 40 AA long and had a different beta sheet topology compared to native rubredoxin. The Co(II)RM1 absorption spectrum had a d-d transition near 700 nm and a LMCT at 340 nm and the Co(II) was displaced upon addition of Zn(II), all consistent with a tetrathiolate environment.[414, 423, 425–426] Surprisingly, even though the protein scaffold was relatively small and simple, CD analysis indicated that it was folded in both the apo and holo states, suggesting a preorganization of the metal binding site. The absorption spectrum of Fe(III)RM1 exhibited expected bands at 370, 490, 600, and 750 nm and the redox potential was on the edge of that for native rubredoxins at 55 mV vs. NTE, indicating that Fe(III)RM1 has a similar Fe-binding environment as native rubredoxin. The most impressive part of this design was its ability to go through 16 redox cycles, well above the previous record for a designed rubredoxin of three cycles.[426] FeRM1 remains the most stable rubredoxin model to redox cycling, a significant achievement.

The minimized rubredoxin structure around the metal binding site had successfully maintained Fe geometry but questions remained. Is the β sheet secondary structure necessary for correct tetrahedral geometry or is it possible to design the same geometry into a much more rigid alpha helical scaffold? Tebo and Pecoraro designed a rubredoxin Cys_4 binding site into the α_3D scaffold, based on a Cys_3 heavy metal binding peptide

Author Manuscript Author Manuscript Author Manuscript Author Manuscript

(α_3DIV).[181, 184, 434] Recent work on mimicking the Cd(II) binding site of CadC had created several Cys_4 binding sites and shown that α_3DIV L21C reproduced the Cd(II)Cys_4 binding site, so this peptide was investigated as a possible rubredoxin mimic (Figure 55).[435]

Fe(II)- and Fe(III)-α_3DIV L21C were characterized by absorption, Mössbauer, EPR, and MCD spectroscopies which all confirmed that the electronics of native rubredoxin had been recapitulated. MCD spectroscopic analysis was particularly compelling as it deconvoluted the absorption spectrum into nine transitions which closely resembled those of Fe(III)rubredoxins from *Clostridium pasterurianum* and *Desulfovibrio gigas*, a first for a rubredoxin model.[436–437] EXAFS analysis found that Fe(II)α_3DIV L21C had an Fe-S distance of 2.32 Å, similar to that of native reduced rubredoxins, indicating that Fe(II)α_3DIV L21C was also a good structural model of rubredoxin.[438–439] The measured redox potential of Fe(II/III)α_3DIV L21C of −75 mV vs. NHE was within the range of native systems, but this construct was only capable of three redox cycles before irreversible bleaching occurred.[440–443] This study proved that the tetrahedral $FeCys_4$ binding site of rubredoxin could be divorced completely from its protein structural environment and a functional model created within an unrelated protein fold, a rigid alpha helical scaffold compared to the native loop structures between beta sheets.

The function of an electron transfer center is either intra- or intermolecular reduction/oxidation. The Aukauloo lab in collaboration with the Pecoraro lab investigated these properties using electron transfer protein mimics to determine the functionality of these *de novo* designs.[444] While the Pecoraro lab has collaborated with the Quaranta lab to examine intermolecular electron transfer properties, we will focus our attention here on intramolecular electron transfers as these are arguably more pertinent to the creation of complex *de novo* enzymes.[444–446] Tebo and Aukauloo first investigated whether apo α_3DH_3 could produce a Tyr radical for long range electron transfer. The redox-active amino acids Tyr and Trp are often used as “pit stops” for long distance electron transfers through a protein matrix.[447] Tyr radicals in particular are vital parts of biological systems that require long-distance electron transfers such as photosystem II and ribonucleotide reductase.[448]

De novo scaffolds designed by Tommos and Dutton have been used to study these amino acid radicals directly through the design of α_3W and α_3Y which are 3HB bundle peptides with redox active amino acids at the 32nd positions (either Trp or Tyr).[449] Using pulsed nonreversible voltammetry, the authors determined that burying these aromatic amino acids within the hydrophobic interior increased the redox potential of Tyr by 900 mV vs NHE but only increased that of Trp by 350 mV vs NHE. Dai and Wand later determined the NMR structure of α_3W which suggested a π-cation interaction between Trp32 and Lys36 at a distance of 4.7 Å, consistent with similar interactions in native proteins.[450–451] Further studies of α_3Y by the Tommos lab determined the Tyr32 redox potential to be 1070 or 910 mV vs NHE at pH 5.5 or 8.5, respectively, using square wave voltammetry.[452] This radical was also surprisingly stable with a half-life of 2 to 10 seconds as determined by time-resolved spectroscopy.[453]

For their study Tebo and Aukaloo attached a $[Ru(II)bpy_3]^{+2}$ photooxidant to the *C*-terminal Cys residue of a variant of α_3DH_3 which would place the chromophore within ~16 Å of

Author Manuscript Author Manuscript Author Manuscript Author Manuscript

Tyr70 (Figure 56).[454] Using nanosecond laser flash photolysis, the rate of electron transfer from Tyr70 to the $[Ru(II)bpy_3]^{+2}$ attached to α_3DH_3 was determined to be $3.3 \times 10^5\ s^{-1}$, consistent with that expected at a distance of ~16 Å. The presence of a Tyr radical was confirmed using X-Band EPR. This showed that a Tyr radical could be produced in this context and was an important first step toward long-distance electron transfer within *de novo* metalloproteins. Design of electron transfer relays, requiring multiple transfers within a scaffold, has only recently been investigated.[402, 420] Tebo and Aukauloo used α_3DIV L12C (the previously described rubredoxin mimic) to determine whether $[Ru(II)bpy_3]^{+2}$ could oxidize the $FeCys_4$ site using Tyr70 as an intermediate.[444]

Transient absorption spectroscopy of the full relay showed that Tyr70 oxidation was the rate determining step at $1.4 \times 10^5\ s^{-1}$ but this was indistinguishable from $Fe(II)Cys_4$ oxidation due to the short distance between Tyr70 and the metal binding site (~5–7 Å). This was confirmed using apo-α_3DIV L12C in which a Tyr70 radical was produced at a similar rate as Fe(III) in the holo construct. Finally, α_3DIV L12C Y70F was tested as a control. This variant showed a 20-fold decrease in $Fe(II)Cys_4$ oxidation rate of $6.3 \times 10^{-3}\ s^{-1}$, demonstrating the critical role of Tyr70 for fast electron transfer. As more complex designs with multiple metal binding sites are targeted by protein designers, electron transfer relays become particularly important.

The most common type of FeS cluster is the [4Fe-4S] cluster.[406] These play a major role in long electron transfer chains in enzymes like hydrogenases.[410] Designing [4Fe-4S] clusters within an alpha helical scaffold is an interesting design problem because most FeS proteins use beta sheet and loop structure around the metal binding sites.[456] A [4Fe-4S] design within an alpha helical scaffold could be repeated in nearby scaffold layers, simplifying the design of [4Fe-4S] chains for long distance electron transfer.[457–458] Grzyb and Noy were the first to report α-helical [4Fe-4S] clusters using what they termed a “metal-first approach”.[459] This strategy identified a useful motif from the [4Fe-4S] cluster protein tryptophanyl-tRNA synthase (PDB 2G36) which contains a cluster bound between several alpha helices and a CXXC motif on a single helix.[460] A 4HB (CCIS1) was designed that incorporated two of these motifs at a reasonable distance to incorporate a [4Fe-4S] cluster (Figure 57).

[4Fe-4S]-CCSI1 was produced by *in situ* chemical synthesis of the cluster according to established protocols with a reconstitution yield of about 75%.[461–462] Absorption spectra of [4Fe-4S]-CCSI1 exhibited a peak at 415 nm with a shoulder at 360 nm, which disappeared upon reduction, while elemental analysis found a ratio of 4.2 (Fe:protein). These analyses confirmed that a [4Fe-4S] cluster was correctly incorporated. Unfortunately, this construct was non-functional as reduction from $[4Fe\text{-}4S]^{+2}$ to $[4Fe\text{-}4S]^{+}$ was irreversible. The authors suspected this was due to sulfur hydrolysis and that addition of secondary sphere H-bonds to the sulfurs could mitigate the issue; as of yet, this has not been reported for this system.[463–465]

Roy and Ghirlanda were the first to create multiple [4Fe-4S] sites within a *de novo* protein using a previously described dimeric scaffold DSD.[70, 466] The DSD scaffold was originally designed to probe domain swapping by the dimeric assembly of helical hairpins where one

Author Manuscript

Author Manuscript

Author Manuscript

Author Manuscript

helix was twice the length of the other, forcing the protein to dimerize in an antiparallel orientation. Incorporating a [4Fe-4S] cluster within the dimer structure created a construct with two clusters separated by 30–34 Å called DSD-bis[4Fe-4S] (holo) and DSD-4Cys (apo). The dimeric assembly of multiple [4Fe-4S] clusters is reminiscent of the gene duplication event thought to be the origin of two-cluster ferredoxins in which 29 residues were duplicated to form the modern protein.[467] The binding site of DSD-bis[4Fe-4S] mirrors that of these ferredoxins with three Cys residues from one monomer and the fourth from the other (Figure 58).

Dimer formation of the scaffold was confirmed by size exclusion chromatography and analytical ultracentrifugation. CD analysis of the apo protein (DSD-4Cys) showed that secondary structure was largely unchanged upon cluster incorporation, surprising given the relatively large clusters, indicating a preorganized metal binding sites. Absorption spectra of DSD-bis[4Fe-4S] had bands at 415 and 360 nm with a 410/280 nm ratio of 0.76, properties within the range of that observed in natural [4Fe-4S] cluster proteins.[468–469] Correct cluster formation was confirmed by visible CD similar to ferredoxins and pulsed electron-electron double resonance analysis consistent with the clusters being 30–34 Å apart.[470–471] Cyclic voltammetry analysis showed a cathodic wave at −478 mV vs NHE, but no anodic wave was observed. While the cathodic wave was within the range of natural [4Fe-4S] cluster proteins, the missing anodic wave indicates that the reduction of DSD-bis[4Fe-4S] is irreversible.[472]

While the above study successfully created a *de novo* protein with two [4Fe-4S] clusters, the 30–34 Å separation is too far for reasonable single-hop electron transfer. In a follow-up study, Roy and Ghirlanda designed DSD-Fdm, a second generation DSD with the two clusters 12 Å apart, within the range for native electron transfer relays (12–14 Å) (Figure 59).[473] EPR spectra of DSD-Fdm did not exhibit the spin-spin interactions often observed when two [4Fe-4S] clusters are at this distance, but this was explained by several factors such as low yield of reduced clusters in the EPR conditions.[474–475] Most importantly, this was the first *de novo* designed [4Fe-4S] cluster scaffold with reversible redox measured by cyclic voltammetry. The determined redox potential of −479 mV vs NHE was consistent with a $[4Fe\text{-}4S]^{2+/1+}$ couple and falls within the expected range of a low potential native [4Fe-4S] cluster.[465, 468, 476] Given this redox potential is similar to what is observed in [4Fe-4S] cluster ferredoxins, the authors determined DSD-Fdm could transfer electrons to cytochrome c_{550}. These results suggest that pairing these two [4Fe-4S] clusters created a redox active electron transfer center, and that this could be incorporated as part of an artificial pathway for synthetic biology applications.

As the *de novo* metalloprotein community pushes from first principles design to the application of these constructs, the question of *in vivo* metalation status looms. Synthetic biology applications require that these constructs be functional *in vivo*, but most *de novo* proteins are purified in apo form and then reconstituted *in vitro*. The few reported examples of *in vivo* metal incorporation rely on structural motifs that permit covalent attachment of a cofactor such as *c*-type hemes or bilins.[90, 477] Control of *in vivo* metal or cluster incorporation without covalent attachment remains unsolved. A recent study used the previously reported CCIS scaffold to investigate the differences between *in vivo* or *in vitro* [4Fe-4S] metalation of this construct.[478] CCIS had been previously reconstituted *in*

Author Manuscript
Author Manuscript
Author Manuscript
Author Manuscript

vitro using $FeCl_3$, Na_2S, and DTT under anaerobic conditions, but showed batch to batch variability with different mixtures of oligomers.[463] *In vivo* reconstitution of CCIS was achieved by inducing expression anaerobically to promote formation of FeS cluster proteins (Figure 60).[479–480] Expression conditions were optimized by following the coloration of cell pellets, brown cell pellets are often observed when expressing native FeS cluster proteins.[481]

Surprisingly, *in vivo* reconstituted CCIS produce only a single oligomer, though this was not the expected monomer but a trimer containing a single [4Fe-4S]. The authors suggested that *in vivo* cluster incorporation may produce a single oligomer due to smoothing of the folding energy landscape within the cellular milieu.[482–483] The trimer of *in vivo* CCIS was confirmed by SEC, ICP-AES which showed 4.4 sulfurs for each iron atom or 12 cysteines per 4Fe4S cluster, and static light scattering. Variants with different Cys to Ser substitutions were used to determine which Cys residues were essential for [4Fe-4S] cluster binding. Cys13 and Cys17 were found to be essential for *in vivo* assembly, while Cys61Ser and Cys65Ser mutations showed no impact on assembly. *In vivo* reconstituted CCIS also differed in its chemical properties. It was more resistant to reduction by dithionite compared to *in vitro* reconstituted CCIS and showed slight oxygen tolerance (20% of cluster remained after O_2 exposure compared to 0% in *in vitro* construct). Given the redox potential of dithionite is −600 mV vs NHE, this suggests that *in vivo* CCIS has a redox potential nearing the limits measured for natural ferredoxins.

Diffraction quality crystals of *in vivo* CCIS were not obtained, but small-angle X-ray scattering (SAXS) was used to get a low-resolution trimeric structure. During *in vivo* incorporation, CCIS unfolds and three copies of helix 1 interact to form the [4Fe-4S] cluster binding site; the remaining Cys residues form disulfides (Figure 61). This was confirmed by expressing a construct that only contained Helix 1, which was able to produce an *in vivo* cluster. Expressing helix 3 (the other helix of CCIS with possible metal binding site Cys residues) did not show *in vivo* cluster incorporation. The differences in the helices of CCIS hint at structural motifs that may be important to engaging with the [4Fe-4S] cluster synthetic pathways of *E. coli*.[484] This study is one of the few where a designed metalloprotein interacts with the cellular machinery responsible for native metalloproteins maturation. *In vivo* production of these proteins accelerates their optimization and, more importantly, understanding of how active constructs can be created *in vivo* will allow *de novo* metalloproteins to participate in synthetic biology solutions.

5.2. Cupredoxins

Cupredoxins have long fascinated the bioinorganic chemistry community with deep colors of blue, green, red, or purple. These vibrant colors are the result of constrained Cu geometries not preferred by either oxidation state using a “Greek key” structural motif typically dominated by beta sheets (Figure 62).[485–486] The color of the bound Cu(II) is dependent on the energy and intensity of LMCT bands between the Cu $d_{x^2-y^2}$ orbital and Cys σ or π molecular orbitals. A brief explanation of the different cupredoxins, their coordination environment, and the absorption and EPR spectroscopy is informative when discussing the results of cupredoxin design projects.

Author Manuscript Author Manuscript Author Manuscript Author Manuscript

Poplar plastocyanin is one of the most well studied blue-copper proteins. It has a $CuHis_2CysMet$ binding site with a short Cu(II)-Cys distance of 2.08 Å, LMCT absorption bands at 460 nm for σ and 597 nm for π with $\epsilon_{\sigma/\pi}$ ratio of 0.05, and EPR hyperfine coupling constant of 63×10^{-4} cm^{-1}.[487–488] Within the group of blue cupredoxins, there are also perturbed blue cupredoxins such as stellacyanin with $CuHis_2CysGln$ coordination producing a Cu(II)-Cys distance of 2.17 Å, LMCT bands at 448 and 604 nm with $\epsilon_{\sigma/\pi}$ ratio of 0.29, and EPR hyperfine coupling constant of 35×10^{-4} cm^{-1}.[489–490] The electron transfer center of Cu nitrite reductase (CuNiR) is a green cupredoxin with $CuHis_2CysMet$ coordination leading to LMCT bands at 457 and 570 nm with $\epsilon_{\sigma/\pi}$ ratio of 0.29, Cu(II)-Cys distance of 2.22 Å, and a hyperfine coupling constant of 73×10^{-4} cm^{-1}.[491–492] The primary coordination spheres of blue and green cupredoxins are all either trigonal planar or distorted tetrahedral with slight changes in the positioning of the Cu caused by varying axial coordination strength leading to electronic differences as explained by the “coupled distortion” model.[486] Red cupredoxins are exemplified by nitrosocyanin with a tetragonal coordination of $CuHis_2GluCysH_2O$, LMCT bands blue shifted relative to previous examples at 390 and 490 nm with $\epsilon_{\sigma/\pi}$ ratio of 3.18, Cu(II)-Cys bond of 2.30 Å, and EPR hyperfine coupling constant of 142×10^{-4} cm^{-1}.[493–494] Purple cupredoxins have binuclear Cu binding sites with two bridging Cys residues about 3.6 Å apart, two equatorial His and various weakly interacting axial groups leading to intense bands at 480 and 530 nm and a complex EPR spectrum with 7-line EPR hyperfine splitting.[495–500]

Schnepf and Hildebrant were some of the first to explore the *de novo* design of cupredoxins using a scaffold of different secondary structure.[501] Their strategy was to create a combinatorial library of 4SCCs using template assembly to incorporate three different helices in AB_2C stoichiometry.[502–503] This was based on a previous study where they created an initial library of 96 constructs with Cu-Cys in tetragonal geometries that showed no cupredoxin-like spectroscopy.[504] Using the most stable of these Cu binding constructs, Mop5, an additional library of 180 proteins was created which altered secondary sphere residues while maintaining the primary sphere (Figure 63). The goal of this library was to determine whether secondary sphere mutations (to change sterics, polarity, or flexibility) could stabilize the bound Cu and permit new Cu coordination geometries.

Constructs were screened by spotting on a sheet and adding $CuCl_2$ to examine the color of each by eye. There were three different colored classes within the library. Three constructs were chosen for further analysis as representatives; Cu-Mop21 (yellow), Cu-Mop22 (purple), and Cu-Mop23 (brown or blue). Cu-Mop21’s yellow absorption spectrum exhibited a strong absorbance at 400 nm, consistent with Cu bound to Cys in a tetragonal geometry similar to the predecessor Cu-Mop5 (Figure 64). Cu-Mop22 (purple class) showed a complex absorption spectrum with bands at 477, 637, and 774 nm indicating a dinuclear CuA site similar to that of cytochrome *c* oxidase.[499, 505] Finally, Cu-Mop23 from the brown or blue category had bands of similar intensity at 428 and 571 nm typical of a cupredoxin; specifically, this spectrum matched that of green cupredoxins such as the electron transfer center of CuNiR.[491]

Resonance Raman spectral analysis determined Cu-S bond lengths using a previously established empirical relationship from natural Cu proteins.[506] Cu-S distances were

Author Manuscript

Author Manuscript

Author Manuscript

Author Manuscript

determined to be 2.23 Å for Cu-Mop21 while Cu-Mop23 was shorter at 2.205 Å as expected based on the green cupredoxin-like absorption spectrum. EPR spectral analysis of Cu-Mop21 and Cu-Mop23 showed that the hyperfine coupling constants did not follow the expected relationship based on absorption spectroscopy. The normal Cu ($>130 \times 10^{-4}$ cm^{-1}) was expected to have a less compressed hyperfine coupling constant than a green cupredoxin ($<100 \times 10^{-4}$ cm^{-1}), but Cu-Mop21 was more compressed (107×10^{-4} cm^{-1}) than Cu-Mop23 (123×10^{-4} cm^{-1}), which is atypical.[507–508] Cu-Mop22 EPR analysis was consistent with its assignment as a dinuclear CuA site with a highly compressed coupling constant of 30×10^{-4} cm^{-1}.[499] This study demonstrated that variations in the secondary sphere of a CuHis$_2$Cys binding site within a *de novo* protein could vary the type of Cu site between tetragonal, green, or purple cupredoxins. It is particularly interesting that these secondary sphere changes could convert the tetragonal Cu-Mop5 to the tetrahedral (based on absorption spectroscopy) Cu-Mop23, given that larger rearrangements were required for similar results in later studies within three-helical bundles.[509]

A rational design approach was later used by Shiga and Tanaka to incorporate the cupredoxin binding site into a 4HB based on a previous His$_2$Glu Cu binding peptide (Figure 65).[510–511] Their design focused on burying the metal binding site to prevent solvent access. This had been shown to stabilize copper sites while leaving space within the hydrophobic core and allowed the metal binding residues to adopt the preferred metal binding conformation.[512] The final construct (AM2C) had absorption spectroscopy which varied based on buffer composition. While in phosphate-buffered saline, Cu(II)-AM2C had a typical blue copper protein spectrum with intense band at 616 nm, weaker band at 474 nm, and extinction coefficient ratio of 0.30. When no chloride was present as an exogenous ligand, the two bands were similar in ratio, and the construct looked more green copper-like. A later study showed that high concentrations of a variety of exogenous ligands such as phosphate, chloride, sulfate or acetate could bind to Cu(II)-AM2C and caused the conversion to the blue cupredoxin-like absorption spectroscopy.[513]

Further work focused on the chloride bound Cu(II)-AM2C (Cu(II)-AM2C-Cl$^-$), as this was the most like the blue cupredoxin target. Cu(II)-AM2C-Cl$^-$ was stable for a couple of hours under aerobic conditions before the absorption spectrum was bleached. Mass spectrometric analysis of the product determined that it was 32 mass units greater than the designed peptide, indicating that a Cys had been oxidized from S to SO$_2$. This bleaching is a common issue with *de novo* produced cupredoxins and has been observed to varying degrees in 3HB cupredoxins as well. EPR spectra of Cu(II)-AM2C-Cl$^-$ exhibited a highly compressed hyperfine coupling constant at 15×10^{-4} cm^{-1}. This value is lower than that observed in native blue copper proteins but has been observed in variants with exogenous ligands such as His117Gly azurin with Cl$^-$ or azide bound.[514–515] Structural analysis via EXAFS determined that the Cu-S distance of Cu(II)-AM2C-Cl$^-$ was surprisingly long at 2.30 Å, on the border of native blue copper proteins.[516–517]

Cu(II)-AM2C was the first rationally designed *de novo* green cupredoxin, and its chloride-bound form was the first *de novo* designed blue cupredoxin. It is particularly interesting that this was possible within the binding site of AM2C where a His$_2$Cys primary sphere is surrounded by Ala residues. Given the work of Schnepf and Hildebrant, and the general

Author Manuscript Author Manuscript Author Manuscript Author Manuscript

requirement of a constrained cupredoxin metal binding geometry, it is surprising that steric enforcement appears unnecessary in this scaffold.

Using the same scaffold, Shiga and Tanaka designed a binuclear purple cupredoxin.[518] Two Cys residues were placed at *i* and *i* + 3 positions of the same helix so that they would be 4 Å apart, similar to the 3.6 Å distance of native CuA sites.[496, 498] 4 His ligands were designed in possible equatorial and axial positions and Ala residues were placed on other nearby helices to allow space for ligating residue rotation (Figure 66). The final construct was called bi-AM2C.

Cu(II)bi-AM2C is purple in color, with an intense absorption band at 488 nm and a shoulder at 530 nm, similar to that seen in native CuA.[495, 499–500] This absorption spectrum decayed with a half-life of 2.4 hours due to oxidation of Cys residues, similar to the previous construct. EPR spectral analysis of Cu(II)bi-AM2C had similar g-values and temperature dependence as native CuA but did not contain the typical 7-line hyperfine splitting pattern. However, not all native CuA sites have discernable hyperfine splitting, so this was consistent with a designed purple cupredoxin.[495, 500, 519–521] EXAFS structural analysis was consistent with 1 Cu-His bond at 1.9 Å, 2 Cu-Cys bonds at 2.21 Å, and a Cu-Cu interaction at 2.51 Å, all of which are similar to those of native CuA.[498] Given the success other labs have shown with incorporating heme binding sites into 4HBs, the authors suggested that heme could be incorporated within their construct to produce an electron transfer chain similar to that in cytochrome *c* oxidase, but this has not yet been reported.[457, 522]

By this point, it had been shown that *de novo* green and purple cupredoxins could be designed combinatorically or rationally, but recreation of the prototypical blue cupredoxin using only amino acid ligands (as well as the less understood red cupredoxin) remained unsolved. The Pecoraro lab used rational design within a 3HB to design cupredoxins and were eventually able to reproduce all of the mono-metal cupredoxin classes within a single scaffold.[509, 523–524] The Pecoraro lab first started with the α_3D scaffold, previously shown to accommodate both Cys_3 or His_3 sites, and determined if a cupredoxin with a $His_2Cys(Met)$ binding site could be recreated.[179, 184, 523] The authors attempted three different classes of cupredoxin designs: α_3D-core (CR), with binding residues placed within the hydrophobic core spanning all three helices; α_3D-chelate (CH), with a chelate motif where the primary binding residues are between two helices; and, α_3D-chelate-core (ChC) with both strategies combined. Seven constructs were designed but three had Cu(II) absorbance spectra that bleached within 5 minutes and were not characterized further. The four remaining constructs were stable for either 10 minutes (α_3D-CR1, α_3D-CH4), 4 hours (α_3D-CH3), or 15 hours (α_3D-ChC2) (Figure 67).

Cu(II) absorption spectra of all but one of these constructs had no discernible Cys-π LMCT and EPR spectra hyperfine coupling constant values typical of "normal" Cu bound to Cys with no cupredoxin character. Within this series, it is interesting that flipping the HXXC chelate motif (Cu(II)α_3D-CH3) to a CXXH (Cu(II)α_3D-CH4) had drastic effects on both the absorption spectra and the longevity of the Cu(II) species, but otherwise the designs were unsuccessful. Cu(II)α_3D-ChC2 was unique among the series of four constructs as its absorption spectrum showed a distinct Cys-π LMCT with $\epsilon_{\sigma/\pi}$ ratio of 2.2, band energies of

Author Manuscript Author Manuscript Author Manuscript Author Manuscript

401 and 499 nm and a mildly compressed hyperfine coupling constant of 136 × 10^{-4} cm^{-1}. These spectroscopic characteristics are consistent with the red cupredoxin nitrosocyanin as well as axial ligand variants of blue cupredoxins such as M121E azurin and M148E rusticyanin.[494, 525–526]

EXAFS analysis of Cu(I) forms of the four constructs was consistent with short Cu(I)-Cys bonds between 2.16 and 2.23 Å suggesting that the Cu(I) state is blue cupredoxin-like even if the Cu(II) state is that of a non-cupredoxin or red cupredoxin.[490, 527–528] The redox potentials of these constructs was 350–500 mV vs. NHE. A separate electron transfer study showed that α_3D-CH3 is capable of rapid intermolecular electron transfer, albeit with a reorganization energy on the upper end of what has been observed in native cupredoxins (1.1 eV).[445, 529–532]

This first study determined that rearrangements in the primary coordination geometry could have drastic effects on the Cu(II) electronic structure, but the Cu(I) geometry and redox potential were less variant. Only Cu(II)α_3D-ChC2 appeared to have an entatic state, while the other three constructs allowed the Cu to enforce its preferred tetragonal geometry.[533–534] α_3D-ChC2 was designed to encapsulate a CXXXH chelate metal binding site within a hydrophobically-constrained box and enforce an entatic state on the Cu(II) ion, but CD analysis indicated that the peptide was in a semi-stable state. There was also the question of whether the absorption spectrum resulted from a nitrosocyanin-like geometry or an axial ligand variant of a blue cupredoxin. Koebke and Pecoraro investigated this construct further to determine the origin of its absorption spectrum with the eventual goal of using this knowledge to create a *de novo* blue cupredoxin.[524]

One possibility for α_3D-ChC2's red-copper spectroscopy is that the pseudo-stable nature of this construct was unable to enforce the entatic state upon the bound Cu(II) and produce a blue copper site. The authors elongated the alpha helical region of the scaffold (a strategy previously used to increase stability in 3SCCs) to make GRANDα_3D (GRα_3D) (Figure 68).[156, 535] They then created a stable version of α_3D-ChC2 called GRα_3D-ChC2, but the Cu(II) absorption and EPR spectroscopies remained that of a red cupredoxin.

Using the crystal structure of GRα_3D, a model of the binding site was created in Pymol. Because the His_2Cys residues spanned only two helices of the scaffold, the Cu(II) would be positioned more toward the helical interface, rather than the hydrophobic interior as originally intended. This would allow the Cu(II) to interact with Glu41 from a nearby Glu41-Arg24 salt bridge (Figure 69). A Cu(II)-Glu interaction could explain the red cupredoxin character of GRα_3D-ChC2 since native nitrosocyanin has a $His_2CysGluH_2O$ coordination sphere and Met to Glu variants of blue copper proteins also have similar absorption spectroscopy.[494, 525–526] E41Q and E41A variants of GRα_3D-ChC2 were designed and lost their cupredoxin-like character to become yellow tetragonal Cu(II) binding sites based on absorption and EPR spectra. This result and MCD analysis of the original GRα_3D-ChC2 confirmed that its red cupredoxin-like spectroscopy was due to a nitrosocyanin-like binding site rather than a Met to Glu variation of a blue copper protein site.[494]

Author Manuscript Author Manuscript Author Manuscript Author Manuscript

Various investigations of native cupredoxins have shown that variants of one cupredoxin class can convert its spectroscopy to that of another class. For example, CuNiR M182T eliminates the axial Met residue to convert a green cupredoxin site to a blue cupredoxin; a more drastic rearrangement by repositioning and converting the axial Met of the blue cupredoxin azurin to Glu can create a red nitrosocyanin-like cupredoxin.[233, 528, 536] Koebke and Pecoraro applied these strategies to GRα_3D-ChC2 to tune the red cupredoxin to green and eventually blue.[509] Their previous study established GRα_3D-ChC2 likely had a His$_2$CysGlu binding site similar to nitrosocyanin, so they reversed the strategy of Tian and Lu by repositioning the Glu axial ligand and converting it to Met.[536] GRα_3D-ChC2 H38M E41H (GRα_3D-ChC3) and GRα_3D-ChC2 H25M E41H (GRα_3D-ChC4) represent the two possible inversions of the active site one could do to reverse the blue to red strategy employed by Tian and Lu (Figure 70).

GRα_3D-ChC3 produced a yellow non-cupredoxin copper thiolate species, and GRα_3D-ChC4 created a convincing green cupredoxin having red-shifted absorbance peaks, $\epsilon_{\sigma/\pi}$ ratio of 0.87, and EPR spectrum indicative of a compressed hyperfine coupling constant (Figure 70). The authors hypothesized that GRα_3D-ChC3 lost the His$_2$Cys primary coordination sphere, similar to variants of azurin which lose their cupredoxin spectroscopy upon mutation of a primary sphere His residue.[537–538] The authors next sought to convert this *de novo* green cupredoxin to blue by removing the axial Met residue in a similar strategy as CuNiR M182T.[528] GRα_3D-ChC2 H25I E41H (GRα_3D-ChC5) proved successful with a $\epsilon_{\sigma/\pi}$ ratio of 0.33, well within the range of perturbed blue cupredoxins previously seen only with exogenous ligands (Figure 71).

Unfortunately, these *de novo* green and blue cupredoxins were relatively unstable, with half-lives less than 30 min. Attempts to use R24 variants to enclose the binding site proved unsuccessful. Also, analysis of the Cu(II)GRα_3D-ChC5 EPR spectrum showed it was a mixture of cupredoxin and tetragonal Cu species in a 1:1 ratio. This ratio varied with pH, possibly because the His41 position is accessible to solvent. Native cupredoxins, on the other hand, are often extremely stable to pH changes.[539–541] That these *de novo* cupredoxins are variant to buffer conditions and bleach over time is a clear barrier to their utilization which warrants further investigation. None-the-less, these derivatives demonstrate, as was observed for rubredoxins, that even a center as sensitive as a blue cupredoxin can be built in a protein fold (without the requirement for non-coded amino acids or exogenous ligands such as chloride) that differs drastically from that found in nature. It is highly likely that a directed evolution approach, beginning with Cu(II)GRα_3D-ChC5 should provide the desired stability and selectivity for a single blue copper species that is desired.

5.3. Summary

The unique spectroscopic features of electron transfer sites like cupredoxins and FeS clusters have made them enticing targets for metalloprotein designers. The FeCys$_4$ metal binding site of rubredoxin was miniaturized by Lombardi and Pavone by recapitulating the minimal secondary structure around the metal.[414] While this successfully recreated the desired spectroscopic features, the construct was not capable of redox and non-functional. Nanda and DeGrado revisited this strategy and created a more complex design with intersubunit

Author Manuscript

Author Manuscript

Author Manuscript

Author Manuscript

interactions that was stable for up to 16 cycles of redox (currently an unbroken record for a *de novo* rubredoxin).[431] More recently Tebo and Pecoraro proved the secondary structural elements around the metal binding site in rubredoxin are unnecessary by using an alpha helical bundle scaffold (Figure 72).[434] This was later combined with a photooxidant as part of a multistep long distance electron transfer chain.[444, 446]

While the binding site amino acids are similar to rubredoxin, the design of [4Fe-4S] clusters requires specific positioning of these amino acids to form the larger cluster. Grzyb and Noy successfully recreated this cluster within an alpha helical scaffold, but even after revisiting the work they were unable to create a redox-stable construct.[459, 463] Roy and Ghirlanda targeted chains of [4Fe-4S] clusters and created a construct with clusters 29–34 Å apart, too far for interaction.[70] These authors later repositioned these two clusters to 12 Å apart and successfully created [4Fe-4S] clusters that could not only interact but could redox cycle and transfer electrons to cytochrome *c* (Figure 72).[473] Most recently, Jagilinki and Nanda created a *de novo* [4Fe-4S] cluster protein that could incorporate the cofactor *in vivo*, opening up a number of possible synthetic biology applications (Figure 72).[478]

Cupredoxins, on the other hand, appear simple but maintaining their constrained metal coordination within a *de novo* scaffold has proved challenging. Schnepf and Hildebrant made the first *de novo* green and purple cupredoxins using a combinatorial approach which varied the sterics and charge of residues within the secondary sphere of the metal binding site.[501] Shiga and Tanaka later used rational design to recreate both green and purple cupredoxins within a 4HB.[511, 518] Their green cupredoxin could be turned blue using exogenous ligands (Figure 72).[513] The Pecoraro lab created a red cupredoxin and showed that one of these constructs could transfer electrons intramolecularly.[445, 523] Reexamining this construct, they determined an unplanned Cu(II)-Glu interaction caused the red cupredoxin-like spectroscopy and created the first *de novo* blue cupredoxin that does not require an exogenous ligand (Figure 72).[509, 524]

Through this work we have learned about the minimal requirements of these electron transfer sites. Rubredoxins and cupredoxins, whose metal binding sites are located within beta sheets and loops, can be at least partially recapitulated within a completely different secondary protein structure. Cupredoxins often have very weak interactions with backbone carbonyls within their primary coordination sphere which is difficult to reproduce in alpha helical scaffolds so it is interesting that this is not necessary to recreate the coordination spheres of red, purple, green, or blue cupredoxins. Through the [4Fe-4S] cluster work, we are beginning to understand the requirements for cluster incorporation *in vivo*. Finally, using rubredoxin as a test, electron transfer between two metal centers in a *de novo* scaffold has been established. There are, however, some notable missing pieces that are under investigated.

While all of these electron transfer sites have been faithfully reproduced from an electronic and structural standpoint, their function leaves much to be desired, particularly when it comes to stability. *De novo* Cu(II) cupredoxins have hours long half-lives before being irreversibly bleached, rubredoxins can at best redox cycle 16 times, and many [4Fe-4S] clusters cannot be reversibly reduced at all. Explorations into factors that impact the

Author Manuscript Author Manuscript Author Manuscript Author Manuscript

redox stability of these designs are sorely needed. Hydrogen-bonding interactions to the primary sphere Cys of cupredoxins may adjust their bleaching tendency. Redesigning the protein matrix around the electron transfer site might stabilize these structures to geometry changes during redox and stabilize redox cycling. Finally, the most functionally successful [4Fe-4S] cluster design used two clusters close enough to interact with one another, so it is possible that the short comings of our designs may be circumvented by combining multiple electron transfer sites in a similar fashion. The prevalence of electron transfer sites in native enzymatic systems suggests that perfecting their design will be a major step forward.

6. Perspective

De novo design of metalloenzymes allows investigators to completely wipe clean everything beyond the primary coordination sphere by incorporating it into a designed scaffold. As the design community moves forward, the next step is to increase design complexity and put back more of these secondary sphere interactions. Below are some areas that have not yet been fully explored as well as some possible means of attacking these problems.

There have been some successful designs which incorporate secondary sphere amino acid interactions to primary sphere residues (such as H-bonds to a coordinating His) but there have been few examples of designs that include substrate-activating interactions. Primary sphere residues are enforced in their position by the metal to which they coordinate and H-bonding with nearby secondary sphere residues. Substrate-activating residues, such as those in carbonic anhydrase or Cu nitrite reductase, have no direct interactions to enforce the necessary orientation, and thus have proven difficult to incorporate. That said, there are a few methods that have recently become applicable to *de novo* metalloprotein design that could solve this conundrum.

Directed evolution is a reliable method for including long range interactions in a designed construct and has been shown to be useful for carbonic anhydrase designs.[194] The DeGrado lab has started implementing whole protein scaffold redesign around metal binding sites to create stable constructs that allow for high resolution structures.[61, 63, 81] A similar method could be used to enforce the intended orientation of substrate-activating residues using the surrounding protein. Finally, balancing random chance and computational rational design, machine learning could offer a unique modern approach to historically difficult problems. For example, recently, natural proteins have been engineered for new functions using a relatively small library and machine learning algorithms to determine a pattern and suggest modifications for desired activity.[542–543] Application of these methods to *de novo* metalloenzyme design has yet to be explored, but it could become a powerful and common tool for protein designers.

Most *de novo* enzymes will not be industrially efficacious on their own, but more likely as part of a larger system. One way that designed constructs could be incorporated into such enzymatic cascades is using synthetic biology to create cell lines that complete a particular function. The limiting factor for designing *de novo* enzymes for such applications is the metalation state of the construct *in vivo*. This question looms over the community in part because many of these peptides are purified by reverse phase HPLC which will

Author Manuscript Author Manuscript Author Manuscript Author Manuscript

strip the protein cofactors if not covalently linked. There have been some interesting steps in this direction such as the work of the Anderson lab to understand the motifs necessary to incorporate *c*-type hemes into *de novo* proteins *in vivo*; or that of Jagilinki and Nanda to investigate how *in vivo* incorporated [4Fe-4S] clusters differ from those incorporated *in vitro*.[90, 109, 478] Studies which investigate the metalation state of overexpressed *de novo* proteins are useful, but more work is needed on *in vivo* design strategies.

Cellular metalation is a complex competition between a large pool of metalloproteins for limited amount of metals at different concentrations.[544] Keeping this in mind, the most important factor for controlling metalation will be how to intentionally set metal affinity of *de novo* constructs and tune them towards a particular metal and, therefore, function *in vivo*. Given that a carbonic anhydrase mimic can be switched to a CuNiR mimic simply by changing the metal from Zn to Cu, it is critical that this control is established. Studies in which metal preference is systematically controlled within *de novo* designed metalloprotein scaffolds are warranted. This should be coupled with metalloproteomic investigations to determine impacts on the metallome within the cell.[545] Coupling changes in metal affinities determined *in vitro* to metalation *in vivo* is an important goal in *de novo* metalloprotein design.

Finally, while there have been studies which recreate catalytic sites, and studies for electron transfer sites, these have not yet been combined. These combinations are regular features in native enzymes and represent an important next step in designs that go beyond the enzyme's primary coordination sphere. The pieces are all there with enzymatic and electron transfer sites designed within the same scaffold in separate studies, but there is more that can be done than remaking what Nature has already accomplished. *De novo* metalloenzyme studies of this type are not limited to mimicking Nature but could combine any electron transfer site with any enzymatic site. Is there a reason that CuNiR uses a cupredoxin for its electron transfer site or could a rubredoxin site work just as well? Could a hydrogenase be created with *c*-type hemes as electron transfer centers instead of [4Fe-4S] clusters? Once the communication between such centers is established, numerous exciting designs become possible.

In conclusion, *de novo* metalloenzymes design "clears the board" of an enzyme's evolutionary accessories, allowing us to strip away everything beyond the primary coordination sphere. As the field has matured, we must push beyond these minimal models and restore some of those features beyond the primary sphere. This review summarizes some of the recent work towards this goal and suggests future avenues that we feel are of particular importance. Once these can be addressed, protein designers will be measurably closer to not only accomplishing what nature has done but creating constructs that are useful beyond academic research. When it comes to such lofty goals for *de novo* metalloprotein design, the sky's the limit.

Biographies

Karl J. Koebke obtained his PhD working with Prof. Andy Pacheco (University of Wisconsin–Milwaukee) on the kinetics of nitric oxide dioxygenation in heme proteins.

Author Manuscript Author Manuscript Author Manuscript Author Manuscript

He then carried out postdoctoral research under Prof. Vincent Pecoraro (University of Michigan), designing a variety of de novo constructs including nitrite reductase and cupredoxin mimics. He went on to work with Dr. Timothy Stemmler (Wayne State University) on FeS cluster biogenesis and Prof. Neil Marsh (University of Michigan) on self-assembling protein nanocages. He now works as a Senior Scientist at Syngenta in the field of insect control.

Tyler B.J. Pinter received his PhD. from the University of Western Ontario (London, Canada) working with Professor Martin Stillman on mass spectrometric studies of metal binding to metallothionein. He next moved to the University of Michigan as an NSERC funded research fellow to work with Professor Vincent Pecoraro on *de novo* designed metalloprotein binding sites. He then moved to Duke University, working with Professor Katherine Franz to investigate metallo-β-lactamases and the impact of metal restriction on the *E. coli* proteome. He is currently at Syngenta where he is implementing mass spectrometric and proteomics strategies to improve seeds research.

Winston received his B.S. in Biochemistry at The University of Mississippi where he worked under Dr. Jonah Jurss studying CO_2 reduction using dinuclear rhenium complexes. Currently, he is working towards his PhD in inorganic chemistry at the University of Michigan under the guidance of Prof. Vincent Pecoraro, exploring *de novo* designed metalloenzymes with novel, unnatural active sites. His research interests also include using both kinetics and a variety of spectroscopic methods to elucidate the structure and electronic contributions to the reactivity of these unnatural active sites.

Vincent L. Pecoraro received his BS in Biochemistry from UCLA in 1977. He completed his PhD with K. N. Raymond at the University of California, Berkeley and then was an NIH Postdoctoral Fellow with W. W. Cleland at the University of Wisconsin, Madison. In 1984, he joined the faculty in the Chemistry Department at the University of Michigan, Ann Arbor, and was promoted to Professor in 1992 and Collegiate Professor in 2005. His research has focused on bioinorganic and metallomacrocyclic chemistry. He has worked for many years on the biological chemistry of manganese, especially dealing with Photosystem II and the manganese catalases. He has published extensively on vanadium coordination chemistry related to vanadium haloperoxidases and on spectroscopic methods for studying vanadyl protein substitution. In 1989, his group first described the molecular class of metallamacrocylces that are known as metallacrowns. His group has also focused on the *de novo* design of peptides capable of binding heavy metals such as Hg(II) and Cd(II) and more recently has developed some of the most active *de novo* designed metallohydrolases and metalloredox enzymes. He also has demonstrated that rubredoxin and blue copper centers can be built in helical scaffolds rather than the native protein folds associated with these centers.

Dr. Pecoraro served as the Bioinorganic Associate Editor of *Inorg. Chem*. for 20 years. He presently is President of SBIC (Society for Biological Inorganic Chemistry) and was the Chairperson for the highly successful virtual meeting called *e*BIC. As well as being Vice-Chair of ICBIC 12 in Ann Arbor in 2005, Dr. Pecoraro has chaired the Metals in Biology Gordon Conference and a Keystone Conference on the same subject. He has been

Author Manuscript Author Manuscript Author Manuscript Author Manuscript

the recipient of numerous honors including an Alexander von Humboldt Award to Senior Scientists (Germany), the Blaise Pascal Chair for Research (ile de France), the Le Studium Professorship, the ACS Award for Distinguished Service in the Advancement of Inorganic Chemistry, the SCF/ACS Prix Francoamerican Lectureship and received the Vanadis Award. He recently received an Honorary Doctorate from Aix-Marseillle University and has been elected as Fellow of both the AAAS and ACS.

Abbreviations

3HB	three helical bundle
3SCC	three-stranded coiled-coil
4AP	4-aminophenol
4BQM	4-benzoquinone monoimine
4HB	four helical bundle
4SCC	four-stranded coiled-coil
ABTS	2,2’-azino-di(2-ethyl-benzothiazoline-6-sulfonic acid
AUC	Analytical ultra-centrifugation
AurF	*para*-aminobenzoate *N*-oxygenase
CA	carbonic anhydrase
CD	circular dichroism
CuNiR	Cu nitrite reductase
DF	Due Ferri
EDA	ethyl diazoacetate
EPR	electron paramagnetic resonance
EXAFS	extended X-ray absorption fine structure
GR	GRAND
HRP	horse radish peroxidase
LPMO	lytic polysaccharide monooxygenase
MCD	magnetic circular dichroism
MD	Molecular Dynamics
MnDPP	Mn diphenylporphyrin
NIR	near-IR

Author Manuscript Author Manuscript Author Manuscript Author Manuscript

NMR	Nuclear Magnetic Resonance
PDB	Protein Data Bank
PHM	peptidylglycine alpha-hydroxylating monooxygenase
***p*NP**	*para*-nitrophenol
***p*NPA**	*para*-nitrophenyl acetate
***p*NPP**	*para*-nitrophenylphosphate
QM/MM	quantum mechanics/ molecular mechanics
Rma-TDE	engineered cytochrome *c* from *Rhodothermus marinus*
SAXS	small-angle X-ray scattering
SOD	superoxide dismutase
TFE	trifluoroethanol
Tm	melting temperature
TMO	toluene mono-oxygenase
VTVH	variable-temperature variable-field
XANES	X-ray absorption near edge spectral

References

1. Huang P-S; Boyken SE; Baker D, The Coming of Age of de Novo Protein Design. Nature 2016, 537, 320–327. [PubMed: 27629638]
2. Korendovych IV; DeGrado WF, De Novo Protein Design, a Retrospective. Q. Rev. Biophys 2020, 53, e3. [PubMed: 32041676]
3. Yu F; Cangelosi VM; Zastrow ML; Tegoni M; Plegaria JS; Tebo AG; Mocny CS; Ruckthong L; Qayyum H; Pecoraro VL, Protein Design: Toward Functional Metalloenzymes. Chem. Rev 2014, 114, 3495–3578. [PubMed: 24661096]
4. Boulanger MJ; Kukimoto M; Nishiyama M; Horinouchi S; Murphy MEP, Catalytic Roles for Two Water Bridged Residues (Asp-98 and His-255) in the Active Site of Copper-Containing Nitrite Reductase. J. Biol. Chem 2000, 275, 23957–23964. [PubMed: 10811642]
5. Berry SM; Strange JN; Bladholm EL; Khatiwada B; Hedstrom CG; Sauer AM, Nitrite Reductase Activity in Engineered Azurin Variants. Inorg. Chem 2016, 55, 4233–4247. [PubMed: 27055058]
6. Isoda N; Yokoyama H; Nojiri M; Suzuki S; Yamaguchi K, Electroreduction of Nitrite to Nitrogen Oxide by a Copper-containing Nitrite Reductase Model Complex Incorporated into Collagen Film. Bioelectrochemistry 2010, 77, 82–88. [PubMed: 19616484]
7. Tegoni M; Yu F; Bersellini M; Penner-Hahn JE; Pecoraro VL, Designing a Functional Type 2 Copper Center that has Nitrite Reductase Activity within α-helical Coiled Coils. PNAS 2012, 109, 21234–21239. [PubMed: 23236170]
8. Kendrew JC; Bodo G; Dintzis HM; Parrish RG; Wyckoff H; Phillips DC, A Three-Dimensional Model of the Myoglobin Molecule Obtained by X-Ray Analysis. Nature 1958, 181, 662–666. [PubMed: 13517261]
9. Meunier B; de Visser SP; Shaik S, Mechanism of Oxidation Reactions Catalyzed by Cytochrome P450 Enzymes. Chem. Rev 2004, 104, 3947–3980. [PubMed: 15352783]

Author Manuscript Author Manuscript Author Manuscript Author Manuscript

10. Morris DR; Hager LP, Chloroperoxidase: I. Isolation and Properties of the Crystalline Glycoprotein. J. Biol. Chem 1966, 241, 1763–1768. [PubMed: 5949836]
11. Sundaramoorthy M; Terner J; Poulos TL, The Crystal Structure of Chloroperoxidase: a Heme Peroxidase-cytochrome P450 Functional Hybrid. Structure 1995, 3, 1367–1378. [PubMed: 8747463]
12. Perutz MF; Muirhead H; Cox JM; Goaman LCG; Mathews FS; McGandy EL; Webb LE, Three-Dimensional Fourier Synthesis of Horse Oxyhaemoglobin at 2.8 Å Resolution : (I) X-ray Analysis. Nature 1968, 219, 29–32. [PubMed: 5659617]
13. Shikama K, The Molecular Mechanism of Autoxidation for Myoglobin and Hemoglobin: A Venerable Puzzle. Chem. Rev 1998, 98, 1357–1374. [PubMed: 11848936]
14. Nicholls P; Fita I; Loewen PC, Enzymology and Structure of Catalases. In Adv. Inorg. Chem, Academic Press: 2000; Vol. 51, pp 51–106.
15. Poulos TL, Heme Enzyme Structure and Function. Chem. Rev 2014, 114, 3919–3962. [PubMed: 24400737]
16. Njuma OJ; Ndontsa EN; Goodwin DC, Catalase in Peroxidase Clothing: Interdependent Cooperation of Two Cofactors in the Catalytic Versatility of KatG. Arch. Biochem. Biophys 2014, 544, 27–39. [PubMed: 24280274]
17. van Deurzen MPJ; van Rantwijk F; Sheldon RA, Selective Oxidations Catalyzed by Peroxidases. Tetrahedron 1997, 53, 13183–13220.
18. Veitch NC, Horseradish Peroxidase: a Modern View of a Classic Enzyme. Phytochemistry 2004, 65, 249–259. [PubMed: 14751298]
19. Jensen RA, Enzyme Recruitment in Evolution of New Function. Annu. Rev. Microbiol 1976, 30, 409–425. [PubMed: 791073]
20. Gibney BR; Dutton PL, De Novo Design and Synthesis of Heme Proteins. In Adv. Inorg. Chem, Academic Press: 2000; Vol. 51, pp 409–456.
21. Grayson KJ; Anderson JLR, The Ascent of Man(made Oxidoreductases). Curr. Opin. Struct. Biol 2018, 51, 149–155. [PubMed: 29754103]
22. Lombardi A; Nastri F; Pavone V, Peptide-Based Heme−Protein Models. Chem. Rev 2001, 101, 3165–3190. [PubMed: 11710067]
23. Nastri F; Lombardi A; Morelli G; Maglio O; D'Auria G; Pedone C; Pavone V, Hemoprotein Models Based on a Covalent Helix–Heme–Helix Sandwich: 1. Design, Synthesis, and Characterization. Chem. Eur. J 1997, 3, 340–349.
24. Nastri F; Lista L; Ringhieri P; Vitale R; Faiella M; Andreozzi C; Travascio P; Maglio O; Lombardi A; Pavone V, A Heme–Peptide Metalloenzyme Mimetic with Natural Peroxidase-Like Activity. Chem. Eur. J 2011, 17, 4444–4453. [PubMed: 21416513]
25. D'Auria G; Maglio O; Nastri F; Lombardi A; Mazzeo M; Morelli G; Paolillo L; Pedone C; Pavone V, Hemoprotein Models Based on a Covalent Helix–Heme–Helix Sandwich: 2. Structural Characterization of Co(III) Mimochrome I δ and δ Isomers. Chem. Eur. J 1997, 3, 350–362.
26. Lombardi A; Nastri F; Sanseverino M; Maglio O; Pedone C; Pavone V, Miniaturized Hemoproteins: Design, Synthesis and Characterization of Mimochrome II. Inorg. Chim. Acta 1998, 275–276, 301–313.
27. Munro OQ; Marques HM, Heme−Peptide Models for Hemoproteins. 1. Solution Chemistry of N-Acetylmicroperoxidase-8. Inorg. Chem 1996, 35, 3752–3767. [PubMed: 11666562]
28. Marques HM, Insights into Porphyrin Chemistry Provided by the Microperoxidases, the Haempeptides Derived from Cytochrome c. Dalton Trans 2007, 4371–4385. [PubMed: 17909648]
29. Yonetani T; Anni H, Yeast Cytochrome c Peroxidase. Coordination and Spin States of Heme Prosthetic Group. J. Biol. Chem 1987, 262, 9547–9554. [PubMed: 3036864]
30. Feis A; Marzocchi MP; Paoli M; Smulevich G, Spin State and Axial Ligand Bonding in the Hydroxide Complexes of Metmyoglobin, Methemoglobin, and Horseradish Peroxidase at Room and Low Temperatures. Biochemistry 1994, 33, 4577–4583. [PubMed: 8161513]
31. Yonetani T; Yamamoto H; Erman JE; Leigh JS Jr.; Reed GH, Electromagnetic Properties of Hemoproteins: V. Optical and Electron Paramagnetic Resonance Characteristics of Nitric Oxide Derivatives of Metalloporphyrin-Apohemoprotein Complexes. J. Biol. Chem 1972, 247, 2447–2455. [PubMed: 4336375]

Author Manuscript Author Manuscript Author Manuscript Author Manuscript

32. Wittenberg BA; Antonini E; Brunori M; Noble RW; Wittenberg JB; Wyman J, Studies on the Equilibria and Kinetics of the Reactions of Peroxidases with Ligands. III. The Dissociation of Carbon Monoxide from Carbon Monoxide Ferro-Horseradish Peroxidase*. Biochemistry 1967, 6, 1970–1974. [PubMed: 6049439]

33. Rossi-Fanelli A; Antonini E, Studies on the Oxygen and Carbon Monoxide Equilibria of Human Myoglobin. Arch. Biochem. Biophys 1958, 77, 478–492. [PubMed: 13584010]

34. Childs RE; Bardsley WG, The Steady-State Kinetics of Peroxidase with 2,2’-azino-di-(3-ethyl-benzthiazoline-6-sulphonic acid) as Chromogen. Biochem. J 1975, 145, 93–103. [PubMed: 1191252]

35. Koduri RS; Tien M, Oxidation of Guaiacol by Lignin Peroxidase: Role of Veratryl Alcohol. J. Biol. Chem 1995, 270, 22254–22258. [PubMed: 7673205]

36. Savenkova MI; Ortiz de Montellano PR, Horseradish Peroxidase: Partial Rescue of the His-42 → Ala Mutant by a Concurrent Asn-70 → Asp Mutation. Arch. Biochem. Biophys 1998, 351, 286–293. [PubMed: 9514658]

37. Ricoux R; Girgenti E; Sauriat-Dorizon H; Blanchard D; Mahy J-P, Regioselective Nitration of Phenol Induced by Catalytic Antibodies. J. Protein Chem 2002, 21, 473–477. [PubMed: 12523651]

38. Budde CL; Beyer A; Munir IZ; Dordick JS; Khmelnitsky YL, Enzymatic Nitration of Phenols. J. Mol. Catal. B: Enzym 2001, 15, 55–64.

39. Faiella M; Maglio O; Nastri F; Lombardi A; Lista L; Hagen WR; Pavone V, De Novo Design, Synthesis and Characterisation of MP3, A New Catalytic Four-Helix Bundle Hemeprotein. Chem. Eur. J 2012, 18, 15960–15971. [PubMed: 23150230]

40. de Ropp JS; Sham S; Asokan A; Newmyer S; Ortiz de Montellano PR; La Mar GN, Influence of the Distal His in Imparting Imidazolate Character to the Proximal His in Heme Peroxidase: 1H NMR Spectroscopic Study of Cyanide-Inhibited His42→Ala Horseradish Peroxidase. J. Am. Chem. Soc 2002, 124, 11029–11037. [PubMed: 12224950]

41. Rodriguez-Lopez JN; Smith AT; Thorneley RNF, Role of Arginine 38 in Horseradish Peroxidase: a Critical Residue for Substrate Binding and Catalysis. J. Biol. Chem 1996, 271, 4023–4030. [PubMed: 8626735]

42. Frolow F; Kalb AJ; Yariv J, Structure of a Unique Twofold Symmetric Haem-binding Site. Nat. Struct. Biol 1994, 1, 453–460. [PubMed: 7664064]

43. Monien BH; Drepper F; Sommerhalter M; Lubitz W; Haehnel W, Detection of Heme Oxygenase Activity in a Library of Four-helix Bundle Proteins: Towards the de Novo Synthesis of Functional Heme Proteins. J. Mol. Biol 2007, 371, 739–753. [PubMed: 17585935]

44. Zhuang J; Amoroso JH; Kinloch R; Dawson JH; Baldwin MJ; Gibney BR, Design of a Five-Coordinate Heme Protein Maquette: A Spectroscopic Model of Deoxymyoglobin. Inorg. Chem 2004, 43, 8218–8220. [PubMed: 15606161]

45. Blumberg WE; Peisach J; Wittenberg BA; Wittenberg JB, The Electronic Structure of Protoheme Proteins: I. an Electron Paramagnetic Resonance and Optical Study of Horseradish Peroxidase and its Derivatives. J. Biol. Chem 1968, 243, 1854–1862. [PubMed: 5646479]

46. Kobayashi N; Nozawa T; Hatano M, Magnetic Circular Dichroism Studies on Acid and Alkaline Forms of Horseradish Peroxidase. Biochim. Biophys. Acta, Protein Struct 1977, 493, 340–351.

47. Nozawa T; Kobayashi N; Hatano M, Magnetic Circular Dichroism Studies on Horseradish Peroxidase. Biochim. Biophys. Acta, Protein Struct 1976, 427, 652–662.

48. Savenkova MI; Kuo JM; Ortiz de Montellano PR, Improvement of Peroxygenase Activity by Relocation of a Catalytic Histidine within the Active Site of Horseradish Peroxidase. Biochemistry 1998, 37, 10828–10836. [PubMed: 9692973]

49. Reedy CJ; Gibney BR, Heme Protein Assemblies. Chem. Rev 2004, 104, 617–650. [PubMed: 14871137]

50. Farid TA; Kodali G; Solomon LA; Lichtenstein BR; Sheehan MM; Fry BA; Bialas C; Ennist NM; Siedlecki JA; Zhao Z, et al. , Elementary Tetrahelical Protein Design for Diverse Oxidoreductase Functions. Nat. Chem. Biol 2013, 9, 826–833. [PubMed: 24121554]

51. Skalicky JJ; Gibney BR; Rabanal F; Bieber Urbauer RJ; Dutton PL; Wand AJ, Solution Structure of a Designed Four-α-Helix Bundle Maquette Scaffold. J. Am. Chem. Soc 1999, 121, 4941–4951.

Author Manuscript Author Manuscript Author Manuscript Author Manuscript

52. Huang SS; Koder RL; Lewis M; Wand AJ; Dutton PL, The HP-1 Maquette: From an Apoprotein Structure to a Structured Hemoprotein Designed to Promote Redox-coupled Proton Exchange. PNAS 2004, 101, 5536–5541. [PubMed: 15056758]

53. Huang SS; Gibney BR; Stayrook SE; Leslie Dutton P; Lewis M, X-ray Structure of a Maquette Scaffold. J. Mol. Biol 2003, 326, 1219–1225. [PubMed: 12589764]

54. Bollen YJM; Westphal AH; Lindhoud S; van Berkel WJH; van Mierlo CPM, Distant Residues Mediate Picomolar Bbinding Affinity of a Protein Cofactor. Nat. Commun 2012, 3, 1010. [PubMed: 22910356]

55. Sela-Culang I; Kunik V; Ofran Y, The Structural Basis of Antibody-Antigen Recognition. Front. immunol 2013, 4. [PubMed: 23386848]

56. van den Bedem H; Bhabha G; Yang K; Wright PE; Fraser JS, Automated Identification of Functional Dynamic Contact Networks from X-ray Crystallography. Nat. Methods 2013, 10, 896–902. [PubMed: 23913260]

57. Koulechova DA; Tripp KW; Horner G; Marqusee S, When the Scaffold Cannot Be Ignored: The Role of the Hydrophobic Core in Ligand Binding and Specificity. J. Mol. Biol 2015, 427, 3316–3326. [PubMed: 26301601]

58. Bender GM; Lehmann A; Zou H; Cheng H; Fry HC; Engel D; Therien MJ; Blasie JK; Roder H; Saven JG, et al. , De Novo Design of a Single-Chain Diphenylporphyrin Metalloprotein. J. Am. Chem. Soc 2007, 129, 10732–10740. [PubMed: 17691729]

59. Fry HC; Lehmann A; Saven JG; DeGrado WF; Therien MJ, Computational Design and Elaboration of a de Novo Heterotetrameric α-Helical Protein That Selectively Binds an Emissive Abiological (Porphinato)zinc Chromophore. J. Am. Chem. Soc 2010, 132, 3997–4005. [PubMed: 20192195]

60. Fry HC; Lehmann A; Sinks LE; Asselberghs I; Tronin A; Krishnan V; Blasie JK; Clays K; DeGrado WF; Saven JG, et al. , Computational de Novo Design and Characterization of a Protein That Selectively Binds a Highly Hyperpolarizable Abiological Chromophore. J. Am. Chem. Soc 2013, 135, 13914–13926. [PubMed: 23931685]

61. Polizzi NF; Wu Y; Lemmin T; Maxwell AM; Zhang S-Q; Rawson J; Beratan DN; Therien MJ; DeGrado WF, De novo design of a Hyperstable Non-natural Protein–Ligand Complex with Sub-Å Accuracy. Nat. Chem 2017, 9, 1157–1164. [PubMed: 29168496]

62. Kaufmann KW; Lemmon GH; Deluca SL; Sheehan JH; Meiler J, Practically Useful: What the Rosetta Protein Modeling Suite can do for you. Biochemistry 2010, 49, 2987–2998. [PubMed: 20235548]

63. Pirro F; Schmidt N; Lincoff J; Widel ZX; Polizzi NF; Liu L; Therien MJ; Grabe M; Chino M; Lombardi A, et al. , Allosteric Cooperation in a De Novo-Designed Two-Domain Protein. PNAS 2020, 117, 33246–33253. [PubMed: 33318174]

64. Yu L; Tanwar DK; Penha EDS; Wolf YI; Koonin EV; Basu MK, Grammar of Protein Domain Architectures. PNAS 2019, 116, 3636–3645. [PubMed: 30733291]

65. Vishwanath S; de Brevern AG; Srinivasan N, Same but not Alike: Structure, Flexibility and Energetics of Domains in Multi-Domain Proteins are Influenced by the Presence of Other Domains. PLoS Comput. Biol 2018, 14, e1006008. [PubMed: 29432415]

66. Chen X; Zaro JL; Shen W-C, Fusion Protein Linkers: Property, Design and Functionality. Adv. Drug Deliv. Rev 2013, 65, 1357–1369. [PubMed: 23026637]

67. Jacobs TM; Williams B; Williams T; Xu X; Eletsky A; Federizon JF; Szyperski T; Kuhlman B, Design of Structurally Distinct Proteins Using Strategies Inspired by Evolution. Science 2016, 352, 687–690. [PubMed: 27151863]

68. Brunette T; Bick MJ; Hansen JM; Chow CM; Kollman JM; Baker D, Modular Repeat Protein Sculpting Using Rigid Helical Junctions. PNAS 2020, 117, 8870–8875. [PubMed: 32245816]

69. Lombardi A; Summa CM; Geremia S; Randaccio L; Pavone V; DeGrado WF, Retrostructural Analysis of Metalloproteins: Application to the Design of a Minimal Model for Diiron Proteins. PNAS 2000, 97, 6298–6305. [PubMed: 10841536]

70. Roy A; Sarrou I; Vaughn MD; Astashkin AV; Ghirlanda G, De Novo Design of an Artificial Bis[4Fe-4S] Binding Protein. Biochemistry 2013, 52, 7586–7594. [PubMed: 24090184]

Author Manuscript

Author Manuscript

Author Manuscript

Author Manuscript

71. Hong J; Kharenko OA; Ogawa MY, Incorporating Electron-Transfer Functionality into Synthetic Metalloproteins from the Bottom-up. Inorg. Chem 2006, 45, 9974–9984. [PubMed: 17140193]
72. Mancini JA; Kodali G; Jiang J; Reddy KR; Lindsey JS; Bryant DA; Dutton PL; Moser CC, Multi-step Excitation Energy Transfer Engineered in Genetic Fusions of Natural and Synthetic Light-harvesting Proteins. J R Soc Interface 2017, 14, 20160896. [PubMed: 28179548]
73. Kajihara R; Oohora K; Hayashi T, Photoinduced Electron Transfer within Supramolecular Hemoprotein Co-assemblies and Heterodimers Containing Fe and Zn Porphyrins. J. Inorg. Biochem 2019, 193, 42–51. [PubMed: 30669065]
74. Mejias SH; Bahrami-Dizicheh Z; Liutkus M; Sommer DJ; Astashkin A; Kodis G; Ghirlanda G; Cortajarena AL, Repeat Proteins as Versatile Scaffolds for Arrays of Redox-active FeS Clusters. Chem. Commun 2019, 55, 3319–3322.
75. Oohora K; Fujimaki N; Kajihara R; Watanabe H; Uchihashi T; Hayashi T, Supramolecular Hemoprotein Assembly with a Periodic Structure Showing Heme–Heme Exciton Coupling. J. Am. Chem. Soc 2018, 140, 10145–10148. [PubMed: 30067348]
76. Zhou J; Grigoryan G, Rapid Search for Tertiary Fragments Reveals Protein Sequence–Structure Relationships. Protein Sci 2015, 24, 508–524. [PubMed: 25420575]
77. Chino M; Leone L; Maglio O; D'Alonzo D; Pirro F; Pavone V; Nastri F; Lombardi A, A De Novo Heterodimeric Due Ferri Protein Minimizes the Release of Reactive Intermediates in Dioxygen-Dependent Oxidation. Angew. Chem. Int. Ed 2017, 56, 15580–15583.
78. Reig AJ; Pires MM; Snyder RA; Wu Y; Jo H; Kulp DW; Butch SE; Calhoun JR; Szyperski TG; Solomon EI, et al. , Alteration of the Oxygen-Dependent Reactivity of de Novo Due Ferri Proteins. Nat Chem 2012, 4, 900–906. [PubMed: 23089864]
79. Torres Martin de Rosales R; Faiella M; Farquhar E; Que L; Andreozzi C; Pavone V; Maglio O; Nastri F; Lombardi A, Spectroscopic and Metal-Binding Properties of DF3: an Artificial Protein Able to Accommodate Different Metal Ions. J. Biol. Inorg. Chem 2010, 15, 717–728. [PubMed: 20225070]
80. Baglia RA; Zaragoza JPT; Goldberg DP, Biomimetic Reactivity of Oxygen-Derived Manganese and Iron Porphyrinoid Complexes. Chem. Rev 2017, 117, 13320–13352. [PubMed: 28991451]
81. Mann SI; Nayak A; Gassner GT; Therien MJ; DeGrado WF, De Novo Design, Solution Characterization, and Crystallographic Structure of an Abiological Mn–Porphyrin-Binding Protein Capable of Stabilizing a Mn(V) Species. J. Am. Chem. Soc 2021, 143, 252–259. [PubMed: 33373215]
82. Huang X; Groves JT, Oxygen Activation and Radical Transformations in Heme Proteins and Metalloporphyrins. Chem. Rev 2018, 118, 2491–2553. [PubMed: 29286645]
83. Sevrioukova IF; Poulos TL, Understanding the Mechanism of Cytochrome P450 3A4: Recent Advances and Remaining Problems. Dalton Trans 2013, 42, 3116–3126. [PubMed: 23018626]
84. Nagano S; Cupp-Vickery JR; Poulos TL, Crystal Structures of the Ferrous Dioxygen Complex of Wild-type Cytochrome P450eryF and Its Mutants, A245S and A245T: Investigation of the Proton Transfer System in P450eryF *. J. Biol. Chem 2005, 280, 22102–22107. [PubMed: 15824115]
85. Jin N; Groves JT, Unusual Kinetic Stability of a Ground-State Singlet Oxomanganese(V) Porphyrin. Evidence for a Spin State Crossing Effect. J. Am. Chem. Soc 1999, 121, 2923–2924.
86. Groves JT; Lee J; Marla SS, Detection and Characterization of an Oxomanganese(V) Porphyrin Complex by Rapid-Mixing Stopped-Flow Spectrophotometry. J. Am. Chem. Soc 1997, 119, 6269–6273.
87. Nam W; Kim I; Lim MH; Choi HJ; Lee JS; Jang HG, Isolation of an Oxomanganese(V) Porphyrin Intermediate in the Reaction of a Manganese(III) Porphyrin Complex and H_2O_2 in Aqueous Solution. Chem. Eur. J 2002, 8, 2067–2071. [PubMed: 11981891]
88. Prokop KA; Neu HM; de Visser SP; Goldberg DP, A Manganese(V)–Oxo π-Cation Radical Complex: Influence of One-Electron Oxidation on Oxygen-Atom Transfer. J. Am. Chem. Soc 2011, 133, 15874–15877. [PubMed: 21888343]
89. Mandimutsira BS; Ramdhanie B; Todd RC; Wang H; Zareba AA; Czernuszewicz RS; Goldberg DP, A Stable Manganese(V)-Oxo Corrolazine Complex. J. Am. Chem. Soc 2002, 124, 15170–15171. [PubMed: 12487581]

Author Manuscript

Author Manuscript

Author Manuscript

Author Manuscript

90. Anderson JLR; Armstrong CT; Kodali G; Lichtenstein BR; Watkins DW; Mancini JA; Boyle AL; Farid TA; Crump MP; Moser CC, et al. , Constructing a Man-Made c-type Cytochrome Maquette in vivo: Electron Transfer, Oxygen Transport and Conversion to a Photoactive Light Harvesting Maquette. Chem. Sci 2014, 5, 507–514. [PubMed: 24634717]

91. Lichtenstein Bruce R.; Farid Tammer A.; Kodali G; Solomon Lee A.; Anderson JLR; Sheehan Molly M.; Ennist Nathan M.; Fry Bryan A.; Chobot Sarah E.; Bialas C, et al. , Engineering Oxidoreductases: Maquette Proteins Designed from Scratch. Biochem. Soc. Trans 2012, 40, 561–566. [PubMed: 22616867]

92. Gibney BR; Isogai Y; Rabanal F; Reddy KS; Grosset AM; Moser CC; Dutton PL, Self-Assembly of Heme A and Heme B in a Designed Four-Helix Bundle: Implications for a Cytochrome c Oxidase Maquette. Biochemistry 2000, 39, 11041–11049. [PubMed: 10998241]

93. Hunter CL; Lloyd E; Eltis LD; Rafferty SP; Lee H; Smith M; Mauk AG, Role of the Heme Propionates in the Interaction of Heme with Apomyoglobin and Apocytochrome b5. Biochemistry 1997, 36, 1010–1017. [PubMed: 9033390]

94. Stevens JM; Mavridou DAI; Hamer R; Kritsiligkou P; Goddard AD; Ferguson SJ, Cytochrome c biogenesis System I. FEBS J 2011, 278, 4170–4178. [PubMed: 21958041]

95. Stevens JM; Daltrop O; Allen JWA; Ferguson SJ, C-type Cytochrome Formation: Chemical and Biological Enigmas. Acc. Chem. Res 2004, 37, 999–1007. [PubMed: 15609992]

96. Koder RL; Anderson JLR; Solomon LA; Reddy KS; Moser CC; Dutton PL, Design and Engineering of an O_2 Transport Protein. Nature 2009, 458, 305–309. [PubMed: 19295603]

97. di Guana C; Lib P; Riggsa PD; Inouyeb H, Vectors that Facilitate the Expression and Purification of Foreign Peptides in Escherichia Coli by Fusion to Maltose-Binding Protein. Gene 1988, 67, 21–30. [PubMed: 2843437]

98. Braun M; Thöny-Meyer L, Biosynthesis of Artificial Microperoxidases by Exploiting the Secretion and Cytochrome c Maturation Apparatuses of Escherichia Coli. PNAS 2004, 101, 12830–12835. [PubMed: 15328415]

99. Arslan E; Schulz H; Zufferey R; Künzler P; Thöny-Meyer L, Overproduction of the Bradyrhizobium Japonicum c-Type Cytochrome Subunits of the cbb3 Oxidase in Escherichia Coli. Biochem. Biophys. Res. Commun 1998, 251, 744–747. [PubMed: 9790980]

100. Teale FWJ, Cleavage of the Haem-Protein Link by Acid Methylethylketone. Biochim. Biophys. Acta 1959, 35, 543. [PubMed: 13837237]

101. Berry EA; Trumpower BL, Simultaneous Determination of Hemes a, b, and c from Pyridine Hemochrome Spectra. Anal. Biochem 1987, 161, 1–15. [PubMed: 3578775]

102. Iakovleva O; Reiner M; Rau H; Haehnel W; Parak F, Mössbauer and EPR Study of a Cytochrome b Model. PCCP 2002, 4, 655–660.

103. Kakar S; Hoffman FG; Storz JF; Fabian M; Hargrove MS, Structure and Reactivity of Hexacoordinate Hemoglobins. Biophys. Chem 2010, 152, 1–14. [PubMed: 20933319]

104. Lu Y; Casimiro DR; Bren KL; Richards JH; Gray HB, Structurally Engineered Cytochromes with Unusual Ligand-Binding Properties: Expression of Saccharomyces Cerevisiae Met-80-->Ala iso-1-Cytochrome c. PNAS 1993, 90, 11456–11459. [PubMed: 8265573]

105. Wallace CJ; Clark-Lewis I, Functional Role of Heme Ligation in Cytochrome c. Effects of Replacement of Methionine 80 with Natural and Non-natural Residues by Semisynthesis. J. Biol. Chem 1992, 267, 3852–3861. [PubMed: 1310985]

106. Meyer TE; Cusanovich MA, Soluble Cytochrome Composition of the Purple Phototrophic Bacterium, Rhodopseudomonas Sphaeroides ATCC 17023. Biochim. Biophys. Acta, Bioenerg 1985, 807, 308–319.

107. Vanderkooi JM; Landesberg R; Hayden GW; Owen CS, Metal-Free and Metal-Substituted Cytochromes c. Use in Characterization of the Cytochrome c Binding Site. Eur. J. Biochem 1977, 81, 339–347. [PubMed: 202455]

108. Şener M; Strümpfer J; Hsin J; Chandler D; Scheuring S; Hunter CN; Schulten K, Förster Energy Transfer Theory as Reflected in the Structures of Photosynthetic Light-Harvesting Systems. Chemphyschem 2011, 12, 518–531. [PubMed: 21344591]

109. Watkins DW; Armstrong CT; Beesley JL; Marsh JE; Jenkins JMX; Sessions RB; Mann S; Ross Anderson JL, A Suite of De Novo c-type Cytochromes for Functional Oxidoreductase Engineering. Biochim. Biophys. Acta, Bioenerg 2016, 1857, 493–502.

110. Dewilde S; Kiger L; Burmester T; Hankeln T; Baudin-Creuza V; Aerts T; Marden MC; Caubergs R; Moens L, Biochemical Characterization and Ligand Binding Properties of Neuroglobin, a Novel Member of the Globin Family. J. Biol. Chem 2001, 276, 38949–38955. [PubMed: 11473128]

111. Clarke TA; Edwards MJ; Gates AJ; Hall A; White GF; Bradley J; Reardon CL; Shi L; Beliaev AS; Marshall MJ, et al. , Structure of a Bacterial Cell Surface Decaheme Electron Conduit. PNAS 2011, 108, 9384–9389. [PubMed: 21606337]

112. Berendsen HJC; van der Spoel D; van Drunen R, GROMACS: A Message-Passing Parallel Molecular Dynamics Implementation. Comput. Phys. Commun 1995, 91, 43–56.

113. Bjelkmar P; Larsson P; Cuendet MA; Hess B; Lindahl E, Implementation of the CHARMM Force Field in GROMACS: Analysis of Protein Stability Effects from Correction Maps, Virtual Interaction Sites, and Water Models. J. Chem. Theory Comput 2010, 6, 459–466. [PubMed: 26617301]

114. Nanda V; Koder RL, Designing Artificial Enzymes by Intuition and Computation. Nat. Chem 2010, 2, 15–24. [PubMed: 21124375]

115. Watkins DW; Armstrong CT; Anderson JLR, De Novo Protein Components for Oxidoreductase Assembly and Biological Integration. Curr. Opin. Chem. Biol 2014, 19, 90–98. [PubMed: 24607598]

116. Watkins DW; Jenkins JMX; Grayson KJ; Wood N; Steventon JW; Le Vay KK; Goodwin MI; Mullen AS; Bailey HJ; Crump MP, et al. , Construction and in Vivo Assembly of a Catalytically Proficient and Hyperthermostable De Novo Enzyme. Nat. Commun 2017, 8, 358. [PubMed: 28842561]

117. Casadei CM; Gumiero A; Metcalfe CL; Murphy EJ; Basran J; Concilio MG; Teixeira SCM; Schrader TE; Fielding AJ; Ostermann A, et al. , Neutron Cryo-Crystallography Captures the Protonation State of Ferryl Heme in a Peroxidase. Science 2014, 345, 193–197. [PubMed: 25013070]

118. Harvey JN; Bathelt CM; Mulholland AJ, QM/MM Modeling of Compound I Active Species in Cytochrome P450, Cytochrome C Peroxidase, and Ascorbate Peroxidase. J. Comput. Chem 2006, 27, 1352–1362. [PubMed: 16788912]

119. Stenner R; Steventon JW; Seddon A; Anderson JLR, A de Novo Peroxidase is Also a Promiscuous yet Stereoselective Carbene Transferase. PNAS 2020, 117, 1419–1428. [PubMed: 31896585]

120. Stenner R; Anderson JLR, Chemoselective N−H insertion Catalyzed by a De Novo Carbene Transferase. Biotechnol. Appl. Biochem 2020, 67, 527–535. [PubMed: 32277840]

121. Jenkins JMX; Noble CEM; Grayson KJ; Mulholland AJ; Anderson JLR, Substrate Promiscuity of a De Novo Designed Peroxidase. J. Inorg. Biochem 2021, 217, 111370. [PubMed: 33621939]

122. Coelho PS; Brustad EM; Kannan A; Arnold FH, Olefin Cyclopropanation via Carbene Transfer Catalyzed by Engineered Cytochrome P450 Enzymes. Science 2013, 339, 307–310. [PubMed: 23258409]

123. Sreenilayam G; Fasan R, Myoglobin-Catalyzed Intermolecular Carbene N–H Insertion with Arylamine Substrates. Chem. Commun 2015, 51, 1532–1534.

124. Kan SBJ; Lewis RD; Chen K; Arnold FH, Directed Evolution of Cytochrome c for Carbon–Silicon Bond Formation: Bringing Silicon to Life. Science 2016, 354, 1048–1051. [PubMed: 27885032]

125. Brandenberg OF; Fasan R; Arnold FH, Exploiting and Engineering Hemoproteins for Abiological Carbene and Nitrene Transfer Reactions. Curr. Opin. Biotechnol 2017, 47, 102–111. [PubMed: 28711855]

126. Wei Y; Tinoco A; Steck V; Fasan R; Zhang Y, Cyclopropanations via Heme Carbenes: Basic Mechanism and Effects of Carbene Substituent, Protein Axial Ligand, and Porphyrin Substitution. J. Am. Chem. Soc 2018, 140, 1649–1662. [PubMed: 29268614]

Author Manuscript

Author Manuscript

Author Manuscript

Author Manuscript

127. Liu Y; Xu W; Zhang J; Fuller W; Schulz CE; Li J, Electronic Configuration and Ligand Nature of Five-Coordinate Iron Porphyrin Carbene Complexes: An Experimental Study. J. Am. Chem. Soc 2017, 139, 5023–5026. [PubMed: 28339195]

128. Lewis RD; Garcia-Borràs M; Chalkley MJ; Buller AR; Houk KN; Kan SBJ; Arnold FH, Catalytic Iron-Carbene Intermediate Revealed in a Cytochrome c Carbene Transferase. PNAS 2018, 115, 7308–7313. [PubMed: 29946033]

129. Arnold FH, Directed Evolution: Bringing New Chemistry to Life. Angew. Chem. Int. Ed 2018, 57, 4143–4148.

130. Henke E; Bornscheuer UT; Schmid RD; Pleiss J, A Molecular Mechanism of Enantiorecognition of Tertiary Alcohols by Carboxylesterases. ChemBioChem 2003, 4, 485–493. [PubMed: 12794858]

131. Kurnasov O; Goral V; Colabroy K; Gerdes S; Anantha S; Osterman A; Begley TP, NAD Biosynthesis: Identification of the Tryptophan to Quinolinate Pathway in Bacteria. Chem. Biol 2003, 10, 1195–1204. [PubMed: 14700627]

132. Nastri F; D'Alonzo D; Leone L; Zambrano G; Pavone V; Lombardi A, Engineering Metalloprotein Functions in Designed and Native Scaffolds. Trends Biochem. Sci 2019, 44, 1022–1040. [PubMed: 31307903]

133. Das PK; Samanta S; McQuarters AB; Lehnert N; Dey A, Valence Tautomerism in Synthetic Models of Cytochrome P450. PNAS 2016, 113, 6611–6616. [PubMed: 27302948]

134. Koebke KJ; Kühl T; Lojou E; Demeler B; Schoepp-Cothenet B; Iranzo O; Pecoraro VL; Ivancich A, The pH-Induced Selectivity Between Cysteine or Histidine Coordinated Heme in an Artificial α-Helical Metalloprotein. Angew. Chem. Int. Ed 2021, 60, 3974–3978.

135. Zastrow ML; Pecoraro VL, Designing Functional Metalloproteins: From Structural to Catalytic Metal Sites. Coord. Chem. Rev 2013, 257, 2565–2588. [PubMed: 23997273]

136. Pinter TBJ; Koebke KJ; Pecoraro VL, Catalysis and Electron Transfer in de Novo Designed Helical Scaffolds. Angew. Chem. Int. Ed 2020, 59, 7678–7699.

137. Ghosh D; Pecoraro VL, Understanding Metalloprotein Folding Using a de Novo Design Strategy. Inorg. Chem 2004, 43, 7902–7915. [PubMed: 15578824]

138. Matzapetakis M; Ghosh D; Weng T-C; Penner-Hahn JE; Pecoraro VL, Peptidic Models for the Binding of Pb(II), Bi(III) and Cd(II) to Mononuclear Thiolate Binding Sites. J. Biol. Inorg. Chem 2006, 11, 876–890. [PubMed: 16855818]

139. Blanke SR; Martinis SA; Sligar SG; Hager LP; Rux JJ; Dawson JH, Probing the Heme Iron Coordination Structure of Alkaline Chloroperoxidase. Biochemistry 1996, 35, 14537–14543. [PubMed: 8931550]

140. Conner KP; Schimpf AM; Cruce AA; McLean KJ; Munro AW; Frank DJ; Krzyaniak MD; Ortiz de Montellano P; Bowman MK; Atkins WM, Strength of Axial Water Ligation in Substrate-Free Cytochrome P450s Is Isoform Dependent. Biochemistry 2014, 53, 1428–1434. [PubMed: 24576089]

141. Moser CC; Sheehan MM; Ennist NM; Kodali G; Bialas C; Englander MT; Discher BM; Dutton PL, Chapter Sixteen - De Novo Construction of Redox Active Proteins. In Methods Enzymol, Pecoraro VL, Ed. Academic Press: 2016; Vol. 580, pp 365–388. [PubMed: 27586341]

142. Smith AT; Pazicni S; Marvin KA; Stevens DJ; Paulsen KM; Burstyn JN, Functional Divergence of Heme-Thiolate Proteins: A Classification Based on Spectroscopic Attributes. Chem. Rev 2015, 115, 2532–2558. [PubMed: 25763468]

143. Walker FA, Magnetic Spectroscopic (EPR, ESEEM, Mössbauer, MCD and NMR) Studies of Low-Spin Ferriheme Centers and Their Corresponding Heme Proteins. Coord. Chem. Rev 1999, 185–186, 471–534.

144. Johnston WA; Hunter DJB; Noble CJ; Hanson GR; Stok JE; Hayes MA; De Voss JJ; Gillam EMJ, Cytochrome P450 Is Present in Both Ferrous and Ferric Forms in the Resting State within Intact Escherichia coli and Hepatocytes. J. Biol. Chem 2011, 286, 40750–40759. [PubMed: 21976668]

145. Dieckmann GR; McRorie DK; Lear JD; Sharp KA; DeGrado WF; Pecoraro VL, The Role of Protonation and Metal Chelation Preferences in Defining the Properties of Mercury-Binding Coiled Coils. J. Mol. Biol 1998, 280, 897–912. [PubMed: 9671558]

Author Manuscript Author Manuscript Author Manuscript Author Manuscript

146. Malashkevich VN; Higgins CD; Almo SC; Lai JR, A switch From Parallel to Antiparallel Strand Orientation in a Coiled-Coil X-ray Structure via Two Core Hydrophobic Mutations. Peptide Sci 2015, 104, 178–185.

147. Choma CT; Lear JD; Nelson MJ; Dutton PL; Robertson DE; DeGrado WF, Design of a Heme-Binding Four-Helix Bundle. J. Am. Chem. Soc 1994, 116, 856–865.

148. Averill BA, Dissimilatory Nitrite and Nitric Oxide Reductases. Chem. Rev 1996, 96, 2951–2964. [PubMed: 11848847]

149. Christianson DW; Fierke CA, Carbonic Anhydrase: Evolution of the Zinc Binding Site by Nature and by Design. Acc. Chem. Res 1996, 29, 331–339.

150. Sheng Y; Abreu IA; Cabelli DE; Maroney MJ; Miller A-F; Teixeira M; Valentine JS, Superoxide Dismutases and Superoxide Reductases. Chem. Rev 2014, 114, 3854–3918. [PubMed: 24684599]

151. Beeson WT; Vu VV; Span EA; Phillips CM; Marletta MA, Cellulose Degradation by Polysaccharide Monooxygenases. Annu. Rev. Biochem 2015, 84, 923–946. [PubMed: 25784051]

152. Ross MO; MacMillan F; Wang J; Nisthal A; Lawton TJ; Olafson BD; Mayo SL; Rosenzweig AC; Hoffman BM, Particulate Methane Monooxygenase Contains Only Mononuclear Copper Centers. Science 2019, 364, 566–570. [PubMed: 31073062]

153. Chufán EE; Prigge ST; Siebert X; Eipper BA; Mains RE; Amzel LM, Differential Reactivity between Two Copper Sites in Peptidylglycine α-Hydroxylating Monooxygenase. J. Am. Chem. Soc 2010, 132, 15565–15572. [PubMed: 20958070]

154. Liang Z; Xue Y; Behravan G; Jonsson B-H; Lindskog S, Importance of the Conserved Active-Site Residues Try7, Glu106 and Thr199 for the Catalytic Function of Human Carbonic Anhydrase II. Eur. J. Biochem 1993, 211, 821–827. [PubMed: 8436138]

155. Zastrow ML; Peacock AFA; Stuckey JA; Pecoraro VL, Hydrolytic Catalysis and Structural Stabilization in a Designed Metalloprotein. Nat Chem 2012, 4, 118–123.

156. Farrer BT; Harris NP; Balchus KE; Pecoraro VL, Thermodynamic Model for the Stabilization of Trigonal Thiolato Mercury(II) in Designed Three-Stranded Coiled Coils. Biochemistry 2001, 40, 14696–14705. [PubMed: 11724584]

157. Farrer BT; McClure CP; Penner-Hahn JE; Pecoraro VL, Arsenic(III)−Cysteine Interactions Stabilize Three-Helix Bundles in Aqueous Solution. Inorg. Chem 2000, 39, 5422–5423. [PubMed: 11154553]

158. Matzapetakis M; Farrer BT; Weng T-C; Hemmingsen L; Penner-Hahn JE; Pecoraro VL, Comparison of the Binding of Cadmium(II), Mercury(II), and Arsenic(III) to the de Novo Designed Peptides TRI L12C and TRI L16C. J. Am. Chem. Soc 2002, 124, 8042–8054. [PubMed: 12095348]

159. Dieckmann GR; McRorie DK; Tierney DL; Utschig LM; Singer CP; O'Halloran TV; Penner-Hahn JE; DeGrado WF; Pecoraro VL, De Novo Design of Mercury-Binding Two- and Three-Helical Bundles. J. Am. Chem. Soc 1997, 119, 6195–6196.

160. Kimura E; Shiota T; Koike T; Shiro M; Kodama M, A Zinc(II) Complex of 1,5,9-triazacyclododecane ([12]aneN3) as a Model for Carbonic Anhydrase. J. Am. Chem. Soc 1990, 112, 5805–5811.

161. Bazzicalupi C; Bencini A; Bianchi A; Fusi V; Giorgi C; Paoletti P; Valtancoli B; Zanchi D, Carboxy and Phosphate Esters Cleavage with Mono- and Dinuclear Zinc(II) Macrocyclic Complexes in Aqueous Solution. Crystal Structure of [Zn2L1(μ-PP)2(MeOH)2](ClO4)2 (L1 = [30]aneN6O4, PP- = Diphenyl Phosphate). Inorg. Chem 1997, 36, 2784–2790. [PubMed: 11669912]

162. Koerner TB; Brown RS, The Hydrolysis of an Activated Ester by a tris(4,5-di-n-propyl-2-imidazolyl)phosphine-Zn2+ Complex in Neutral Micellar Medium as a Model for Carbonic Anhydrase. Can. J. Chem 2002, 80, 183–191.

163. Verpoorte JA; Mehta S; Edsall JT, Esterase Activities of Human Carbonic Anhydrases B and C. J. Biol. Chem 1967, 242, 4221–4229. [PubMed: 4964830]

164. Innocenti A; Scozzafava A; Parkkila S; Puccetti L; De Simone G; Supuran CT, Investigations of the Esterase, Phosphatase, and Sulfatase Activities of the Cytosolic Mammalian Carbonic

Author Manuscript Author Manuscript Author Manuscript Author Manuscript

Anhydrase Isoforms I, II, and XIII with 4-nitrophenyl Esters as Substrates. Bioorg. Med. Chem. Lett 2008, 18, 2267–2271. [PubMed: 18353640]

165. Krebs JF; Ippolito JA; Christianson DW; Fierke CA, Structural and Functional Importance of a Conserved Hydrogen Bond Network in Human Carbonic Anhydrase II. J. Biol. Chem 1993, 268, 27458–27466. [PubMed: 8262987]
166. Slebocka-Tilk H; Cocho JL; Frackman Z; Brown RS, Carbonic Anhydrase Models. 5. Tris(4,5-di-n-propyl-2-imidazolyl)phosphine-zinc(2+) and bis(4,5-di-isopropyl-2-imidazolyl)-2-imidazolylphosphine-zinc(2+). Catalysts Facilitating Hydrogen Carbonate Carbon Dioxide (HCO3- CO2) Interconversion. J. Am. Chem. Soc 1984, 106, 2421–2431.
167. Zhang X; van Eldik R, A Functional Model for Carbonic Anhydrase: Thermodynamic and Kinetic Study of a Tetraazacyclododecane Complex of Zinc(Ii). Inorg. Chem 1995, 34, 5606–5614.
168. Jackman JE; Merz KM; Fierke CA, Disruption of the Active Site Solvent Network in Carbonic Anhydrase II Decreases the Efficiency of Proton Transfer. Biochemistry 1996, 35, 16421–16428. [PubMed: 8987973]
169. Zastrow ML; Pecoraro VL, Influence of Active Site Location on Catalytic Activity in de Novo-Designed Zinc Metalloenzymes. J. Am. Chem. Soc 2013, 135, 5895–5903. [PubMed: 23516959]
170. Peacock AFA; Iranzo O; Pecoraro VL, Harnessing Natures Ability to Control Metal Ion Coordination Geometry Using de Novo Designed Peptides. Dalton Trans 2009, 2271–2280. [PubMed: 19290357]
171. Matzapetakis M; Pecoraro VL, Site-Selective Metal Binding by Designed α-Helical Peptides. J. Am. Chem. Soc 2005, 127, 18229–18233. [PubMed: 16366576]
172. Iranzo O; Chakraborty S; Hemmingsen L; Pecoraro VL, Controlling and Fine Tuning the Physical Properties of Two Identical Metal Coordination Sites in De Novo Designed Three Stranded Coiled Coil Peptides. J. Am. Chem. Soc 2011, 133, 239–251. [PubMed: 21162521]
173. Kiyokawa T; Kanaori K; Tajima K; Kawaguchi M; Mizuno T; Oku J.-i.; Tanaka T, Selective Formation of AAB- and ABC-Type Heterotrimeric α-Helical Coiled Coils. Chem. Eur. J 2004, 10, 3548–3554. [PubMed: 15252802]
174. Schnarr NA; Kennan AJ, Peptide Tic-Tac-Toe: Heterotrimeric Coiled-Coil Specificity from Steric Matching of Multiple Hydrophobic Side Chains. J. Am. Chem. Soc 2002, 124, 9779–9783. [PubMed: 12175236]
175. Schnarr NA; Kennan AJ, Coiled-Coil Formation Governed by Unnatural Hydrophobic Core Side Chains. J. Am. Chem. Soc 2001, 123, 11081–11082. [PubMed: 11686721]
176. Tolbert AE; Ervin CS; Ruckthong L; Paul TJ; Jayasinghe-Arachchige VM; Neupane KP; Stuckey JA; Prabhakar R; Pecoraro VL, Heteromeric Three-Stranded Coiled Coils Designed Using a Pb(II)(Cys)(3) Template Mediated Strategy. Nat. Chem 2020, 12, 405–411. [PubMed: 32123337]
177. Neupane KP; Pecoraro VL, Probing a Homoleptic PbS3 Coordination Environment in a Designed Peptide Using 207Pb NMR Spectroscopy: Implications for Understanding the Molecular Basis of Lead Toxicity. Angew. Chem. Int. Ed 2010, 49, 8177–8180.
178. Neupane KP; Pecoraro VL, Pb-207 NMR Spectroscopy Reveals that Pb(II) Coordinates with Glutathione (GSH) and Tris Cysteine Zinc Finger Proteins in a PbS3 Coordination Environment. J. Inorg. Biochem 2011, 105, 1030–1034. [PubMed: 21625408]
179. Cangelosi VM; Deb A; Penner-Hahn JE; Pecoraro VL, A De Novo Designed Metalloenzyme for the Hydration of CO2. Angew. Chem. Int. Ed 2014, 53, 7900–7903.
180. Walsh STR; Cheng H; Bryson JW; Roder H; DeGrado WF, Solution Structure and Dynamics of a de Novo Designed Three-Helix Bundle Protein. PNAS 1999, 96, 5486–5491. [PubMed: 10318910]
181. Bryson JW; Desjarlais JR; Handel TM; Degrado WF, From Coiled Coils to Small Globular Proteins: Design of a Native-Like Three-Helix Bundle. Protein Sci 1998, 7, 1404–1414. [PubMed: 9655345]
182. Walsh STR; Sukharev VI; Betz SF; Vekshin NL; DeGrado WF, Hydrophobic Core Malleability of a De Novo Designed Three-helix Bundle Protein. J. Mol. Biol 2001, 305, 361–373. [PubMed: 11124911]

Author Manuscript Author Manuscript Author Manuscript Author Manuscript

183. Plegaria JS; Dzul SP; Zuiderweg ERP; Stemmler TL; Pecoraro VL, Apoprotein Structure and Metal Binding Characterization of a de Novo Designed Peptide, α3DIV, that Sequesters Toxic Heavy Metals. Biochemistry 2015, 54, 2858–2873. [PubMed: 25790102]

184. Chakraborty S; Kravitz JY; Thulstrup PW; Hemmingsen L; DeGrado WF; Pecoraro VL, Realization of a Designed Three-Helix Bundle Capable of Binding Heavy Metals in a Tris(Cysteine) Environment. Angew. Chem. Int. Ed. Engl 2011, 50, 2049–2053. [PubMed: 21344549]

185. Jewell DA; Tu C; Paranawithana SR; Tanhauser SM; LoGrasso PV; Laipis PJ; Silverman DN, Enhancement of the Catalytic Properties of Human Carbonic Anhydrase III by Site-Directed Mutagenesis. Biochemistry 1991, 30, 1484–1490. [PubMed: 1899618]

186. Grishin NV; Phillips MA, The Subunit Interfaces of Oligomeric Enzymes are Conserved to a Similar Extent to the Overall Protein Sequences. Protein Sci 1994, 3, 2455–2458. [PubMed: 7757001]

187. Ali MH; Imperiali B, Protein Oligomerization: How and Why. Biorg. Med. Chem 2005, 13, 5013–5020.

188. Sonavane S; Chakrabarti P, Cavities and Atomic Packing in Protein Structures and Interfaces. PLoS Comput. Biol 2008, 4, e1000188. [PubMed: 19005575]

189. Gao M; Skolnick J, The Distribution of Ligand-Binding Pockets Around Protein-Protein Interfaces Suggests a General Mechanism for Pocket Formation. PNAS 2012, 109, 3784–3789. [PubMed: 22355140]

190. Salgado EN; Faraone-Mennella J; Tezcan FA, Controlling Protein−Protein Interactions through Metal Coordination: Assembly of a 16-Helix Bundle Protein. J. Am. Chem. Soc 2007, 129, 13374–13375. [PubMed: 17929927]

191. Der BS; Machius M; Miley MJ; Mills JL; Szyperski T; Kuhlman B, Metal-Mediated Affinity and Orientation Specificity in a Computationally Designed Protein Homodimer. J. Am. Chem. Soc 2012, 134, 375–385. [PubMed: 22092237]

192. Eathiraj S; Pan X; Ritacco C; Lambright DG, Structural Basis of Family-Wide Rab GTPase Recognition by Rabenosyn-5. Nature 2005, 436, 415–419. [PubMed: 16034420]

193. Der BS; Edwards DR; Kuhlman B, Catalysis by a De Novo Zinc-Mediated Protein Interface: Implications for Natural Enzyme Evolution and Rational Enzyme Engineering. Biochemistry 2012, 51, 3933–3940. [PubMed: 22510088]

194. Studer S; Hansen DA; Pianowski ZL; Mittl PRE; Debon A; Guffy SL; Der BS; Kuhlman B; Hilvert D, Evolution of a Highly Active and Enantiospecific Metalloenzyme from Short Peptides. Science 2018, 362, 1285–1288. [PubMed: 30545884]

195. MacBeath G; Hilvert D, Hydrolytic Antibodies: Variations on a Theme. Chem. Biol 1996, 3, 433–445. [PubMed: 8807874]

196. Bolon DN; Mayo SL, Enzyme-Like Proteins by Computational Design. PNAS 2001, 98, 14274–14279. [PubMed: 11724958]

197. Richter F; Blomberg R; Khare SD; Kiss G; Kuzin AP; Smith AJT; Gallaher J; Pianowski Z; Helgeson RC; Grjasnow A, et al. , Computational Design of Catalytic Dyads and Oxyanion Holes for Ester Hydrolysis. J. Am. Chem. Soc 2012, 134, 16197–16206. [PubMed: 22871159]

198. Moroz YS; Dunston TT; Makhlynets OV; Moroz OV; Wu Y; Yoon JH; Olsen AB; McLaughlin JM; Mack KL; Gosavi PM, et al. , New Tricks for Old Proteins: Single Mutations in a Nonenzymatic Protein Give Rise to Various Enzymatic Activities. J. Am. Chem. Soc 2015, 137, 14905–14911. [PubMed: 26555770]

199. Burton AJ; Thomson AR; Dawson WM; Brady RL; Woolfson DN, Installing Hydrolytic Activity into a Completely de Novo Protein Framework. Nat. Chem 2016, 8, 837–844. [PubMed: 27554410]

200. Song WJ; Tezcan FA, A Designed Supramolecular Protein Assembly with in vivo Enzymatic Activity. Science 2014, 346, 1525–1528. [PubMed: 25525249]

201. Rufo CM; Moroz YS; Moroz OV; Stöhr J; Smith TA; Hu X; DeGrado WF; Korendovych IV, Short Peptides Self-Assemble to Produce Catalytic Amyloids. Nat. Chem 2014, 6, 303–309. [PubMed: 24651196]

202. Radzicka A; Wolfenden R, A Proficient Enzyme. Science 1995, 267, 90–93. [PubMed: 7809611]

Author Manuscript Author Manuscript Author Manuscript Author Manuscript

203. Zastrow ML; Pecoraro VL, Designing Hydrolytic Zinc Metalloenzymes. Biochemistry 2014, 53, 957–978. [PubMed: 24506795]

204. Stocking EM; Williams RM, Chemistry and Biology of Biosynthetic Diels–Alder Reactions. Angew. Chem. Int. Ed 2003, 42, 3078–3115.

205. Minami A; Oikawa H, Recent Advances of Diels–Alderases Involved in Natural Product Biosynthesis. J. Antibiot 2016, 69, 500–506.

206. Jeon B.-s.; Wang S-A; Ruszczycky MW; Liu H.-w., Natural [4 + 2]-Cyclases. Chem. Rev 2017, 117, 5367–5388. [PubMed: 28441874]

207. Jamieson CS; Ohashi M; Liu F; Tang Y; Houk KN, The Expanding World of Biosynthetic Pericyclases: Cooperation of Experiment and Theory for Discovery. Nat. Prod. Rep 2019, 36, 698–713. [PubMed: 30311924]

208. Basler S; Studer S; Zou Y; Mori T; Ota Y; Camus A; Bunzel HA; Helgeson RC; Houk KN; Jiménez-Osés G, et al. , Efficient Lewis Acid Catalysis of an Abiological Reaction in a de Novo Protein Scaffold. Nat. Chem 2021, 13, 231–235. [PubMed: 33526894]

209. Romesberg FE; Spiller B; Schultz PG; Stevens RC, Immunological Origins of Binding and Catalysis in a Diels-Alderase Antibody. Science 1998, 279, 1929–1933. [PubMed: 9506942]

210. Gouverneur VE; Houk KN; Pascual-Teresa B. d.; Beno B; Janda KD; Lerner RA, Control of the exo and endo Pathways of the Diels-Alder Reaction by Antibody Catalysis. Science 1993, 262, 204–208. [PubMed: 8211138]

211. Siegel JB; Zanghellini A; Lovick HM; Kiss G; Lambert AR; St.Clair JL; Gallaher JL; Hilvert D; Gelb MH; Stoddard BL, et al. , Computational Design of an Enzyme Catalyst for a Stereoselective Bimolecular Diels-Alder Reaction. Science 2010, 329, 309–313. [PubMed: 20647463]

212. Preiswerk N; Beck T; Schulz JD; Milovník P; Mayer C; Siegel JB; Baker D; Hilvert D, Impact of Scaffold Rigidity on the Design and Evolution of an Artificial Diels-Alderase. PNAS 2014, 111, 8013–8018. [PubMed: 24847076]

213. Fringuelli F; Piermatti O; Pizzo F; Vaccaro L, Recent Advances in Lewis Acid Catalyzed Diels−Alder Reactions in Aqueous Media. Eur. J. Org. Chem 2001, 2001, 439–455.

214. Kim HJ; Ruszczycky MW; Choi S.-h.; Liu Y.-n.; Liu H.-w., Enzyme-Catalysed [4+2] Cycloaddition is a Key Step in the Biosynthesis of Spinosyn A. Nature 2011, 473, 109–112. [PubMed: 21544146]

215. Fage CD; Isiorho EA; Liu Y; Wagner DT; Liu H.-w.; Keatinge-Clay AT, The Structure of SpnF, a Standalone Enzyme that Catalyzes [4 + 2] Cycloaddition. Nat. Chem. Biol 2015, 11, 256–258. [PubMed: 25730549]

216. Byrne MJ; Lees NR; Han L-C; van der Kamp MW; Mulholland AJ; Stach JEM; Willis CL; Race PR, The Catalytic Mechanism of a Natural Diels–Alderase Revealed in Molecular Detail. J. Am. Chem. Soc 2016, 138, 6095–6098. [PubMed: 27140661]

217. Zhang Z; Jamieson CS; Zhao Y-L; Li D; Ohashi M; Houk KN; Tang Y, Enzyme-Catalyzed Inverse-Electron Demand Diels–Alder Reaction in the Biosynthesis of Antifungal Ilicicolin H. J. Am. Chem. Soc 2019, 141, 5659–5663. [PubMed: 30905148]

218. Berman HM; Westbrook J; Feng Z; Gilliland G; Bhat TN; Weissig H; Shindyalov IN; Bourne PE, The Protein Data Bank. Nucleic Acids Res 2000, 28, 235–242. [PubMed: 10592235]

219. Greenwald J; Riek R, On the Possible Amyloid Origin of Protein Folds. J. Mol. Biol 2012, 421, 417–426. [PubMed: 22542525]

220. Carny O; Gazit E, A Model for the Role of Short Self-Assembled Peptides in the Very Early Stages of the Origin of Life. FASEB J 2005, 19, 1051–1055. [PubMed: 15985527]

221. DeGrado WF; Lear JD, Induction of Peptide Conformation at Apolar Water Interfaces. 1. A Study with Model Peptides of Defined Hydrophobic Periodicity. J. Am. Chem. Soc 1985, 107, 7684–7689.

222. Eisenberg D; Jucker M, The Amyloid State of Proteins in Human Diseases. Cell 2012, 148, 1188–1203. [PubMed: 22424229]

223. Colletier J-P; Laganowsky A; Landau M; Zhao M; Soriaga AB; Goldschmidt L; Flot D; Cascio D; Sawaya MR; Eisenberg D, Molecular Basis for Amyloid-β Polymorphism. PNAS 2011, 108, 16938–16943. [PubMed: 21949245]

Author Manuscript

Author Manuscript

Author Manuscript

Author Manuscript

224. Nowick JS, Exploring β-Sheet Structure and Interactions with Chemical Model Systems. Acc. Chem. Res 2008, 41, 1319–1330. [PubMed: 18798654]

225. Minor DL; Kim PS, Measurement of the Beta-Sheet-Forming Propensities of Amino Acids. Nature 1994, 367, 660–663. [PubMed: 8107853]

226. O'Neil K; DeGrado W, A Thermodynamic Scale for the Helix-Forming Tendencies of the Commonly Occurring Amino Acids. Science 1990, 250, 646–651. [PubMed: 2237415]

227. Coleman JE; Coleman RV, Magnetic Circular Dichroism of Co(II) Carbonic Anhydrase. J. Biol. Chem 1972, 247, 4718–4728. [PubMed: 4626366]

228. Makhlynets OV; Gosavi PM; Korendovych IV, Short Self-Assembling Peptides Are Able to Bind to Copper and Activate Oxygen. Angew. Chem. Int. Ed 2016, 55, 9017–9020.

229. Lengyel Z; Rufo CM; Moroz YS; Makhlynets OV; Korendovych IV, Copper-Containing Catalytic Amyloids Promote Phosphoester Hydrolysis and Tandem Reactions. ACS Catal 2018, 8, 59–62. [PubMed: 30319881]

230. Brown RS; Curtis NJ; Huguet J, Tris(4,5-diisopropylimidazol-2-yl)phosphine:zinc(2+). A Catalytically Active Model for Carbonic Anhydrase. J. Am. Chem. Soc 1981, 103, 6953–6959.

231. Suzuki S; Kataoka K; Yamaguchi K, Metal Coordination and Mechanism of Multicopper Nitrite Reductase. Acc. Chem. Res 2000, 33, 728–735. [PubMed: 11041837]

232. Wasser IM; de Vries S; Moënne-Loccoz P; Schröder I; Karlin KD, Nitric Oxide in Biological Denitrification: Fe/Cu Metalloenzyme and Metal Complex NOx Redox Chemistry. Chem. Rev 2002, 102, 1201–1234. [PubMed: 11942794]

233. Olesen K; Veselov A; Zhao Y; Wang Y; Danner B; Scholes CP; Shapleigh JP, Spectroscopic, Kinetic, and Electrochemical Characterization of Heterologously Expressed Wild-Type and Mutant Forms of Copper-Containing Nitrite Reductase from Rhodobacter sphaeroides 2.4.3. Biochemistry 1998, 37, 6086–6094. [PubMed: 9558347]

234. Merkle AC; Lehnert N, Binding and Activation of Nitrite and Nitric Oxide by Copper Nitrite Reductase and Corresponding Model Complexes. Dalton Trans 2012, 41, 3355–3368. [PubMed: 21918782]

235. Jacobson F; Pistorius A; Farkas D; De Grip W; Hansson Ö; Sjölin L; Neutze R, pH Dependence of Copper Geometry, Reduction Potential, and Nitrite Affinity in Nitrite Reductase *. J. Biol. Chem 2007, 282, 6347–6355. [PubMed: 17148448]

236. Kau LS; Spira-Solomon DJ; Penner-Hahn JE; Hodgson KO; Solomon EI, X-ray Absorption Edge Determination of the Oxidation State and Coordination Number of Copper. Application to the Type 3 Site in Rhus vernicifera Laccase and its Reaction with Oxygen. J. Am. Chem. Soc 1987, 109, 6433–6442.

237. Chen K; Yuldasheva S; Penner-Hahn JE; O'Halloran TV, An Atypical Linear Cu(I)−S2 Center Constitutes the High-Affinity Metal-Sensing Site in the CueR Metalloregulatory Protein. J. Am. Chem. Soc 2003, 125, 12088–12089. [PubMed: 14518983]

238. Prenesti E; Daniele PG; Prencipe M; Ostacoli G, Spectrum–Structure Correlation for Visible Absorption Spectra of Copper(II) Complexes in Aqueous Solution. Polyhedron 1999, 18, 3233–3241.

239. Xiao Z; Loughlin F; George GN; Howlett GJ; Wedd AG, C-Terminal Domain of the Membrane Copper Transporter Ctr1 from Saccharomyces cerevisiae Binds Four Cu(I) Ions as a Cuprous-Thiolate Polynuclear Cluster: Sub-femtomolar Cu(I) Affinity of Three Proteins Involved in Copper Trafficking. J. Am. Chem. Soc 2004, 126, 3081–3090. [PubMed: 15012137]

240. Suzuki S; Yamaguchi K; Kataoka K; Kobayashi K; Tagawa S; Kohzuma T; Shidara S; Iwasaki H; Deligeer, Spectroscopic Characterization and Intramolecular Electron Transfer Processes of Native and Type 2 Cu-depleted Nitrite Reductases. J. Biol. Inorg. Chem 1997, 2, 265–274.

241. Monzani E; Koolhaas GJAA; Spandre A; Leggieri E; Casella L; Gullotti M; Nardin G; Randaccio L; Fontani M; Zanello P, et al. , Binding of Nitrite and its Reductive Activation to Nitric Oxide at Biomimetic Copper Centers. J. Biol. Inorg. Chem 2000, 5, 251–261. [PubMed: 10819470]

242. Evans JP; Blackburn NJ; Klinman JP, The Catalytic Role of the Copper Ligand H172 of Peptidylglycine α-Hydroxylating Monooxygenase: A Kinetic Study of the H172A Mutant. Biochemistry 2006, 45, 15419–15429. [PubMed: 17176064]

Author Manuscript

Author Manuscript

Author Manuscript

Author Manuscript

243. Kline CD; Mayfield M; Blackburn NJ, HHM Motif at the CuH-Site of Peptidylglycine Monooxygenase is a pH-Dependent Conformational Switch. Biochemistry 2013, 52, 2586–2596. [PubMed: 23530865]

244. Prigge ST; Eipper BA; Mains RE; Amzel LM, Dioxygen Binds End-On to Mononuclear Copper in a Precatalytic Enzyme Complex. Science 2004, 304, 864–867. [PubMed: 15131304]

245. Yu F; Penner-Hahn JE; Pecoraro VL, De Novo-Designed Metallopeptides with Type 2 Copper Centers: Modulation of Reduction Potentials and Nitrite Reductase Activities. J. Am. Chem. Soc 2013, 135, 18096–18107. [PubMed: 24182361]

246. Churg AK; Warshel A, Control of the Redox Potential of Cytochrome and Microscopic Dielectric Effects in Proteins. Biochemistry 1986, 25, 1675–1681. [PubMed: 3011070]

247. Kuila D; Fee JA, Evidence for a Redox-Linked Ionizable Group Associated with the [2Fe-2S] Cluster of Thermus Rieske Protein. J. Biol. Chem 1986, 261, 2768–2771. [PubMed: 3949746]

248. Varadarajan R; Zewert T; Gray H; Boxer S, Effects of Buried Ionizable Amino Acids on the Reduction Potential of Recombinant Myoglobin. Science 1989, 243, 69–72. [PubMed: 2563171]

249. Hellwig P; Behr J; Ostermeier C; Richter O-MH; Pfitzner U; Odenwald A; Ludwig B; Michel H; Mäntele W, Involvement of Glutamic Acid 278 in the Redox Reaction of the Cytochrome c Oxidase from Paracoccus denitrificans Investigated by FTIR Spectroscopy. Biochemistry 1998, 37, 7390–7399. [PubMed: 9585553]

250. Koebke KJ; Yu F; Salerno E; Stappen CV; Tebo AG; Penner-Hahn JE; Pecoraro VL, Modifying the Steric Properties in the Second Coordination Sphere of Designed Peptides Leads to Enhancement of Nitrite Reductase Activity. Angew. Chem. Int. Ed 2018, 57, 3954–3957.

251. Ruckthong L; Peacock AFA; Pascoe CE; Hemmingsen L; Stuckey JA; Pecoraro VL, d-Cysteine Ligands Control Metal Geometries within de Novo Designed Three-Stranded Coiled Coils. Chem. - Eur. J 2017, 23, 8232–8243. [PubMed: 28384393]

252. Ruckthong L; Deb A; Hemmingsen L; Penner-Hahn JE; Pecoraro VL, Incorporation of Second Coordination Sphere d-Amino Acids Alters Cd(II) Geometries in Designed Thiolate-Rich Proteins. J. Biol. Inorg. Chem 2018, 23, 123–135. [PubMed: 29218636]

253. Ruckthong L; Stuckey JA; Pecoraro VL, How Second Coordination Sphere Modifications Can Impact Metal Structures in Proteins: A Crystallographic Evaluation. Chem. - Eur. J 2019, 25, 6773–6787. [PubMed: 30861211]

254. Koebke KJ; Yu F; Van Stappen C; Pinter TBJ; Deb A; Penner-Hahn JE; Pecoraro VL, Methylated Histidines Alter Tautomeric Preferences that Influence the Rates of Cu Nitrite Reductase Catalysis in Designed Peptides. J. Am. Chem. Soc 2019, 141, 7765–7775. [PubMed: 30983335]

255. Prigge ST; Kolhekar AS; Eipper BA; Mains RE; Amzel LM, Amidation of Bioactive Peptides: The Structure of Peptidylglycine α-Hydroxylating Monooxygenase. Science 1997, 278, 1300–1305. [PubMed: 9360928]

256. Fukuda Y; Tse KM; Nakane T; Nakatsu T; Suzuki M; Sugahara M; Inoue S; Masuda T; Yumoto F; Matsugaki N, et al. , Redox-Coupled Proton Transfer Mechanism in Nitrite Reductase Revealed by Femtosecond Crystallography. PNAS 2016, 113, 2928–2933. [PubMed: 26929369]

257. Karlin S; Zhu Z-Y; Karlin KD, The Extended Environment of Mononuclear Metal Centers in Protein Structures. PNAS 1997, 94, 14225–14230. [PubMed: 9405594]

258. Koebke KJ; Tebo AG; Manickas EC; Deb A; Penner-Hahn JE; Pecoraro VL, Nitrite Reductase Activity within an Antiparallel de Novo Scaffold. J. Biol. Inorg. Chem 2021, 26, 855–862. [PubMed: 34487215]

259. Mathieu E; Tolbert AE; Koebke KJ; Tard C; Iranzo O; Penner-Hahn JE; Policar C; Pecoraro V, Rational De Novo Design of a Cu Metalloenzyme for Superoxide Dismutation. Chem. Eur. J 2020, 26, 249–258. [PubMed: 31710732]

260. Tocheva EI; Eltis LD; Murphy MEP, Conserved Active Site Residues Limit Inhibition of a Copper-Containing Nitrite Reductase by Small Molecules. Biochemistry 2008, 47, 4452–4460. [PubMed: 18358002]

261. Policar C, Mimicking SODs, Why and How: Bio-Inspired Manganese Complexes as SOD Mimics. In Redox Active Therapeutics, Reboucas JS; Batinic-Haberle I; Spasojevic I; Warner DS; St. Clair D, Eds. Springer: 2016; pp 125–164.

Author Manuscript Author Manuscript Author Manuscript Author Manuscript

262. Abreu IA; Cabelli DE, Superoxide Dismutases—a Review of the Metal-Associated Mechanistic Variations. Biochim. Biophys. Acta 2010, 1804, 263–274. [PubMed: 19914406]

263. Aguirre JD; Culotta VC, Battles with Iron: Manganese in Oxidative Stress Protection. J. Biol. Chem 2012, 287, 13541–13548. [PubMed: 22247543]

264. Barondeau DP; Kassmann CJ; Bruns CK; Tainer JA; Getzoff ED, Nickel Superoxide Dismutase Structure and Mechanism. Biochemistry 2004, 43, 8038–8047. [PubMed: 15209499]

265. Gleason JE; Galaleldeen A; Peterson RL; Taylor AB; Holloway SP; Waninger-Saroni J; Cormack BP; Cabelli DE; Hart PJ; Culotta VC, Candida albicans SOD5 Represents the Prototype of an Unprecedented Class of Cu-only Superoxide Dismutases Required for Pathogen Defense. PNAS 2014, 111, 5866–5871. [PubMed: 24711423]

266. Spagnolo L; Törö I; D'Orazio M; O'Neill P; Pedersen JZ; Carugo O; Rotilio G; Battistoni A; Djinović-Carugo K, Unique Features of the sodC -encoded Superoxide Dismutase from Mycobacterium tuberculosis, a Fully Functional Copper-containing Enzyme Lacking Zinc in the Active Site. J. Biol. Chem 2004, 279, 33447–33455. [PubMed: 15155722]

267. Robinett NG; Peterson RL; Culotta VC, Eukaryotic Copper-only Superoxide Dismutases (SODs): A New Class of SOD Enzymes and SOD-like Protein Domains. J. Biol. Chem 2018, 293, 4636–4643. [PubMed: 29259135]

268. Forman HJ; Fridovich I, Superoxide Dismutase: A Comparison of Rate Constants. Arch. Biochem. Biophys 1973, 158, 396–400. [PubMed: 4354035]

269. Choudhury SB; Lee J-W; Davidson G; Yim Y-I; Bose K; Sharma ML; Kang S-O; Cabelli DE; Maroney MJ, Examination of the Nickel Site Structure and Reaction Mechanism in Streptomyces seoulensis Superoxide Dismutase. Biochemistry 1999, 38, 3744–3752. [PubMed: 10090763]

270. Stallings WC; Pattridge KA; Strong RK; Ludwig ML, The structure of Manganese Superoxide Dismutase from Thermus thermophilus HB8 at 2.4-A Resolution. J. Biol. Chem 1985, 260, 16424–16432. [PubMed: 4066716]

271. Ishida M; Dohmae N; Shiro Y; Isogai Y, Synthesis of Biotinylated Heme and its Application to Panning Heme-binding Proteins. Anal. Biochem 2003, 321, 138–141. [PubMed: 12963066]

272. Singh UP; Singh RK; Isogai Y; Shiro Y, Design and Synthesis of de Novo Peptide for Manganese Binding. Int J Pept Res Ther 2006, 12, 379–385.

273. Cohn M; Townsend J, A Study of Manganous Complexes by Paramagnetic Resonance Absorption. Nature 1954, 173, 1090–1091.

274. Solomon EI; Heppner DE; Johnston EM; Ginsbach JW; Cirera J; Qayyum M; Kieber-Emmons MT; Kjaergaard CH; Hadt RG; Tian L, Copper Active Sites in Biology. Chem. Rev 2014, 114, 3659–3853. [PubMed: 24588098]

275. McCord JM; Fridovich I, Superoxide Dismutase: An Enzymic Function for Erythrocuprein (Hemocuprein). J. Biol. Chem 1969, 244, 6049–6055. [PubMed: 5389100]

276. Fridovich I, Quantitative Aspects of the Production of Superoxide Anion Radical by Milk Xanthine Oxidase. J. Biol. Chem 1970, 245, 4053–4057. [PubMed: 5496991]

277. Sutherland MW; Learmonth BA, The Tetrazolium Dyes MTS and XTT Provide New Quantitative Assays for Superoxide and Superoxide Dismutase. Free Radical Res 1997, 27, 283–289. [PubMed: 9350432]

278. Batinić-Haberle I; Rebouças JS; Spasojević I, Superoxide Dismutase Mimics: Chemistry, Pharmacology, and Therapeutic Potential. Antioxid. Redox Signal 2010, 13, 877–918. [PubMed: 20095865]

279. Batinic-Haberle I; Tovmasyan A; Roberts ER; Vujaskovic Z; Leong KW; Spasojevic I, SOD Therapeutics: Latest Insight into Their Structure-Activity Relationships and Impact on the Cellular Redox-based Signaling Pathways. Antioxid Redox Signal 2014, 20, 2372–2415. [PubMed: 23875805]

280. Vance CK; Miller A-F, Novel Insights into the Basis for Escherichia coli Superoxide Dismutase's Metal Ion Specificity from Mn-Substituted FeSOD and Its Very High Em. Biochemistry 2001, 40, 13079–13087. [PubMed: 11669646]

281. Holm RH; Kennepohl P; Solomon EI, Structural and Functional Aspects of Metal Sites in Biology. Chem. Rev 1996, 96, 2239–2314. [PubMed: 11848828]

Author Manuscript Author Manuscript Author Manuscript Author Manuscript

282. Árus D; Jancsó A; Szunyogh D; Matyuska F; Nagy NV; Hoffmann E; Körtvélyesi T; Gajda T, On the possible roles of N-terminal His-rich domains of Cu, Zn SODs of some Gram-negative bacteria. J. Inorg. Biochem 2012, 106, 10–18. [PubMed: 22105012]

283. Mazurenko I; de Poulpiquet A; Lojou E, Recent Developments in High Surface Area Bioelectrodes for Enzymatic Fuel Cells. Curr Opin Electrochem 2017, 5, 74–84.

284. Fukuzumi S; Yamada Y; Karlin KD, Hydrogen Peroxide as a Sustainable Energy Carrier: Electrocatalytic Production of Hydrogen Peroxide and the Fuel Cell. Electrochim. Acta 2012, 82, 493–511. [PubMed: 23457415]

285. Miglbauer E; Wójcik PJ; Głowacki ED, Single-compartment Hydrogen Peroxide Fuel Cells with poly(3,4-ethylenedioxythiophene) Cathodes. Chem. Commun 2018, 54, 11873–11876.

286. Kaim W; Rall J, Copper—A “Modern” Bioelement. Angew. Chem. Int. Ed. Engl 1996, 35, 43–60.

287. Liu J; Chakraborty S; Hosseinzadeh P; Yu Y; Tian S; Petrik I; Bhagi A; Lu Y, Metalloproteins Containing Cytochrome, Iron–Sulfur, or Copper Redox Centers. Chem. Rev 2014, 114, 4366–4469. [PubMed: 24758379]

288. Vaaje-Kolstad G; Westereng B; Horn SJ; Liu Z; Zhai H; Sørlie M; Eijsink VGH, An Oxidative Enzyme Boosting the Enzymatic Conversion of Recalcitrant Polysaccharides. Science 2010, 330, 219–222. [PubMed: 20929773]

289. Bertini L; Breglia R; Lambrughi M; Fantucci P; De Gioia L; Borsari M; Sola M; Bortolotti CA; Bruschi M, Catalytic Mechanism of Fungal Lytic Polysaccharide Monooxygenases Investigated by First-Principles Calculations. Inorg. Chem 2018, 57, 86–97. [PubMed: 29232119]

290. Mitra S; Prakash D; Rajabimoghadam K; Wawrzak Z; Prasad P; Wu T; Misra SK; Sharp JS; Garcia-Bosch I; Chakraborty S, De Novo Design of a Self-Assembled Artificial Copper Peptide that Activates and Reduces Peroxide. ACS Catal 2021, 11, 10267–10278. [PubMed: 36188417]

291. Hemsworth GR; Taylor EJ; Kim RQ; Gregory RC; Lewis SJ; Turkenburg JP; Parkin A; Davies GJ; Walton PH, The Copper Active Site of CBM33 Polysaccharide Oxygenases. J. Am. Chem. Soc 2013, 135, 6069–6077. [PubMed: 23540833]

292. Macedo S; Pechlaner M; Schmid W; Weik M; Sato K; Dennison C; Djinovic-Carugo K, Can Soaked-in Scavengers Protect Metalloprotein Active Sites from Reduction During Data Collection? J. Synchrotron Radiat 2009, 16, 191–204. [PubMed: 19240331]

293. Kjaergaard CH; Qayyum MF; Wong SD; Xu F; Hemsworth GR; Walton DJ; Young NA; Davies GJ; Walton PH; Johansen KS, et al. , Spectroscopic and Computational Insight into the Activation of O_2 by the Mononuclear Cu Center in Polysaccharide Monooxygenases. PNAS 2014, 111, 8797–8802. [PubMed: 24889637]

294. Mann SI; Heinisch T; Ward TR; Borovik AS, Peroxide Activation Regulated by Hydrogen Bonds within Artificial Cu Proteins. J. Am. Chem. Soc 2017, 139, 17289–17292. [PubMed: 29117678]

295. Bissaro B; Røhr ÅK; Müller G; Chylenski P; Skaugen M; Forsberg Z; Horn SJ; Vaaje-Kolstad G; Eijsink VGH, Oxidative Cleavage of Polysaccharides by Monocopper Enzymes Depends on H_2O_2. Nat. Chem. Biol 2017, 13, 1123–1128. [PubMed: 28846668]

296. Bissaro B; Streit B; Isaksen I; Eijsink VGH; Beckham GT; DuBois JL; Røhr ÅK, Molecular Mechanism of the Chitinolytic Peroxygenase Reaction. PNAS 2020, 117, 1504–1513. [PubMed: 31907317]

297. Paradisi A; Johnston EM; Tovborg M; Nicoll CR; Ciano L; Dowle A; McMaster J; Hancock Y; Davies GJ; Walton PH, Formation of a Copper(II)–Tyrosyl Complex at the Active Site of Lytic Polysaccharide Monooxygenases Following Oxidation by H_2O_2. J. Am. Chem. Soc 2019, 141, 18585–18599. [PubMed: 31675221]

298. Reuillard B; Ly KH; Hildebrandt P; Jeuken LJC; Butt JN; Reisner E, High Performance Reduction of H_2O_2 with an Electron Transport Decaheme Cytochrome on a Porous ITO Electrode. J. Am. Chem. Soc 2017, 139, 3324–3327. [PubMed: 28221032]

299. Reuillard B; Le Goff A; Holzinger M; Cosnier S, Non-covalent Functionalization of Carbon Nanotubes with Boronic Acids for the Wiring of Glycosylated Redox Enzymes in Oxygen-reducing Biocathodes. J Mater Chem B 2014, 2, 2228–2232. [PubMed: 32261710]

Author Manuscript Author Manuscript Author Manuscript Author Manuscript

300. Baesjou PJ; Driessen WL; Challa G; Reedijk J, A Kinetic Study of the Copper-catalysed Oxidative Coupling of 2,6-dimethylphenol. The Role of Copper, Base and Phenol Concentrations. J. Mol. Catal. A: Chem 1998, 135, 273–283.
301. Baesjou PJ; Driessen WL; Challa G; Reedijk J, A Kinetic and Spectroscopic Study on the Copper Catalyzed Oxidative Coupling Polymerization of 2,6-dimethylphenol. X-ray Structure of the Catalyst Precursor tetrakis (N-methylimidazole) bis(nitrato) copper(II). J. Mol. Catal. A: Chem 1996, 110, 195–210.
302. Cassagnes L-E; Hervé V; Nepveu F; Hureau C; Faller P; Collin F, The Catalytically Active Copper-Amyloid-Beta State: Coordination Site Responsible for Reactive Oxygen Species Production. Angew. Chem. Int. Ed 2013, 52, 11110–11113.
303. Peisach J; Blumberg WE, Structural Implications Derived from the Analysis of Electron Paramagnetic Resonance Spectra of Natural and Artificial Copper Proteins. Arch. Biochem. Biophys 1974, 165, 691–708. [PubMed: 4374138]
304. Lavey BJ; Janda KD, Catalytic Antibody Mediated Hydrolysis of Paraoxon. J. Org. Chem 1996, 61, 7633–7636. [PubMed: 11667704]
305. Goldsmith M; Ashani Y; Margalit R; Nyska A; Mirelman D; Tawfik DS, A New Post-intoxication Treatment of Paraoxon and Parathion Poisonings Using an Evolved PON1 Variant and Recombinant GOT1. Chem. Biol. Interact 2016, 259, 242–251. [PubMed: 27256520]
306. Kirby SD; Norris JR; Richard Smith J; Bahnson BJ; Cerasoli DM, Human Paraoxonase Double Mutants Hydrolyze V and G Class Organophosphorus Nerve Agents. Chem. Biol. Interact 2013, 203, 181–185. [PubMed: 23159884]
307. Xiang DF; Kolb P; Fedorov AA; Meier MM; Fedorov LV; Nguyen TT; Sterner R; Almo SC; Shoichet BK; Raushel FM, Functional Annotation and Three-Dimensional Structure of Dr0930 from Deinococcus radiodurans, a Close Relative of Phosphotriesterase in the Amidohydrolase Superfamily. Biochemistry 2009, 48, 2237–2247. [PubMed: 19159332]
308. Ugwumba IN; Ozawa K; Xu Z-Q; Ely F; Foo J-L; Herlt AJ; Coppin C; Brown S; Taylor MC; Ollis DL, et al. , Improving a Natural Enzyme Activity through Incorporation of Unnatural Amino Acids. J. Am. Chem. Soc 2011, 133, 326–333. [PubMed: 21162578]
309. Xu Y; Yamamoto N; Ruiz DI; Kubitz DS; Janda KD, Squaric Monoamide Monoester as a New Class of Reactive Immunization Hapten for Catalytic Antibodies. Bioorg. Med. Chem. Lett 2005, 15, 4304–4307. [PubMed: 16046128]
310. Kennedy DJ; Mayer BP; Baker SE; Valdez CA, Kinetics and Speciation of Paraoxon Hydrolysis by Zinc(II)–azamacrocyclic Catalysts. Inorg. Chim. Acta 2015, 436, 123–131.
311. Morrow JR; Trogler WC, Hydrolysis of Phosphate Triesters with Copper(II) Catalysts. Inorg. Chem 1989, 28, 2330–2333.
312. Kuo LY; Perera NM, Paraoxon and Parathion Hydrolysis by Aqueous Molybdenocene Dichloride (Cp2MoCl2): First Reported Pesticide Hydrolysis by an Organometallic Complex. Inorg. Chem 2000, 39, 2103–2106. [PubMed: 12526519]
313. Nordlund P; Eklund H, Di-iron—carboxylate Proteins. Curr. Opin. Struct. Biol 1995, 5, 758–766. [PubMed: 8749363]
314. Lange SJ; Que L, Oxygen Activating Nonheme Iron Enzymes. Curr. Opin. Chem. Biol 1998, 2, 159–172. [PubMed: 9667935]
315. Wallar BJ; Lipscomb JD, Dioxygen Activation by Enzymes Containing Binuclear Non-Heme Iron Clusters. Chem. Rev 1996, 96, 2625–2658. [PubMed: 11848839]
316. Feig AL; Lippard SJ, Reactions of Non-Heme Iron(II) Centers with Dioxygen in Biology and Chemistry. Chem. Rev 1994, 94, 759–805.
317. Summa CM; Lombardi A; Lewis M; DeGrado WF, Tertiary Templates for the Design of Diiron Proteins. Curr. Opin. Struct. Biol 1999, 9, 500–508. [PubMed: 10449377]
318. Lawson DM; Artymiuk PJ; Yewdall SJ; Smith JMA; Livingstone JC; Treffry A; Luzzago A; Levi S; Arosio P; Cesareni G, et al. , Solving the Structure of Human H Ferritin by Genetically Engineering Intermolecular Crystal Contacts. Nature 1991, 349, 541–544. [PubMed: 1992356]
319. deMaré F; Kurtz DM; Nordlund P, The structure of Desulfovibrio vulgaris Rubrerythrin Reveals a Unique Combination of Rubredoxin-like FeS4 and Ferritin-like Diiron Domains. Nat. Struct. Biol 1996, 3, 539–546. [PubMed: 8646540]

Author Manuscript Author Manuscript Author Manuscript Author Manuscript

320. Sieker LC; Holmes M; Trong IL; Turley S; Santarsiero BD; Liu MY; LeGall J; Stenkamp RE, Alternative Metal-binding Sites in Rubrerythrin. Nat. Struct. Biol 1999, 6, 308–309. [PubMed: 10201393]

321. Andersson ME; Högbom M; Rinaldo-Matthis A; Andersson KK; Sjöberg B-M; Nordlund P, The Crystal Structure of an Azide Complex of the Diferrous R2 Subunit of Ribonucleotide Reductase Displays a Novel Carboxylate Shift with Important Mechanistic Implications for Diiron-Catalyzed Oxygen Activation. J. Am. Chem. Soc 1999, 121, 2346–2352.

322. Lindqvist Y; Huang W; Schneider G; Shanklin J, Crystal Structure of Delta9 Stearoyl-acyl Carrier Protein Desaturase from Castor Seed and its Relationship to Other Di-iron Proteins. EMBO J 1996, 15, 4081–4092. [PubMed: 8861937]

323. Rosenzweig AC; Brandstetter H; Whittington DA; Nordlund P; Lippard SJ; Frederick CA, Crystal Structures of the Methane Monooxygenase Hydroxylase from Methylococcus capsulatus (Bath): Implications for Substrate Gating and Component Interactions. Proteins: Struct. Funct. Genet 1997, 29, 141–152. [PubMed: 9329079]

324. Desjarlais JR; Handel TM, De Novo Design of the Hydrophobic Cores of Proteins. Protein Sci 1995, 4, 2006–2018. [PubMed: 8535237]

325. Le Brun NE; Keech AM; Mauk MR; Mauk A. Grant; Andrews SC; Thomson AJ; Moore GR, Charge Compensated Binding of Divalent Metals to Bacterioferritin: H+ Release Associated with Cobalt(II) and Zinc(II) Binding at Dinuclear Metal Sites. FEBS Lett 1996, 397, 159–163. [PubMed: 8955338]

326. Di Costanzo L; Wade H; Geremia S; Randaccio L; Pavone V; DeGrado WF; Lombardi A, Toward the de Novo Design of a Catalytically Active Helix Bundle: A Substrate-Accessible Carboxylate-Bridged Dinuclear Metal Center. J. Am. Chem. Soc 2001, 123, 12749–12757. [PubMed: 11749531]

327. Atta M; Nordlund P; Aberg A; Eklund H; Fontecave M, Substitution of Manganese for Iron in Ribonucleotide Reductase from Escherichia coli. Spectroscopic and Crystallographic Characterization. J. Biol. Chem 1992, 267, 20682–20688. [PubMed: 1328209]

328. Rosenzweig AC; Nordlund P; Takahara PM; Frederick CA; Lippard SJ, Geometry of the Soluble Methane Monooxygenase Catalytic Diiron Center in Two Oxidation States. Chem. Biol 1995, 2, 409–418.

329. Pasternak A; Kaplan J; Lear JD; Degrado WF, Proton and Metal Ion-dependent Assembly of a Model Diiron Protein. Protein Sci 2001, 10, 958–969. [PubMed: 11316876]

330. Garbett K; Darnall DW; Klotz IM; Williams RJP, Spectroscopy and Structure of Hemerythrin. Arch. Biochem. Biophys 1969, 135, 419–434. [PubMed: 4312075]

331. Reem RC; McCormick JM; Richardson DE; Devlin FJ; Stephens PJ; Musselman RL; Solomon EI, Spectroscopic Studies of the Coupled Binuclear Ferric Active Site in Methemerythrins and Oxyhemerythrin: the Electronic Structure of Each Iron Center and the Iron-oxo and Iron-peroxide Bonds. J. Am. Chem. Soc 1989, 111, 4688–4704.

332. Fox BG; Shanklin J; Ai J; Loehr TM; Sanders-Loehr J, Resonance Raman Evidence for an Fe-O-Fe Center in Stearoyl-ACP Desaturase. Primary Sequence Identity with Other Diiron-Oxo Proteins. Biochemistry 1994, 33, 12776–12786. [PubMed: 7947683]

333. Dunn JBR; Addison AW; Bruce RE; Loehr JS; Loehr TM, Comparison of Hemerythrins from Four Species of Sipunculids by Optical Absorption, Circular Dichroism, Fluorescence Emission, and Resonance Raman Spectroscopy. Biochemistry 1977, 16, 1743–1749. [PubMed: 856259]

334. Whittington DA; Lippard SJ, Crystal Structures of the Soluble Methane Monooxygenase Hydroxylase from Methylococcus capsulatus (Bath) Demonstrating Geometrical Variability at the Dinuclear Iron Active Site. J. Am. Chem. Soc 2001, 123, 827–838. [PubMed: 11456616]

335. Logan DT; deMaré F; Persson BO; Slaby A; Sjöberg B-M; Nordlund P, Crystal Structures of Two Self-Hydroxylating Ribonucleotide Reductase Protein R2 Mutants: Structural Basis for the Oxygen-Insertion Step of Hydroxylation Reactions Catalyzed by Diiron Proteins. Biochemistry 1998, 37, 10798–10807. [PubMed: 9692970]

336. Maglio O; Nastri F; Pavone V; Lombardi A; DeGrado WF, Preorganization of Molecular Binding Sites in Designed Diiron Proteins. PNAS 2003, 100, 3772–3777. [PubMed: 12655072]

Author Manuscript Author Manuscript Author Manuscript Author Manuscript

337. Xu J; Baase WA; Baldwin E; Matthews BW, The Response of T4 Lysozyme to Large-to-Small Substitutions within the Core and its Relation to the Hydrophobic Effect. Protein Sci 1998, 7, 158–177. [PubMed: 9514271]

338. Pace CN, Contribution of the Hydrophobic Effect to Globular Protein Stability. J. Mol. Biol 1992, 226, 29–35. [PubMed: 1619660]

339. Bryson JW; Betz SF; Lu HS; Suich DJ; Zhou HX; O'Neil KT; DeGrado WF, Protein Design: a Hierarchic Approach. Science 1995, 270, 935–941. [PubMed: 7481798]

340. Myers JK; Pace CN; Scholtz JM, Helix Propensities Are Identical in Proteins and Peptides. Biochemistry 1997, 36, 10923–10929. [PubMed: 9283083]

341. Ruckthong L; Zastrow ML; Stuckey JA; Pecoraro VL, A Crystallographic Examination of Predisposition versus Preorganization in de Novo Designed Metalloproteins. J. Am. Chem. Soc 2016, 138, 11979–11988. [PubMed: 27532255]

342. Kaplan J; DeGrado WF, De Novo Design of Catalytic Proteins. PNAS 2004, 101, 11566–11570. [PubMed: 15292507]

343. Summa CM; Rosenblatt MM; Hong J-K; Lear JD; DeGrado WF, Computational de Novo Design, and Characterization of an A2B2 Diiron Protein. J. Mol. Biol 2002, 321, 923–938. [PubMed: 12206771]

344. Witt ON, XXIV.—On Colouring Matters Derived from Diazo-compounds. J. Chem. Soc., Trans 1879, 35, 179–189.

345. Ullmann F; Gnaedinger J, Über Indamine. Berichte der deutschen chemischen Gesellschaft 1912, 45, 3437–3446.

346. Corbett JF, Benzoquinone Imines. Part V. Mechanism and Kinetics of the Reaction of p-Benzoquinone Monoimines with m-Phenylenediamines. J. Chem. Soc. B. Phys. Org 1969, 823–826.

347. Faiella M; Andreozzi C; de Rosales RTM; Pavone V; Maglio O; Nastri F; DeGrado WF; Lombardi A, An Artificial Di-iron Oxo-protein with Phenol Oxidase Activity. Nat. Chem. Biol 2009, 5, 882–884. [PubMed: 19915535]

348. Lahr SJ; Engel DE; Stayrook SE; Maglio O; North B; Geremia S; Lombardi A; DeGrado WF, Analysis and Design of Turns in α-Helical Hairpins. J. Mol. Biol 2005, 346, 1441–1454. [PubMed: 15713492]

349. Koval IA; Gamez P; Belle C; Selmeczi K; Reedijk J, Synthetic Models of the Active Site of Catechol Oxidase: Mechanistic Studies. Chem. Soc. Rev 2006, 35, 814–840. [PubMed: 16936929]

350. Corbett JF; Gamson EP, Benzoquinone Imines. Part XI. Mechanism and Kinetics of the Reaction of p-Benzoquinone Di-imines with Aniline and its Derivatives. J. Chem. Soc., Perkin trans 2 1972, 1531–1537.

351. Kolberg M; Strand KR; Graff P; Kristoffer Andersson K, Structure, Function, and Mechanism of Ribonucleotide Reductases. Biochim. Biophys. Acta, Proteins Proteomics 2004, 1699, 1–34.

352. Shanklin J; Guy JE; Mishra G; Lindqvist Y, Desaturases: Emerging Models for Understanding Functional Diversification of Diiron-containing Enzymes. J. Biol. Chem 2009, 284, 18559–18563. [PubMed: 19363032]

353. Berthold DA; Stenmark P, Membrane-Bound Diiron Carboxylate Proteins. Annu. Rev. Plant Biol 2003, 54, 497–517. [PubMed: 14503001]

354. Solomon EI; Brunold TC; Davis MI; Kemsley JN; Lee S-K; Lehnert N; Neese F; Skulan AJ; Yang Y-S; Zhou J, Geometric and Electronic Structure/Function Correlations in Non-Heme Iron Enzymes. Chem. Rev 2000, 100, 235–350. [PubMed: 11749238]

355. Lippard SJ, Hydroxylation of C-H Bonds at Carboxylate-Bridged Diiron Centres. Philos Trans A Math Phys Eng Sci 2005, 363, 861–877. [PubMed: 15901540]

356. Peters JW; Lanzilotta WN; Lemon BJ; Seefeldt LC, X-ray Crystal Structure of the Fe-Only Hydrogenase (CpI) from Clostridium pasteurianum to 1.8 Angstrom Resolution. Science 1998, 282, 1853–1858. [PubMed: 9836629]

357. Iyer RB; Silaghi-Dumitrescu R; Kurtz DM; Lanzilotta WN, High-resolution Crystal Structures of Desulfovibrio vulgaris (Hildenborough) Nigerythrin: Facile, Redox-dependent Iron Movement,

Author Manuscript

Author Manuscript

Author Manuscript

Author Manuscript

Domain Interface Variability, and Peroxidase Activity in the Rubrerythrins. J. Biol. Inorg. Chem 2005, 10, 407–416. [PubMed: 15895271]

358. Jin S; Kurtz DM; Liu Z-J; Rose J; Wang B-C, X-ray Crystal Structures of Reduced Rubrerythrin and Its Azide Adduct: A Structure-Based Mechanism for a Non-Heme Diiron Peroxidase. J. Am. Chem. Soc 2002, 124, 9845–9855. [PubMed: 12175244]

359. Tempel W; Liu Z-J; Schubot FD; Shah A; Weinberg MV; Jenney FE Jr.; Arendall III WB; Adams MWW; Richardson JS; Richardson DC, et al. , Structural Genomics of Pyrococcus furiosus: X-ray Crystallography Reveals 3D Domain Swapping in Rubrerythrin. Proteins: Struct. Funct. Genet 2004, 57, 878–882. [PubMed: 15468318]

360. Johnson DC; Dean DR; Smith AD; Johnson MK, Structure, Function, and Formation of Biological Iron-Sulfur Clusters. Annu. Rev. Biochem 2005, 74, 247–281. [PubMed: 15952888]

361. Yu C-A; Wen X; Xiao K; Xia D; Yu L, Inter- and Intra-molecular Electron Transfer in the Cytochrome bc(1) Complex. Biochim. Biophys. Acta 2002, 1555, 65–70. [PubMed: 12206893]

362. Silaghi-Dumitrescu R; Kurtz DM; Ljungdahl LG; Lanzilotta WN, X-ray Crystal Structures of Moorella thermoacetica FprA. Novel Diiron Site Structure and Mechanistic Insights into a Scavenging Nitric Oxide Reductase. Biochemistry 2005, 44, 6492–6501. [PubMed: 15850383]

363. Calhoun JR; Kono H; Lahr S; Wang W; DeGrado WF; Saven JG, Computational Design and Characterization of a Monomeric Helical Dinuclear Metalloprotein. J. Mol. Biol 2003, 334, 1101–1115. [PubMed: 14643669]

364. Zocher G; Winkler R; Hertweck C; Schulz GE, Structure and Action of the N-oxygenase AurF from Streptomyces thioluteus. J. Mol. Biol 2007, 373, 65–74. [PubMed: 17765264]

365. Choi YS; Zhang H; Brunzelle JS; Nair SK; Zhao H, In Vitro Reconstitution and Crystal Structure of p-Aminobenzoate N-Oxygenase (AurF) Involved in Aureothin Biosynthesis. PNAS 2008, 105, 6858–6863. [PubMed: 18458342]

366. Snyder RA; Betzu J; Butch SE; Reig AJ; DeGrado WF; Solomon EI, Systematic Perturbations of Binuclear Non-heme Iron Sites: Structure and Dioxygen Reactivity of de Novo Due Ferri Proteins. Biochemistry 2015, 54, 4637–4651. [PubMed: 26154739]

367. Yang Y-S; Broadwater JA; Pulver SC; Fox BG; Solomon EI, Circular Dichroism and Magnetic Circular Dichroism Studies of the Reduced Binuclear Non-Heme Iron Site of Stearoyl-ACP Δ9-Desaturase: Substrate Binding and Comparison to Ribonucleotide Reductase. J. Am. Chem. Soc 1999, 121, 2770–2783.

368. Yang Y-S; Baldwin J; Ley BA; Bollinger JM; Solomon EI, Spectroscopic and Electronic Structure Description of the Reduced Binuclear Non-Heme Iron Active Site in Ribonucleotide Reductase from E. coli: Comparison to Reduced Δ9 Desaturase and Electronic Structure Contributions to Differences in O_2 Reactivity. J. Am. Chem. Soc 2000, 122, 8495–8510.

369. Korboukh VK; Li N; Barr EW; Bollinger JM; Krebs C, A Long-Lived, Substrate-Hydroxylating Peroxodiiron(III/III) Intermediate in the Amine Oxygenase, AurF, from Streptomyces thioluteus. J. Am. Chem. Soc 2009, 131, 13608–13609. [PubMed: 19731912]

370. Solomon EI; Pavel EG; Loeb KE; Campochiaro C, Magnetic Circular Dichroism Spectroscopy as a Probe of the Geometric and Electronic Structure of Non-heme Ferrous Enzymes. Coord. Chem. Rev 1995, 144, 369–460.

371. Bell CB; Calhoun JR; Bobyr E; Wei P.-p.; Hedman B; Hodgson KO; DeGrado WF; Solomon EI, Spectroscopic Definition of the Biferrous and Biferric Sites in de Novo Designed Four-Helix Bundle DFsc Peptides: Implications for O_2 Reactivity of Binuclear Non-Heme Iron Enzymes. Biochemistry 2009, 48, 59–73. [PubMed: 19090676]

372. Calhoun JR; Bell CB; Smith TJ; Thamann TJ; DeGrado WF; Solomon EI, Oxygen Reactivity of the Biferrous Site in the de Novo Designed Four Helix Bundle Peptide DFsc: Nature of the “Intermediate” and Reaction Mechanism. J. Am. Chem. Soc 2008, 130, 9188–9189. [PubMed: 18572936]

373. Snyder RA; Butch SE; Reig AJ; DeGrado WF; Solomon EI, Molecular-Level Insight into the Differential Oxidase and Oxygenase Reactivities of de Novo Due Ferri Proteins. J. Am. Chem. Soc 2015, 137, 9302–9314. [PubMed: 26090726]

374. McCormick MS; Sazinsky MH; Condon KL; Lippard SJ, X-ray Crystal Structures of Manganese(II)-Reconstituted and Native Toluene/o-Xylene Monooxygenase Hydroxylase Reveal

Rotamer Shifts in Conserved Residues and an Enhanced View of the Protein Interior. J. Am. Chem. Soc 2006, 128, 15108–15110. [PubMed: 17117860]

375. Bailey LJ; Fox BG, Crystallographic and Catalytic Studies of the Peroxide-Shunt Reaction in a Diiron Hydroxylase. Biochemistry 2009, 48, 8932–8939. [PubMed: 19705873]

376. Chino M; Leone L; Maglio O; Lombardi A, Chapter Twenty-One - Designing Covalently Linked Heterodimeric Four-Helix Bundles. In Methods Enzymol, Pecoraro VL, Ed. Academic Press: 2016; Vol. 580, pp 471–499. [PubMed: 27586346]

377. Kolb HC; Finn MG; Sharpless KB, Click Chemistry: Diverse Chemical Function from a Few Good Reactions. Angew. Chem. Int. Ed 2001, 40, 2004–2021.

378. Bock VD; Hiemstra H; van Maarseveen JH, CuI-Catalyzed Alkyne–Azide “Click” Cycloadditions from a Mechanistic and Synthetic Perspective. Eur. J. Org. Chem 2006, 2006, 51–68.

379. Bertini I; Luchinat C, High Spin Cobalt(II) as a Probe for the Investigation of Metalloproteins. Adv Inorg Biochem 1984, 6, 71–111. [PubMed: 6442958]

380. Sazinsky MH; Merkx M; Cadieux E; Tang S; Lippard SJ, Preparation and X-ray Structures of Metal-Free, Dicobalt and Dimanganese Forms of Soluble Methane Monooxygenase Hydroxylase from Methylococcus capsulatus (Bath). Biochemistry 2004, 43, 16263–16276. [PubMed: 15610020]

381. Olson TL; Espiritu E; Edwardraja S; Simmons CR; Williams JC; Ghirlanda G; Allen JP, Design of Dinuclear Manganese Cofactors for Bacterial Reaction Centers. Biochim. Biophys. Acta, Bioenerg 2016, 1857, 539–547.

382. Olson TL; Espiritu E; Edwardraja S; Canarie E; Flores M; Williams JC; Ghirlanda G; Allen JP, Biochemical and Spectroscopic Characterization of Dinuclear Mn-sites in Artificial Four-helix Bundle Proteins. Biochim. Biophys. Acta, Bioenerg 2017, 1858, 945–954. [PubMed: 28882760]

383. Umena Y; Kawakami K; Shen J-R; Kamiya N, Crystal Structure of Oxygen-evolving Photosystem II at a Resolution of 1.9 Å. Nature 2011, 473, 55–60. [PubMed: 21499260]

384. Suga M; Akita F; Hirata K; Ueno G; Murakami H; Nakajima Y; Shimizu T; Yamashita K; Yamamoto M; Ago H, et al. , Native Structure of Photosystem II at 1.95 Å Resolution Viewed by Femtosecond X-ray Pulses. Nature 2015, 517, 99–103. [PubMed: 25470056]

385. Cox N; Pantazis DA; Neese F; Lubitz W, Biological Water Oxidation. Acc. Chem. Res 2013, 46, 1588–1596. [PubMed: 23506074]

386. Britt RD; Oyala PH, One Step Closer to O_2. Science 2014, 345, 736–736. [PubMed: 25124415]

387. Cox N; Retegan M; Neese F; Pantazis DA; Boussac A; Lubitz W, Electronic Structure of the Oxygen-evolving Complex in Photosystem II Prior to O-O Bond Formation. Science 2014, 345, 804–808. [PubMed: 25124437]

388. Pokhrel R; Brudvig GW, Oxygen-evolving Complex of Photosystem II: Correlating Structure with Spectroscopy. PCCP 2014, 16, 11812–11821. [PubMed: 24700294]

389. Yano J; Yachandra V, Mn4Ca Cluster in Photosynthesis: Where and How Water is Oxidized to Dioxygen. Chem. Rev 2014, 114, 4175–4205. [PubMed: 24684576]

390. Rappaport F; Diner BA, Primary Photochemistry and Energetics Leading to the Oxidation of the (Mn)4Ca Cluster and to the Evolution of Molecular Oxygen in Photosystem II. Coord. Chem. Rev 2008, 252, 259–272.

391. Renger G, Light Induced Oxidative Water Splitting in Photosynthesis: Energetics, Kinetics and Mechanism. J. Photochem. Photobiol. B: Biol 2011, 104, 35–43.

392. Pace RJ; Stranger R; Petrie S, Why Nature Chose Mn for the Water Oxidase in Photosystem II. Dalton Trans 2012, 41, 7179–7189. [PubMed: 22580684]

393. Debus RJ, Protein Ligation of the Photosynthetic Oxygen-evolving Center. Coord. Chem. Rev 2008, 252, 244–258. [PubMed: 18496594]

394. Barber J, Photosystem II: The Water-Splitting Enzyme of Photosynthesis. Cold Spring Harb. Symp 2012, 77, 295–307.

395. Cardona T; Sedoud A; Cox N; Rutherford AW, Charge Separation in Photosystem II: A Comparative and Evolutionary Overview. Biochim. Biophys. Acta, Bioenerg 2012, 1817, 26–43.

Author Manuscript Author Manuscript Author Manuscript Author Manuscript

Author Manuscript
Author Manuscript
Author Manuscript
Author Manuscript

396. Bao H; Dilbeck PL; Burnap RL, Proton Transport Facilitating Water-oxidation: the Role of Second Sphere Ligands Surrounding the Catalytic Metal Cluster. Photosynth. Res 2013, 116, 215–229. [PubMed: 23975203]
397. Allen JP; Williams JC, The Evolutionary Pathway from Anoxygenic to Oxygenic Photosynthesis Examined by Comparison of the Properties of Photosystem II and Bacterial Reaction Centers. Photosynth. Res 2011, 107, 59–69. [PubMed: 20449659]
398. Geremia S; Di Costanzo L; Randaccio L; Engel DE; Lombardi A; Nastri F; DeGrado WF, Response of a Designed Metalloprotein to Changes in Metal Ion Coordination, Exogenous Ligands, and Active Site Volume Determined by X-ray Crystallography. J. Am. Chem. Soc 2005, 127, 17266–17276. [PubMed: 16332076]
399. DeGrado WF; Di Costanzo L; Geremia S; Lombardi A; Pavone V; Randaccio L, Sliding Helix and Change of Coordination Geometry in a Model Di-MnII Protein. Angew. Chem. Int. Ed 2003, 42, 417–420.
400. Marcus RA; Sutin N, Electron Transfers in Chemistry and Biology. Biochim Biophys Acta Rev Bioenerg 1985, 811, 265–322.
401. Beratan D; Onuchic J; JR W; Gray H, Electron-tunneling Pathways in Proteins. Science 1992, 258, 1740–1741. [PubMed: 1334572]
402. Moser CC; Keske JM; Warncke K; Farid RS; Dutton PL, Nature of Biological Electron Transfer. Nature 1992, 355, 796–802. [PubMed: 1311417]
403. Barynin VV; Whittaker JW, Manganese Catalase. In Handbook of Metalloproteins, 2004.
404. Whittaker JW, Non-heme Manganese Catalase – The ‘Other’ Catalase. Arch. Biochem. Biophys 2012, 525, 111–120. [PubMed: 22198285]
405. Barynin VV; Whittaker MM; Antonyuk SV; Lamzin VS; Harrison PM; Artymiuk PJ; Whittaker JW, Crystal Structure of Manganese Catalase from Lactobacillus plantarum. Structure 2001, 9, 725–738. [PubMed: 11587647]
406. Meyer J, Iron–sulfur Protein Folds, Iron–Sulfur Chemistry, and Evolution. J. Biol. Inorg. Chem 2008, 13, 157–170. [PubMed: 17992543]
407. Friedrich T; Steinmüller K; Weiss H, The Proton-pumping Respiratory Complex I of Bacteria and Mitochondria and its Homologue in Chloroplasts. FEBS Lett 1995, 367, 107–111. [PubMed: 7796904]
408. Ghirardi ML; Posewitz MC; Maness P-C; Dubini A; Yu J; Seibert M, Hydrogenases and Hydrogen Photoproduction in Oxygenic Photosynthetic Organisms. Annu. Rev. Plant Biol 2007, 58, 71–91. [PubMed: 17150028]
409. Fontecilla-Camps JC; Volbeda A; Cavazza C; Nicolet Y, Structure/Function Relationships of [NiFe]- and [FeFe]-Hydrogenases. Chem. Rev 2007, 107, 4273–4303. [PubMed: 17850165]
410. Lubitz W; Ogata H; Rüdiger O; Reijerse E, Hydrogenases. Chem. Rev 2014, 114, 4081–4148. [PubMed: 24655035]
411. Grimme RA; Lubner CE; Bryant DA; Golbeck JH, Photosystem I/Molecular Wire/Metal Nanoparticle Bioconjugates for the Photocatalytic Production of H_2. J. Am. Chem. Soc 2008, 130, 6308–6309. [PubMed: 18439011]
412. Ihara M; Nishihara H; Yoon K-S; Lenz O; Friedrich B; Nakamoto H; Kojima K; Honma D; Kamachi T; Okura I, Light-driven Hydrogen Production by a Hybrid Complex of a [NiFe]-Hydrogenase and the Cyanobacterial Photosystem I. Photochem. Photobiol 2006, 82, 676–682. [PubMed: 16542111]
413. Imlay JA, Iron-Sulphur Clusters and the Problem with Oxygen. Mol. Microbiol 2006, 59, 1073–1082. [PubMed: 16430685]
414. Lombardi A; Marasco D; Maglio O; Di Costanzo L; Nastri F; Pavone V, Miniaturized Metalloproteins: Application to Iron–Sulfur Proteins. PNAS 2000, 97, 11922–11927. [PubMed: 11050226]
415. Sieker LC; Stenkamp RE; Legall J, [14] Rubredoxin in Crystalline State. In Methods Enzymol, Academic Press: 1994; Vol. 243, pp 203–216. [PubMed: 7830611]
416. Dauter Z; Sieker LC; Wilson KS, Refinement of Rubredoxin from Desulfovibrio vulgaris at 1.0 A with and without Restraints. Acta Cryst. B 1992, 48, 42–59. [PubMed: 1616692]
417. Pavone V, On β-hairpin Classification. Int. J. Biol. Macromol 1988, 10, 238–240.

Author Manuscript

Author Manuscript

Author Manuscript

Author Manuscript

418. Pavone V; Gaeta G; Lombardi A; Nastri F; Maglio O; Isernia C; Saviano M, Discovering Protein Secondary Structures: Classification and Description of Isolated α-turns. Biopolymers 1996, 38, 705–721. [PubMed: 8652792]

419. Gunasekaran K; Gomathi L; Ramakrishnan C; Chandrasekhar J; Balaram P, Conformational Interconversions in Peptide β-turns: Analysis of Turns in Proteins and Computational Estimates of Barriers. J. Mol. Biol 1998, 284, 1505–1516. [PubMed: 9878367]

420. Gibney BR; Mulholland SE; Rabanal F; Dutton PL, Ferredoxin and Ferredoxin–heme Maquettes. PNAS 1996, 93, 15041–15046. [PubMed: 8986760]

421. Sakamoto S; Ueno A; Mihara H, Design and Synthesis of Haem-binding Peptides. Relationship Between Haem-binding Properties and Catalytic Activities. J. Chem. Soc., Perkin trans 2 1998, 2395–2404.

422. Nastri F; Lombardi A; D'Andrea LD; Sanseverino M; Maglio O; Pavone V, Miniaturized Hemoproteins. Peptide Sci 1998, 47, 5–22.

423. May SW; Kuo J-Y, Preparation and Properties of Cobalt(II) Rubredoxin. Biochemistry 1978, 17, 3333–3338. [PubMed: 687587]

424. Moura I; Teixeira M; Moura JJG; LeGall J, Spectroscopic Studies of Cobalt and Nickel Substituted Rubredoxin and Desulforedoxin. J. Inorg. Biochem 1991, 44, 127–139. [PubMed: 1664851]

425. Farinas E; Regan L, The de Novo Design of a Rubredoxin-like Fe Site. Protein Sci 1998, 7, 1939–1946. [PubMed: 9761474]

426. Benson DE; Wisz MS; Liu W; Hellinga HW, Construction of a Novel Redox Protein by Rational Design: Conversion of a Disulfide Bridge into a Mononuclear Iron−Sulfur Center. Biochemistry 1998, 37, 7070–7076. [PubMed: 9585516]

427. Berg JM; Merkle DL, On the Metal Ion Specificity of Zinc Finger Proteins. J. Am. Chem. Soc 1989, 111, 3759–3761.

428. Krizek BA; Merkle DL; Berg JM, Ligand Variation and Metal Ion Binding Specificity in Zinc Finger Peptides. Inorg. Chem 1993, 32, 937–940.

429. Im S-C; Sykes AG, Kinetic Studies on the Redox Reactions of Clostridium pasteurianum Rubredoxin. J. Chem. Soc., Dalton Trans 1996, 2219–2222.

430. Eidsness MK; Burden AE; Richie KA; Kurtz DM; Scott RA; Smith ET; Ichiye T; Beard B; Min T; Kang C, Modulation of the Redox Potential of the [Fe(SCys)4] Site in Rubredoxin by the Orientation of a Peptide Dipole. Biochemistry 1999, 38, 14803–14809. [PubMed: 10555962]

431. Nanda V; Rosenblatt MM; Osyczka A; Kono H; Getahun Z; Dutton PL; Saven JG; DeGrado WF, De Novo Design of a Redox-Active Minimal Rubredoxin Mimic. J. Am. Chem. Soc 2005, 127, 5804–5805. [PubMed: 15839675]

432. Cochran AG; Skelton NJ; Starovasnik MA, Tryptophan Zippers: Stable, Monomeric β-hairpins. PNAS 2001, 98, 5578–5583. [PubMed: 11331745]

433. Kono H; Saven JG, Statistical Theory for Protein Combinatorial Libraries. Packing Interactions, Backbone Flexibility, and the Sequence Variability of a Main-chain Structure. J. Mol. Biol 2001, 306, 607–628. [PubMed: 11178917]

434. Tebo AG; Pinter TBJ; García-Serres R; Speelman AL; Tard C; Sénéque O; Blondin G; Latour J-M; Penner-Hahn J; Lehnert N, et al. , Development of a Rubredoxin-Type Center Embedded in a de Novo-Designed Three-Helix Bundle. Biochemistry 2018, 57, 2308–2316. [PubMed: 29561598]

435. Tebo AG; Hemmingsen L; Pecoraro VL, Variable Primary Coordination Environments of Cd(II) Binding to Three Helix Bundles Provide a Pathway for Rapid Metal Exchange. Metallomics 2015, 7, 1555–1561. [PubMed: 26503746]

436. Rivoal JC; Briat B; Cammack R; Hall DO; Rao KK; Douglas IN; Thomson AJ, The Low Temperature Magnetic Circular Dichroism Spectra of Iron-Sulphur Proteins I. Oxidised Rubredoxin. Biochim. Biophys. Acta, Protein Struct 1977, 493, 122–131.

437. Oganesyan VS; George SJ; Cheesman MR; Thomson AJ, A Novel, General Method of Analyzing Magnetic Circular Dichroism Spectra and Magnetization Curves of High-spin Metal Ions: Application to the Protein Oxidized Rubredoxin, Desulfovibrio gigas. J. Chem. Phys 1999, 110, 762–777.

Author Manuscript

Author Manuscript

Author Manuscript

Author Manuscript

438. George GN; Pickering IJ; Prince RC; Zhou ZH; Adams MWW, X-ray Absorption Spectroscopy of Pyrococcus furiosus Rubredoxin. J. Biol. Inorg. Chem 1996, 1, 226–230.

439. Wegner P; Bever M; Schünemann V; Trautwein AX; Schmidt C; Bönisch H; Gnida M; Meyer-Klaucke W, Iron–Sulfur Proteins Investigated by EPR-, Mössbauer- and EXAFS-Spectroscopy. Hyperfine Interact 2004, 156, 293–298.

440. Lovenberg W; Sobel BE, Rubredoxin: a New Electron Transfer Protein from Clostridium pasteurianum. PNAS 1965, 54, 193–199. [PubMed: 5216351]

441. Bönisch H; Schmidt CL; Bianco P; Ladenstein R, Ultrahigh-resolution Study on Pyrococcus abyssi Rubredoxin: II. Introduction of an O–H···Sγ–Fe Hydrogen Bond Increased the Reduction Potential by 65 mV. J. Biol. Inorg. Chem 2007, 12, 1163–1171. [PubMed: 17712580]

442. Moura I; Xavier AV; Cammack R; Bruschi M; Le Gall J, A Comparative Spectroscopic Study of Two Non-haem Iron Proteins Lacking Labile Sulphide from Desulphovibrio gigas. Biochim. Biophys. Acta, Protein Struct 1978, 533, 156–162.

443. Jenney FE; Adams MWW, [5] Rubredoxin from Pyrococcus furiosus. In Methods Enzymol, Academic Press: 2001; Vol. 334, pp 45–55. [PubMed: 11398483]

444. Tebo A; Quaranta A; Pecoraro VL; Aukauloo A, Enhanced Photoinduced Electron Transfer Through a Tyrosine Relay in a de Novo Designed Protein Scaffold Bearing a Photoredox Unit and a FeIIS4 Site. ChemPhotoChem 2021, 5, 665–668.

445. Plegaria JS; Herrero C; Quaranta A; Pecoraro VL, Electron Transfer Activity of a de Novo Designed Copper Center in a Three-helix Bundle Fold. Biochim. Biophys. Acta, Bioenerg 2016, 1857, 522–530.

446. Tebo AG; Quaranta A; Herrero C; Pecoraro VL; Aukauloo A, Intramolecular Photogeneration of a Tyrosine Radical in a Designed Protein. ChemPhotoChem 2017, 1, 89–92. [PubMed: 29046892]

447. Barry BA, Proton Coupled Electron Transfer and Redox Active Tyrosines in Photosystem II. J Photochem Photobiol B 2011, 104, 60–71. [PubMed: 21419640]

448. Dempsey JL; Winkler JR; Gray HB, Proton-Coupled Electron Flow in Protein Redox Machines. Chem. Rev 2010, 110, 7024–7039. [PubMed: 21082865]

449. Tommos C; Skalicky JJ; Pilloud DL; Wand AJ; Dutton PL, De Novo Proteins as Models of Radical Enzymes. Biochemistry 1999, 38, 9495–9507. [PubMed: 10413527]

450. Minoux H; Chipot C, Cation−π Interactions in Proteins: Can Simple Models Provide an Accurate Description? J. Am. Chem. Soc 1999, 121, 10366–10372.

451. Dai Q-H; Tommos C; Fuentes EJ; Blomberg MRA; Dutton PL; Wand AJ, Structure of a de Novo Designed Protein Model of Radical Enzymes. J. Am. Chem. Soc 2002, 124, 10952–10953. [PubMed: 12224922]

452. Berry BW; Martínez-Rivera MC; Tommos C, Reversible Voltammograms and a Pourbaix Diagram for a Protein Tyrosine Radical. PNAS 2012, 109, 9739–9743. [PubMed: 22675121]

453. Glover SD; Jorge C; Liang L; Valentine KG; Hammarström L; Tommos C, Photochemical Tyrosine Oxidation in the Structurally Well-Defined α3Y Protein: Proton-Coupled Electron Transfer and a Long-Lived Tyrosine Radical. J. Am. Chem. Soc 2014, 136, 14039–14051. [PubMed: 25121576]

454. Campagna S; Puntoriero F; Nastasi F; Bergamini G; Balzani V, Photochemistry and Photophysics of Coordination Compounds: Ruthenium. In Photochemistry and Photophysics of Coordination Compounds I, Balzani V; Campagna S, Eds. Springer Berlin Heidelberg: Berlin, Heidelberg, 2007; pp 117–214.

455. Xiao Z; Lavery MJ; Ayhan M; Scrofani SDB; Wilce MCJ; Guss JM; Tregloan PA; George GN; Wedd AG, The Rubredoxin from Clostridium pasteurianum: Mutation of the Iron Cysteinyl Ligands to Serine. Crystal and Molecular Structures of Oxidized and Dithionite-Treated Forms of the Cys42Ser Mutant. J. Am. Chem. Soc 1998, 120, 4135–4150.

456. Burroughs AM; Balaji S; Iyer LM; Aravind L, Small but Versatile: the Extraordinary Functional and Structural Diversity of the β-grasp Fold. Biol. Direct 2007, 2, 18. [PubMed: 17605815]

457. Cochran FV; Wu SP; Wang W; Nanda V; Saven JG; Therien MJ; DeGrado WF, Computational De Novo Design and Characterization of a Four-Helix Bundle Protein that Selectively Binds a Nonbiological Cofactor. J. Am. Chem. Soc 2005, 127, 1346–1347. [PubMed: 15686346]

Author Manuscript Author Manuscript Author Manuscript Author Manuscript

458. McAllister KA; Zou H; Cochran FV; Bender GM; Senes A; Fry HC; Nanda V; Keenan PA; Lear JD; Saven JG, et al. , Using α-Helical Coiled-Coils to Design Nanostructured Metalloporphyrin Arrays. J. Am. Chem. Soc 2008, 130, 11921–11927. [PubMed: 18710226]

459. Grzyb J; Xu F; Weiner L; Reijerse EJ; Lubitz W; Nanda V; Noy D, De Novo Design of a Non-natural Fold for an Iron–Sulfur Protein: Alpha-helical Coiled-coil with a Four-iron Four-sulfur Cluster Binding Site in its Central Core. Biochim. Biophys. Acta, Bioenerg 2010, 1797, 406–413.

460. Han GW; Yang X-L; McMullan D; Chong YE; Krishna SS; Rife CL; Weekes D; Brittain SM; Abdubek P; Ambing E, et al. , Structure of a Tryptophanyl-tRNA Synthetase Containing an Iron-Sulfur Cluster. Acta Cryst. F 2010, 66, 1326–1334.

461. Scott MP; Biggins J, Introduction of a [4Fe-4S (S-cys)4]+1,+2 Iron-Sulfur Center into a Four-α helix Protein Using Design Parameters from the Domain of the Fx Cluster in the Photosystem I Reaction Center. Protein Sci 1997, 6, 340–346. [PubMed: 9041635]

462. Sow T-C; Pedersen MV; Christensen HEM; Ooi B-L, Total Synthesis of a Miniferredoxin. Biochem. Biophys. Res. Commun 1996, 223, 360–364. [PubMed: 8670287]

463. Grzyb J; Xu F; Nanda V; Łuczkowska R; Reijerse E; Lubitz W; Noy D, Empirical and Computational Design of Iron-Sulfur Cluster Proteins. Biochim. Biophys. Acta, Bioenerg 2012, 1817, 1256–1262.

464. Kennedy ML; Gibney BR, Proton Coupling to [4Fe-4S]2+/+ and [4Fe-4Se]2+/+ Oxidation and Reduction in a Designed Protein. J. Am. Chem. Soc 2002, 124, 6826–6827. [PubMed: 12059194]

465. Antonkine ML; Koay MS; Epel B; Breitenstein C; Gopta O; Gärtner W; Bill E; Lubitz W, Synthesis and Characterization of de Novo Designed Peptides Modelling the Binding Sites of [4Fe–4S] Clusters in Photosystem I. Biochim. Biophys. Acta, Bioenerg 2009, 1787, 995–1008.

466. Ogihara NL; Ghirlanda G; Bryson JW; Gingery M; DeGrado WF; Eisenberg D, Design of Three-dimensional Domain-swapped Dimers and Fibrous Oligomers. PNAS 2001, 98, 1404–1409. [PubMed: 11171963]

467. Eck RV; Dayhoff MO, Evolution of the Structure of Ferredoxin Based on Living Relics of Primitive Amino Acid Sequences. Science 1966, 152, 363–366. [PubMed: 17775169]

468. Sweeney WV; Rabinowitz JC, Proteins Containing 4Fe-4S Clusters: An Overview. Annu. Rev. Biochem 1980, 49, 139–161. [PubMed: 6250442]

469. Jin Z; Heinnickel M; Krebs C; Shen G; Golbeck JH; Bryant DA, Biogenesis of Iron-Sulfur Clusters in Photosystem I: Holo-Nfua from the Cyanobacterium synechococcus Sp. Pcc 7002 Rapidly and Efficiently Transfers [4fe-4s] Clusters to Apo-Psac in Vitro. J. Biol. Chem 2008, 283, 28426–28435. [PubMed: 18694929]

470. Stephens PJ; Thomson AJ; Dunn JBR; Keiderling TA; Rawlings J; Rao KK; Hall DO, Circular Dichroism and Magnetic Circular Dichroism of Iron-Sulfur Proteins. Biochemistry 1978, 17, 4770–4778. [PubMed: 728385]

471. Milov AD; Maryasov AG; Tsvetkov YD, Pulsed Electron Double Resonance (PELDOR) and its Applications in Free-radicals Research. Appl. Magn. Reson 1998, 15, 107–143.

472. Koay MS; Antonkine ML; Gärtner W; Lubitz W, Modelling Low-Potential [Fe4S4] Clusters in Proteins. Chem. Biodivers 2008, 5, 1571–1587. [PubMed: 18729093]

473. Roy A; Sommer DJ; Schmitz RA; Brown CL; Gust D; Astashkin A; Ghirlanda G, A de Novo Designed 2[4Fe-4S] Ferredoxin Mimic Mediates Electron Transfer. J. Am. Chem. Soc 2014, 136, 17343–17349. [PubMed: 25437708]

474. Mathews R; Charlton S; Sands RH; Palmer G, On the Nature of the Spin Coupling between the Iron-Sulfur Clusters in the Eight-Iron Ferredoxins. J. Biol. Chem 1974, 249, 4326–4328. [PubMed: 4368981]

475. Torres RA; Lovell T; Noodleman L; Case DA, Density Functional and Reduction Potential Calculations of Fe4S4 Clusters. J. Am. Chem. Soc 2003, 125, 1923–1936. [PubMed: 12580620]

476. Smith ET; Feinberg BA, Redox Properties of Several Bacterial Ferredoxins Using Square Wave Voltammetry. J. Biol. Chem 1990, 265, 14371–14376. [PubMed: 2387857]

477. Mancini JA; Sheehan M; Kodali G; Chow BY; Bryant DA; Dutton PL; Moser CC, De Novo Synthetic Biliprotein Design, Assembly and Excitation Energy Transfer. J R Soc Interface 2018, 15, 20180021. [PubMed: 29618529]

Author Manuscript Author Manuscript Author Manuscript Author Manuscript

478. Jagilinki BP; Ilic S; Trncik C; Tyryshkin AM; Pike DH; Lubitz W; Bill E; Einsle O; Birrell JA; Akabayov B, et al. , In Vivo Biogenesis of a de Novo Designed Iron–Sulfur Protein. ACS Synth. Biol 2020, 9, 3400–3407. [PubMed: 33186033]

479. Clark DP, The Fermentation Pathways of Escherichia coli. FEMS Microbiol. Rev 1989, 5, 223–34. [PubMed: 2698228]

480. Kuchenreuther JM; Grady-Smith CS; Bingham AS; George SJ; Cramer SP; Swartz JR, High-Yield Expression of Heterologous [FeFe] Hydrogenases in Escherichia coli. PLOS ONE 2010, 5, e15491. [PubMed: 21124800]

481. Schönheit P; Wäscher C; Thauer RK, A Rapid Procedure for the Purification of Ferredoxin from Clostridia Using Polyethyleneimine. FEBS Lett 1978, 89, 219–222. [PubMed: 658409]

482. Hingorani KS; Gierasch LM, Comparing Protein Folding in Vitro and in Vivo: Foldability Meets the Fitness Challenge. Curr. Opin. Struct. Biol 2014, 24, 81–90. [PubMed: 24434632]

483. Christiansen A; Wang Q; Cheung MS; Wittung-Stafshede P, Effects of Macromolecular Crowding Agents on Protein Folding in Vitro and in Silico. Biophys. Rev 2013, 5, 137–145. [PubMed: 28510156]

484. Roche B; Aussel L; Ezraty B; Mandin P; Py B; Barras F, Iron/Sulfur Proteins Biogenesis in Prokaryotes: Formation, Regulation and Diversity. Biochim. Biophys. Acta, Bioenerg 2013, 1827, 455–469.

485. Solomon EI, Spectroscopic Methods in Bioinorganic Chemistry: Blue to Green to Red Copper Sites. Inorg. Chem 2006, 45, 8012–8025. [PubMed: 16999398]

486. Solomon EI; Hadt RG, Recent Advances in Understanding Blue Copper Proteins. Coord. Chem. Rev 2011, 255, 774–789.

487. Scott RA; Hahn JE; Doniach S; Freeman HC; Hodgson KO, Polarized X-ray Absorption Spectra of Oriented Plastocyanin Single Crystals. Investigation of Methionine-Copper Coordination. J. Am. Chem. Soc 1982, 104, 5364–5369.

488. Penfield KW; Gay RR; Himmelwright RS; Eickman NC; Norris VA; Freeman HC; Solomon EI, Spectroscopic Studies on Plastocyanin Single Crystals: a Detailed Electronic Structure Determination of the Blue Copper Active Site. J. Am. Chem. Soc 1981, 103, 4382–4388.

489. Malmström BG; Reinhammar B; Vänngård T, The State of Copper in Stellacyanin and Laccase from the Lacquer Tree Rhus vernicifera. Biochim. Biophys. Acta, Bioenerg 1970, 205, 48–57.

490. DeBeer S; Randall DW; Nersissian AM; Valentine JS; Hedman B; Hodgson KO; Solomon EI, X-ray Absorption Edge and EXAFS Studies of the Blue Copper Site in Stellacyanin: Effects of Axial Amide Coordination. J. Phys. Chem. B 2000, 104, 10814–10819.

491. LaCroix LB; Shadle SE; Wang Y; Averill BA; Hedman B; Hodgson KO; Solomon EI, Electronic Structure of the Perturbed Blue Copper Site in Nitrite Reductase: Spectroscopic Properties, Bonding, and Implications for the Entatic/Rack State. J. Am. Chem. Soc 1996, 118, 7755–7768.

492. Tocheva EI; Rosell FI; Mauk AG; Murphy MEP, Side-On Copper-Nitrosyl Coordination by Nitrite Reductase. Science 2004, 304, 867–870. [PubMed: 15131305]

493. Arciero DM; Pierce BS; Hendrich MP; Hooper AB, Nitrosocyanin, a Red Cupredoxin-like Protein from Nitrosomonas europaea. Biochemistry 2002, 41, 1703–1709. [PubMed: 11827513]

494. Basumallick L; Sarangi R; DeBeer George S; Elmore B; Hooper AB; Hedman B; Hodgson KO; Solomon EI, Spectroscopic and Density Functional Studies of the Red Copper Site in Nitrosocyanin: Role of the Protein in Determining Active Site Geometric and Electronic Structure. J. Am. Chem. Soc 2005, 127, 3531–3544. [PubMed: 15755175]

495. Slutter CE; Sanders D; Wittung P; Malmström BG; Aasa R; Richards JH; Gray HB; Fee JA, Water-Soluble, Recombinant CuA-Domain of the Cytochrome ba3 Subunit II from Thermus thermophilus. Biochemistry 1996, 35, 3387–3395. [PubMed: 8639488]

496. Tsukihara T; Aoyama H; Yamashita E; Tomizaki T; Yamaguchi H; Shinzawa-Itoh K; Nakashima R; Yaono R; Yoshikawa S, Structures of Metal Sites of Oxidized Bovine Heart Cytochrome c Oxidase at 2.8 A. Science 1995, 269, 1069–74. [PubMed: 7652554]

497. Wilmanns M; Lappalainen P; Kelly M; Sauer-Eriksson E; Saraste M, Crystal Structure of the Membrane-Exposed Domain from a Respiratory Quinol Oxidase Complex with an Engineered Dinuclear Copper Center. PNAS 1995, 92, 11955–11959. [PubMed: 8618822]

Author Manuscript Author Manuscript Author Manuscript Author Manuscript

498. Robinson H; Ang MC; Gao Y-G; Hay MT; Lu Y; Wang AHJ, Structural Basis of Electron Transfer Modulation in the Purple CuA Center. Biochemistry 1999, 38, 5677–5683. [PubMed: 10231517]

499. Farrar JA; Neese F; Lappalainen P; Kroneck PMH; Saraste M; Zumft WG; Thomson AJ, The Electronic Structure of CuA: A Novel Mixed-Valence Dinuclear Copper Electron-Transfer Center. J. Am. Chem. Soc 1996, 118, 11501–11514.

500. Riester J; Zumft WG; Kroneck PMH, Nitrous Oxide Reductase from Pseudomonas stutzeri. Eur. J. Biochem 1989, 178, 751–762. [PubMed: 2536326]

501. Schnepf R; Haehnel W; Wieghardt K; Hildebrandt P, Spectroscopic Identification of Different Types of Copper Centers Generated in Synthetic Four-Helix Bundle Proteins. J. Am. Chem. Soc 2004, 126, 14389–14399. [PubMed: 15521758]

502. Mutter M; Altmann E; Altmann K-H; Hersperger R; Koziej P; Nebel K; Tuchsecherer G; Vuilleumier S; Gremlich H-U; Müller K, The Construction of New Proteins. Part III. Artificial Folding Units by Assembly of Amphiphilic Secondary Structures on a Template. Helv. Chim. Acta 1988, 71, 835–847.

503. Rau HK; DeJonge N; Haehnel W, Combinatorial Synthesis of Four-Helix Bundle Hemoproteins for Tuning of Cofactor Properties. Angew. Chem. Int. Ed. Engl 2000, 39, 250–253. [PubMed: 10649392]

504. Schnepf R; Hörth P; Bill E; Wieghardt K; Hildebrandt P; Haehnel W, De Novo Design and Characterization of Copper Centers in Synthetic Four-Helix-Bundle Proteins. J. Am. Chem. Soc 2001, 123, 2186–2195. [PubMed: 11456864]

505. Andrew CR; Fraczkiewicz R; Czernuszewicz RS; Lappalainen P; Saraste M; Sanders-Loehr J, Identification and Description of Copper-Thiolate Vibrations in the Dinuclear CuA Site of Cytochrome c Oxidase. J. Am. Chem. Soc 1996, 118, 10436–10445.

506. Andrew CR; Sanders-Loehr J, Copper−Sulfur Proteins: Using Raman Spectroscopy to Predict Coordination Geometry. Acc. Chem. Res 1996, 29, 365–372.

507. Palmer AE; Randall DW; Xu F; Solomon EI, Spectroscopic Studies and Electronic Structure Description of the High Potential Type 1 Copper Site in Fungal Laccase: Insight into the Effect of the Axial Ligand. J. Am. Chem. Soc 1999, 121, 7138–7149.

508. Andrew CR; Yeom H; Valentine JS; Karlsson BG; van Pouderoyen G; Canters GW; Loehr TM; Sanders-Loehr J; Bonander N, Raman Spectroscopy as an Indicator of Cu-S Bond Length in Type 1 and Type 2 Copper Cysteinate Proteins. J. Am. Chem. Soc 1994, 116, 11489–11498.

509. Koebke KJ; Alfaro VS; Pinter TBJ; Deb A; Lehnert N; Tard C; Penner-Hahn JE; Pecoraro VL, Traversing the Red–Green–Blue Color Spectrum in Rationally Designed Cupredoxins. J. Am. Chem. Soc 2020, 142, 15282–15294. [PubMed: 32786767]

510. Shiga D; Nakane D; Inomata T; Masuda H; Oda M; Noda M; Uchiyama S; Fukui K; Takano Y; Nakamura H, et al. , The Effect of the Side Chain Length of Asp and Glu on Coordination Structure of Cu2+ in a de Novo Designed Protein. Biopolymers 2009, 91, 907–916. [PubMed: 19598226]

511. Shiga D; Nakane D; Inomata T; Funahashi Y; Masuda H; Kikuchi A; Oda M; Noda M; Uchiyama S; Fukui K, et al. , Creation of a Type 1 Blue Copper Site within a de Novo Coiled-Coil Protein Scaffold. J. Am. Chem. Soc 2010, 132, 18191–18198. [PubMed: 21126081]

512. Daugherty RG; Wasowicz T; Gibney BR; DeRose VJ, Design and Spectroscopic Characterization of Peptide Models for the Plastocyanin Copper-Binding Loop. Inorg. Chem 2002, 41, 2623–2632. [PubMed: 12005485]

513. Shiga D; Hamano Y; Kamei M; Funahashi Y; Masuda H; Sakaguchi M; Ogura T; Tanaka T, Tuning the Geometries of a de Novo Blue Copper Protein by Axial Interactions. J. Biol. Inorg. Chem 2012, 17, 1025–1031. [PubMed: 22752182]

514. Den Blaauwen T; Hoitink CWG; Canters GW; Han J; Loehr TM; Sanders-Loehr J, Resonance Raman Spectroscopy of the Azurin His117Gly Mutant. Interconversion of Type 1 and Type 2 Copper Sites Through Exogenous Ligands. Biochemistry 1993, 32, 12455–12464. [PubMed: 8241136]

Author Manuscript Author Manuscript Author Manuscript Author Manuscript

515. Den Blaauwen T; Canters GW, Creation of Type-1 and Type-2 Copper Sites by Addition of Exogenous Ligands to the Pseudomonas aeruginosa Azurin His117Gly Mutant. J. Am. Chem. Soc 1993, 115, 1121–1129.

516. Koch M; Velarde M; Harrison MD; Echt S; Fischer M; Messerschmidt A; Dennison C, Crystal Structures of Oxidized and Reduced Stellacyanin from Horseradish Roots. J. Am. Chem. Soc 2005, 127, 158–166. [PubMed: 15631465]

517. Li H; Webb SP; Ivanic J; Jensen JH, Determinants of the Relative Reduction Potentials of Type-1 Copper Sites in Proteins. J. Am. Chem. Soc 2004, 126, 8010–8019. [PubMed: 15212551]

518. Shiga D; Funahashi Y; Masuda H; Kikuchi A; Noda M; Uchiyama S; Fukui K; Kanaori K; Tajima K; Takano Y, et al. , Creation of a Binuclear Purple Copper Site within a de Novo Coiled-Coil Protein. Biochemistry 2012, 51, 7901–7907. [PubMed: 22989113]

519. Hay M; Richards JH; Lu Y, Construction and Characterization of an Azurin Analog for the Purple Copper Site in Cytochrome c Oxidase. PNAS 1996, 93, 461–464. [PubMed: 8552661]

520. Antholine WE; Kastrau DHW; Steffens GCM; Buse G; Zumft WG; Kroneck PMH, A Comparative EPR Investigation of the Multicopper Proteins Nitrous-oxide Reductase and Cytochrome c Oxidase. Eur. J. Biochem 1992, 209, 875–881. [PubMed: 1330560]

521. Malmström BG; Aasa R, The Nature of the CuA Center in Cytochrome c Oxidase. FEBS Lett 1993, 325, 49–52. [PubMed: 8390373]

522. Rabanal F; DeGrado WF; Dutton PL, Toward the Synthesis of a Photosynthetic Reaction Center Maquette: A Cofacial Porphyrin Pair Assembled between Two Subunits of a Synthetic Four-Helix Bundle Multiheme Protein. J. Am. Chem. Soc 1996, 118, 473–474.

523. Plegaria JS; Duca M; Tard C; Friedlander TJ; Deb A; Penner-Hahn JE; Pecoraro VL, De Novo Design and Characterization of Copper Metallopeptides Inspired by Native Cupredoxins. Inorg. Chem 2015, 54, 9470–9482. [PubMed: 26381361]

524. Koebke KJ; Ruckthong L; Meagher JL; Mathieu E; Harland J; Deb A; Lehnert N; Policar C; Tard C; Penner-Hahn JE, et al. , Clarifying the Copper Coordination Environment in a de Novo Designed Red Copper Protein. Inorg. Chem 2018, 57, 12291–12302. [PubMed: 30226758]

525. Karlsson BG; Tsai L-C; Nar H; Sanders-Loehr J; Bonander N; Langer V; Sjölin L, X-ray Structure Determination and Characterization of the Pseudomonas aeruginosa Azurin Mutant Met121Glu. Biochemistry 1997, 36, 4089–4095. [PubMed: 9100002]

526. Hall JF; Kanbi LD; Strange RW; Hasnain SS, Role of the Axial Ligand in Type 1 Cu Centers Studied by Point Mutations of Met148 in Rusticyanin. Biochemistry 1999, 38, 12675–12680. [PubMed: 10504237]

527. DeBeer George S; Basumallick L; Szilagyi RK; Randall DW; Hill MG; Nersissian AM; Valentine JS; Hedman B; Hodgson KO; Solomon EI, Spectroscopic Investigation of Stellacyanin Mutants: Axial Ligand Interactions at the Blue Copper Site. J. Am. Chem. Soc 2003, 125, 11314–11328. [PubMed: 16220954]

528. Basumallick L; Szilagyi RK; Zhao Y; Shapleigh JP; Scholes CP; Solomon EI, Spectroscopic Studies of the Met182Thr Mutant of Nitrite Reductase: Role of the Axial Ligand in the Geometric and Electronic Structure of Blue and Green Copper Sites. J. Am. Chem. Soc 2003, 125, 14784–14792. [PubMed: 14640653]

529. Di Bilio AJ; Hill MG; Bonander N; Karlsson BG; Villahermosa RM; Malmström BG; Winkler JR; Gray HB, Reorganization Energy of Blue Copper: Effects of Temperature and Driving Force on the Rates of Electron Transfer in Ruthenium- and Osmium-Modified Azurins. J. Am. Chem. Soc 1997, 119, 9921–9922.

530. Skov LK; Pascher T; Winkler JR; Gray HB, Rates of Intramolecular Electron Transfer in Ru(bpy)2(im)(His83)-Modified Azurin Increase below 220 K. J. Am. Chem. Soc 1998, 120, 1102–1103.

531. Sigfridsson K; Ejdebäck M; Sundahl M; Hansson Ö, Electron Transfer in Ruthenium-Modified Spinach Plastocyanin Mutants. Arch. Biochem. Biophys 1998, 351, 197–206. [PubMed: 9514646]

532. McCleskey TM; Winkler JR; Gray HB, Driving-Force Effects on the Rates of Bimolecular Electron-Transfer Reactions. J. Am. Chem. Soc 1992, 114, 6935–6937.

Author Manuscript Author Manuscript Author Manuscript Author Manuscript

533. Malmström BG, Rack-induced Bonding in Blue-copper Proteins. Eur. J. Biochem 1994, 223, 711–718. [PubMed: 8055947]

534. Wittung-Stafshede P; Hill MG; Gomez E; Di Bilio AJ; Karlsson BG; Leckner J; Winkler JR; Gray HB; Malmström BG, Reduction Potentials of Blue and Purple Copper Proteins in Their Unfolded States: a Closer Look at Rack-induced Coordination. J. Biol. Inorg. Chem 1998, 3, 367–370.

535. Su JY; Hodges RS; Kay CM, Effect of Chain Length on the Formation and Stability of Synthetic α-Helical Coiled Coils. Biochemistry 1994, 33, 15501–15510. [PubMed: 7803412]

536. Tian S; Liu J; Cowley RE; Hosseinzadeh P; Marshall NM; Yu Y; Robinson H; Nilges MJ; Blackburn NJ; Solomon EI, et al. , Reversible S-nitrosylation in an Engineered Azurin. Nat. Chem 2016, 8, 670–677. [PubMed: 27325093]

537. Den Blaauwen T; Van de Kamp M; Canters GW, Type I and II Copper Sites Obtained by External Addition of Ligands to a His117Gly Azurin Mutant. J. Am. Chem. Soc 1991, 113, 5050–5052.

538. van Pouderoyen G; Andrew CR; Loehr TM; Sanders-Loehr J; Mazumdar S; Hill HAO; Canters GW, Spectroscopic and Mechanistic Studies of Type-1 and Type-2 Copper Sites in Pseudomonas aeruginosa Azurin As Obtained by Addition of External Ligands to Mutant His46Gly. Biochemistry 1996, 35, 1397–1407. [PubMed: 8634269]

539. Fernández CO; Sannazzaro AI; Vila AJ, Alkaline Transition of Rhus vernicifera Stellacyanin, an Unusual Blue Copper Protein. Biochemistry 1997, 36, 10566–10570. [PubMed: 9265638]

540. Abdelhamid RF; Obara Y; Kohzuma T, Alkaline Transition of Pseudoazurin Met16X Mutant Proteins: Protein Stability Influenced by the Substitution of Met16 in the Second Sphere Coordination. J. Inorg. Biochem 2008, 102, 1373–1379. [PubMed: 18343503]

541. Groeneveld CM; Canters GW; Aasa R; Reinhammar B, EPR of Azurins from Pseudomonas aeruginosa and Alcaligenes denitrificans Demonstrates pH-Dependence of the Copper-site Geometry in Pseudomonas aeruginosa protein. J. Inorg. Biochem 1987, 31, 143–154. [PubMed: 2828541]

542. Saito Y; Oikawa M; Nakazawa H; Niide T; Kameda T; Tsuda K; Umetsu M, Machine-Learning-Guided Mutagenesis for Directed Evolution of Fluorescent Proteins. ACS Synth. Biol 2018, 7, 2014–2022. [PubMed: 30103599]

543. Yang KK; Wu Z; Arnold FH, Machine-Learning-Guided Directed Evolution for Protein Engineering. Nat. Methods 2019, 16, 687–694. [PubMed: 31308553]

544. Foster AW; Osman D; Robinson NJ, Metal Preferences and Metallation. J. Biol. Chem 2014, 289, 28095–28103. [PubMed: 25160626]

545. Maret W, Metalloproteomics, Metalloproteomes, and the Annotation of Metalloproteins. Metallomics 2009, 2, 117–125. [PubMed: 21069142]

Author Manuscript

Author Manuscript

Author Manuscript

Author Manuscript

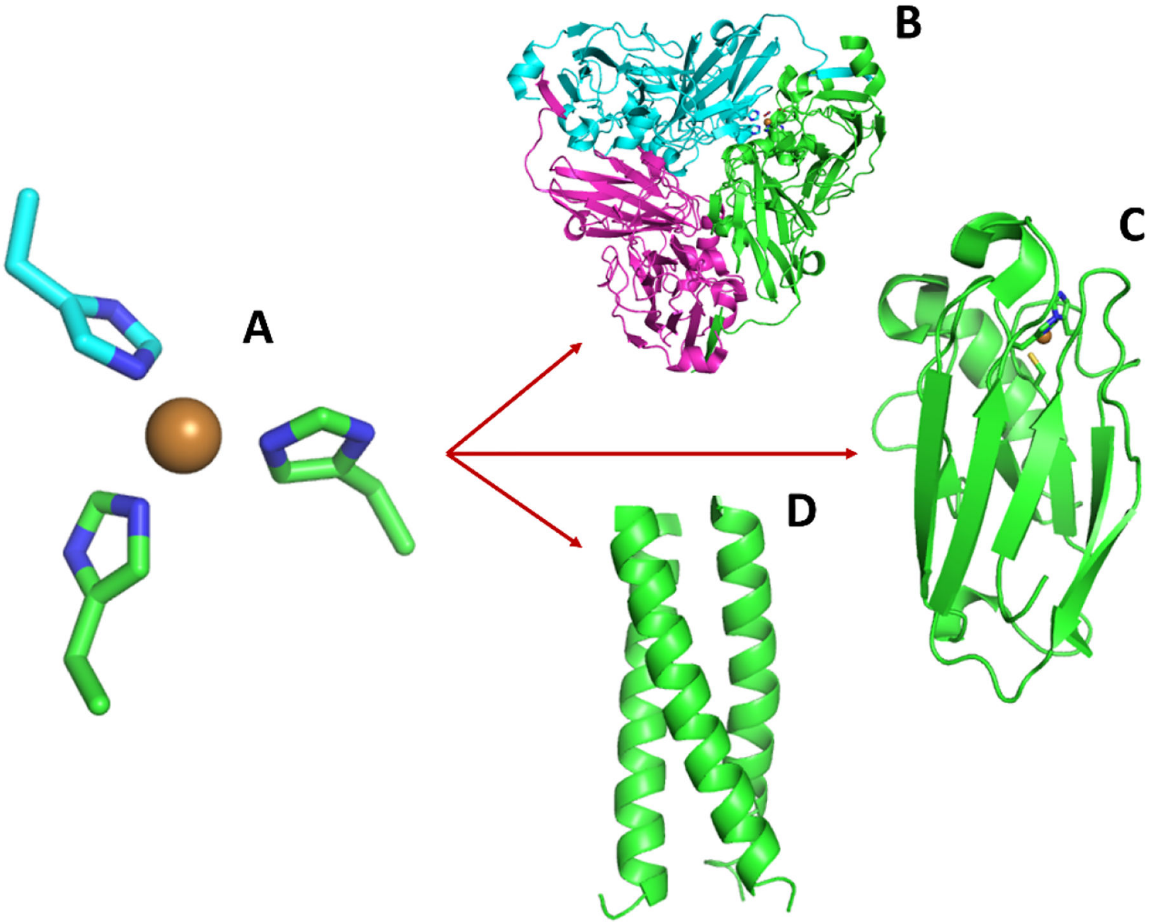

Figure 1:

Illustration of (**A**) the primary coordination sphere of CuNiR's enzymatic site with different strategies used to investigate its properties within proteins: (**B**) reengineering of CuNiR itself (1SJM) to eliminate the secondary sphere, (**C**) native protein engineering of azurin (4AZU) to incorporate an enzymatic site, and (**D**) de novo design of a $CuHis_3$ site within a generic protein fold (3PBJ).

Author Manuscript

Author Manuscript

Author Manuscript

Author Manuscript

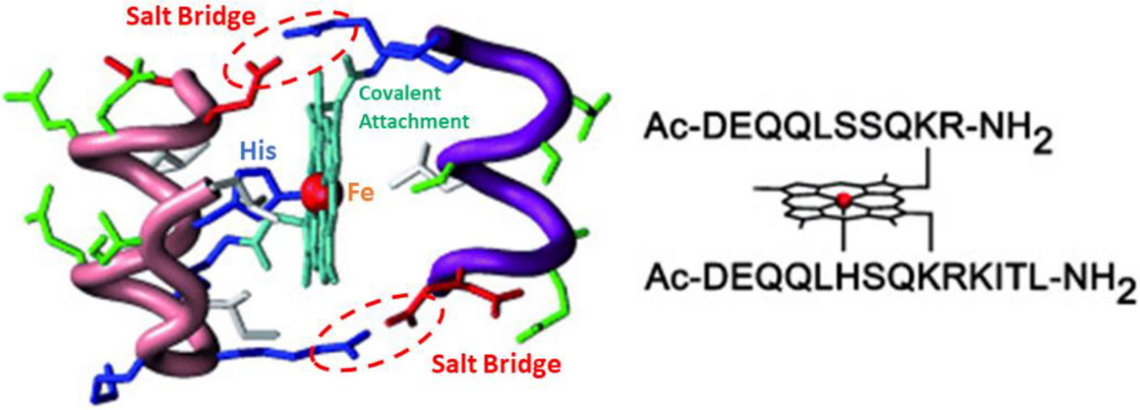

Figure 2:

Fe(III)-Mimochrome represented as a model structure along with its amino acid sequence. Adapted with permission from ref 24. Copyright 2011 Wiley-VCH Verlag GmbH & Co.

Author Manuscript
Author Manuscript
Author Manuscript
Author Manuscript

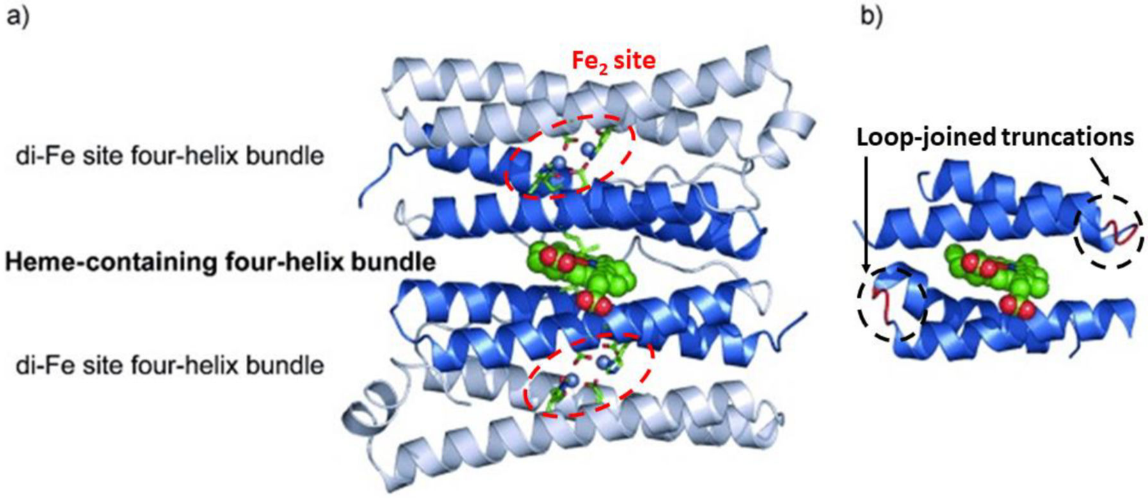

Figure 3:

(**A**) Dimeric subunit of Bacterioferritin [PDB 1BRF] with heme group represented as spheres and coordinating residues represented as sticks. (**B**) Minimal structural subunit used for the design of MP3. Adapted with permission from ref 39. Copyright 2012 Wiley-VCH Verlag GmbH & Co.

Author Manuscript Author Manuscript Author Manuscript Author Manuscript

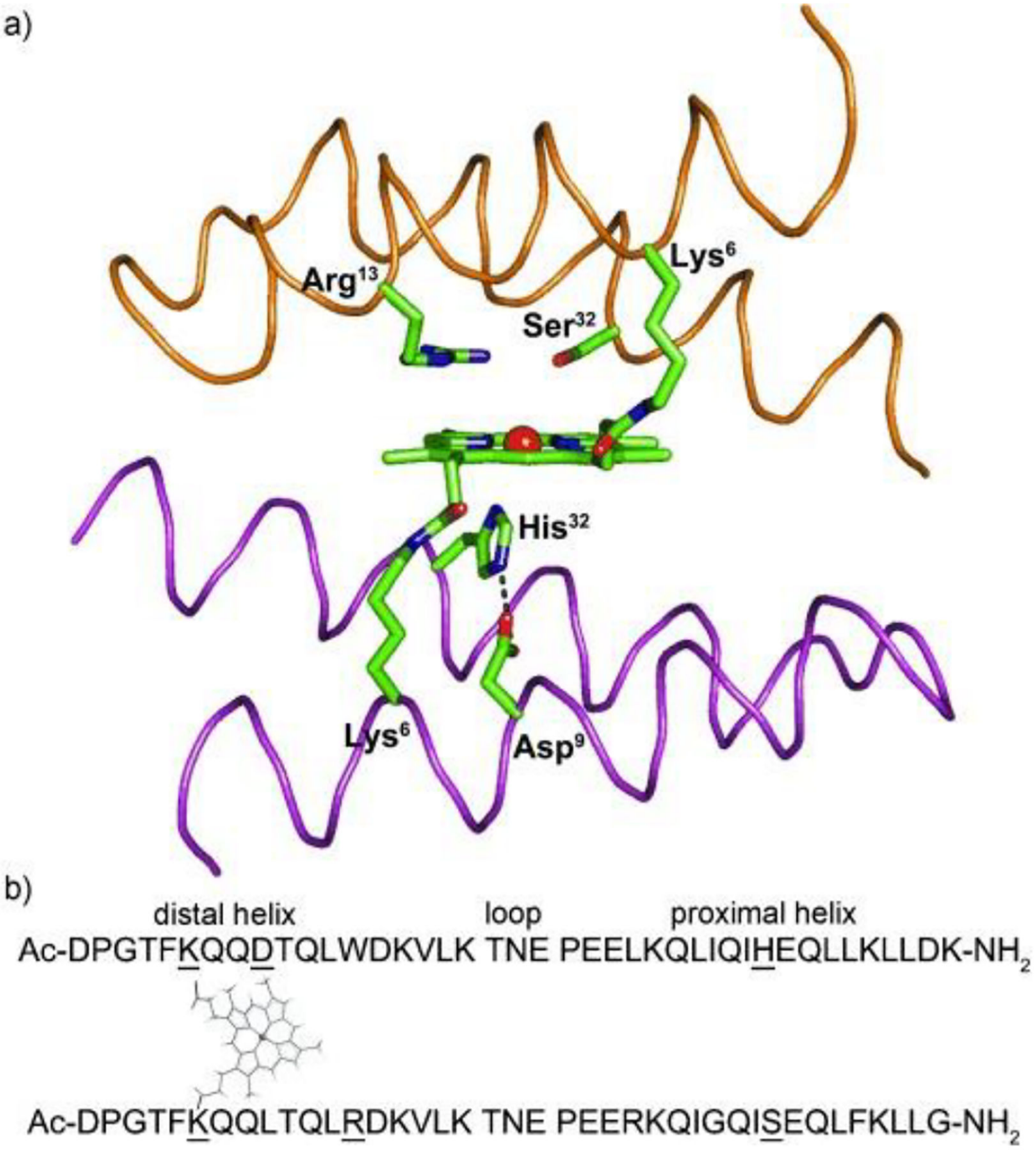

Figure 4:

(**A**) Structural model of MP3 with key residues represented as sticks and a putative hydrogen bond as a dashed line and (**B**) sequence representation with key sidechains underlined. Reprinted with permission ref 39. Copyright 2012 Wiley-VCH Verlag GmbH & Co.

Author Manuscript Author Manuscript Author Manuscript Author Manuscript

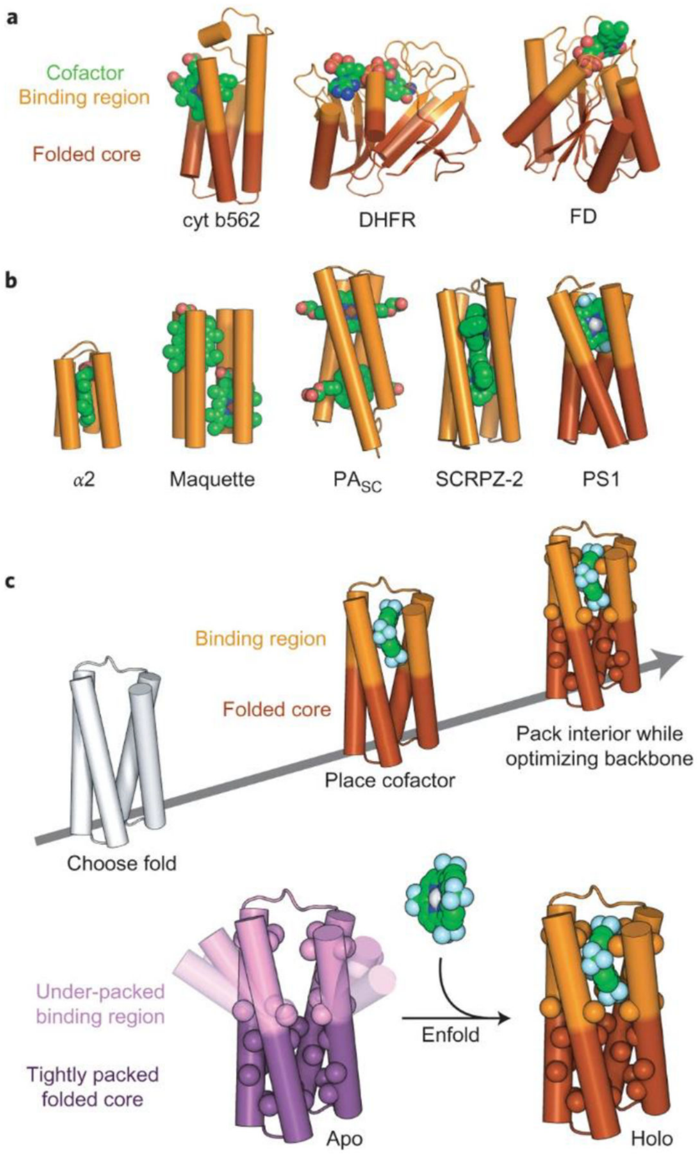

Figure 5:

(**A**) Natural cofactor binding proteins that exemplify folded-cores supporting cofactor binding region. cyt b562, cytochrome b562 (PDB 256B); DHFR, dihydrofolate reductase (PDB 8DFR); FD, flavodoxin (PDB 1CZU). (**B**) A selection of designed tetra-helical porphyrin-binding proteins. (**C**) Holistic metalloprotein design. First core residues in both the binding region (light color) and folded core (dark color) are optimized with a flexible backbone. The optimized holoprotein now has a tightly packed folded core and binding region around the bound cofactor, while the apoprotein leaves the binding region flexible. Reprinted with permission ref 61. Copyright 2017 Macmilan Publishers Limited.

Author Manuscript

Author Manuscript

Author Manuscript

Author Manuscript

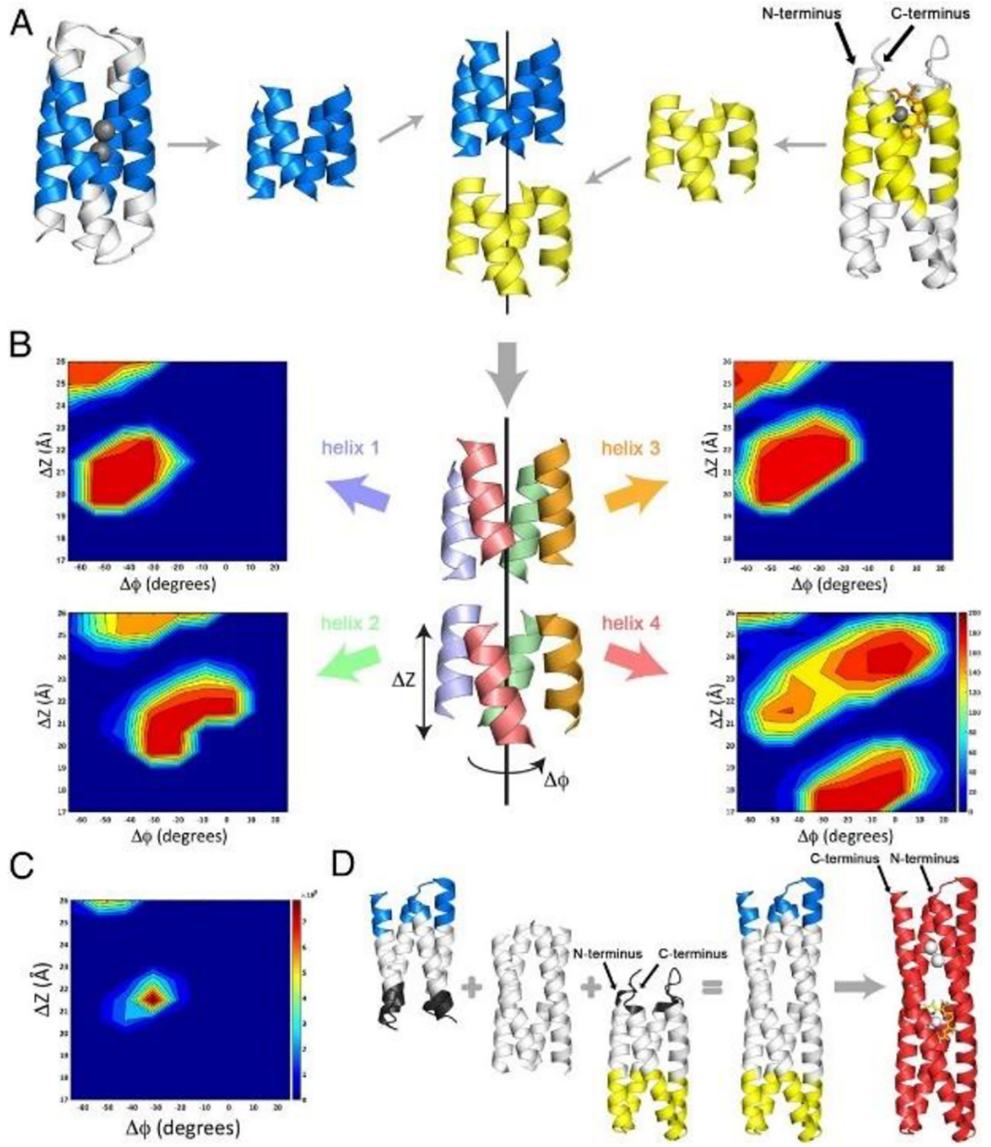

Figure 6:

The design of DFP1 from Due Ferr (DF) and porphyrin-binding sequence (PS1) (**A**) Both helical bundles are aligned along a common axis, reducing the number of degrees of freedom to two: the relative translation along the bundle axis, ΔZ, and the relative rotation about the bundle axis, ΔΦ). The segments surrounding the dimetal in DF and porphyrin in PS1 were used to identify each bundle axis. (**B**) Search of (ΔZ,ΔΦ) space for each disjointed helix pair during which one helix is kept stable while the other is translated (ΔZ) or rotated the about the bundle axis. A 2D plot of the (ΔZ,ΔΦ) space reveals noticeable “hotspots” that represents designable structural matches as peaks. (**C**) The product of each (ΔZ,ΔΦ) space results in an overall bundle designability space where peaks represent the optimal positions of the two bundles. (**D**) The final design combines the two helical bundles into a single construct using the previously determined optimal relative orientation. Reprinted with permission ref 63. Copyright 2020 National Academy of Sciences.

Author Manuscript Author Manuscript Author Manuscript Author Manuscript

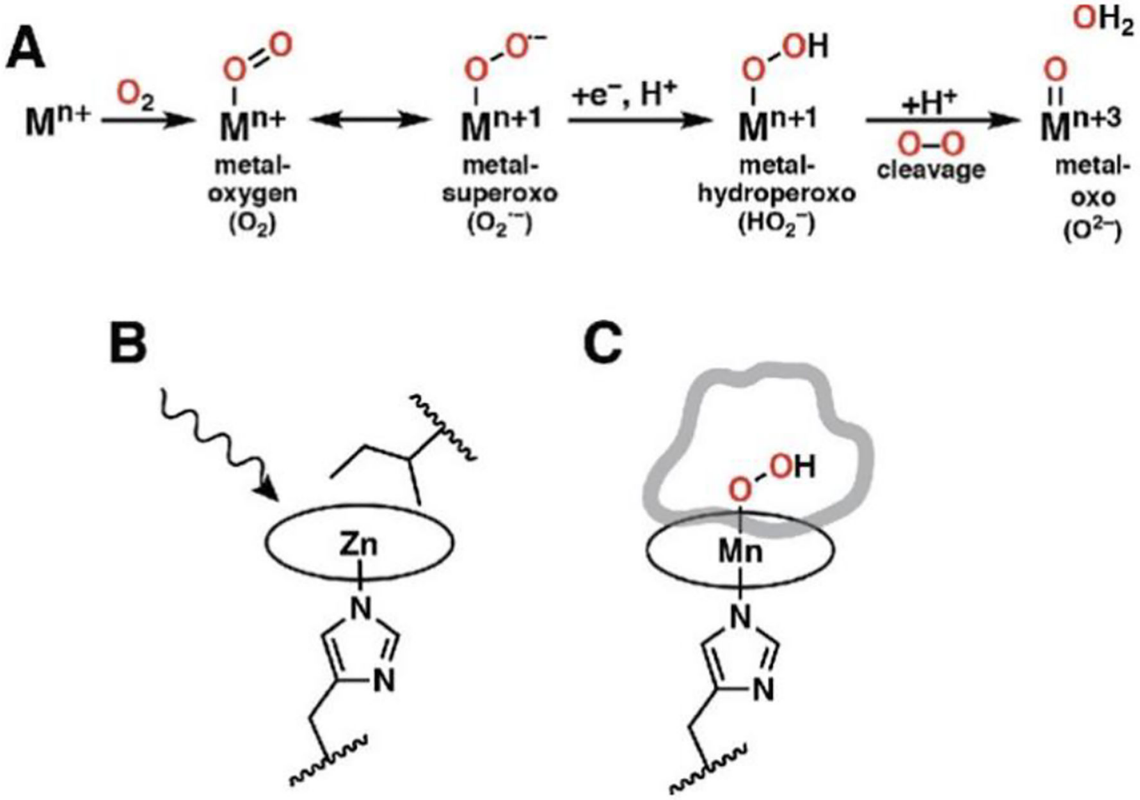

Figure 7:

(**A**) Interconversions of metal-oxygen intermediates within heme proteins. (**B**) and (**C**) Designed functions of (**B**) PS1 and (**C**) MPP1. Removing the steric bulk of isoleucine during the design of MPP1 allowed dioxygen to be accommodated above the Mn center. Circles represent porphyrin macrocycles. Adapted with permission from ref 81. Copyright 2021 American Chemical Society

Author Manuscript Author Manuscript Author Manuscript Author Manuscript

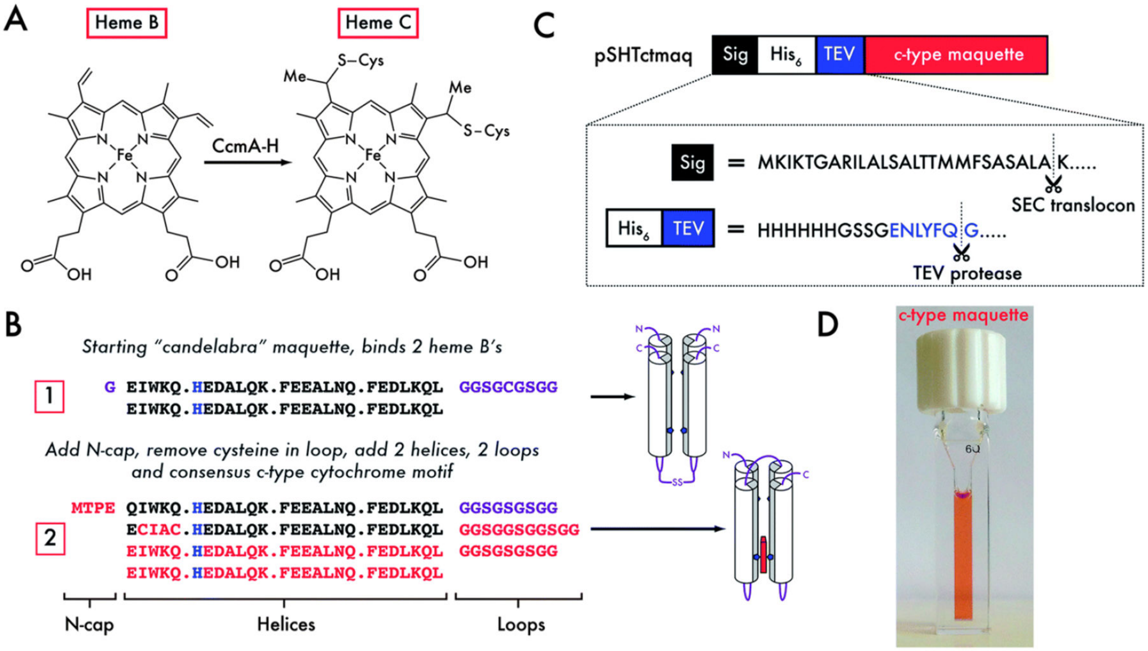

Figure 8:

Artificial *c*-type cytochrome expression (**A**) Thioether linkages covalently attach Heme B to the protein backbone to make Heme C via cytochrome *c* maturation proteins. (**B**) Glycine and serine 1,2 loops and 4-residue N-cap (MTPE) were introduced to break the symmetry of the 4-helix bundle and add rigidity at the N-terminus. The *c*-type heme recognition sequence (CXXCH) promotes heme incorporation by the *E. coli* cytochrome *c* maturation proteins. Mutations between iterations are highlighted in red, heme ligating histidine residues and N-terminal loops are in purple. Cartoon illustrations on the right highlight the relative positions of the ligating histidine (blue pentagons), loops and N-/C-termini (purple lines), and heme C accommodation into the 4-helix bundle (red rectangular box). (**C**) Primary sequence of artificial *c*-type cytochrome. (**D**) Cuvette of *c*-type maquette showcasing successful heme incorporation. Reprinted with permission from ref 90. Copyright 2014 The Royal Society of Chemistry.

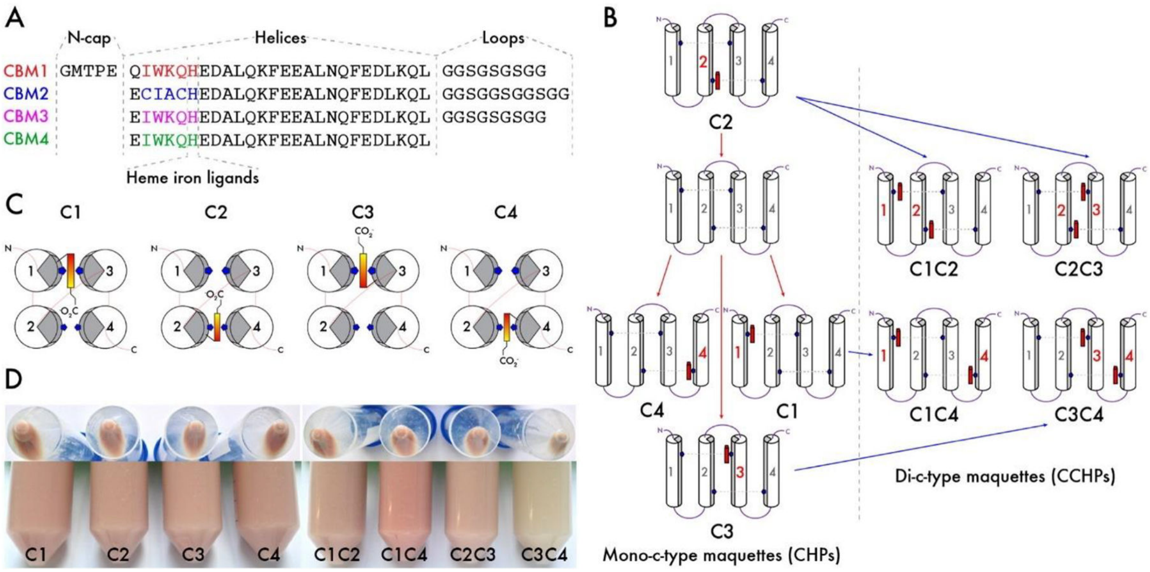

Figure 9:

(**A**) Amino acid sequence of C2 (**B**) Successive rounds of C2 mutagenesis carried out to design various mono- or diheme binding peptides with His residues represented as blue pentagons and heme C as red/yellow rectangles. (**C**) Schematic highlighting binding orientation in mono-heme C maquettes. (**D**) *E. coli* after 4 hours expressing various *c*-type heme maquettes. Adapted with permission from ref 109. Copyright 2015 Elsevier B.V.

Author Manuscript Author Manuscript Author Manuscript Author Manuscript

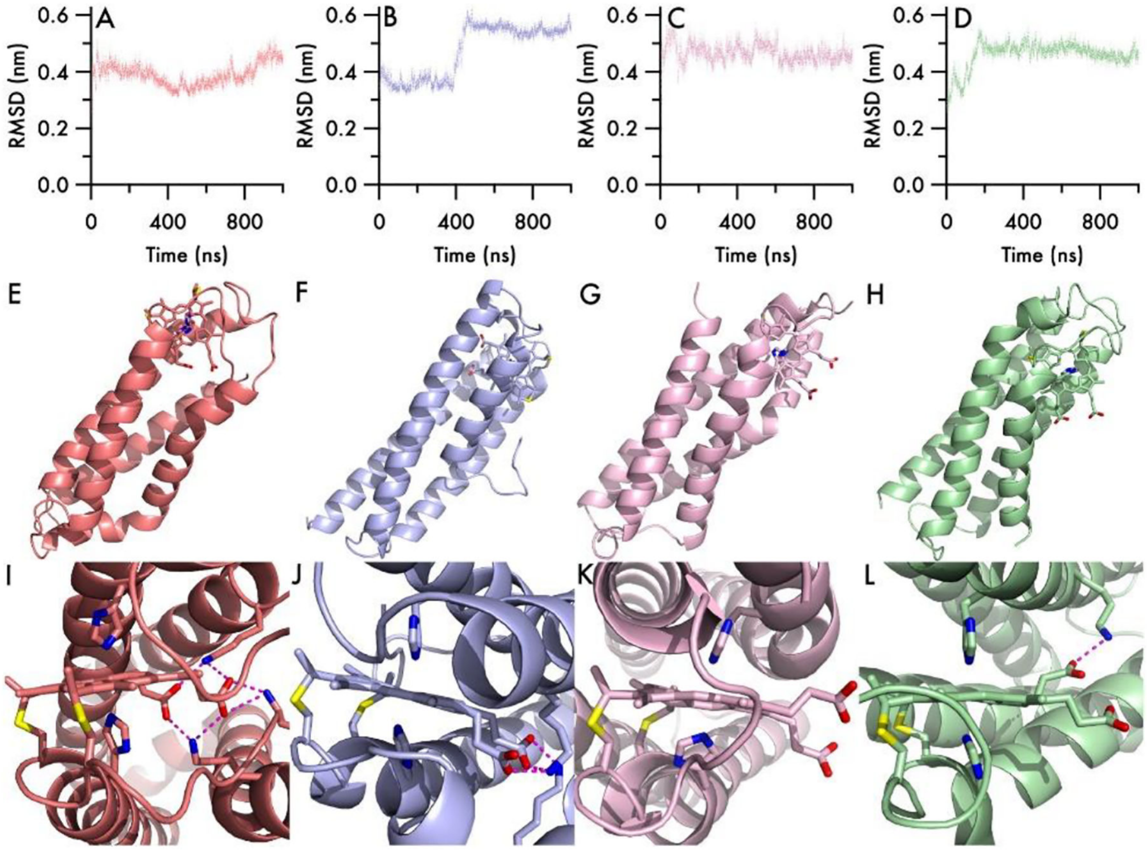

Figure 10:

MD simulations of various *c*-type heme maquettes. (**A-D**) Root mean squared deviation traces compared to the starting structure over 1 μs MD simulations of C1 (red), C2 (blue), C3 (pink) and C4 (green). (**E-H**) Side view and (**I-L**) close-up view of heme C after 1 μs with heme and interacting residues represented as sticks. Reprinted with permission from ref 109. Copyright 2015 Elsevier B.V.

Author Manuscript
Author Manuscript
Author Manuscript
Author Manuscript

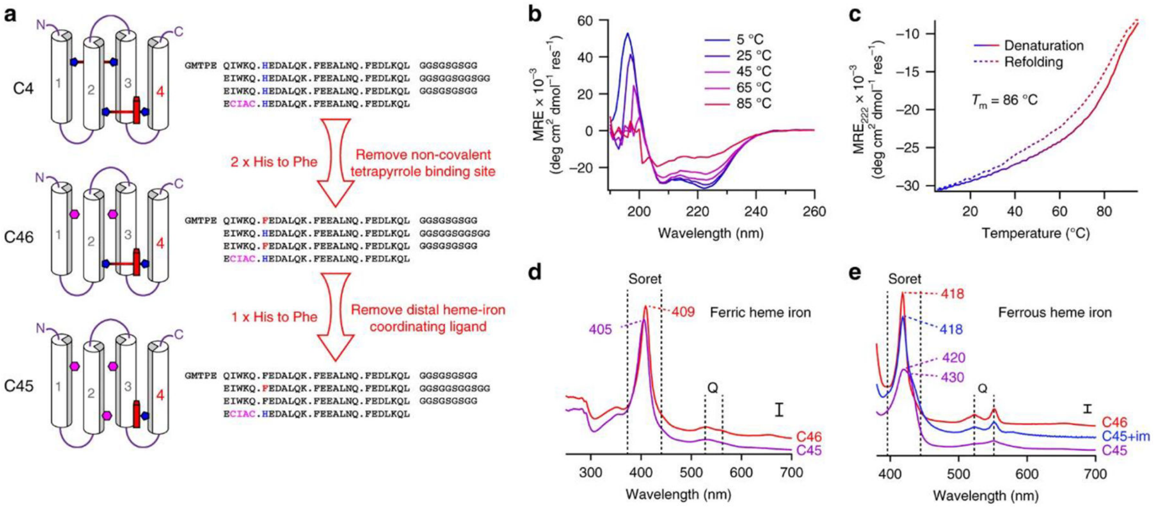

Figure 11:

(**A**) Illustration highlighting the design of an artificial peroxidase (C45) by removing 3 of the 4 histidine side chains to create a protein with a mono-histidine ligated C type heme site (C45). (**B**) Far-UV circular dichroism spectra of C45 as a function of temperature. (**C**) Reversable temperature dependence of the 222nm CD band. Optical Absorption spectra of ferric (**D**) and ferrous (**E**) C45 (purple) and C46 (red) with the spectrum of exogenous imidazole added to C45 in blue. Reprinted with permission from ref 116. Copyright 2017 Springer Nature.

Author Manuscript

Author Manuscript

Author Manuscript

Author Manuscript

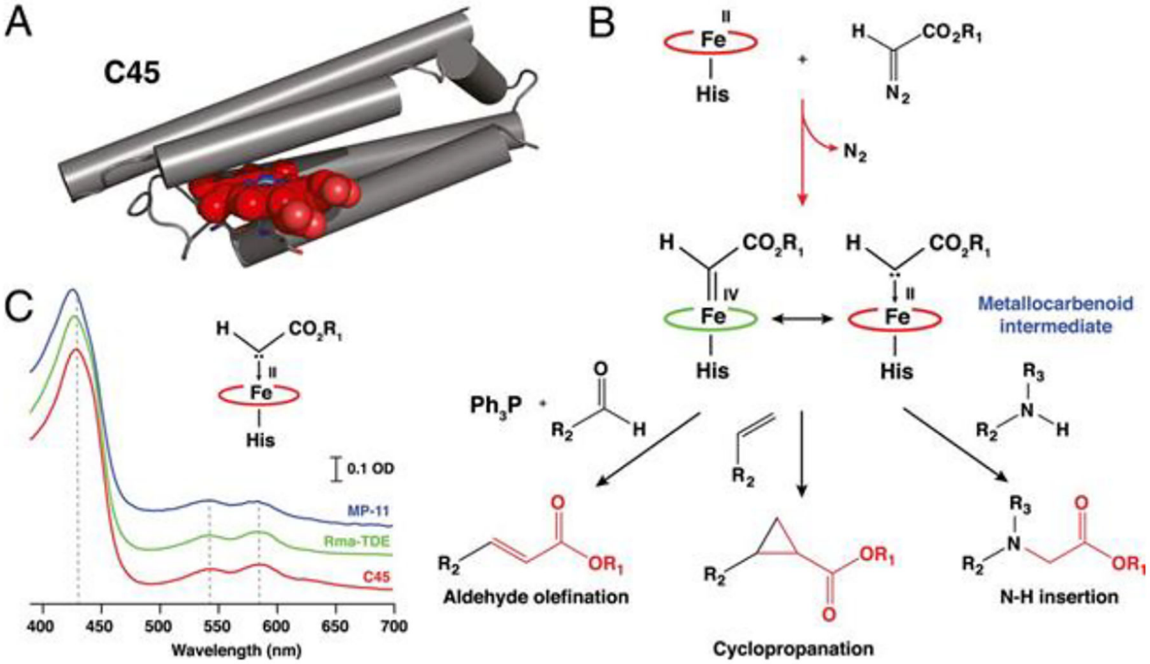

Figure 12:

(**A**) Structural snapshot of *c*-type cytochrome maquette, C45, during molecular-dynamics simulation. (**B**) Example of proposed reactivity of heme-based metallocarbenoid intermediates. (**C**) Stopped-flow optical absorption spectra of C45 (red), engineered Rma-TDE (green), and MP-11 (blue), treated with Ethyl Diazoacetate (EDA). Reprinted with permission from ref 119. Copyright 2020 National Academy of Sciences.

Author Manuscript Author Manuscript Author Manuscript Author Manuscript

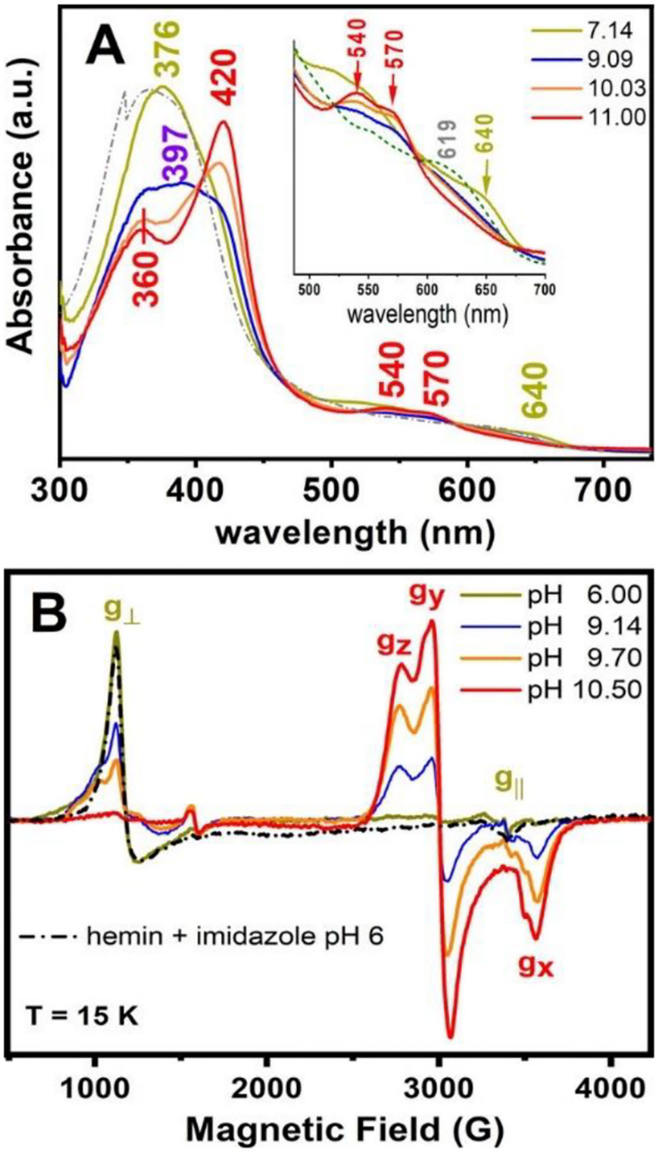

Figure 13:

(**A**) Optical absorption and (**B**) 9-GHz EPR spectra of GRW-L16CL30H mini-heme protein at various pH conditions compared to absorption spectrum of hemin in buffer (pH 7, dash-dotted curve), and EPR spectrum of histidine bound hemin (pH 6, dash-dotted curve). Reprinted with permission from ref 134. Copyright 2020 John Wiley & Sons, Inc.

Author Manuscript Author Manuscript Author Manuscript Author Manuscript

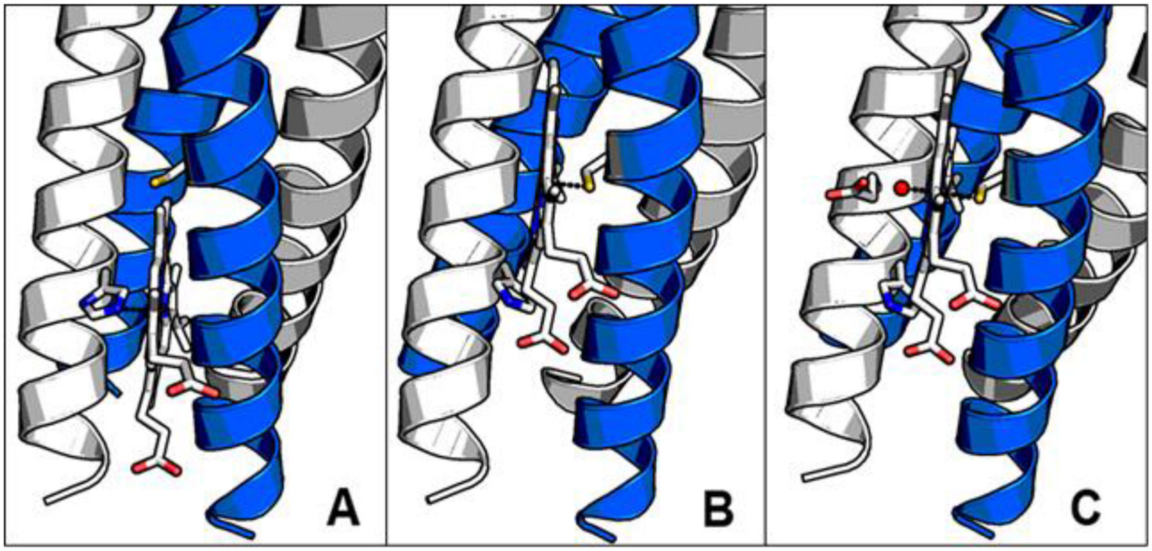

Figure 14:

Illustrations of the dimer of antiparallel 2SCC (with one heme per 2SCC) proposed for the folding of GRW-L16CL30H peptides upon complexation with heme. pH dependent coordination modes: (**A**) His-pentacoordinated heme (pH 7), (**B**) Cys-pentacoordinated heme (pH 9.0) and (**C**) Cys/hydroxy hexacoordinated heme (pH 10.5) derived from spectroscopic characterization. Reprinted with permission from ref 134. Copyright 2020 John Wiley & Sons, Inc.

Author Manuscript Author Manuscript Author Manuscript Author Manuscript

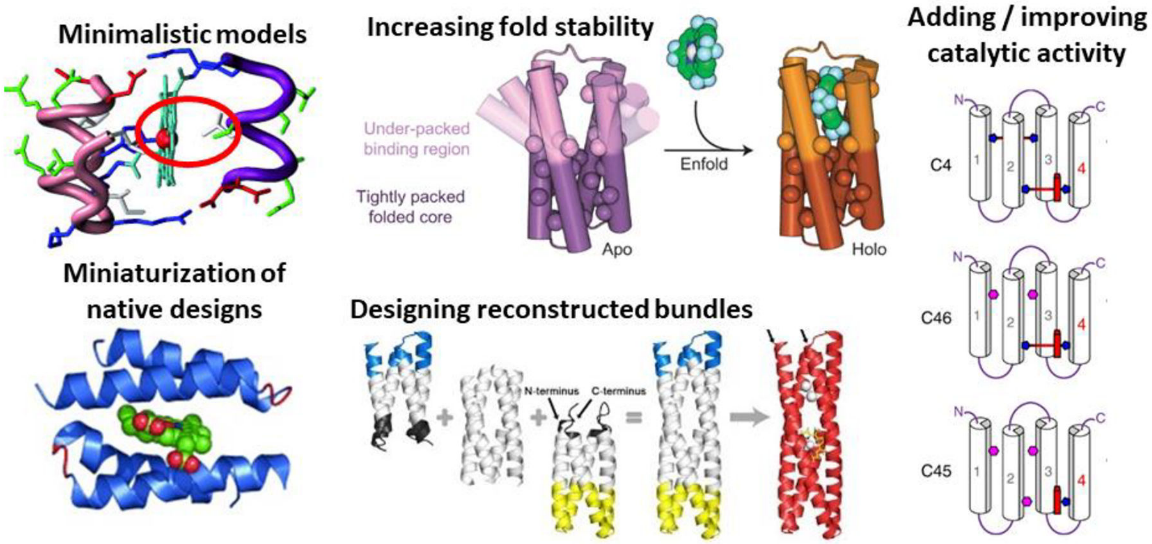

Figure 15:

Summary of recent advances in the *de novo* protein design of heme enzymes highlighted in this review. Adapted with permission from the appropriate references as specified in source figures previously in manuscript.

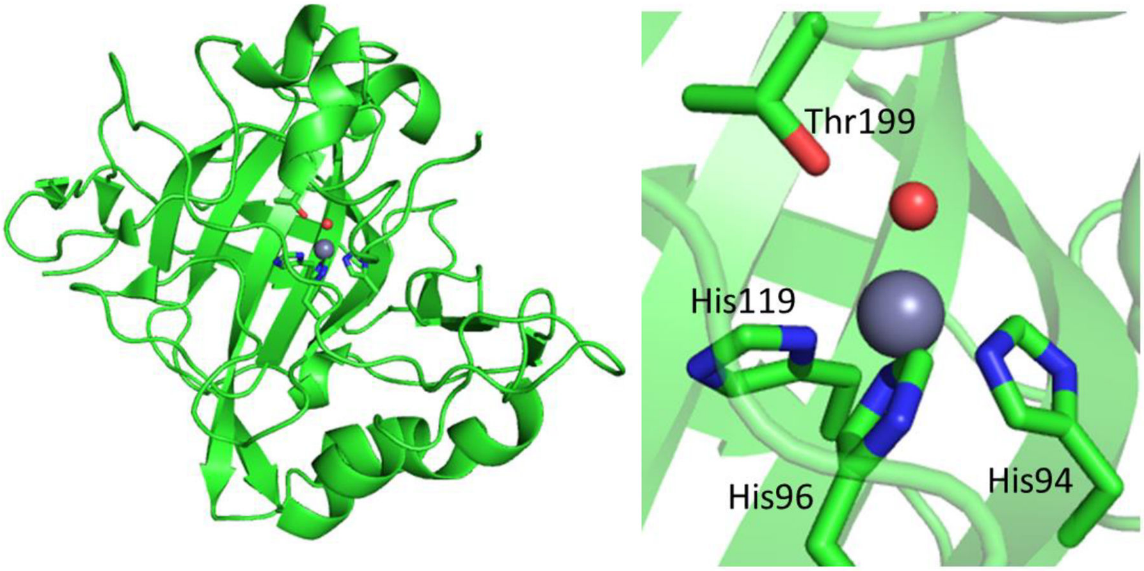

Figure 16:

Pymol illustrations of the overall protein fold (left) and Zn active site (right) of human carbonic anhydrase II (PDB 2CBA). Zn(II) ions are shown as silver spheres and water oxygen as a red sphere. All amino acids that either coordinate Zn(II) or empirically determined to improve catalysis are depicted as sticks.

Author Manuscript Author Manuscript Author Manuscript Author Manuscript

Author Manuscript Author Manuscript Author Manuscript Author Manuscript

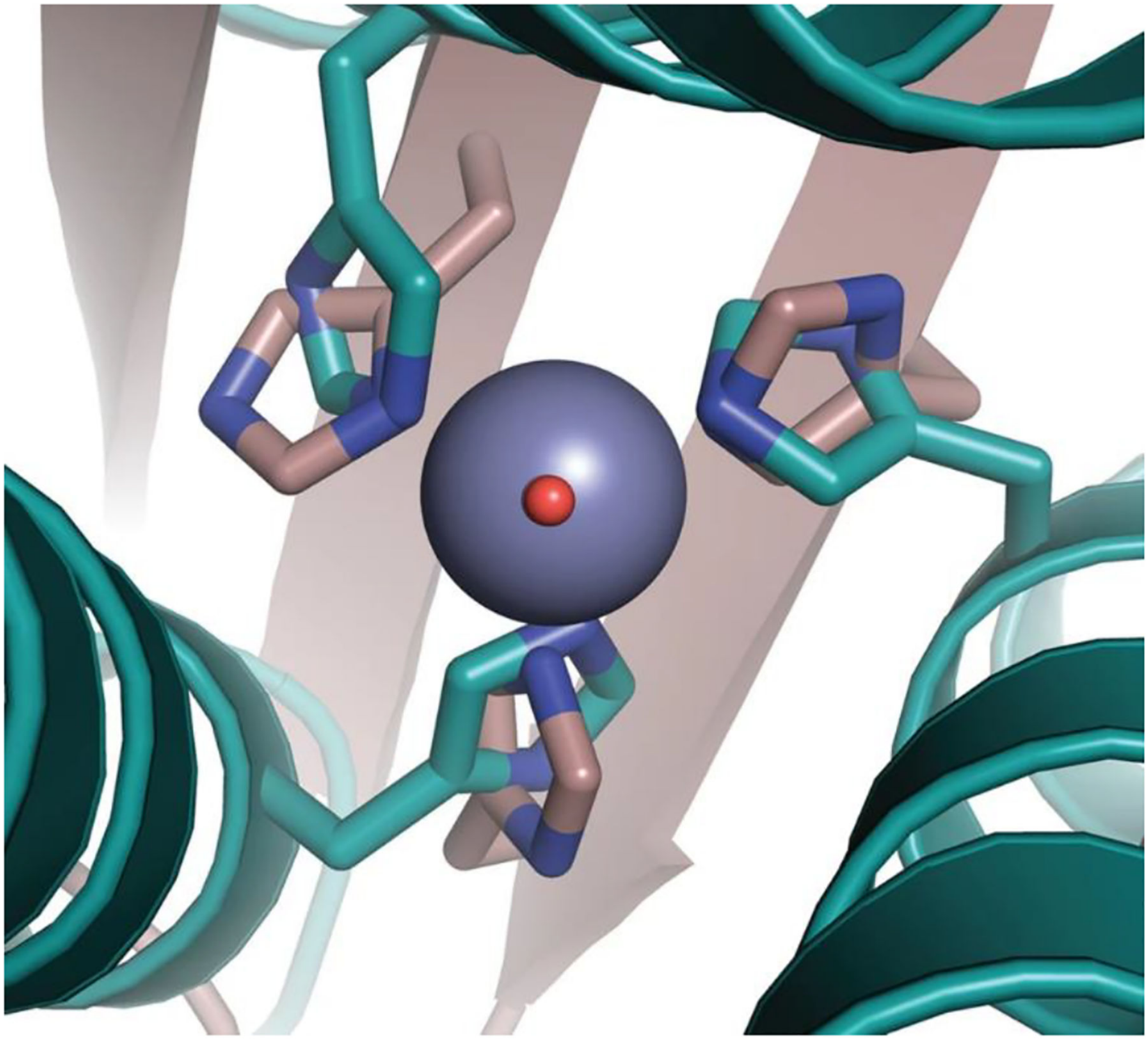

Figure 17:

Structural comparison of $[Hg(II)]_S[Zn(II)(H_2O/OH^-)]_N(CSL9PenL23H)_3{}^{n+}$ in cyan (pdb 3PBJ) and carbonic anhydrase II in tan (pdb 2CBA). The primary coordination spheres between the two active sites share many features; however, they differ in the proposed N_ε or N_δ binding modes to the Zn(II) ion and orientation of the histidine side chains. Reprinted with permission from ref 155. Copyright 2012 Macmillan Publishers Limited.

Author Manuscript

Author Manuscript

Author Manuscript

Author Manuscript

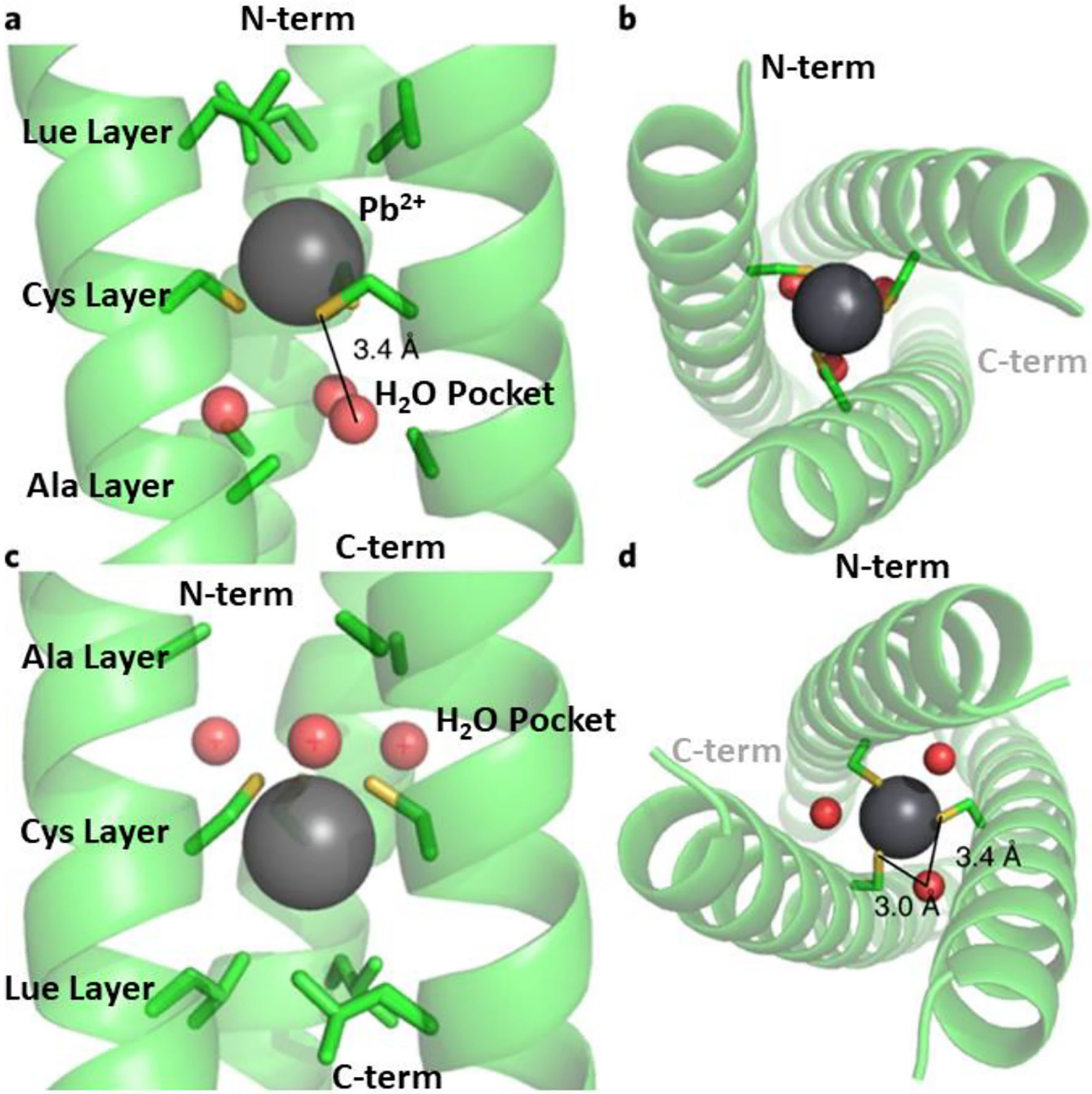

Figure 18:

A d-site Pb(II)Cys$_3$ site from both a side (**A**) and top (**B**) view with a water-Cys distance of 3.4 Å shown as a solid line. An a-site Pb(II)Cys$_3$ from both a side (**C**) and top (**D**) with a water–Cys distances of 3.0 Å and 3.4 Å. The Zn(II) binding site is omitted for clarity. Adapted with permission from ref 176. Copyright 2020 Springer Nature

Author Manuscript Author Manuscript Author Manuscript Author Manuscript

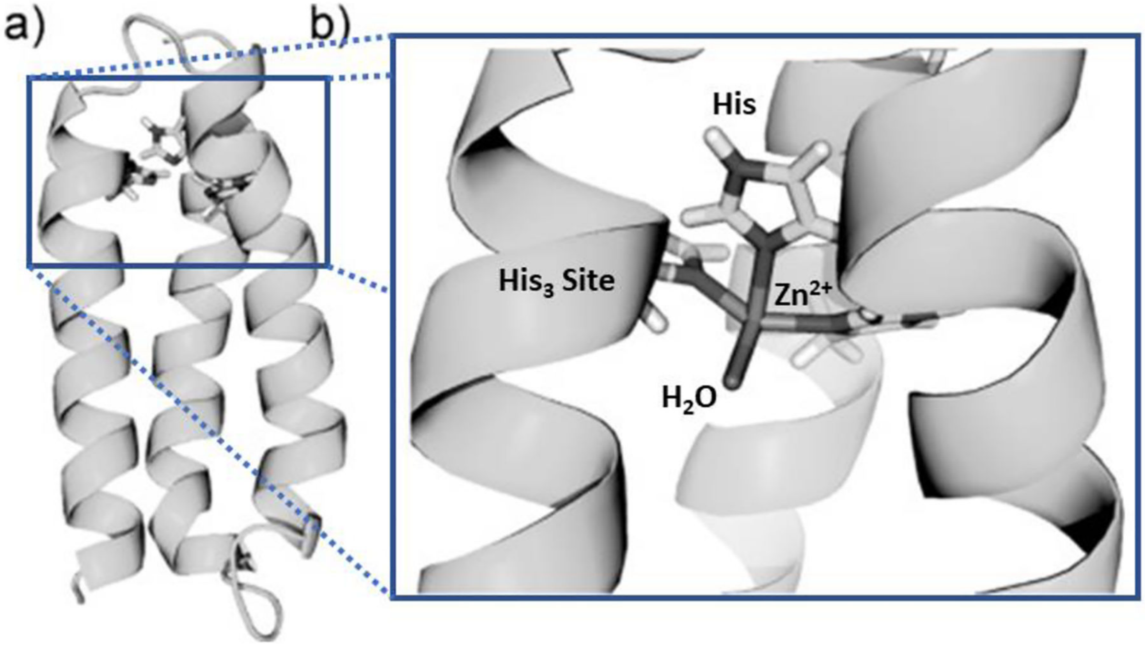

Figure 19:

Illustration of α$_3$D H3 highlighting the (**A**) overall protein fold and (**B**) active site, Zn(II)His$_3$O. These Pymol models were derived from the NMR solution structure of α$_3$D (PDB 2A3D) Adapted with permission from ref 179. Copyright 2014 Wiley-VCH Verlag GmbH & Co.

Author Manuscript Author Manuscript Author Manuscript Author Manuscript

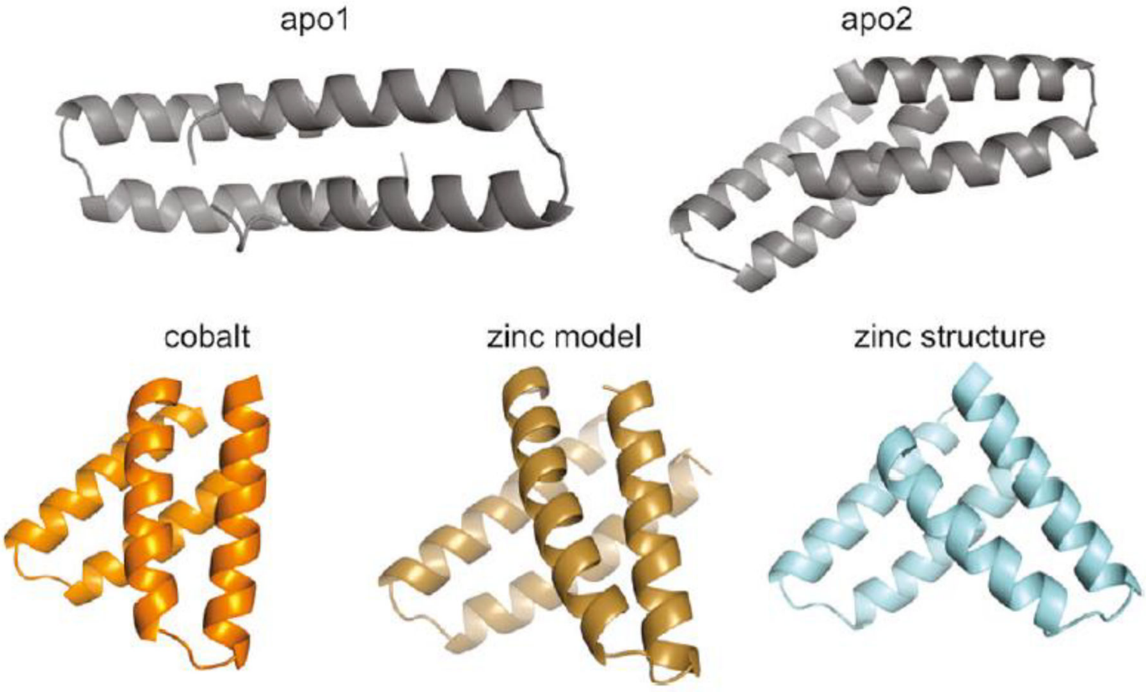

Figure 20:
Different orientational configurations of apo-MID1, Zn(II)MID1, Co(II)MID1 showcasing the change in bundle orientation upon metal binding. Binding of either Zn(II) (cyan) or Co(II) (orange) prompt the formation of orientations similar to the predicted Zn(II) model (tan). Adapted with permission from ref 191. Copyright 2012 American Chemical Society.

Author Manuscript

Author Manuscript

Author Manuscript

Author Manuscript

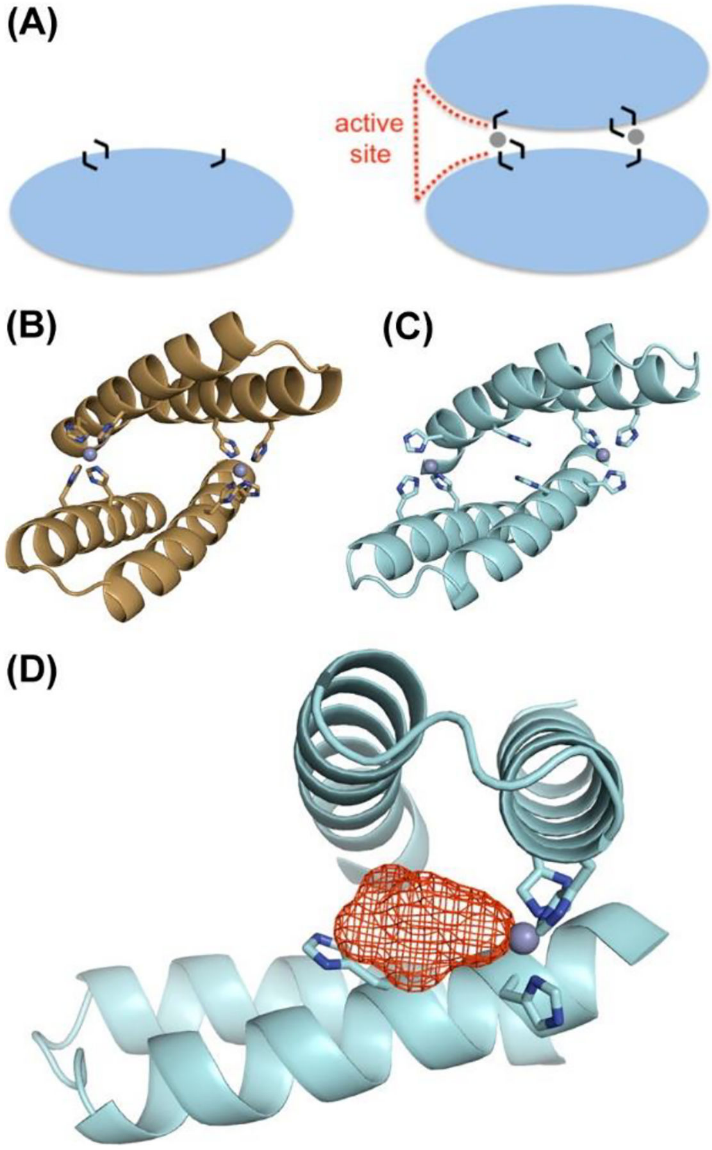

Figure 21:

Metal mediated interface leads to a *de novo* active site. (**A**) Metal templated homodimer formation naturally results in substrate clefts (red dash) while acting as a catalytic active site (black lines represent histidine and gray spheres represent zinc ions). Comparison of Zn(II)MID1 (**B**) computationally predicted and (**C**) experimentally solved crystal structures reveals a three-histidine coordinated Zn(II) ion in the final structure. (**D**) Both a substrate cleft (red mesh) and an open coordination site around the Zn(II) ion were observed in the solid-state structure hinting at possible Zn(II)MID1 catalytic activity. Adapted with permission from ref 193. Copyright 2012 American Chemical Society.

Author Manuscript
Author Manuscript
Author Manuscript
Author Manuscript

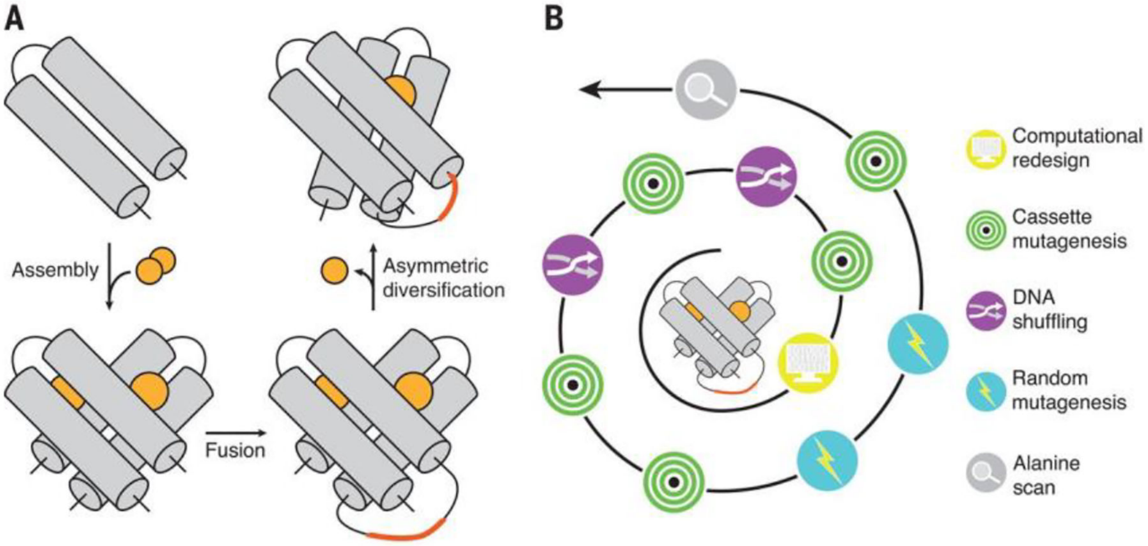

Figure 22:

(**A**) Design of MID1sc10 by Zinc templated helix-turn-helix fragments formation, followed by fusion and asymmetric diversification. (**B**) Illustration of the step-by-step design procress in the final asymmetric diversification. Reprinted with permission from ref 194. Copyright 2017 American Association for the Advancement of Science.

Author Manuscript

Author Manuscript

Author Manuscript

Author Manuscript

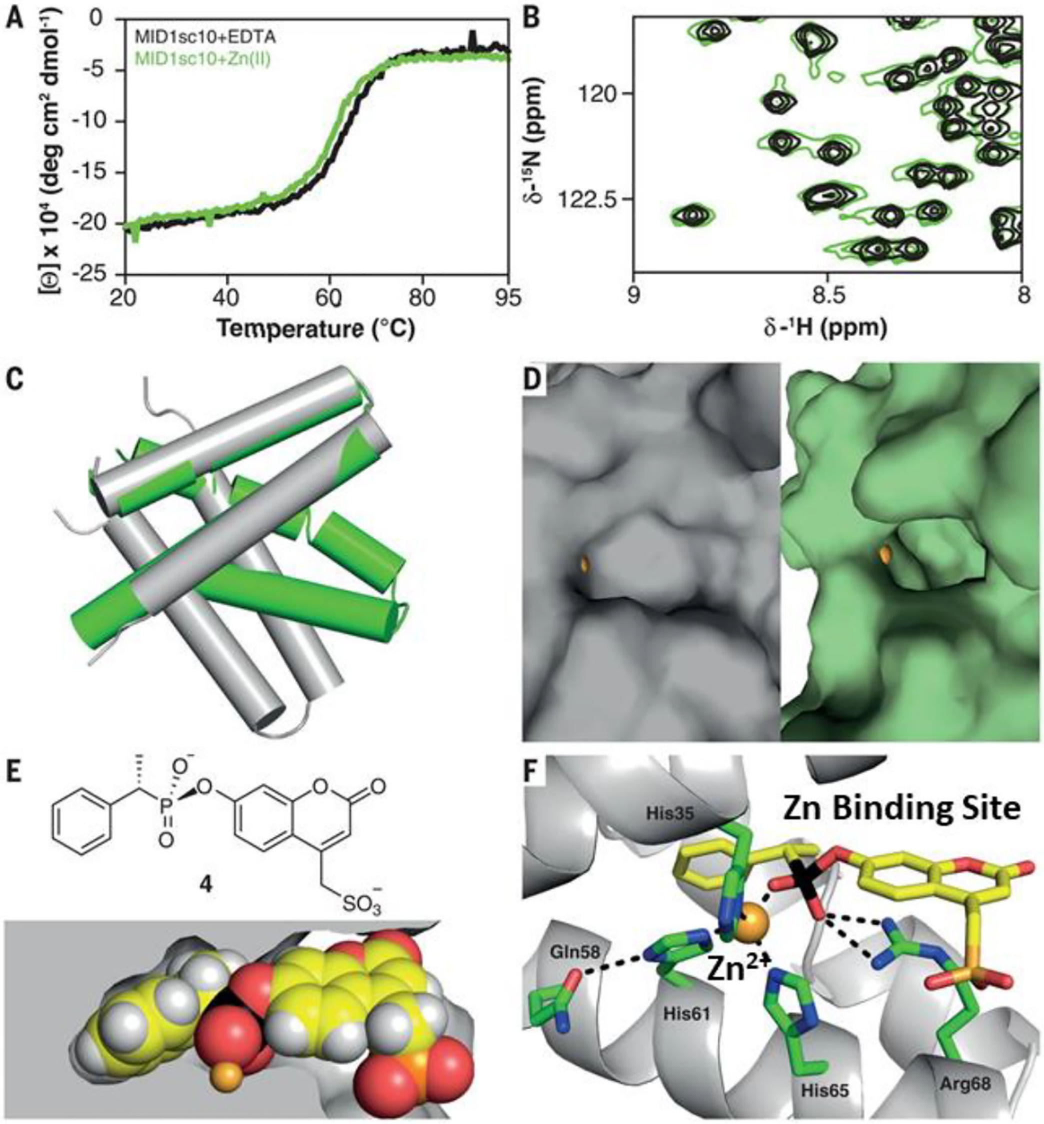

Figure 23:

(**A**) Thermal stability of apo-MID1sc10 (black) and holo-MID1sc10 (green). (**B**) 1H-15N-HSQC spectra apo-MID1sc10 (black) and holo-MID1sc10 (green). (**C**) Overlayed structures of MID1sc10 (green) and MID1 (gray) showing the change in crossover angle. (**D**) Structures illustrating the shallow binding site of MID1 (graph) compared to the deep pocket in MID1sc10 (green). (**E**) Active site view of the tight fit of phosphonate 4 in the binding pocket of MID1sc10. (**F**) Phosphonate 4 coordinated to the Zn(II)His$_3$ active site in MID1sc10. Adapted with permission from ref 194. Copyright 2017 American Association for the Advancement of Science.

Author Manuscript Author Manuscript Author Manuscript Author Manuscript

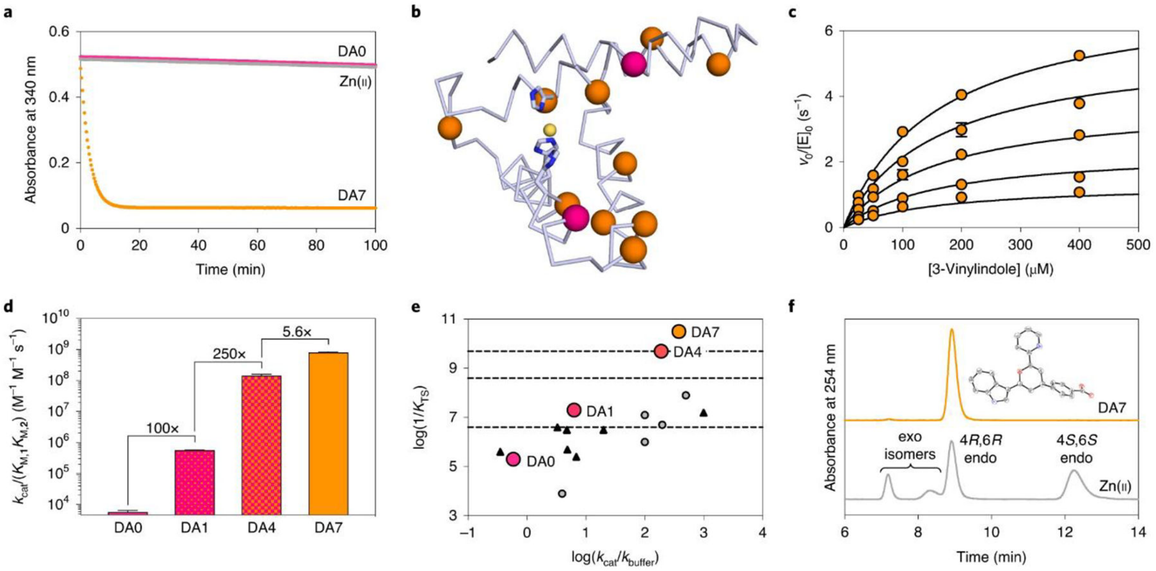

Figure 24:

(**A**) Comparison of Azalchalcone reacting with 3-vinylindole kinetics as catalyzed by free Zn(II) (grey), DA0 (magenta) or DA7 (orange). (**B**) Model structure of MID1sc highlighting the active site with Zn(II) in yellow and the amino acid positions which were mutated either based on computation (magenta) or acquired during evolution (orange). (**C**) Steady state kinetic analysis of DA7. (**D**) Plot of catalytic efficiency over the course of directed evolutionary design showing a 140,000-fold increase. (**E**) Double logarithmic plot of effective molarity versus catalytic proficiency. (**F**) Chiral HPLC analysis highlighting the catalytic stereoselectivity of DA7 (orange) compared to free Zn(II) (grey). Reprinted with permission from ref 208. Copyright 2021 Springer Nature.

Author Manuscript Author Manuscript Author Manuscript Author Manuscript

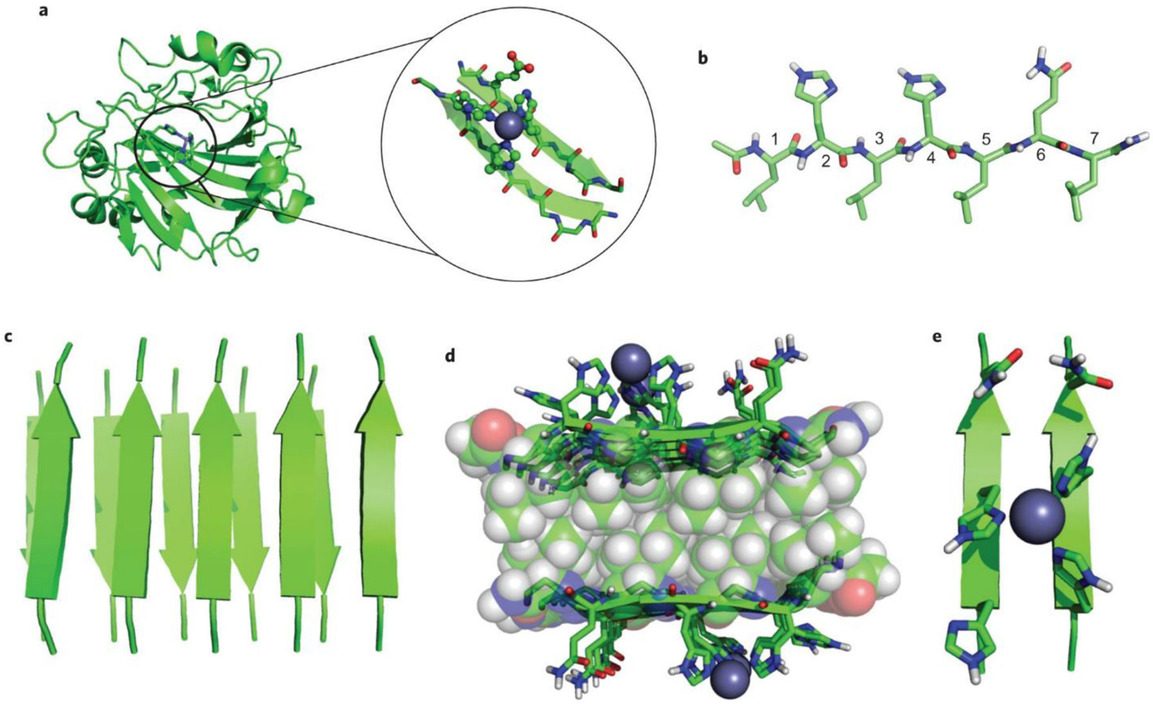

Figure 25:

(**A**) Structure with zoomed-in active site of human carbonic anhydrase (**B**) β-strand configuration of designed peptide **11** (Ac-IHIHIQI-$CONH_2$) with residue positions numbered. (**C-E**) Computational model of **11** in fibrils including the (**C**) overall fold, (**D**) hydrophobic core, and (**E**) primary coordination sphere around Zn(II). Adapted with permission from ref 201. Copyright 2014 Macmillan Publishers Limited.

Author Manuscript

Author Manuscript

Author Manuscript

Author Manuscript

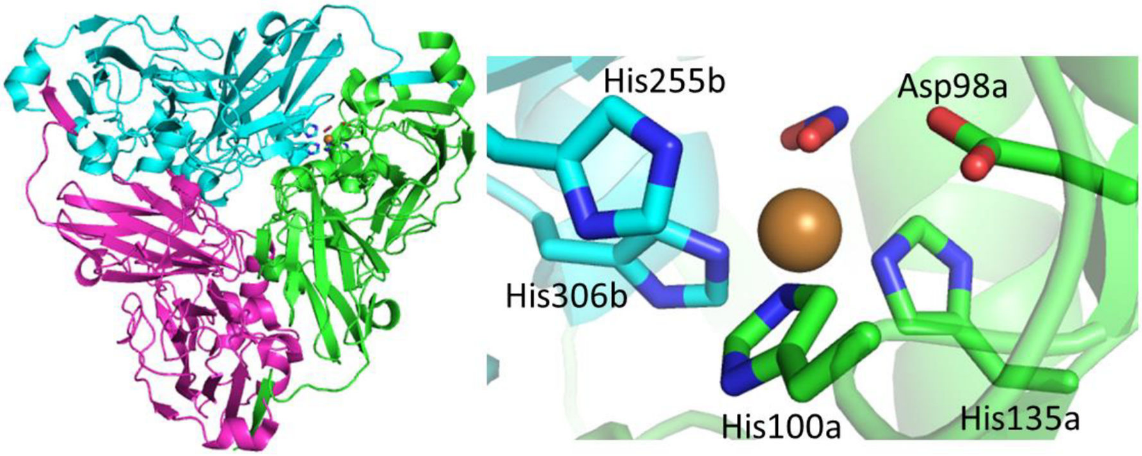

Figure 26:

Pymol illustrations of the overall protein fold (left) and Cu enzyme active site (right) of Copper nitrite reductase (PDB 1SJM). Chains A, B, and C are in green, blue, and magenta respectively. Cu(II) ions are depicted as copper spheres while nitrite substrate and all amino acids that either coordinate Cu(II) or empirically determined to improve catalysis are depicted as sticks.

Author Manuscript
Author Manuscript
Author Manuscript
Author Manuscript

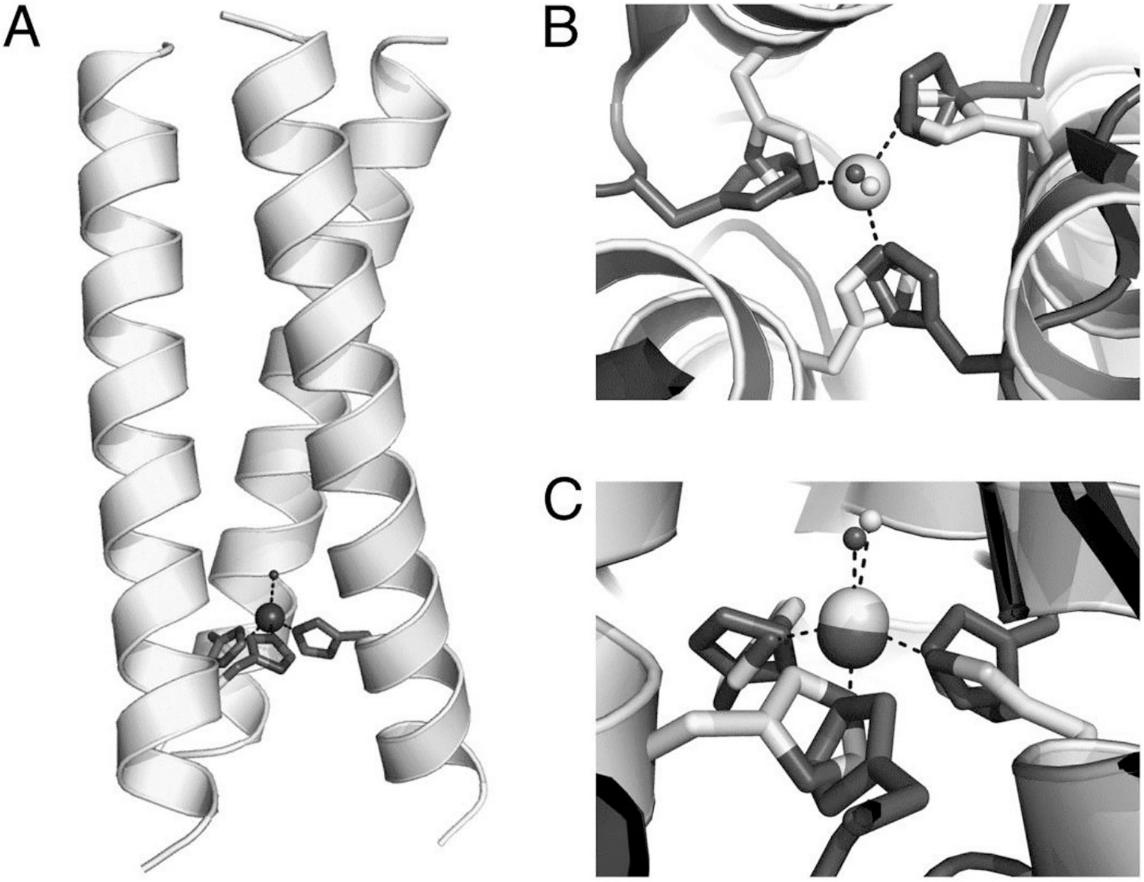

Figure 27:

(**A**) Model of Cu(I)/Cu(II)(TRIL23H)$_3$ derived from Hg(II)$_S$[Zn(II)$_N$(H$_2$O)](CSL9CL23H)$_3$ (PDB 3PBJ). (**B**) Zn(II)(His)$_3$ site along the pseudo three-fold axis of Hg(II)$_S$[Zn(II)$_N$(H$_2$O)](CSL9CL23H)$_3$ (light gray), overlayed with the type 2 center in *R. sphaeroides* nitrite reductase (PDB 2DY2, dark gray). (**C**) Alternative side view of the two metal sites in **B**. Reprinted with permission from ref 7. Copyright 2012 National Academy of Sciences.

Author Manuscript Author Manuscript Author Manuscript Author Manuscript

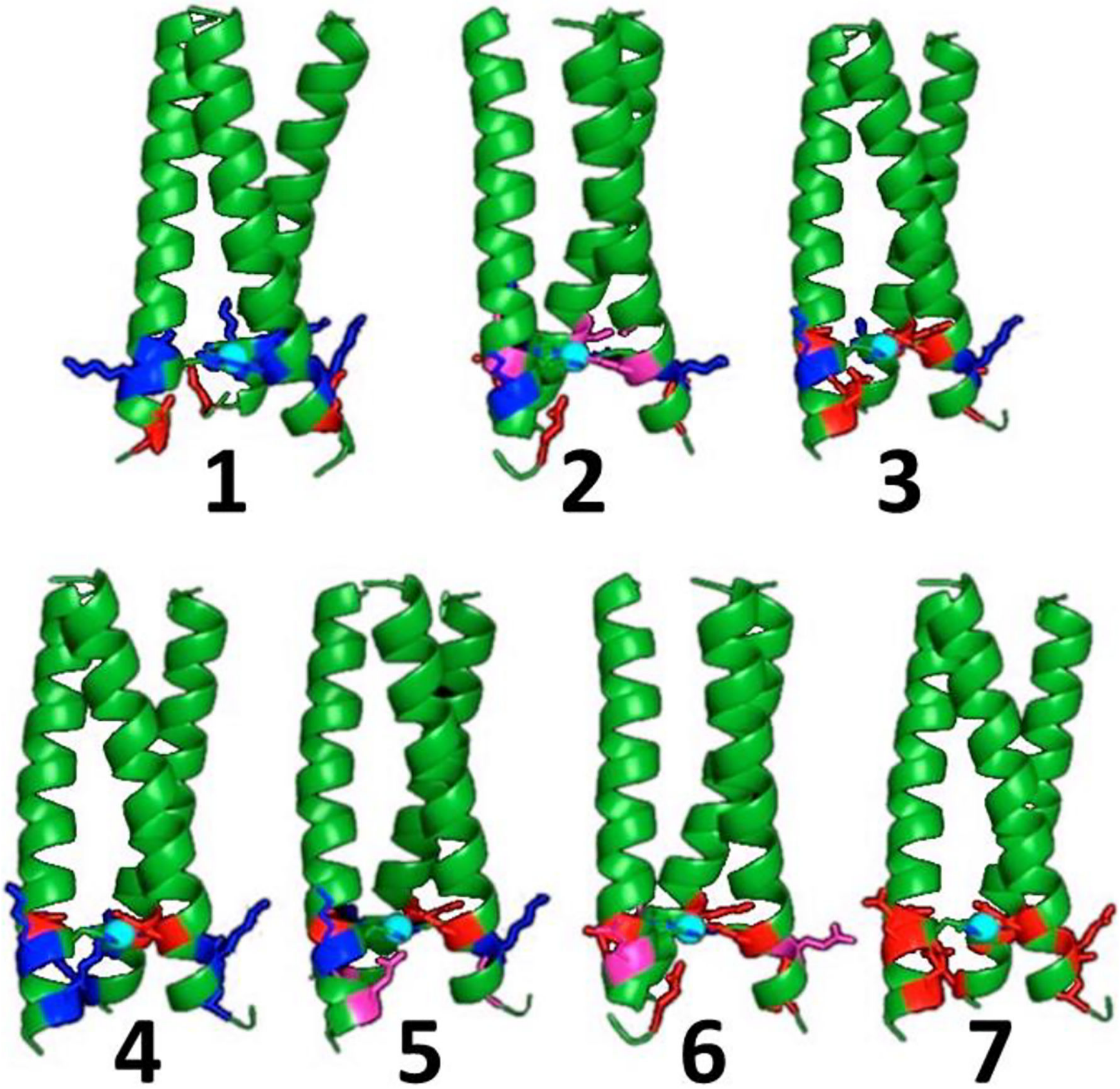

Figure 28:

Structural models of (**1**) TRI-H, (**2**) TRI-HK22Q, (**3**) TRI-EH, (**4**) TRI-EHE27K, (**5**) TRI-EHE27Q, (**6**) TRI-EHK24Q, and (**7**) TRI-EHK24E based on Zn(II)$_{-N}$Hg(II)$_{-S}$(CSL9PenL23H)$_3$ (PDB 3PBJ). Adjusted with permission from ref 245. Copyright 2013 American Chemical Society.

Author Manuscript Author Manuscript Author Manuscript Author Manuscript

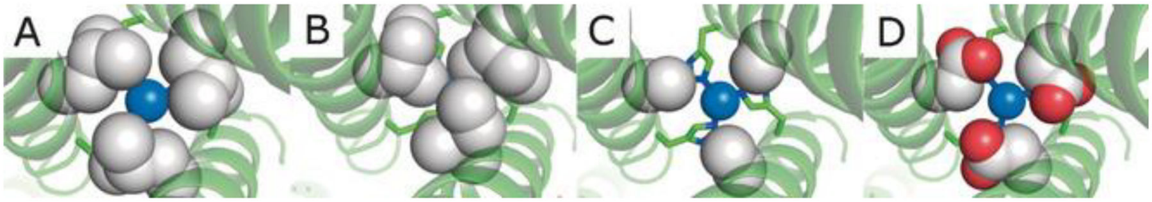

Figure 29:

Structural models of TRIW-H (**A**) L19I, (**B**) L19, (**C**) L19A, and (**D**) L19D illustrating modifications to the steric bulk above the copper active site. These models were constructed using the crystal structure of Zn(II)$_{-N}$Hg(II)$_{-S}$(CSL9PenL23H)$_3^+$ (PDB 3PBJ) or Zn(II)(H$_2$O)(**GRAND-CS**L12AL16C)$_3^-$ (PDB 5KB2). Reprinted with permission from ref 250. Copyright 2018 Wiley-VCH Verlag GmbH & Co.

Author Manuscript

Author Manuscript

Author Manuscript

Author Manuscript

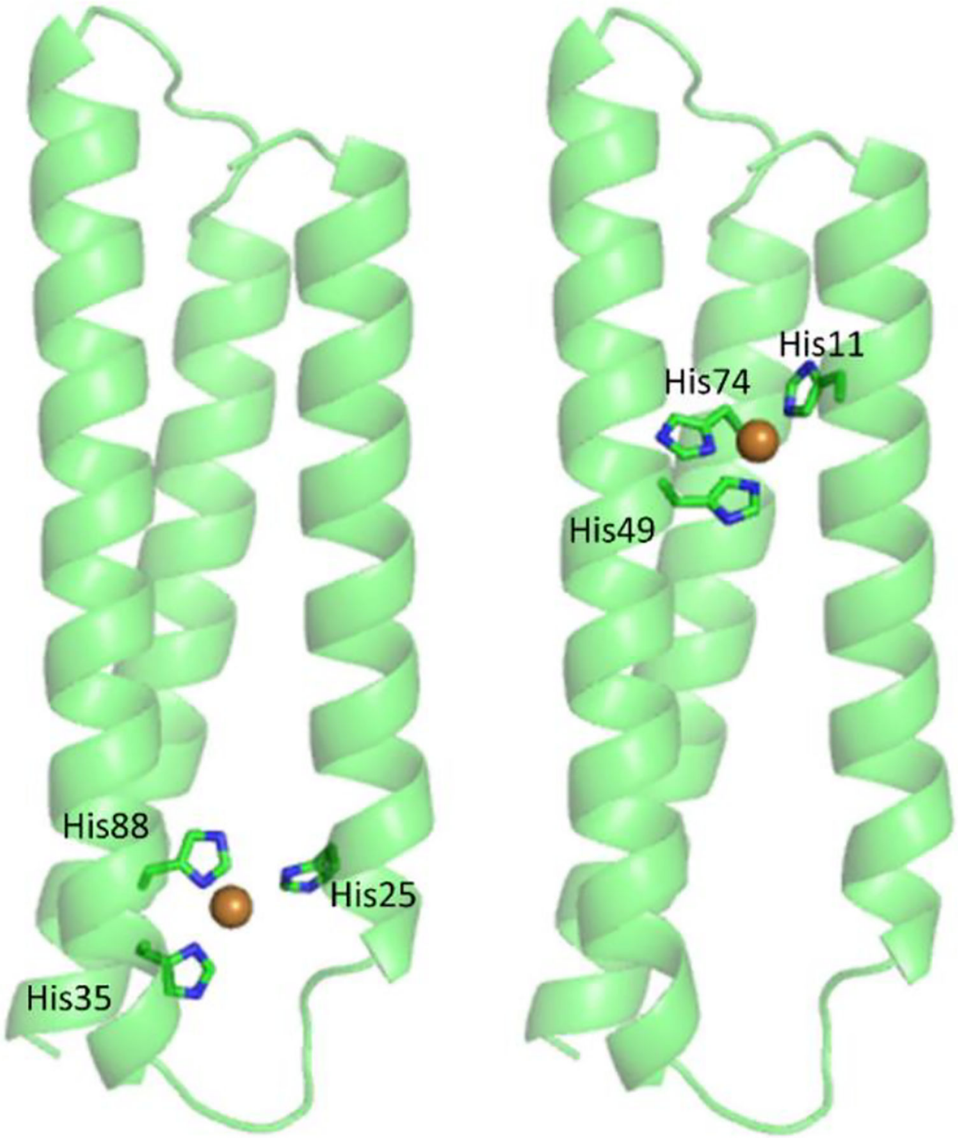

Figure 30:

Structural models of GRα$_3$D H3 (left) and GRα$_3$D H3$_{\text{Nterm}}$ (right) to illustrate relative position of the metal binding sites within the overall GRα$_3$D fold. Models were made using the crystal structural of GRα$_3$D (PDB 6DS9). Reprinted with permission from ref 258. Copyright 2021 Springer Nature.

Author Manuscript Author Manuscript Author Manuscript Author Manuscript

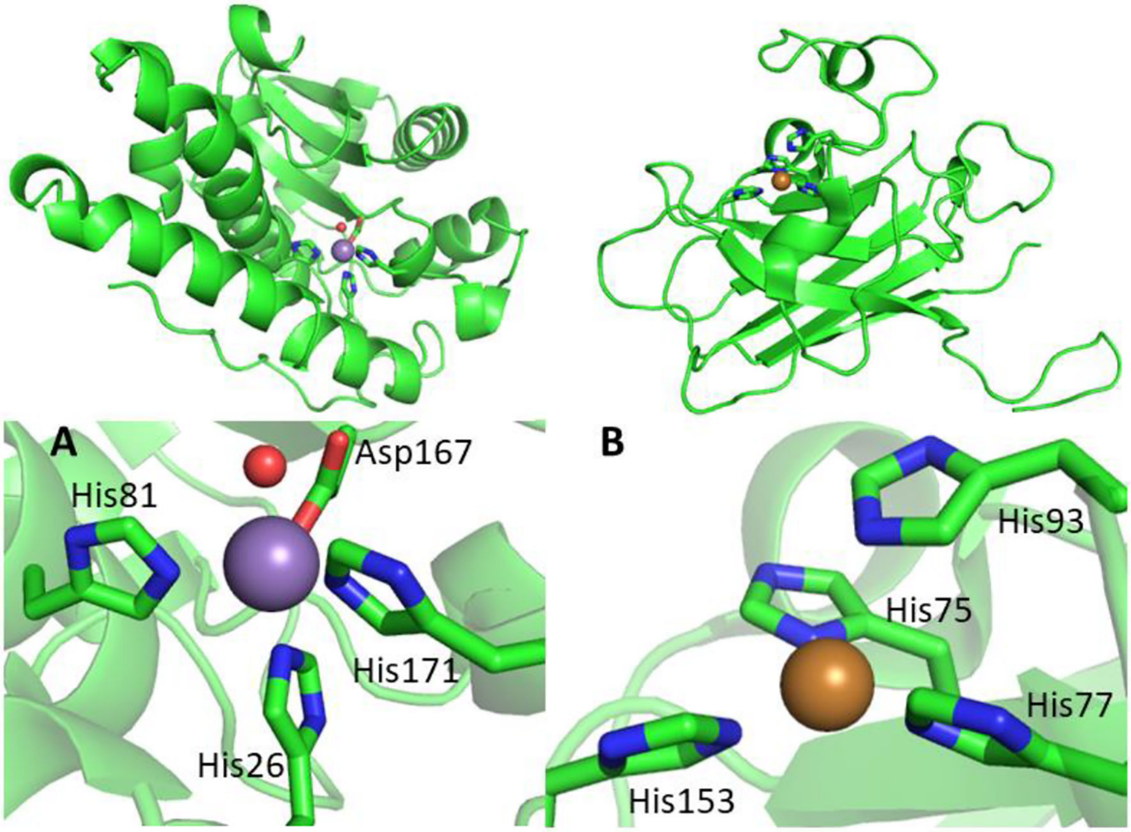

Figure 31:

Pymol illustrations of the overall protein fold (top) and enzyme active site (bottom) of (A) Mn superoxide dismutase (pdb 1VEW) or (B) Cu-only superoxide dismutase (PDB 4N3U). Mn(II) ions are depicted as silver spheres, Cu(II) ions are depicted as copper spheres, and waters are depicted as red spheres.

Author Manuscript

Author Manuscript

Author Manuscript

Author Manuscript

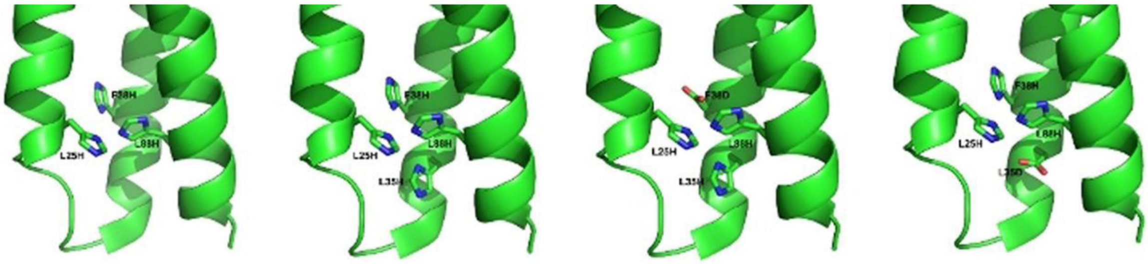

Figure 32:

Structural models of His_3 (H3), His_4 (H4), His_2AspHis (H2DH), and His_3Asp (H3D) active sites designed into $GR\alpha_3D$ (PDB 6DS9). Reprinted with permission from ref 259. Copyright 2019 John Wiley & Sons, Inc.

Author Manuscript
Author Manuscript
Author Manuscript
Author Manuscript

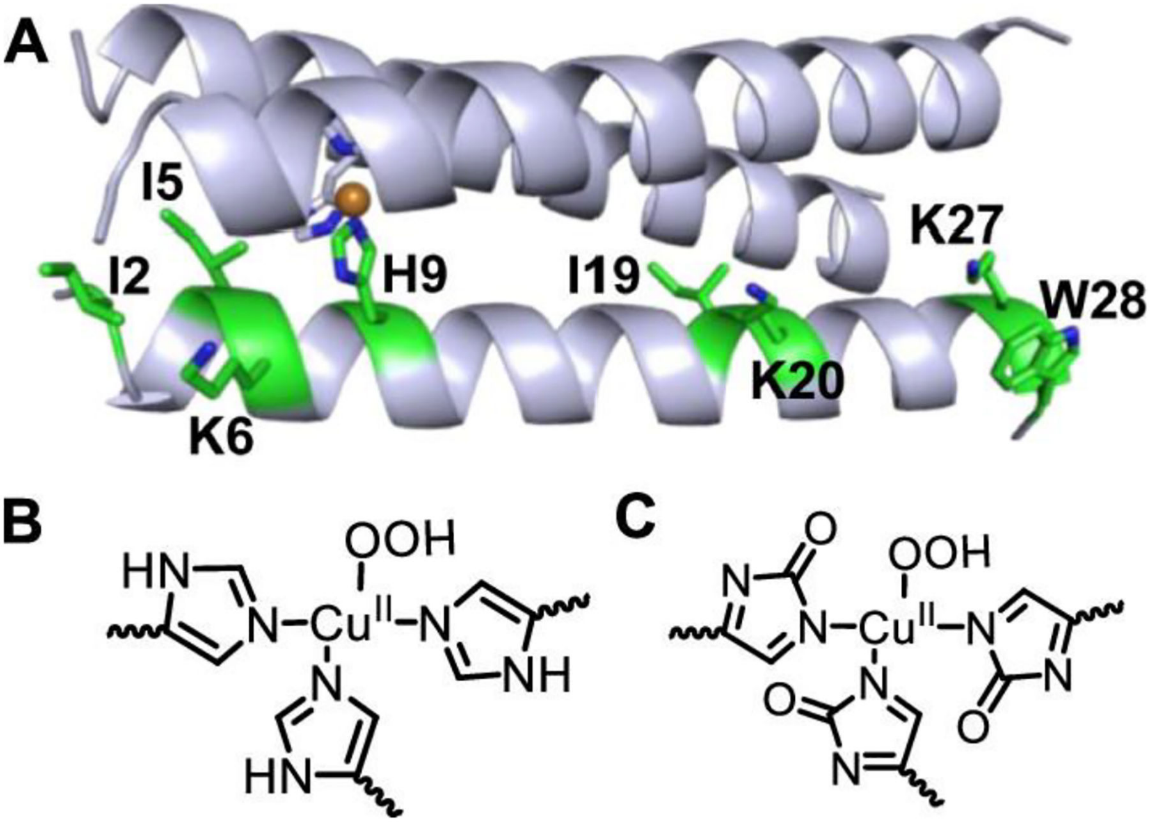

Figure 33:

(**A**) Structure of ArCuP highlighting the oxidizable residues on one strand as detected by LC-MS/MS. Proposed Cu(II)-OOH intermediates showing (**B**) unoxidized His residues or (**C**) proposed oxidative damage to the primary active site during catalysis. Reprinted with permission from ref 290. Copyright 2021 American Chemical Society.

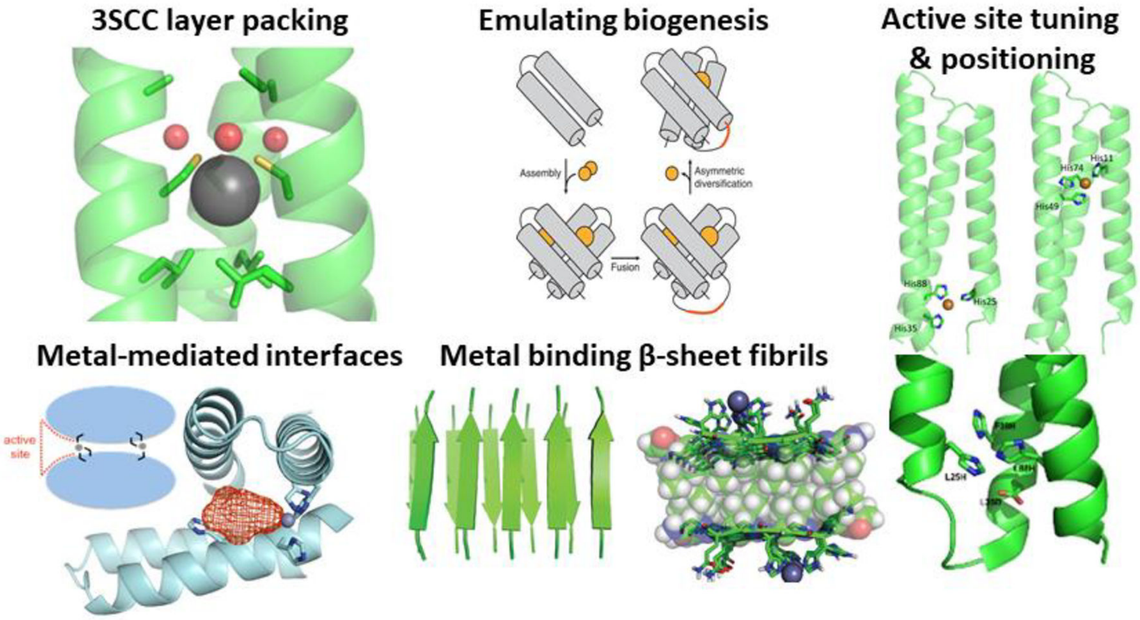

Figure 34:

Summary of recent advances in the *de novo* protein design of mono-metal enzymes highlighted in this review. Adapted with permission from the appropriate references as specified in source figures previously in manuscript.

Author Manuscript Author Manuscript Author Manuscript Author Manuscript

Author Manuscript Author Manuscript Author Manuscript Author Manuscript

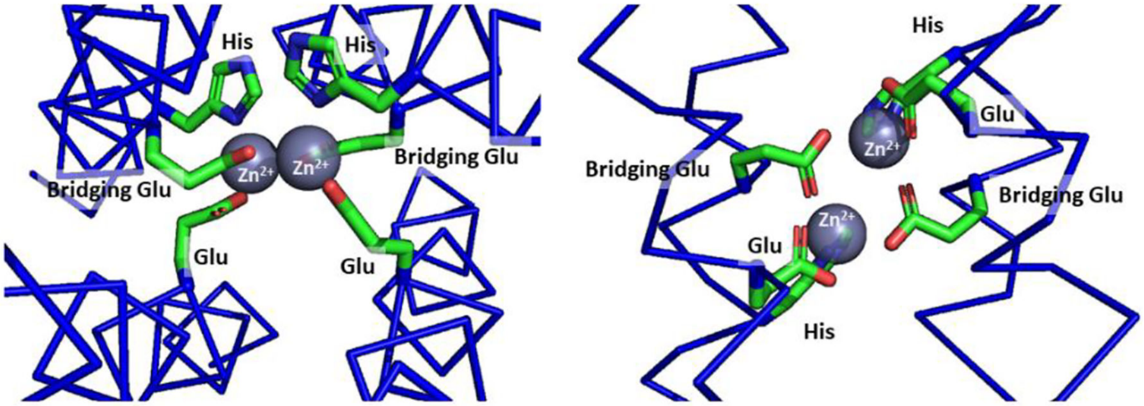

Figure 35:

Structure of an idealized diiron protein used for retrostructural analysis showcasing D2 symmetry and coordinating amino acids. Adapted with permission from ref 42. Copyright 2000 National Academy of Sciences.

Author Manuscript

Author Manuscript

Author Manuscript

Author Manuscript

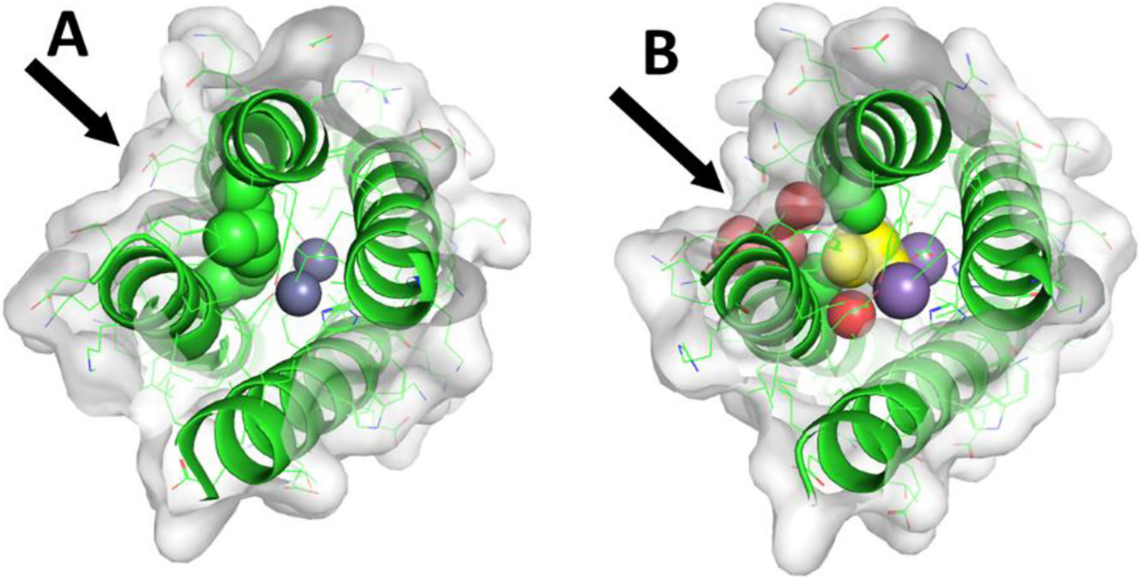

Figure 36:

(Left) Top view of DF1 active site which illustrates poor substrate access to the metal center (Violet Spheres) due to L13 and L13’ (green sphere). (Right) Illustration of L13A and L13’A mutations that open substrate access to the metal center (dimethyl sulfoxide is represented by yellow spheres and water is represented by red spheres). Adapted with permission from ref 326. Copyright 2001 American Chemical Society.

Author Manuscript Author Manuscript Author Manuscript Author Manuscript

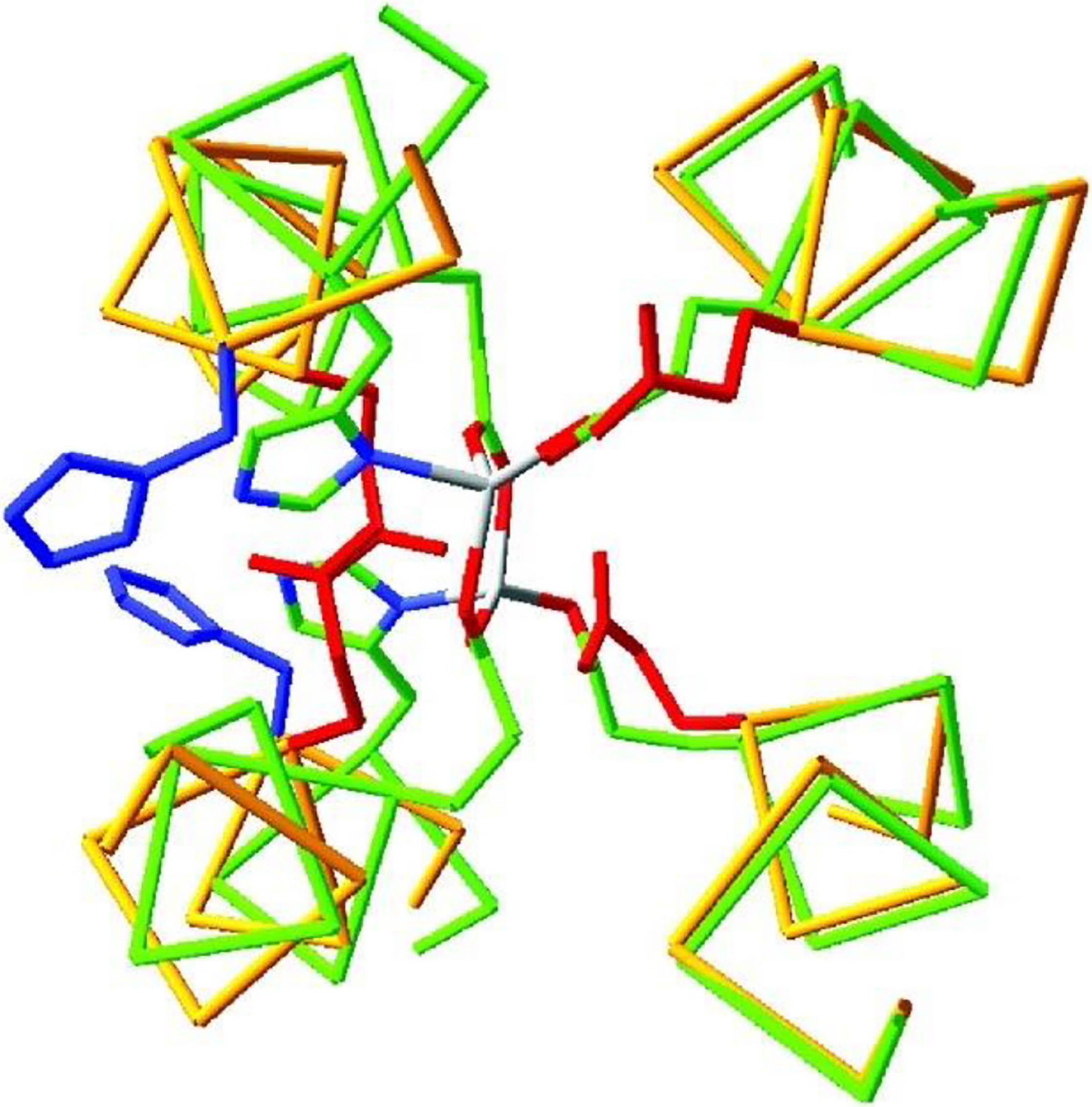

Figure 37:

Structural overlay of apo-DF1 and Di-Zn(II)-DF1 (side chains are plotted with Corey–Pauling–Koltun colors (C, green; N, blue; O, red) for the Di-Zn(II)-DF1 structure and the backbone of apo-DF1 is in yellow, the Glu side chain is in red, and the His residue is in blue.) The two right helices overlay with a higher degree of similarity than the two left helices which perturb and increase the exposure of His and Glu chains. Reprinted with permission from ref 336. Copyright 2003 National Academy of Sciences.

Author Manuscript Author Manuscript Author Manuscript Author Manuscript

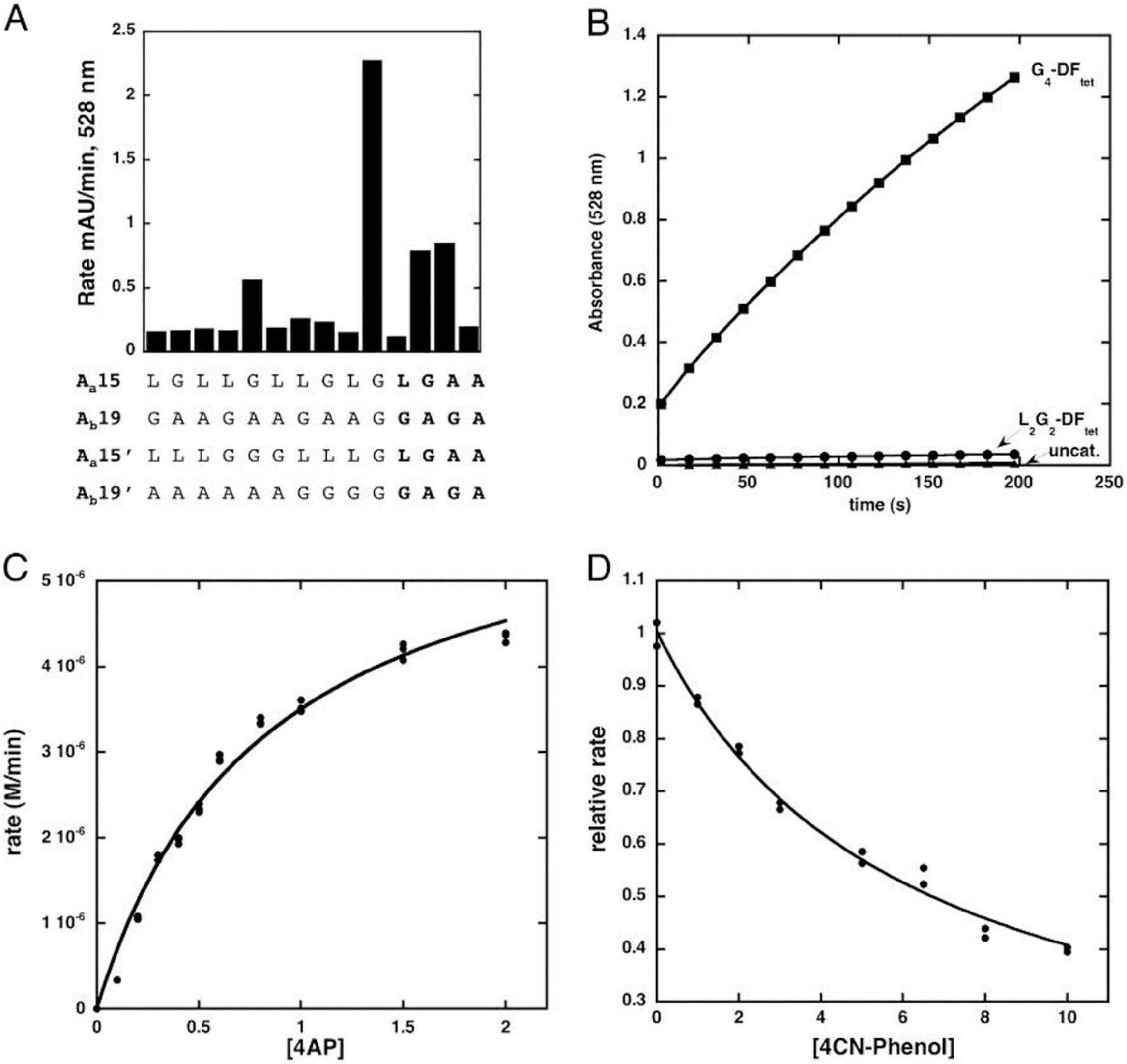

Figure 38:

(**A**) Rate of 4AP oxidation catalyzed by variants of DFtet AaAbB2 and DFtet. Bolded entries are from DFtet-A2B2. (**B**) Oxidation of 100 μM 4AP by G4-DFtet (squares) and L2G2-DFtet (diamonds) and the background reaction (triangles). (**C**) Steady state kinetic analysis of 4AP oxidation catalyzed by G4-DFtet. (**D**) Oxidation of 4AP competitively inhibited by 4CP. Reprinted with permission from ref 342. Copyright 2004 American Chemical Society.

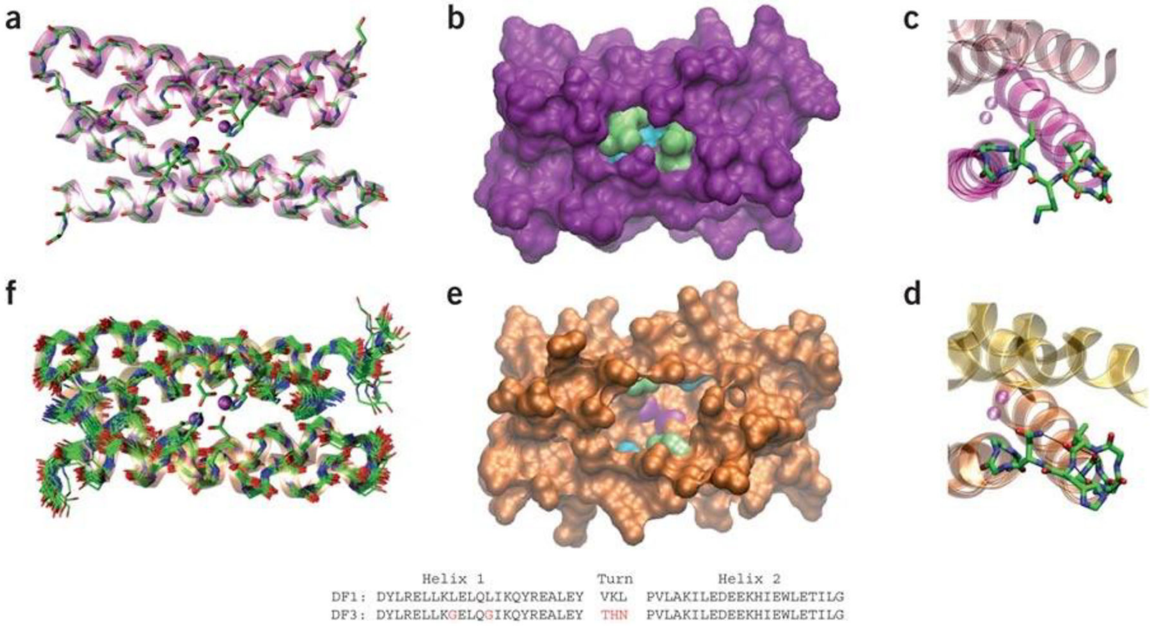

Figure 39:

(**A**) Crystal Structure of Di-Zn(II)-DF1 (PDB: 1JMB?). (**B**) Representation of Di-Zn(II)-DF1 emphasizing limited accessibility to active site (residue 9 (lime) and residue 13 (cyan)). (**C**) Di-Zn(II)-DF1 loop structure. (**D**) Di-Zn(II)-DF3 loop structure. (**E**) Representation of Di-Zn(II)-DF3 emphasizing improved accessibility to active site ((residue 9 (lime) and residue 13 (cyan)). (**F**) Overlay of 30 minimized structures of di-Zn(II)-DF3 from solution NMR. Reprinted with permission from ref 347. Copyright 2009 Nature America, Inc.

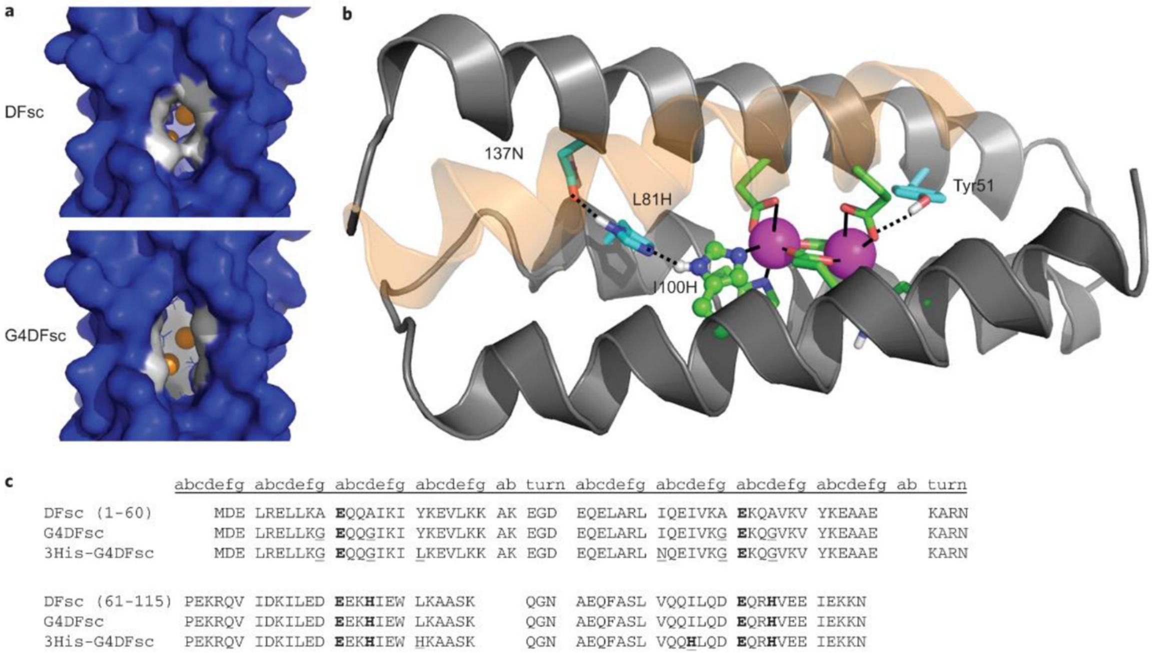

```
               abcdefg abcdefg abcdefg abcdefg ab turn abcdefg abcdefg abcdefg abcdefg ab turn
DFsc (1-60)        MDE LRELLKA EQQAIKI YKEVLKK AK EGD  EQELARL IQEIVKA EKQAVKV YKEAAE     KARN
G4DFsc             MDE LRELLKG EQQGIKI YKEVLKK AK EGD  EQELARL IQEIVKG EKQGVKV YKEAAE     KARN
3His-G4DFsc        MDE LRELLKG EQQGIKI LKEVLKK AK EGD  EQELARL NQEIVKG EKQGVKV YKEAAE     KARN

DFsc (61-115) PEKRQV IDKILED EEKHIEW LKAASK     QGN  AEQFASL VQQILQD EQRHVEE IEKKN
G4DFsc        PEKRQV IDKILED EEKHIEW LKAASK     QGN  AEQFASL VQQILQD EQRHVEE IEKKN
3His-G4DFsc   PEKRQV IDKILED EEKHIEW HKAASK     QGN  AEQFASL VQQHLQD EQRHVEE IEKKN
```

Figure 40:

(**A**) DFsc (top) and G4DFsc (bottom) represented as surface models to emphasize reduction in steric bulk from four Ala to Gly mutations in G4DFsc. (**B**) Structure of 3His-G2DFsc variant (PDB 2LFD) which emphasizes the active site histidine residue (H100) and supporting mutations (I37N and L81H). (**C**) Amino-acid sequences for DFsc, G4DFsc, and 3His-G4DFsc (Metal-binding residues are bolded and mutations are underlined). Reprinted with permission from ref 78. Copyright 2012 Macmillan Publishers Limited.

Author Manuscript
Author Manuscript
Author Manuscript
Author Manuscript

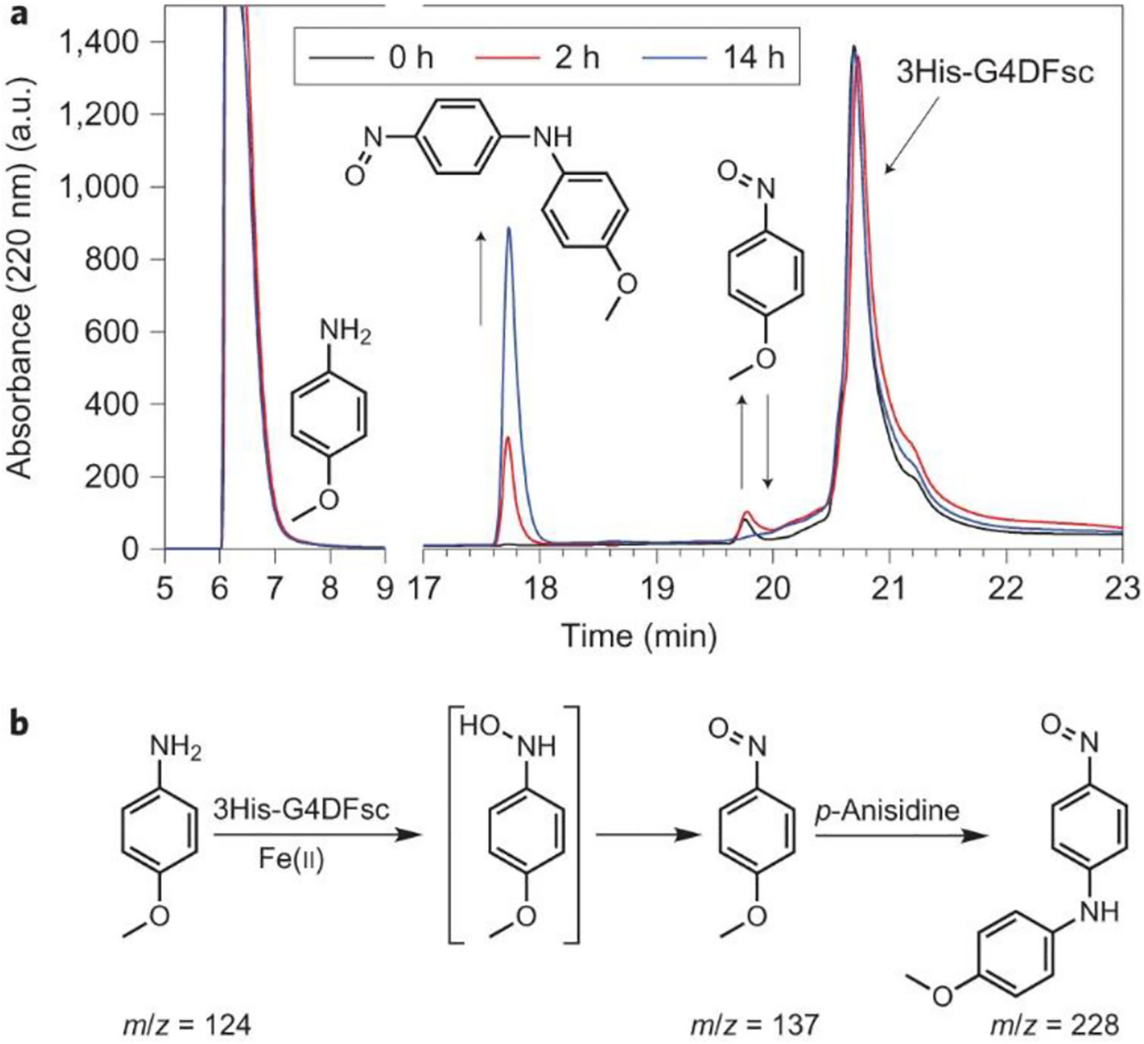

Figure 41:

(**A**) Reaction mixtures of 3His-G4DFsc with *p*-anisidine at various time points after mixing analyzed with HPLC chromatography. (**B**) Proposed oxidation reaction of *p*-anisidine to *p*-nitrosoanisole and eventual formation of 4-nitroso-4′-methoxydiphenylamine. Reprinted with permission from ref 78. Copyright 2012 Macmillan Publishers Limited.

Author Manuscript Author Manuscript Author Manuscript Author Manuscript

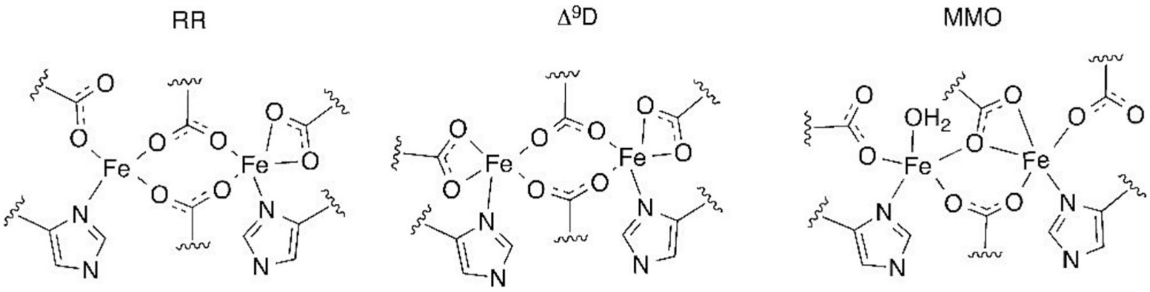

Figure 42:

Proposed structures of the diferrous sites in ribonucleotide reductase (RR), Δ9-desaturase (Δ^9D), and soluble methane monooxygenase (MMO). Reprinted with permission from ref 366. Copyright 2015 American Chemical Society.

Author Manuscript

Author Manuscript

Author Manuscript

Author Manuscript

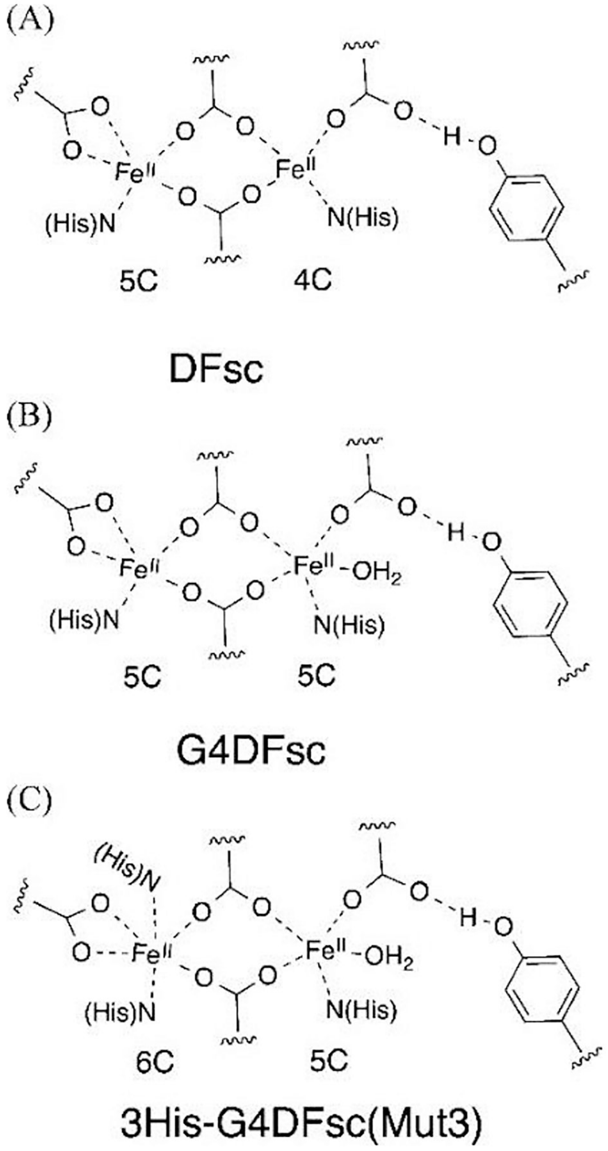

Figure 43:

Proposed structures of the diferrous forms of (**A**) DFsc, (**B**) the 4A → 4G 2His variants of DFsc, and (**C**) 3His-G4DFsc(Mut3). Reprinted with permission from ref 366. Copyright 2015 American Chemical Society.

Author Manuscript

Author Manuscript

Author Manuscript

Author Manuscript

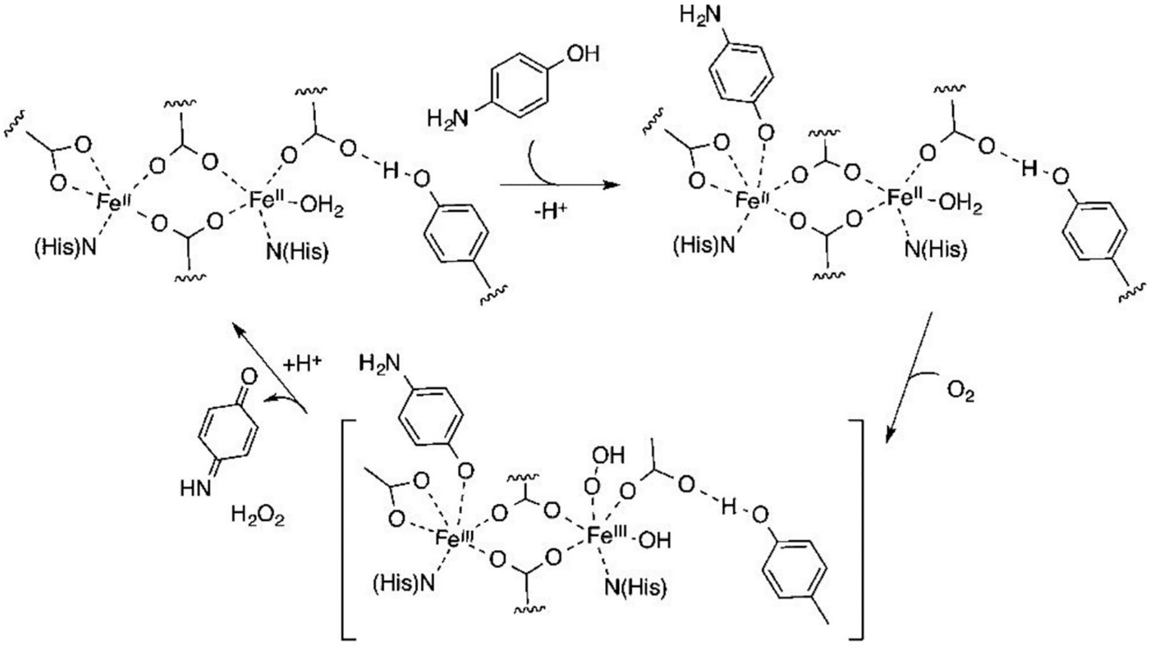

Figure 44:

Mechanism of 4-aminophenol oxidation by diferrous protein. Reprinted with permission from ref 373. Copyright 2015 American Chemical Society.

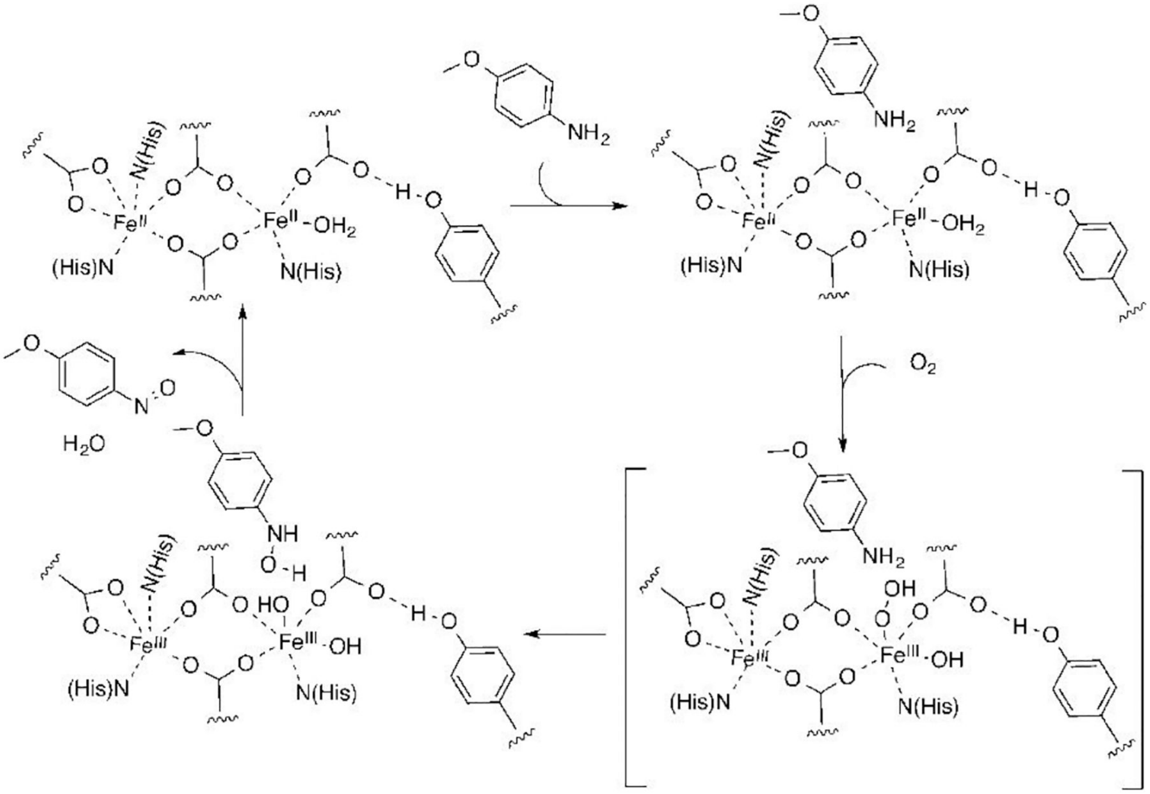

Figure 45:

Mechanism of O-atom transfer to *p*-anisidine by 3His-G4DFsc(Mut3). Reprinted with permission from ref 373. Copyright 2015 American Chemical Society.

Author Manuscript

Author Manuscript Author Manuscript Author Manuscript Author Manuscript

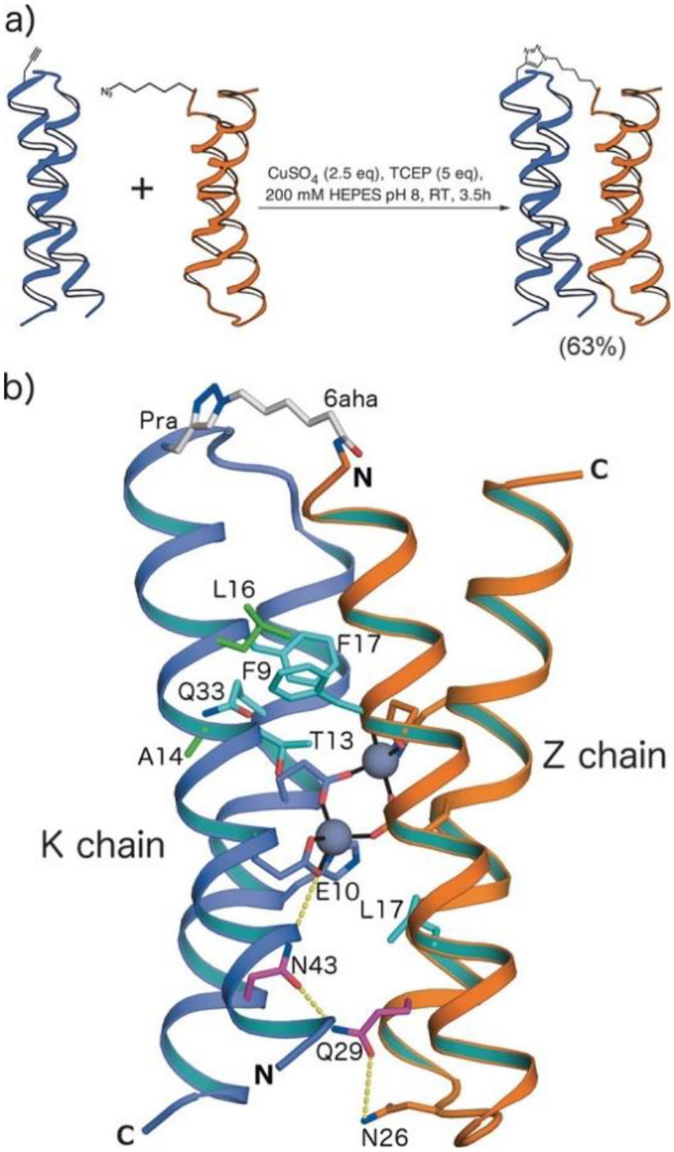

Figure 46:

(**A**) Click reaction to form DF-C1 with the K-chain in blue and Z-chain in orange. (**B**) Computational model of ZnII-DF-C1. Classes of mutations are represented as: (cyan) active site access, substrate recognition and catalysis, (magenta) H-bond network, or (green) packing improvement. Hydrogen bonds are represented by dashed yellow lines. Reprinted with permission from ref 77. Copyright 2017 Wiley-VCH GmbH & Co.

Author Manuscript Author Manuscript Author Manuscript Author Manuscript

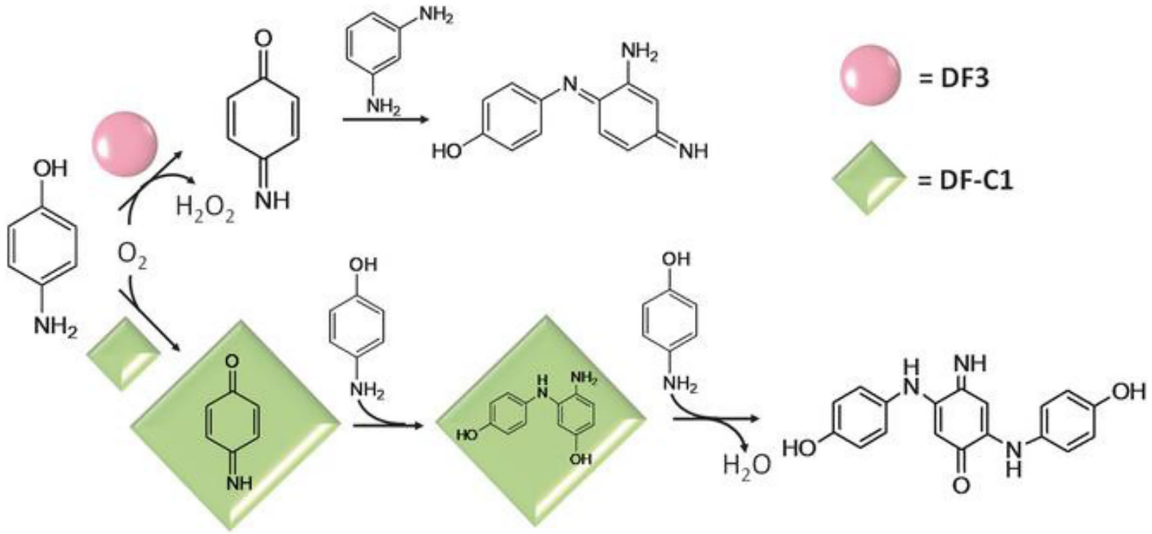

Figure 47:

O_2-dependend oxidation of 4AP catalyzed by FeII-DF3 or FeII-DF-C1. With DF3, MPD quenched the 4BQM once released into solution; however, 4BQM remains bound to the active site of DF-C1 and couples to another molecular of 4AP before release. Reprinted with permission from ref 77. Copyright 2017 Wiley-VCH GmbH & Co.

Author Manuscript Author Manuscript Author Manuscript Author Manuscript

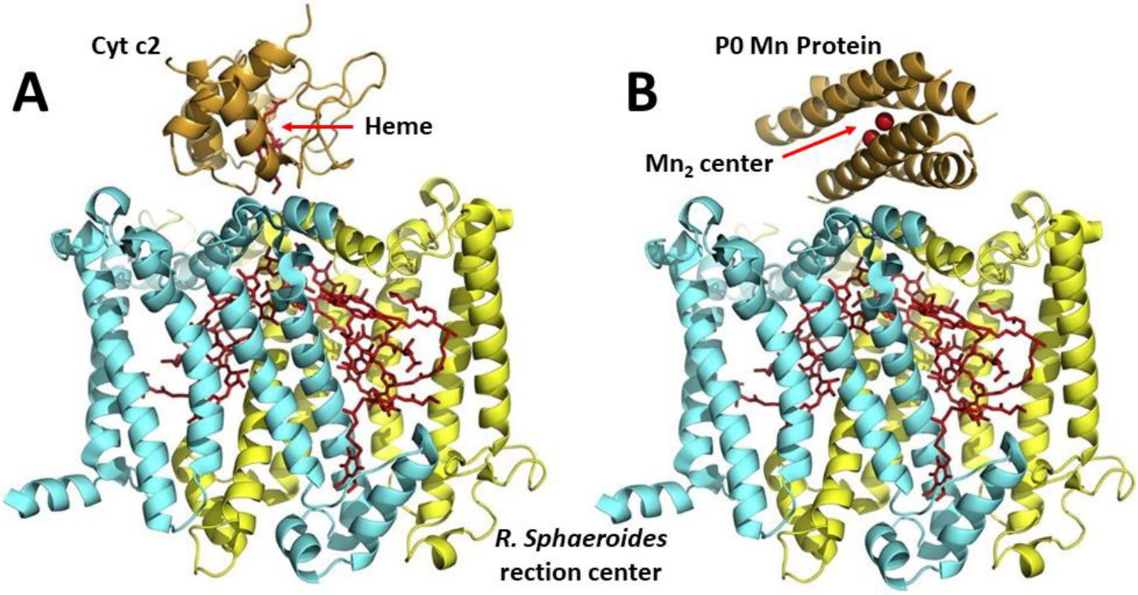

Figure 48:

Illustration comparing reaction centers with bound cytochrome *c*2 and P0 Mn protein. Structures highlight the cofactors (red), L (yellow) and M (cyan) subunits of the reaction center with the bound cytochrome *c*2 (orange) and heme (red) (PDB code 1L9B). Adapted with permission from ref 381. Copyright 2016 Elsevier B.V.

Author Manuscript

Author Manuscript

Author Manuscript

Author Manuscript

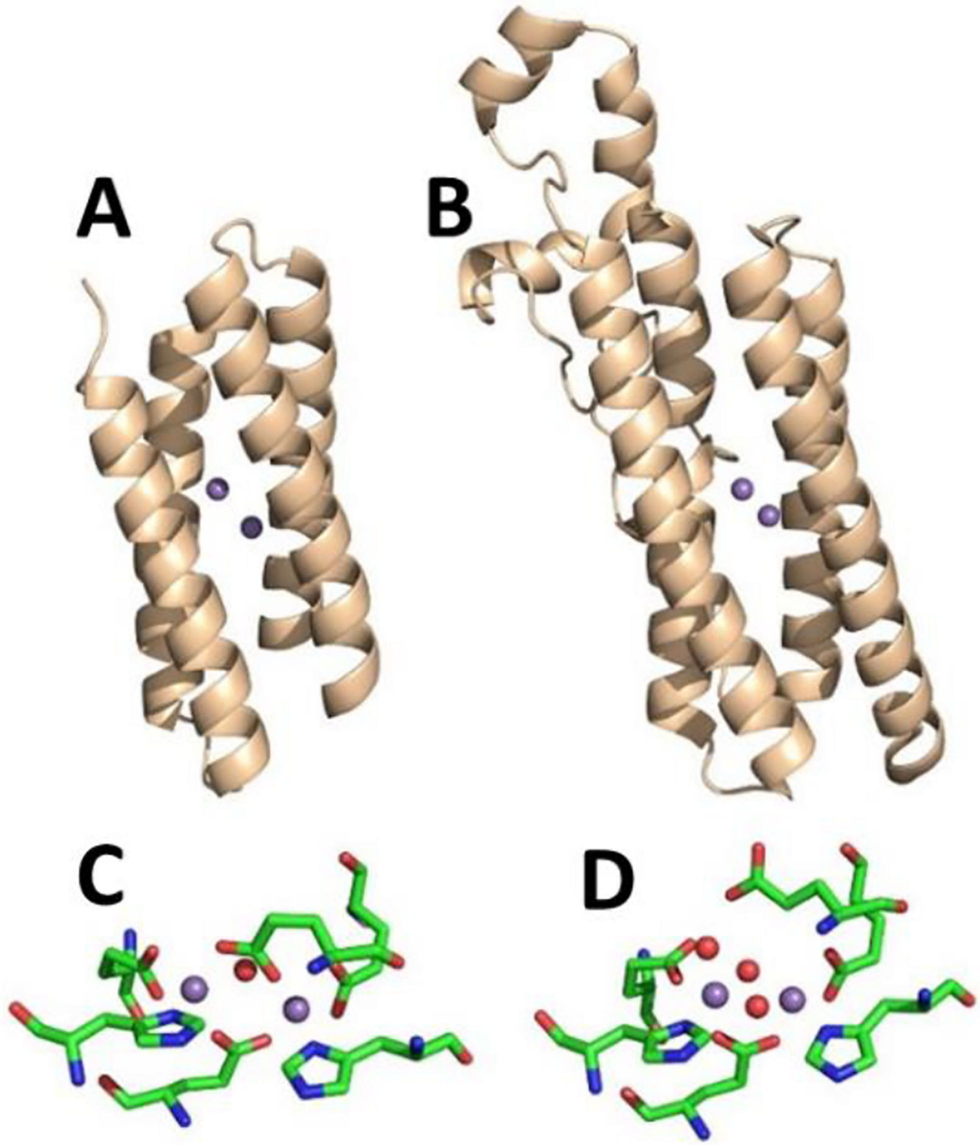

Figure 49:

X-ray structures of P0 Mn-protein (**A** and **C**) and *Lactobacillus plantarum* Mn-catalase (**B** and **D**) with overall structures (**A** and **B**) and Mn_2-clusters (**C** and **D**). PDB 5C39 and 1JKU. Adapted with permission from ref 382. Copyright 2016 Elsevier B.V.

Author Manuscript Author Manuscript Author Manuscript Author Manuscript

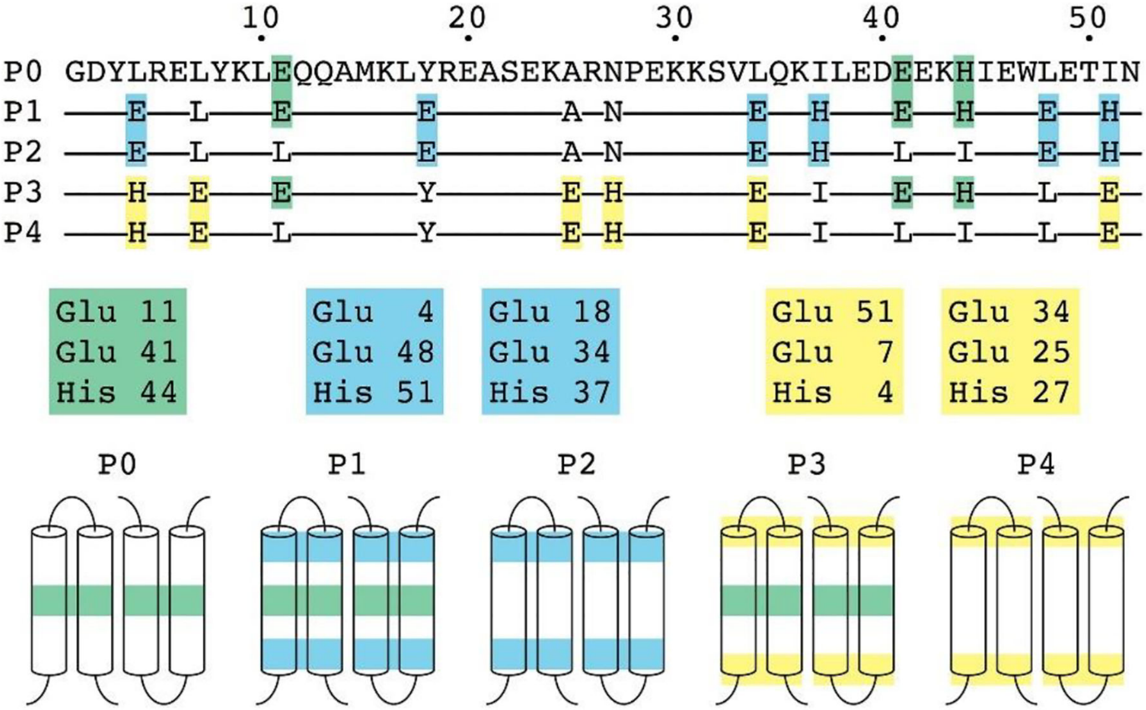

Figure 50:

Illustration of the design evolution of metal-binding sites in the Mn-protein. From the protein sequence of DF2t (P0), additional dinuclear binding sites were designed to yield four new proteins (P1, P2, P3, and P4). Reprinted with permission from ref 382. Copyright 2016 Elsevier B.V.

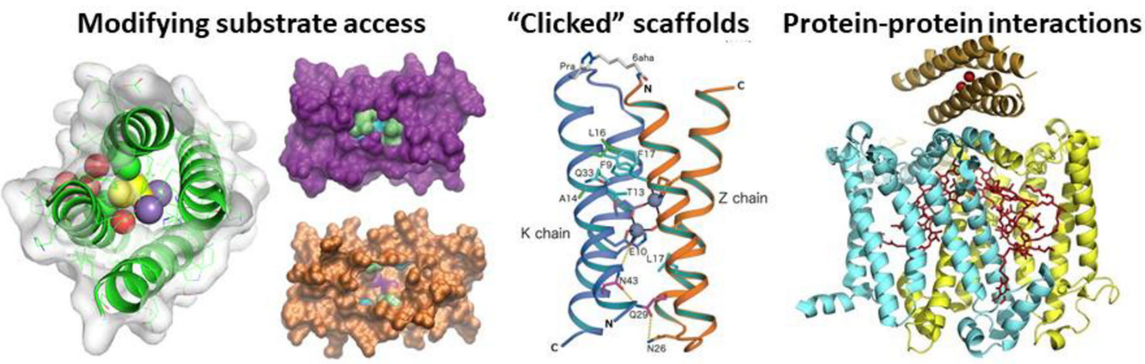

Figure 51:

Summary of recent advances in the *de novo* protein design of di-metal enzymes highlighted in this review. Adapted with permission from the appropriate references as specified in source figures previously in manuscript.

Author Manuscript

Author Manuscript

Author Manuscript

Author Manuscript

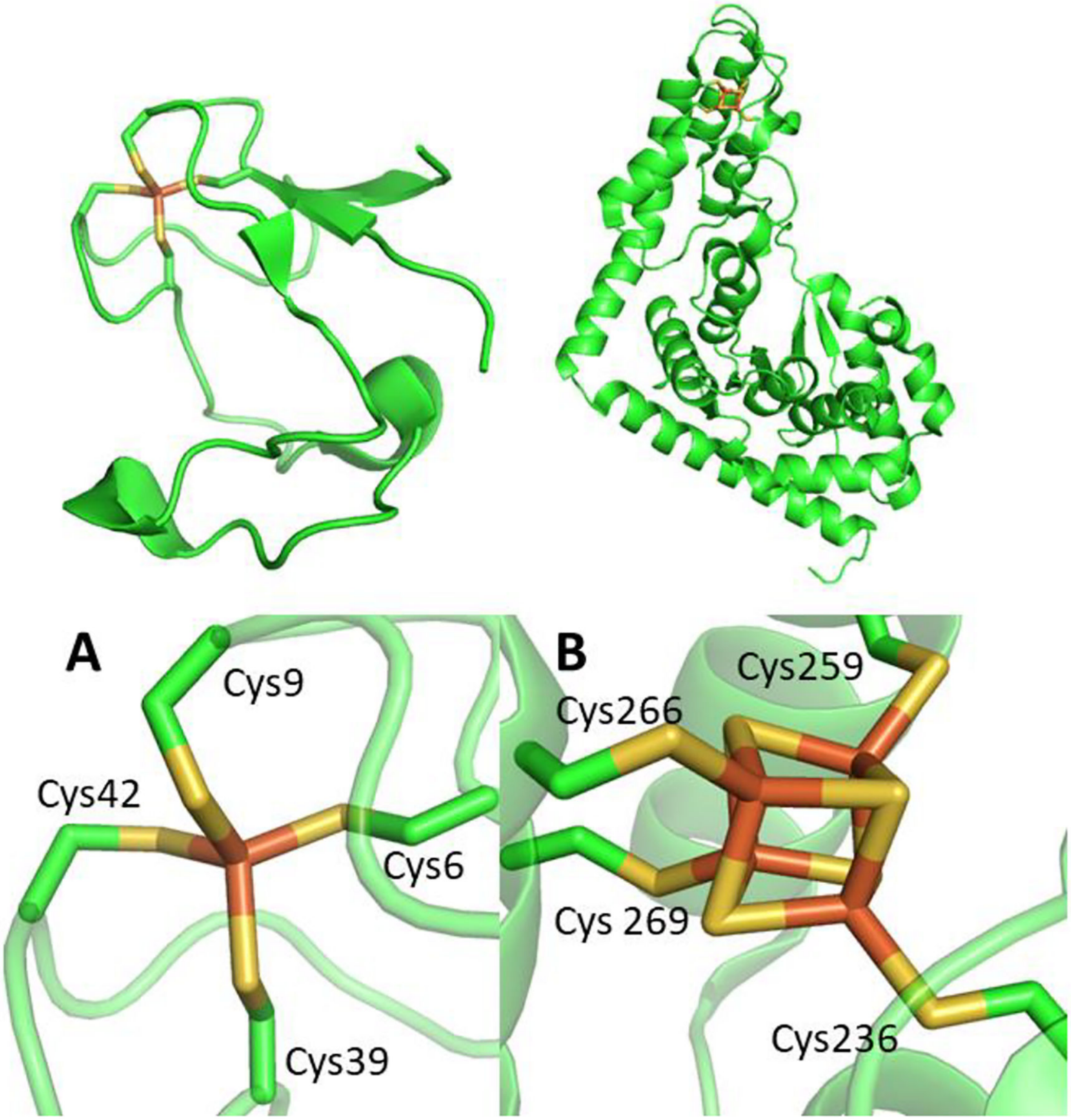

Figure 52:

Pymol illustrations of the overall protein fold (top) and metal binding site (bottom) of (A) Rubredoxin (pdb 8RXN) or (B) Tryptophanyl-tRNA synthetase (pdb 2G36). FeS clusters and coordinating Cys residues are depicted as sticks.

Author Manuscript

Author Manuscript

Author Manuscript

Author Manuscript

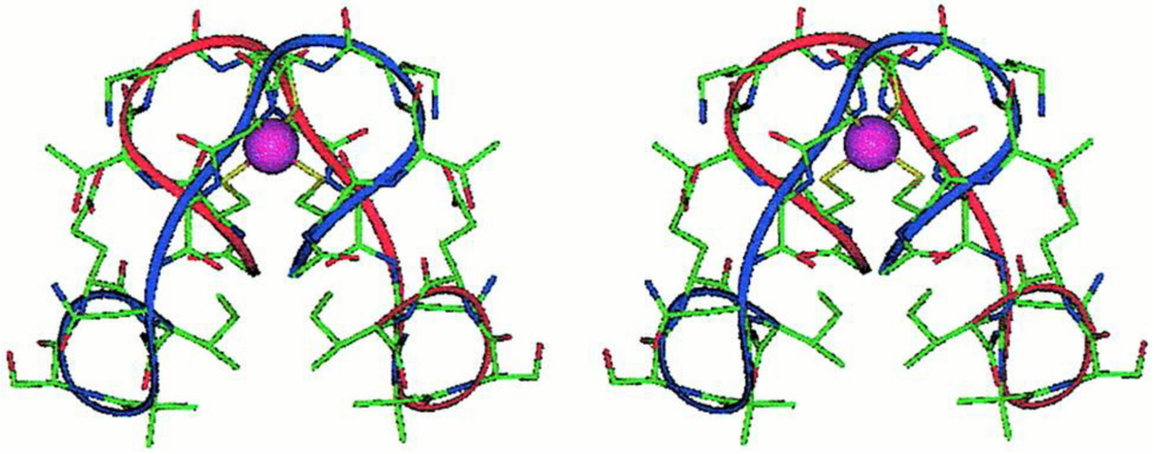

Figure 53:

Computational model of Fe(II)-METP complex. Reprinted with permission from ref 414. Copyright 2000 National Academy of Sciences.

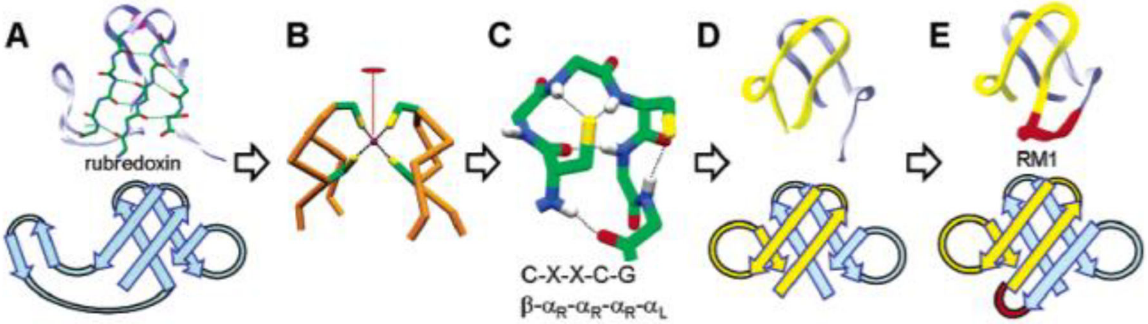

Figure 54:

Illustration of design workflow for RM1: (**A**) Topology of native rubredoxin. (**B**) C_2 symmetric active site. (**C**) Minimal geometry around active site. Illustration showing (**D**) miniRM and RM1 (**E**) with Trpzip linker shown in red. Reprinted with permission from ref 431. Copyright 2005 American Chemical Society

Author Manuscript
Author Manuscript
Author Manuscript
Author Manuscript

Author Manuscript

Author Manuscript

Author Manuscript

Author Manuscript

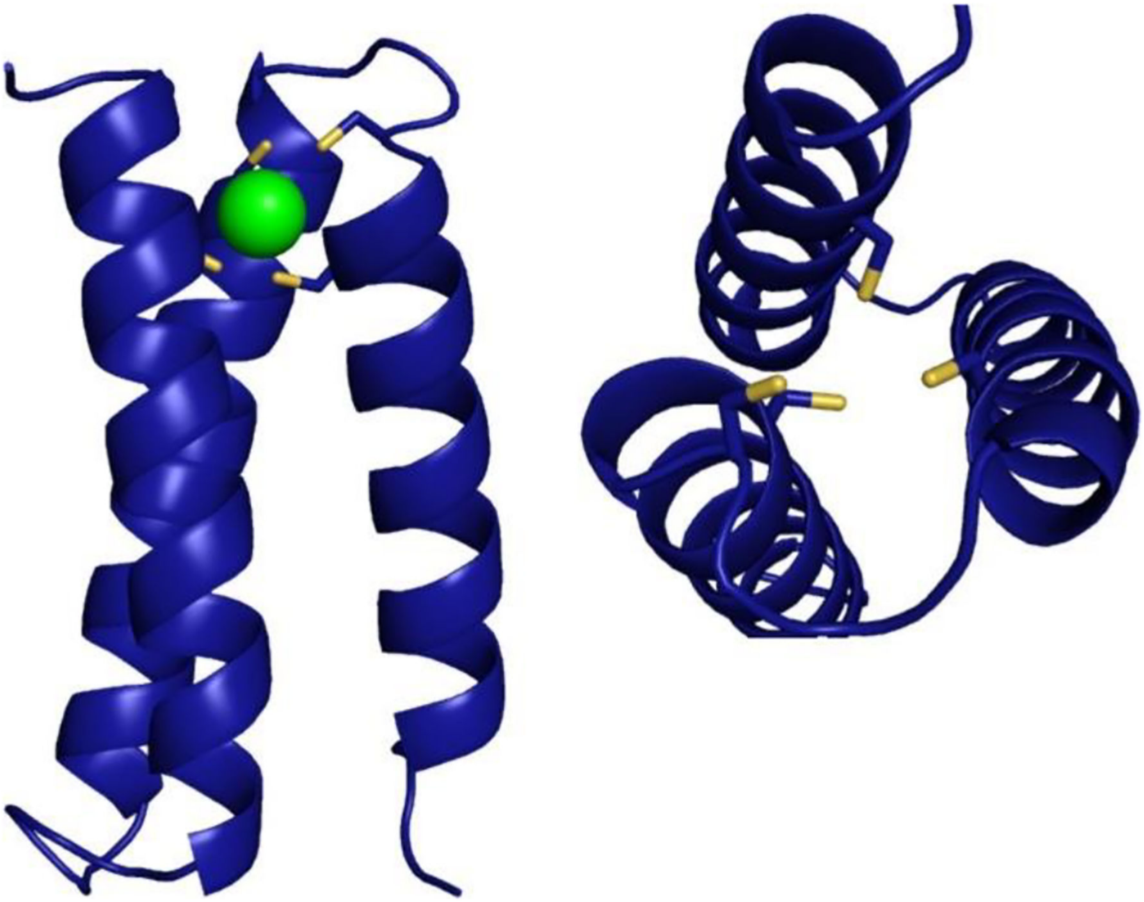

Figure 55:

Illustration of the designed rubredoxin, α_3DIV-L21C-Fe, derived from the NMR structure of α_3DIV (PDB 2MTQ). Reprinted with permission from ref 181. Copyright 2018 American Chemical Society.

Author Manuscript Author Manuscript Author Manuscript Author Manuscript

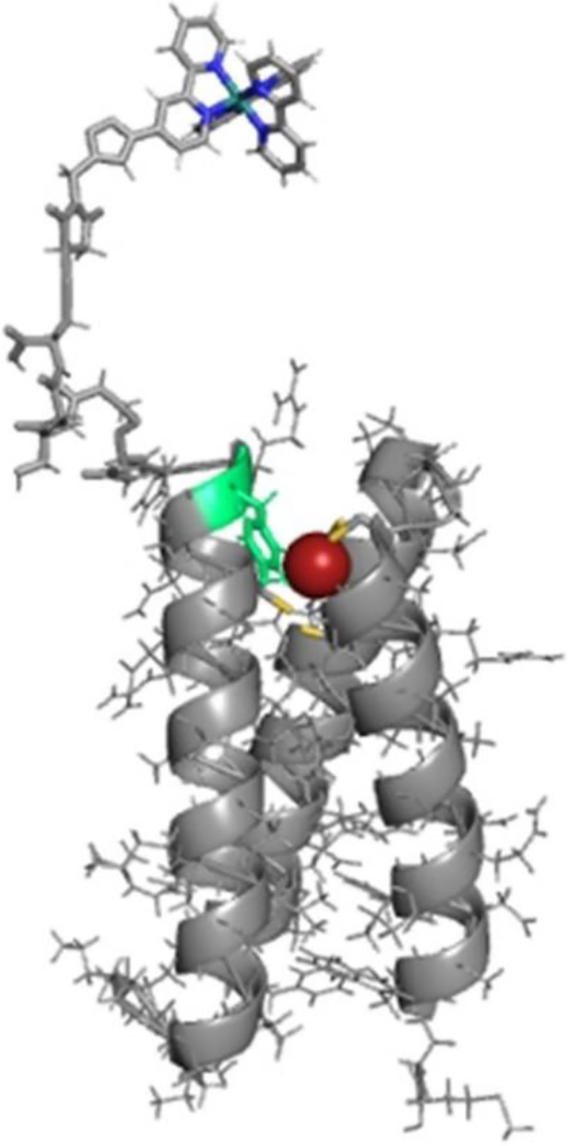

Figure 56:

Illustration of α_3DIV-L21C-Rubpymal derived from the solution structure of α_3DIV (PDB 2MTQ). Tyr70 is shown in green. Reprinted with permission from ref 444. Copyright 2017 Wiley-VCH Verlag GmbH & Co.

Author Manuscript Author Manuscript Author Manuscript Author Manuscript

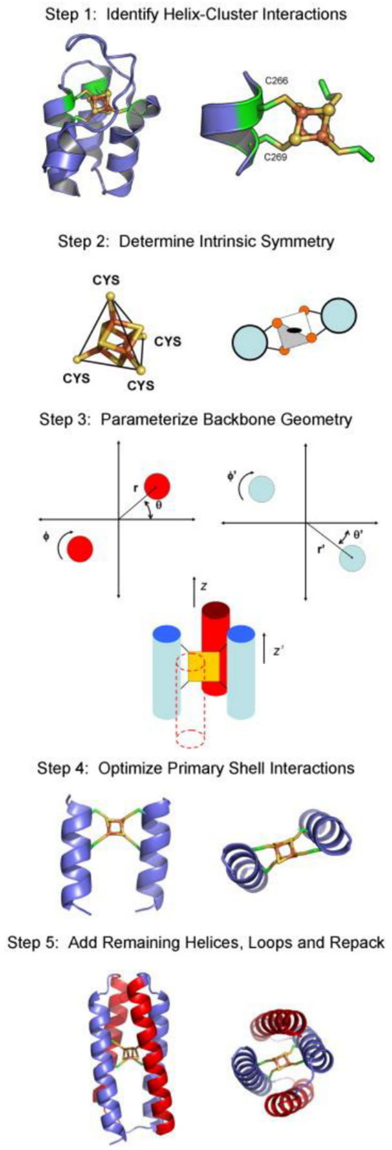

Figure 57:

Design of a [4Fe-4S] cluster binding site in a computationally derived four-helix bundle. Reprinted with permission from ref 459. Copyright 2009 Elsevier B.V.

Author Manuscript Author Manuscript Author Manuscript Author Manuscript

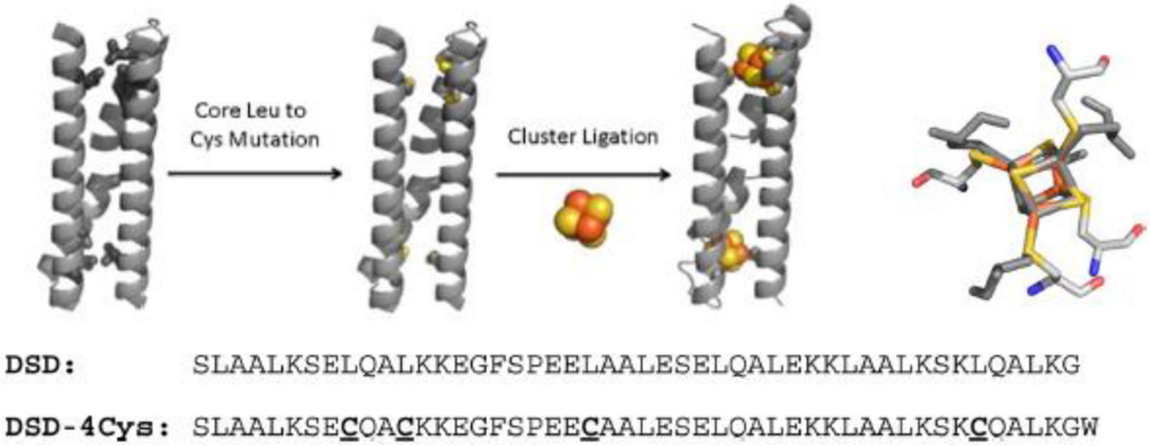

Figure 58:

Design of DSD-bis[4Fe-4S]. Structure of DSD (PDB 2G6U) serves as a starting point into which a [4Fe-4S] cluster binding site was docked by mutating the appropriate leucine residues to cysteines (highlighted in bold in sequences). Reprinted with permission from ref 70. Copyright 2013 American Chemical Society

Author Manuscript

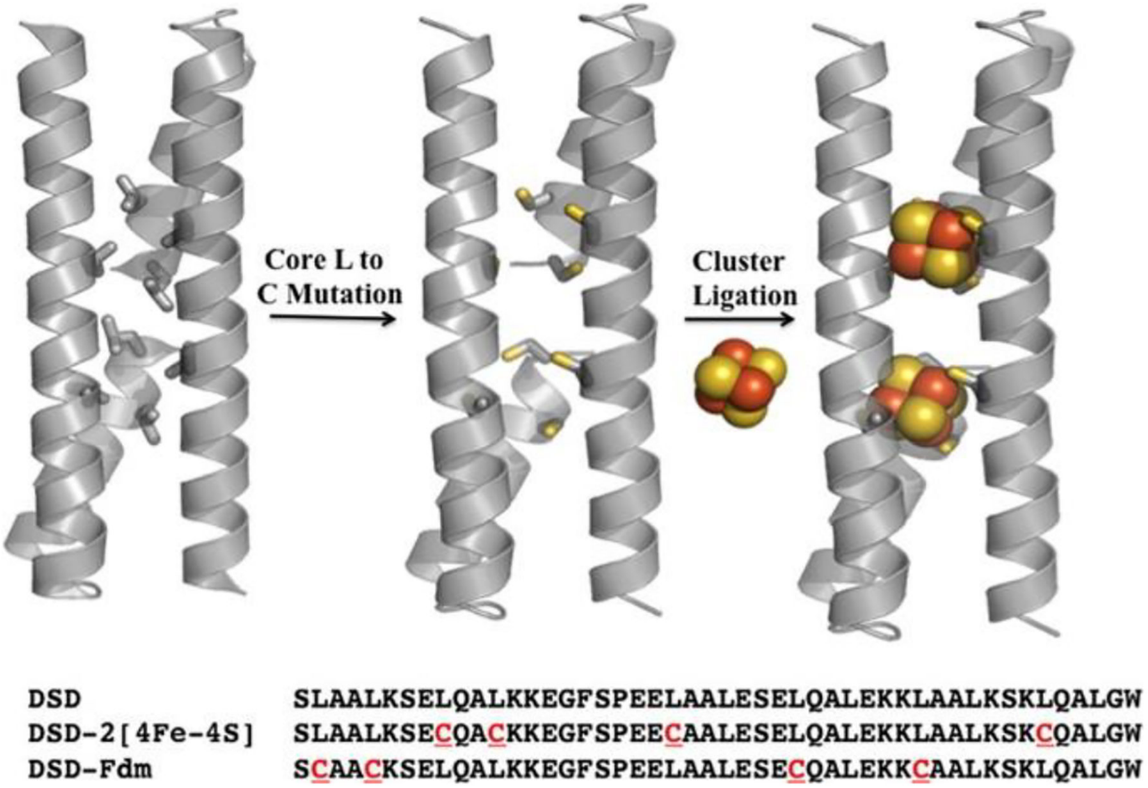

Figure 59:

Strategy for DSD-Fdm design (top) and sequence comparison of DSD, DSD-2[4Fe4S], and DSD-Fdm (bottom). Reprinted with permission from ref 473. Copyright 2014 American Chemical Society

Author Manuscript Author Manuscript Author Manuscript Author Manuscript

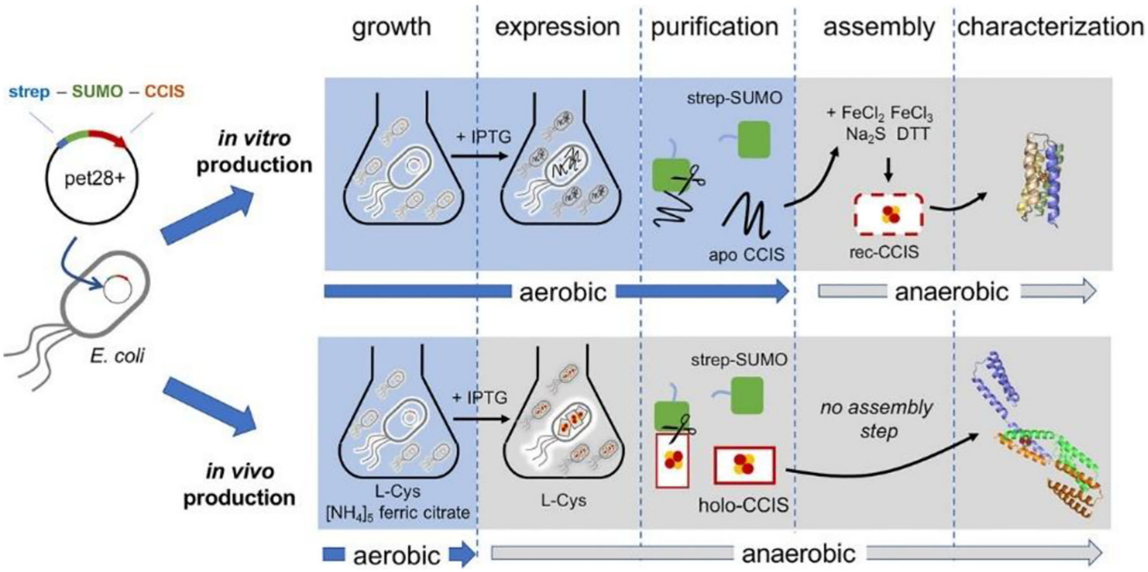

Figure 60:

Process of producing [4Fe-4S] cluster bound CCIS *in vitro* vs *in vivo*. Reprinted with permission from ref 478. Copyright 2020 American Chemical Society.

Author Manuscript Author Manuscript Author Manuscript Author Manuscript

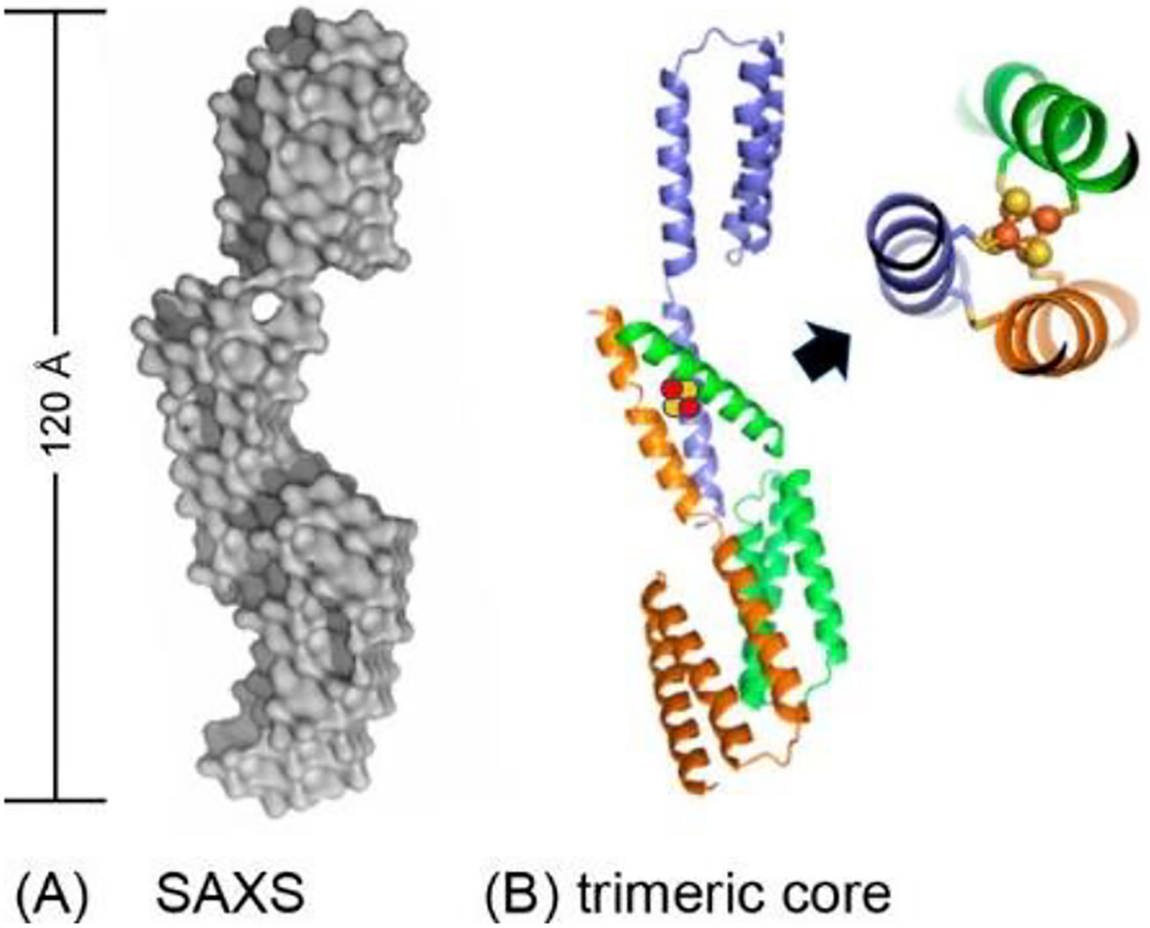

Figure 61:

(**A**) SAXS derived model of holo-CCIS. (**B**) Structure of a three-lobed trimer contained within an antiparallel three-helix bundle to fit the observed SAXS density. Adapted with permission from ref 478. Copyright 2020 American Chemical Society

Author Manuscript Author Manuscript Author Manuscript Author Manuscript

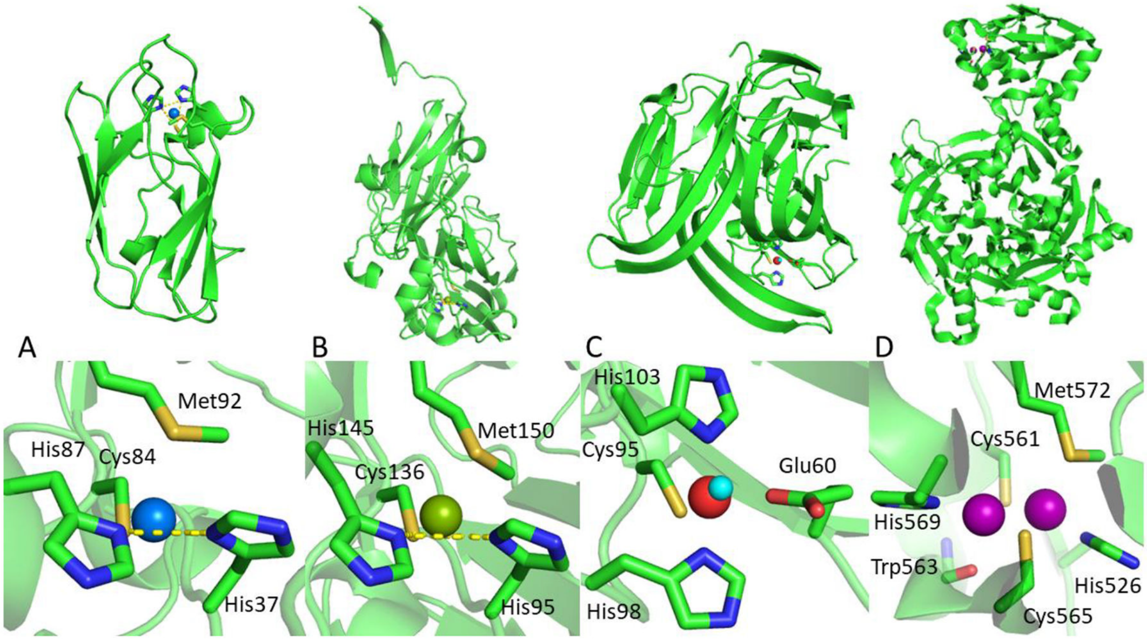

Figure 62:

Pymol illustrations of the overall protein fold and Cu binding sites of (**A**) plastocyanin (4DPB), (**B**) Cu nitrite reductase (1SJM), (**C**) nitrosocyanin (1IBY), and (**D**) nitrous oxide reductase (1FWX). Cu(II) ions are depicted as blue, green, red, or purple spheres, water as a cyan sphere, and the N_δHis-N_δHis-Cys plane as a dashed line to emphasize the shifting position of Cu between plastocyanin and Cu nitrite reductase. Adapted with permission from ref 524. Copyright 2020 American Chemical Society.

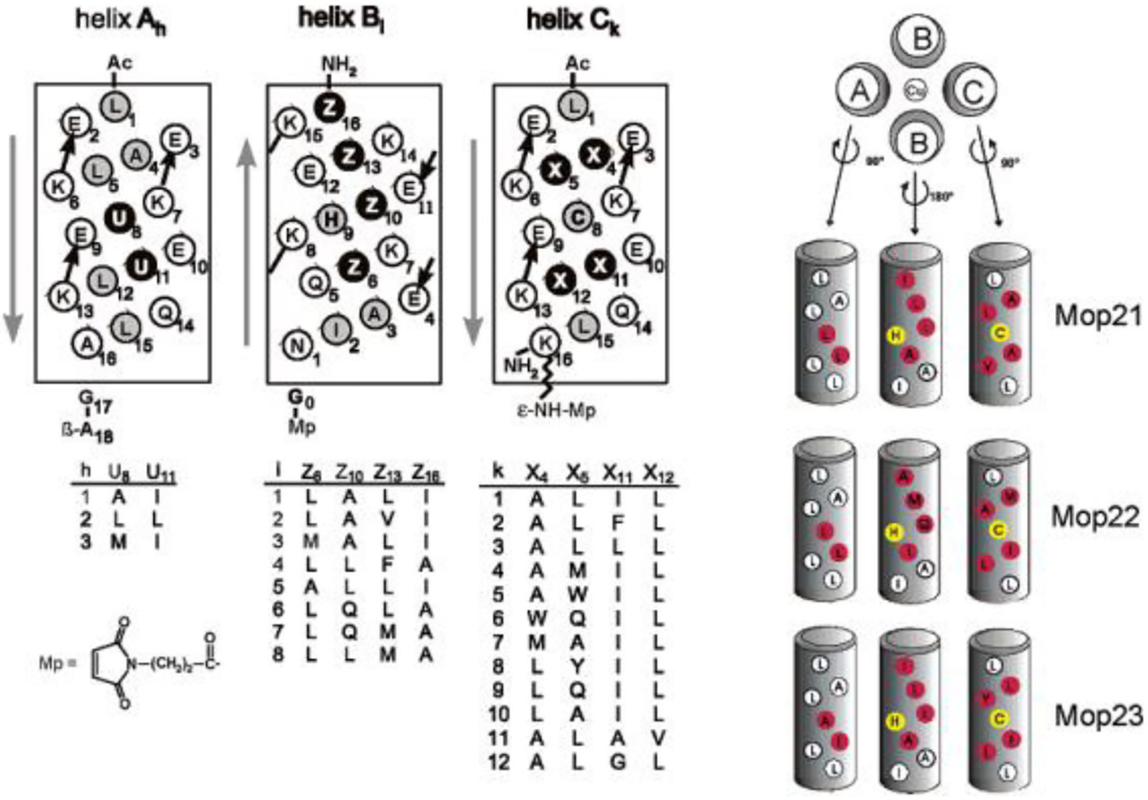

h	U_8	U_{11}
1	A	I
2	L	L
3	M	I

i	Z_6	Z_{10}	Z_{13}	Z_{16}
1	L	A	L	I
2	L	A	V	I
3	M	A	L	I
4	L	L	F	A
5	A	L	L	I
6	L	Q	L	A
7	L	Q	M	A
8	L	L	M	A

k	X_4	X_5	X_{11}	X_{12}
1	A	L	I	L
2	A	L	F	L
3	A	L	L	L
4	A	M	I	L
5	A	W	I	L
6	W	Q	I	L
7	M	A	I	L
8	L	Y	I	L
9	L	Q	I	L
10	L	A	I	L
11	A	L	A	V
12	A	L	G	L

Figure 63:

(Left) Helices A_h, B_i, and C_k represented as helical nets. Filled black circles correspond to varied positions and invariant hydrophobic or polar residues are represented by gray and open circles, respectively. (Right) Illustration of the helices that make up Mop21 ($A_2(B_5)_2C_{11}$), Mop22 ($A_2(B_7)_2C_4$), and Mop23 ($A_1(B_5)_2C_8$) with ligating residues in yellow and varied positions in red. Reprinted with permission from ref 501. Copyright 2004 American Chemical Society

Author Manuscript Author Manuscript Author Manuscript Author Manuscript

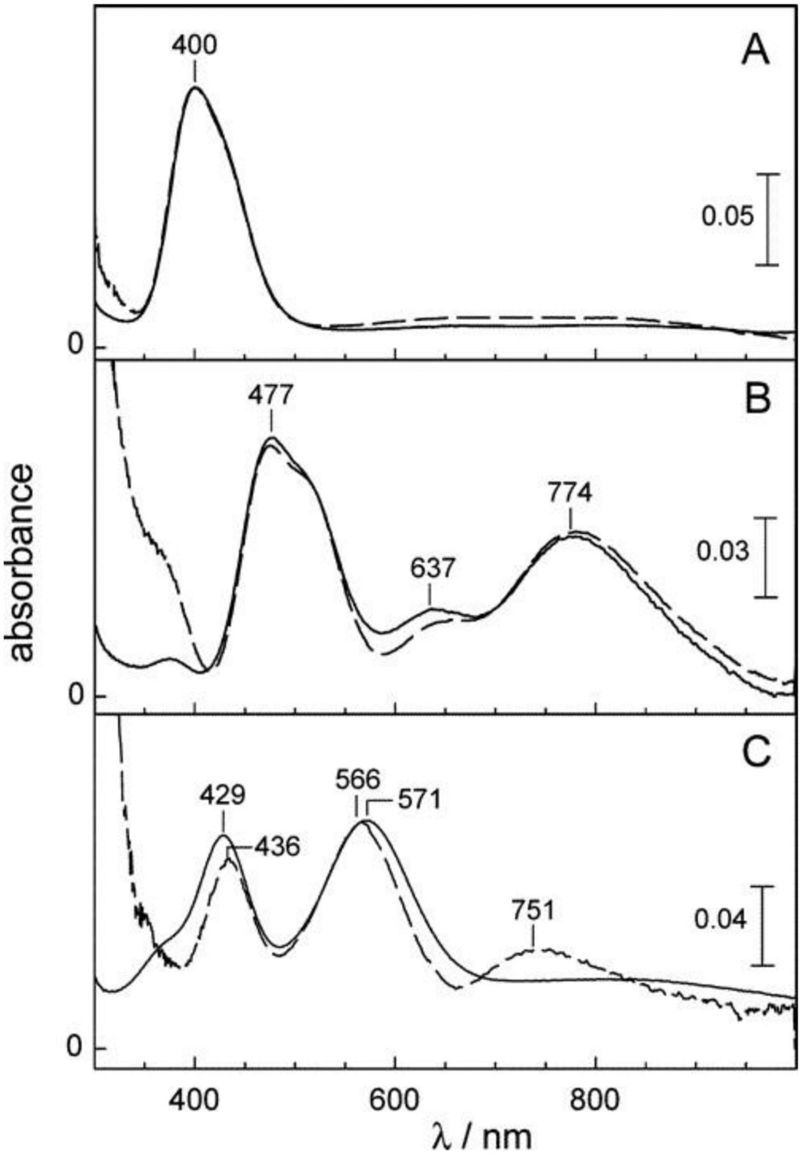

Figure 64:

Electronic absorption spectra of Cu(II) bound (**A**) Mop21 (**B**) Mop22, and (**C**) Mop23 with solution spectra represented by solid lines and solid phase spectra by dashed lines. Reprinted with permission from ref 501. Copyright 2004 American Chemical Society

Author Manuscript Author Manuscript Author Manuscript Author Manuscript

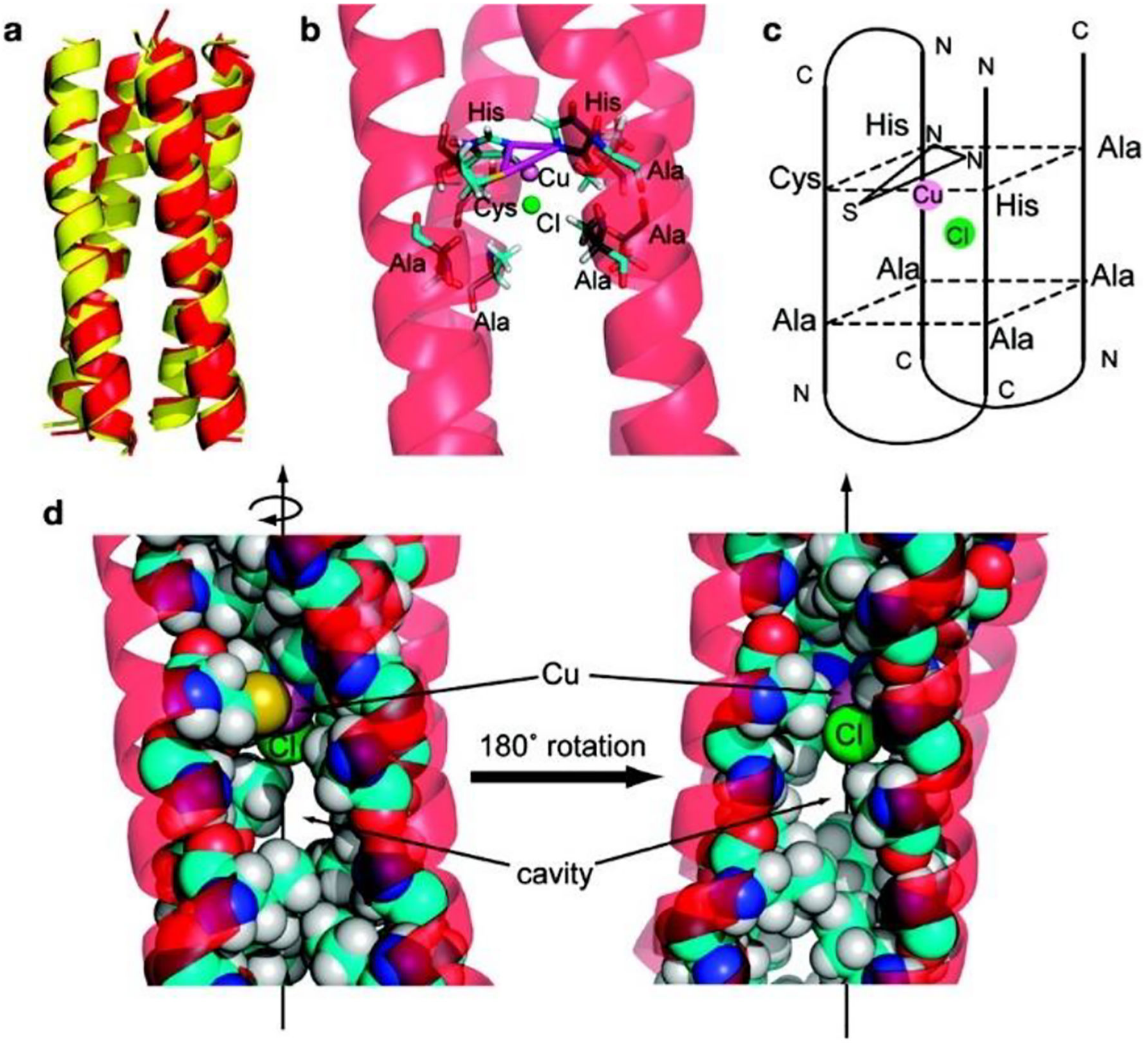

Figure 65:

(**A**) Overlay emphasizing similarity between starting structure of AM2C−Cu^{2+} and its energy minimized structure. (**B**) Side view of the minimized active site of AM2C−Cu^{2+}. (**C**) Schematic of the minimized structure of AM2C−Cu^{2+}. (**D**) Space filled model of AM2C−Cu^{2+}, highlighting the inner packing with internal residues represented by spheres. Reprinted with permission from ref 510. Copyright 2010 American Chemical Society

Author Manuscript

Author Manuscript

Author Manuscript

Author Manuscript

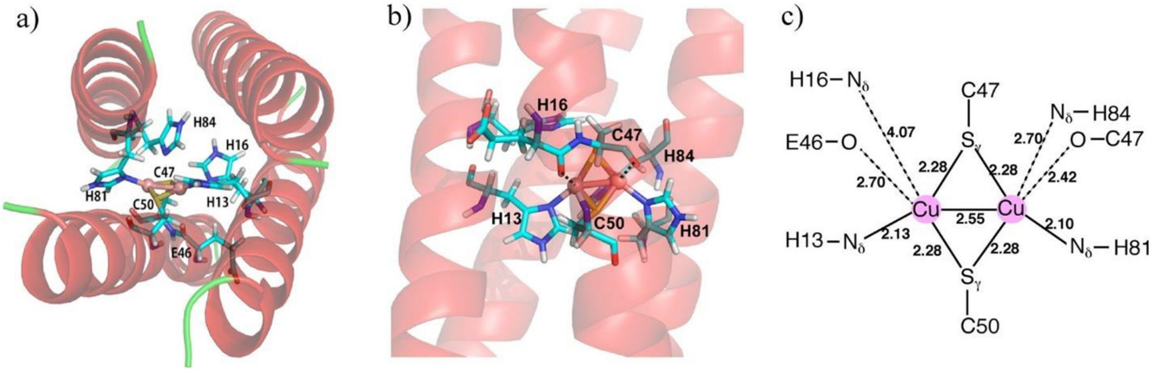

Figure 66:

(**A**) Bottom view, (**B**) Side view, and (**C**) schematic of an energy minimized bi-AM2C–$(Cu)_2$ structure. Dotted lines represent suspected axial interactions. Reprinted with permission from ref 511. Copyright 2012 American Chemical Society.

Author Manuscript

Author Manuscript

Author Manuscript

Author Manuscript

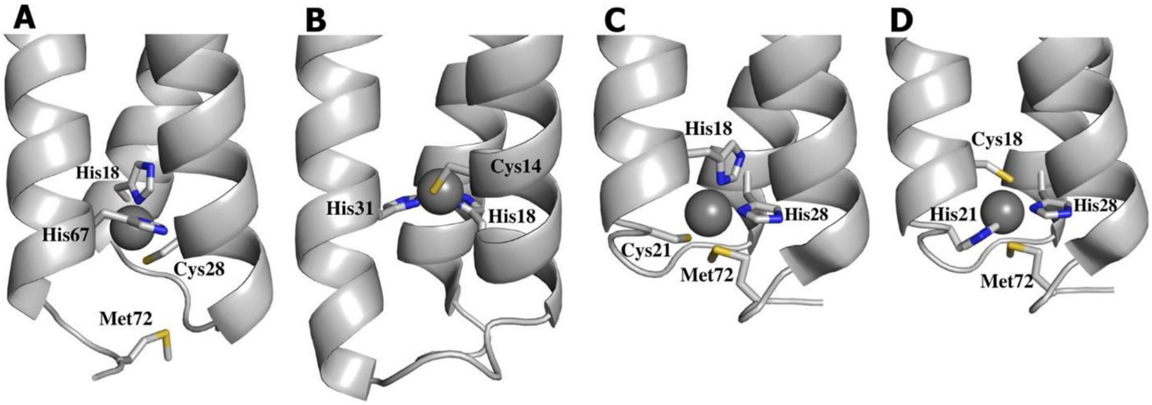

Figure 67:

EXAFS based structural models of (**A**) Cu(I)α_3D-CR1, (**B**) Cu(I)α_3D-ChC2, (**C**) Cu(I)α_3D-CH3, and (**D**) Cu(I)α_3D-CH4. Reprinted with permission from ref 179. Copyright 2015 American Chemical Society

Author Manuscript Author Manuscript Author Manuscript Author Manuscript

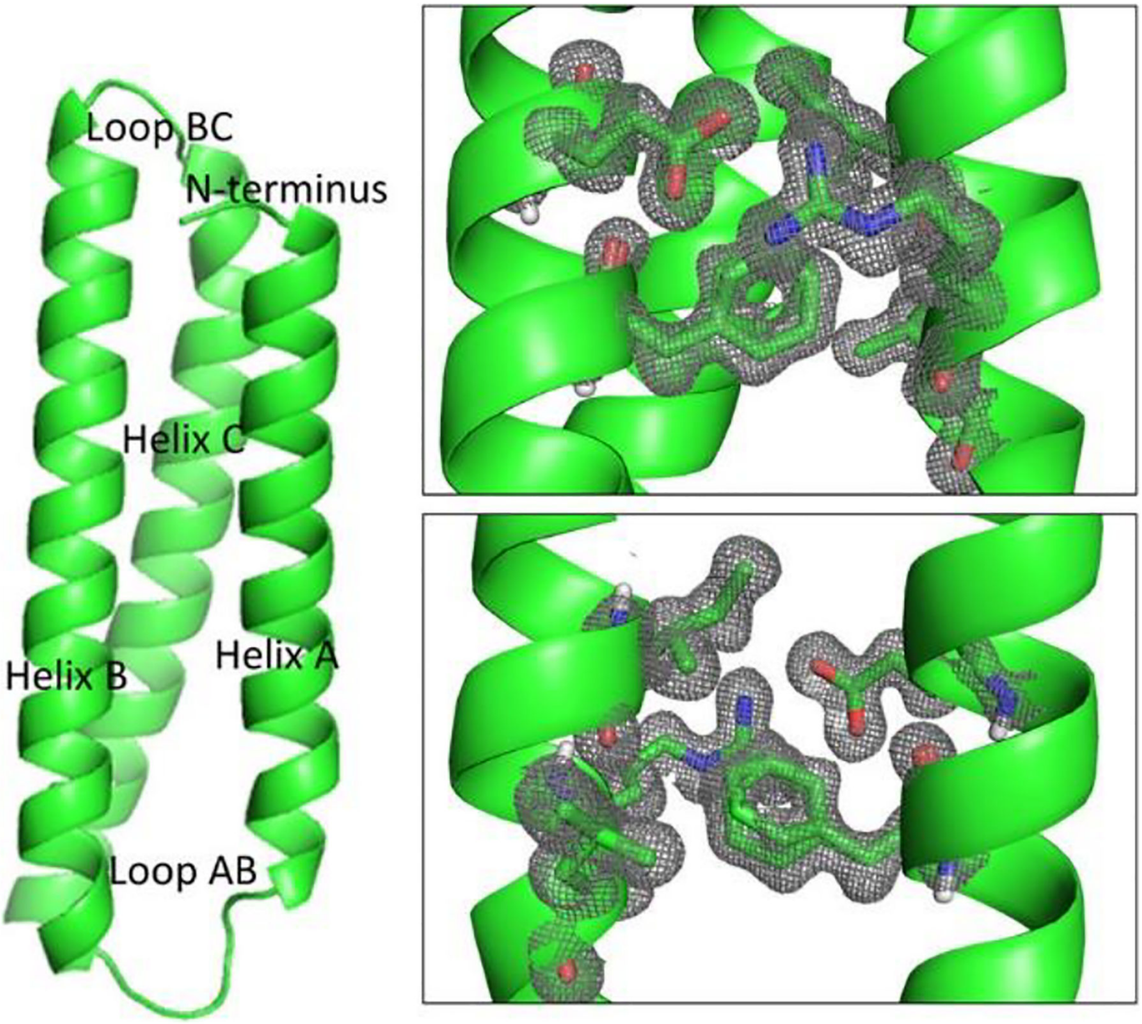

Figure 68:

(Left) Overall secondary structure of GRα_3D. (Right) Overlaid stick representation and the 2Fo – Fc electron density map (gray grid) contoured at 1σ of the Ile21, Arg24, Leu25, Phe38, and Glu41. Reprinted with permission from ref 524. Copyright 2018 American Chemical Society.

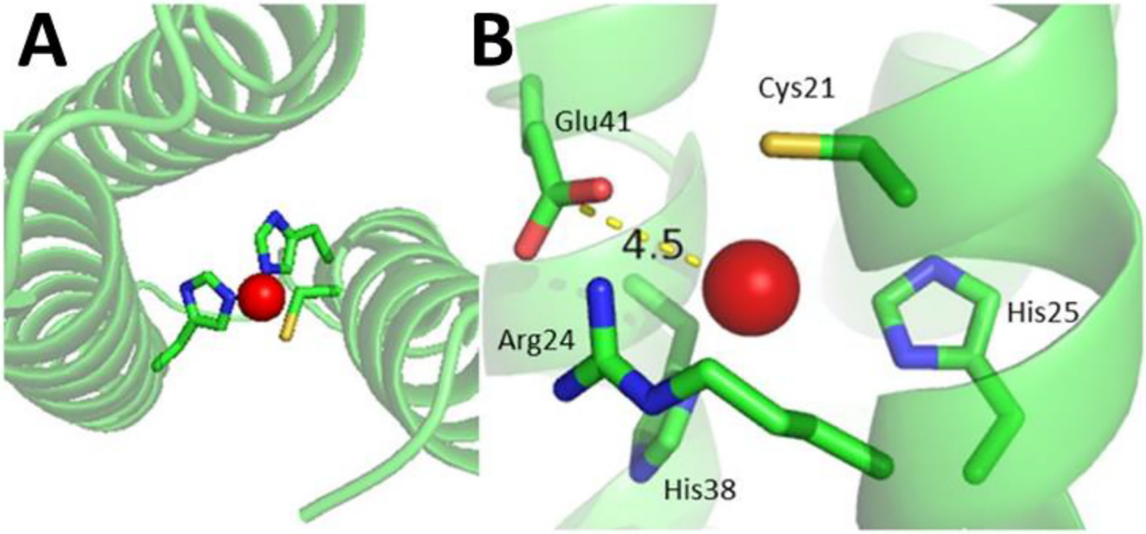

Figure 69:

Pymol made model of GRα_3D-ChC2 highlighting the expected position of the metal binding site from a bird’s eye (**A**) or side view (**B**). Adapted with permission from ref 524. Copyright 2018 American Chemical Society.

Author Manuscript Author Manuscript Author Manuscript Author Manuscript

Author Manuscript

Author Manuscript

Author Manuscript

Author Manuscript

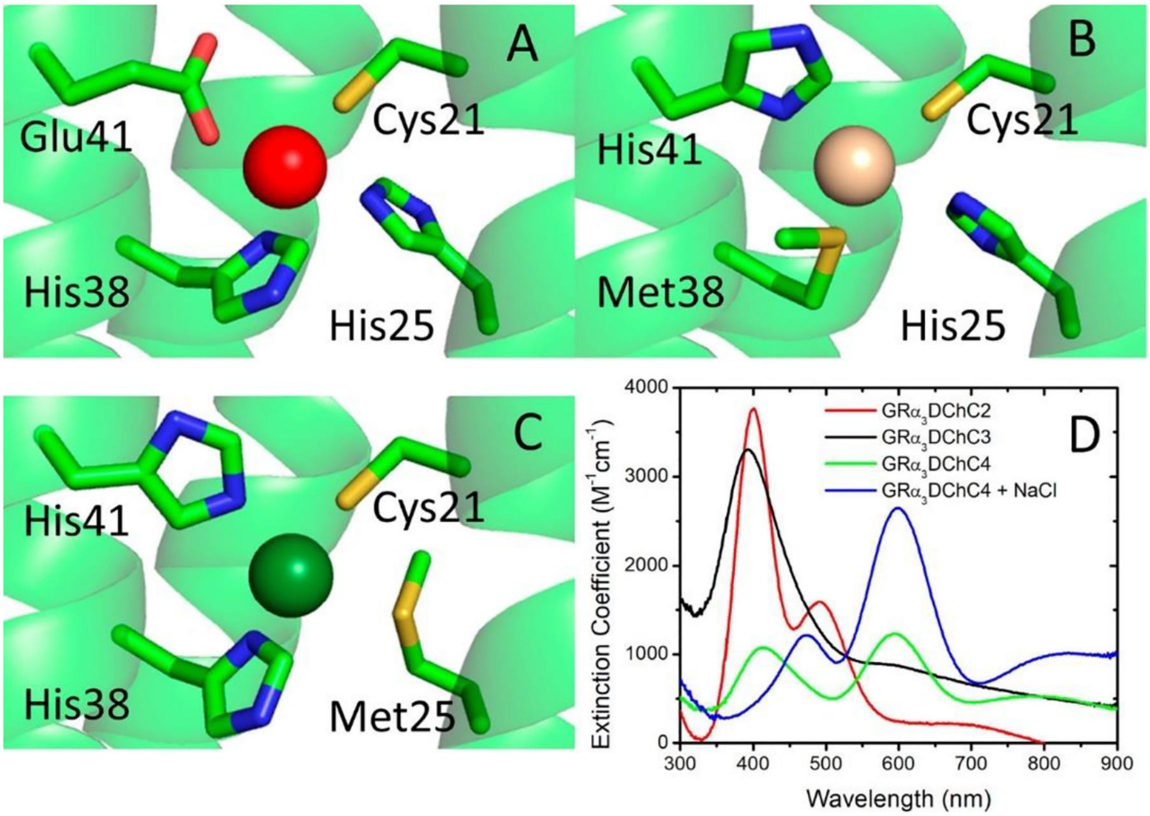

Figure 70:

Pymol created models of (**A**) GRα_3D-ChC2, (**B**) GRα_3D-ChC3, and (**C**) GRα_3D-ChC4 derived from the crystal structure of GRα_3D (PDB 6DS9). (**D**) Optical absorption spectra of each *de novo* designed protein as well as GRα_3D-ChC4 in the presence of excess NaCl. Reprinted with permission from ref 509. Copyright 2020 American Chemical Society.

Author Manuscript

Author Manuscript

Author Manuscript

Author Manuscript

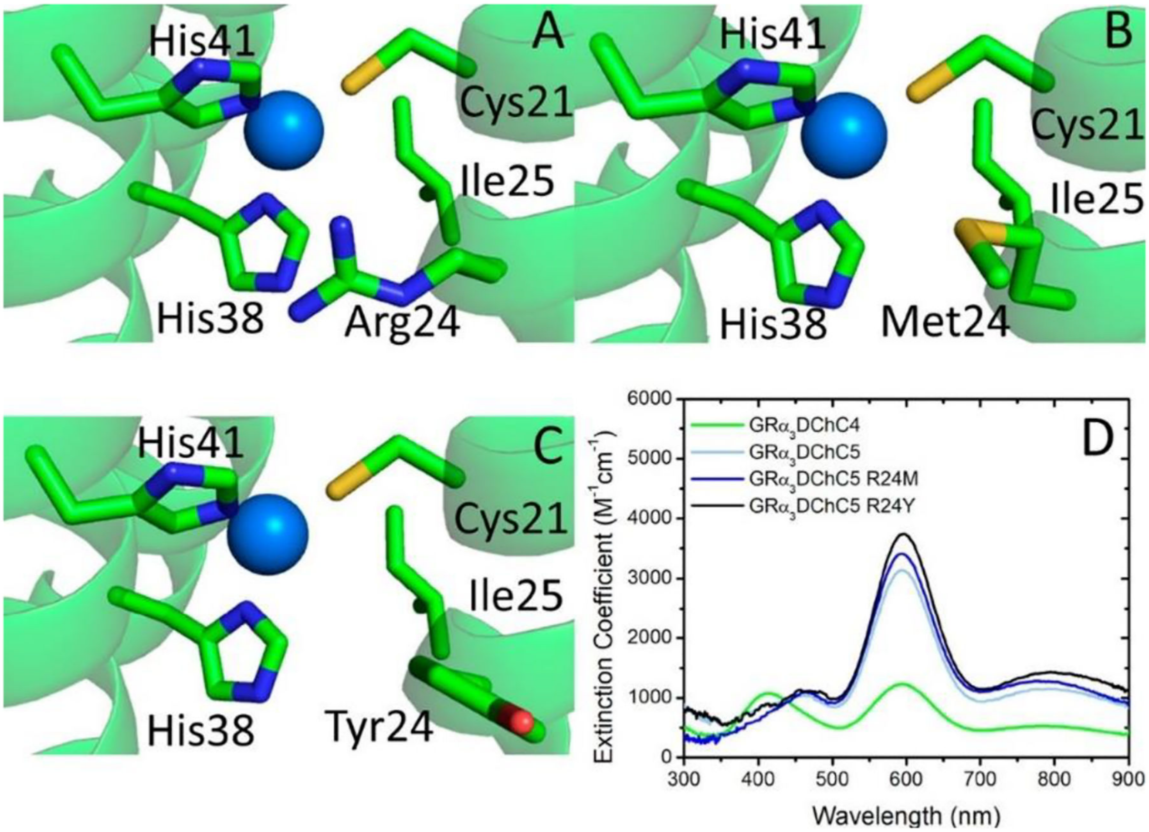

Figure 71:

Pymol created models of (**A**) GRα_3D-ChC5, (**B**) GRα_3D-ChC5 R24M, and (**C**) GRα_3D-ChC5 R24Y derived from the crystal structure of GRα_3D (PDB 6DS9). (**D**) Optical absorption spectra of these proteins compared to the parent construct GRα_3D-ChC4. Reprinted with permission from ref 509. Copyright 2020 American Chemical Society.

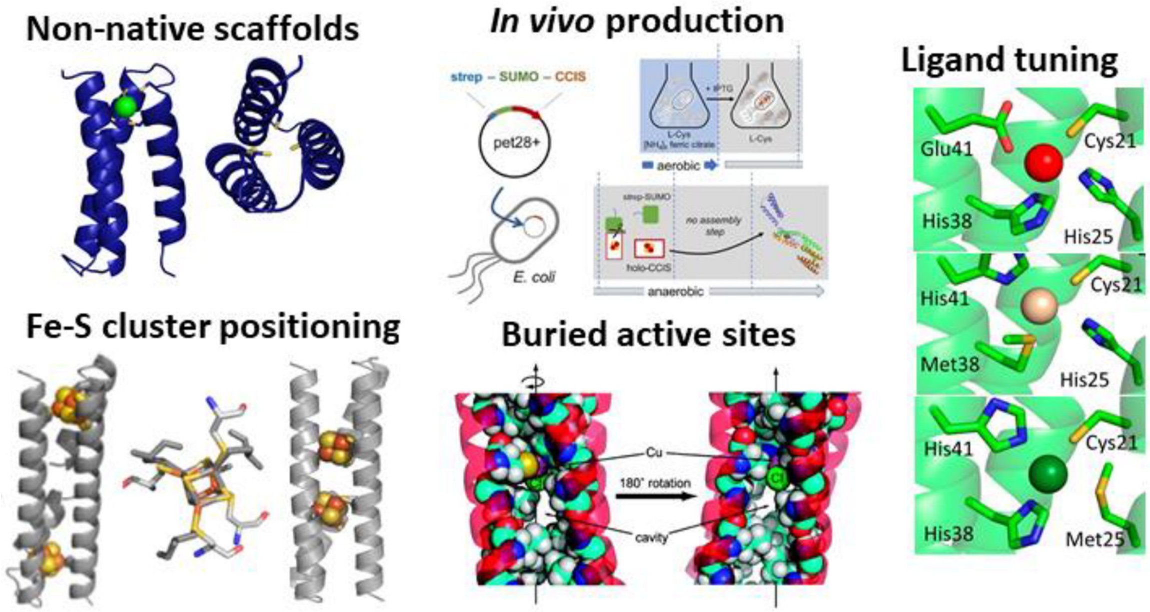

Figure 72:

Summary of recent advances in the *de novo* protein design of electron transfer sites highlighted in this review. Adapted with permission from the appropriate references as specified in source figures previously in manuscript.

Author Manuscript Author Manuscript Author Manuscript Author Manuscript

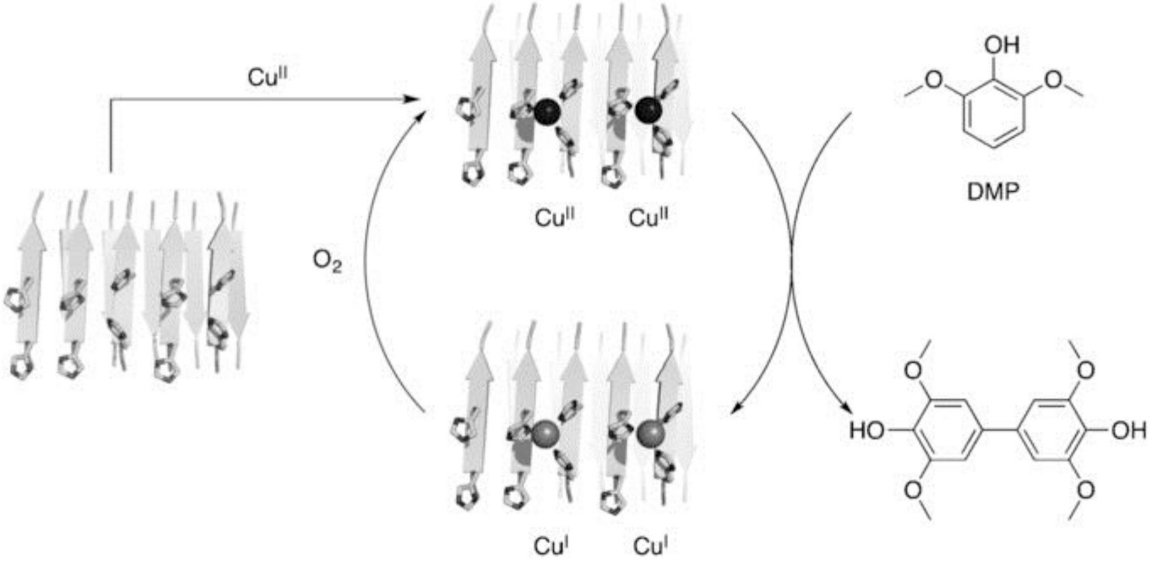

Scheme 1:

Oxidation of dimethoxyphenol mediated by copper bound to amyloid peptides. Reprinted with permission from ref 228. Copyright 2021 American Chemical Society.

Author Manuscript Author Manuscript Author Manuscript Author Manuscript

Table 1.

Comparison of Catalytic Efficiencies for Native and Model Carbonic Anhydrase

Protein	pNPA Esterase	CO_2 Hydrolysis
CA (II)[a] (pH 9.0)[168]	k_{cat}=2.1 s^{-1} K_M=5.8 mM k_{cat}/K_M= 362 M^{-1} s^{-1}	k_{cat}=8.2 × 10^5 s^{-1} K_M= 8.9 mM k_{cat}/K_M=9.2 × 10^7 M^{-1} s^{-1}
TRIL9CL23H (pH 9.0)	k_{cat}=3.8 × 10^{-2} s^{-1} K_M=2.1 mM k_{cat}/K_M=17.6 M^{-1} s^{-1}	k_{cat}=1.8 × 10^3 s^{-1} K_M=10.0 mM k_{cat}/K_M=1.8×10^5 M^{-1} s^{-1}
TRIL9HL23C (pH 9.0)	k_{cat}=1.1 × 10^{-2} s^{-1} K_M= 1.1 mM k_{cat}/K_M= 9.7 M^{-1} s^{-1}	N/A
TRIL9CL19H (pH 9.0)	k_{cat}=1.0 × 10^{-2} s^{-1} K_M=2.3 mM k_{cat}/K_M= 4.5 M^{-1} s^{-1}	N/A
α_3D-H3 (pH 9.0)	N/A	k_{cat}=103 s^{-1} K_m= 7.3 mM k_{cat}/K_M=1.5 × 10^4 M^{-1} s^{-1}
IHIHIQI β-strand (pH 10.3)	k_{cat}/K_M= 360 M^{-1} s^{-1}	N/A
Tris(4,5-di-n-propyl-2-imidazolyl)phosphine (pH 6.55)[230]	N/A	k_2= 2480 M^{-1} s^{-1}
MID1 (pH 9.0)	k_{cat}= 0.28 s^{-1} K_M= 0.42 mM k_{cat}/K_M= 18 M^{-1} s^{-1}	N/A
MID1sc	k_{cat}= 0.011 s^{-1} k_{cat}/K_M= 18 M^{-1} s^{-1}	N/A
MID1sc10	k_{cat}= 1.64 s^{-1} K_M= 1.67 µM k_{cat}/K_M= 9.8 × 10^5 M^{-1} s^{-1}	N/A

[a] CO_2 Hydrolysis was performed at pH 8.8

Table 2.

Comparison of Kinetics Parameters of Native and Model CuNiR.

Protein	k’ (s^{-1})	k_{cat} (s^{-1})	K_M (M)	k_{cat}/K_M (M^{-1} s^{-1})
AfCuNiR pH 6.5[260]	--	620	1.5×10^{-4}	4.1×10^{6}
$[CuMe_2bpa(H_2O)(ClO_4)]^+$ (in water pH 5.5)[6]	--	5.3×10^{-5}	0.0025	0.021
$[CuMe_2bpa(H_2O)(ClO_4)]^+$ (on electrode pH 5.5)[6]	--	0.063	0.0015	42
TRI-H	4.6×10^{-4}	N/A	N/A	N/A
TRI-H L19A	3.5×10^{-2}	0.23 (±0.03)	0.24 (±0.03)	1.0 (±0.3)
TRI-δ_mH	0.12	1.5 (±0.1)	0.18 (±0.02)	8.3 (±0.1)
TRI-δ_mH L19A	0.30	1.5 (±0.1)	0.13 (±0.01)	11 (±0.1)
TRIW-H L19D	2.4×10^{-2}	N/A	N/A	N/A
TRIW-H L26A	2.2×10^{-2}	N/A	N/A	N/A

Author Manuscript Author Manuscript Author Manuscript Author Manuscript

Author Manuscript
Author Manuscript
Author Manuscript
Author Manuscript

Table 3.

Comparison of Kinetics Parameters of Native and Model SODs at Physiological pH

Protein	Activity (M^{-1} s^{-1})	$E_{1/2}$ (mV vs NHE)
MnSOD[268]	3.78×10^9 (pH 7.8)	407
FeSOD[268]	3.25×10^9 (pH 7.8)	220[280]
Cu only SOD[265]	1.8×10^9 (pH 7.25)	N/A
NiSOD[264]	7.0×10^8 (pH 7.5)	290
Cu/Zn SOD[265]	1.2×10^9 (pH 7.25)	400[281]
N-term Cu/Zn model HADHDHKK[282]	1.2×10^7 (pH 7.0)	N/A
GRα_3D H4	1.8×10^6 (pH 7.5)	463
GRα_3D H3D	2.6×10^6 (pH 7.5)	470
GRα_3D H3	3.0×10^6 (pH 7.5)	550
GRα_3D H2DH	12.6×10^6 (pH 7.5)	420

Author Manuscript Author Manuscript Author Manuscript Author Manuscript

Table 4.

Comparison of Spectroscopic Parameters of Rubredoxin and Designed Proteins

Protein	λ_{nm} (Δe) (M^{-1} cm^{-1})	E^0 mV (vs NHE)	Mössbauer (Ox.) (δ and ΔE_Q in mm/s, D in cm^{-1}, A in T)	Mössbauer (Red.) (δ and ΔE_Q in mm/s, D in cm^{-1}, A in T)
α_3DIV- L21C	595 (1200) 491 (2700) 345 (5000)	−75 (pH 8.5)	$\delta/\Delta E_Q = 0.26/-0.5$ $\eta = 0.0$ $D = +0.5$, $E/D = 0.15$ $A_{xx,yy,zz} = (-15.9, -16, -17)$	$\delta/\Delta E_Q = 0.80/-3.07$ $\eta = 2$ $D = +2.5$ $E/D = 0.24$ $A_{xx,yy,zz} = (-5, -4.1, -20)$
Rubredoxin	750 (350)[455] 570 (3200) 490 (6600) 370 (7710)	−90 to +50	$\delta/\Delta E_Q = 0.24/-0.5$[439] $\eta = 0.2$ $D = +1.9$ $E/D = 0.23$ $A_{xx,yy,zz} = (-16, -15.9, -16.9)$	$\delta/\Delta E_Q = 0.70/-3.25$ $\eta = 0.65$ $D = +7.4$ $E/D = 0.28$ $A_{xx,yy,zz} = (-20.1, -8.3, -30.1)$
FeRM1[3]	750 (~500) 600 (~1500) 490 (~2900) 370 (~6800)	+55 (pH 7.5)	N/A	N/A

Author Manuscript Author Manuscript Author Manuscript Author Manuscript

Table 5.

Comparison of Spectroscopic Parameters between Native Cupredoxins and Designed Cupredoxins

Protein	σ LMCT (ε) M^{-1} cm^{-1}	π LMCT (ε) M-1 cm-1	$\varepsilon_\sigma/\varepsilon_\pi$	Half-Life of Cu(II) Signal	E_0 (mV vs NHE)	Cu^{II}–S(Cys) R (Å) ($\sigma^2 \times 10^{-3}$ Å^2)	Cu^{I}–S(Cys) R (Å) ($\sigma^2 \times 10^{-3}$ Å^2)
Nitrosocyanin[494]	390nm (7000)	550nm (2200)	3.2	N/A	+85	2.30 (3.2)	2.21 (4.0)
A cNiR[491]	457nm (2590)	570nm (1490)	1.75	N/A	+240	2.22[a]	2.21[a]
Plastocyanin[488]	460nm (400)	597nm (5200)	0.05	N/A	+372	2.08[a]	2.19[a]
C.s Stellacyanin[489]	448nm (1150)	604 (4000)	0.29	N/A	+184	2.17 (4.2)	2.22 (1.6)
GRα_3D-ChC2	400nm (3760)	490nm (1600)	2.33	8 h	+530	2.23 (10.6)	2.17 (5.8)
GRα_3D-ChC3	395nm (3760)	600nm (870)	3.80	5 mins	--	2.18 (13.1)	2.20 (7.7)
GRα_3D-ChC4	410nm (1070)	595nm (1230)	0.87	15 mins	+475	2.25 (9.5)	2.20 (6.0)
GRα_3D-ChC5	460nm (1035)	595nm (3130)	0.33	30 mins	+475	2.26 (9.1)	2.20 (6.0)
Mop21	400 (6100)	--	N/A	N/A	N/A	2.23[b]	N/A
Mop22	477nm (4040)	525nm (--)	N/A	N/A	N/A	N/A	N/A
Mop23	429nm (--)	571nm (1000)	N/A	N/A	N/A	2.205[b]	N/A
Cu(II)-AM2C	474 nm	616nm	0.30	N/A	N/A	2.30 (10.0)	N/A

[a] Distances from EXAFS analysis were not available, so those determined crystallographically are shown in the table.

[b] Resonance Raman spectral analysis was used to estimate the Cu-S bond length.